Direct drive superconducting generators for INNWIND.EU wind turbines

Agreement n.:	308974
Duration	November 2012 – October 2017
Co-ordinator:	DTU Wind

Document information

Document Name:	**Direct drive superconducting generators for INNWIND.EU wind turbines**
Document Number:	**Deliverable D 3.11. Superconducting generators**
Author:	**Asger Bech Abrahamsen, Dong Liu and Henk Polinder**
Document Type	Report
Dissemination level	PU
Review:	**Henk Polinder**
Date:	**12 February 2018 – resubmission after review**
WP:	**Electromechanical conversion WP 3**
Task:	**Superconducting generators 3.11**
Approval:	Approved by WP Leader

TABLE OF CONTENTS

(INNWIND.EU, Deliverable 3.11, Superconducting generators)

(INNWIND.EU, Deliverable 3.11, Superconducting generators)

1 SUMMARY

This report constitute the final deliverable in the INNWIND.EU project on design and demonstrations of superconducting direct drive generators for wind turbines in the power range between 10 to 20 MW and installed at 50 m of water.

The superconducting direct drive generators examined are radial field electrical machines with the field windings made of superconducting wires and a conventional armature winding based on copper wire wound in magnetic steel structures and operated at ambient temperature.

Two types of superconducting materials examined are the medium temperature superconductor MgB_2 (magnesium di-boride) in the form of wires and the high temperature superconductor $RBa_2Cu_3O_{6+x}$ (Rare-Earth Barium Copper Oxide or RBCO) in the form of coated conductor tapes.

Superconducting field coils have been designed, constructed and tested in order to provide input to the generator design and optimization in terms of the magnetic field dependent critical current of the superconductors and the unit cost of the wire and tapes.

The demonstration of the MgB_2 technology was done by building a race track coil with an opening of 0.3 m and a straight section of 0.5 m holding 5 km of MgB_2 wire. The coil was tested by cooling it down to $T \sim$ 20 K (- 253 ^{o}C) and it was concluded that it reached the design current, but some damages were present in the wires after winding in 8 out of the 10 double pancake coils stacked in the race track coil. The damages resulted in additional heating and a quench of the coil. It was found that some of the soldering connection between the pancakes were damaged and subsequent testing showed that 6 out of 8 pancake coils sustained their properties after the quench. Based on the demonstration then the MgB_2 coil technology is estimated to be at a Technology Readiness Level of TRL = 4 (Demonstrated in laboratory environment). The demonstration coil was designed by DTU and the construction and test was done by SINTEF.

The properties of the MgB_2 wire were used to design and optimize 10 and 20 MW direct drive generators with a range of different topologies with no magnetic steel laminates (air-cored) and varying to magnetic steel laminates on both the field and armature structure (iron-cored). The optimization of the topologies was obtained from a formulation of the Levelized Cost of Energy (LCoE) of the INNWIND.EU turbines and foundations equipped with superconducting direct drive generators. It has been found that with the present critical current of the MgB_2 wire and cost of 4 €/m as provided by Columbus Superconductors, the most feasible topology is the iron cored generator, where expensive superconductor is replaced by cheap magnetic steel. The optimal 10 MW generator is found to have a diameter of D = 8.4 m and a length of L = 1.33 m. It has been integrated as a front mounted generator into the INNWIND.EU nacelle based on the Kingpin design of DNV-GL. The generator mass is estimated to be 286 tons and it holds about 24 km of MgB_2 wire. The generator has been scaled up to 20 MW, where the diameter of D = 10.8 m and length of L = 2.25 m is obtained. The weight is estimated to be 688 tons. This is resulting in a Rotor Nacelle Assembly (RNA) mass scaling as function of the turbine rotor diameter ranging between 178 m and 252 m, which is slightly better than the INNWIND.EU reference design. The MgB_2 generators have been compared to the expected performance of Permanent Magnet Direct Drive generators and it is concluded that the superconducting MgB_2 generator are currently too expensive but most likely also too heavy compared to the PMDD. It is proposed that comparisons between a superconducting and PMDD wind turbine design is done by determining the total cost of the superconductors, the cryostat needed to provide the thermal insulation and the cooling machines needed to keep the low operation temperature and then the cost of the $R_2Fe_{14}B$ (Rare earth iron boron) permanent magnet needed for the direct drive. It has been found that the cryostat and cooling machine cost is about 5 times higher than the cost of the MgB_2 superconductors for the 10 MW generator, which is illustrating that in order to make the superconducting direct drive more competitive, cost reduction on the superconductor will only help a little, but cost reductions on cryostat and cooling machines are needed. This comparison can also be turned around and one can ask what the cost of the $R_2Fe_{14}B$ permanent magnet

(INNWIND.EU, Deliverable 3.11, Superconducting generators)

material should be in order for the two technologies to be equal. Here the analysis is indicating a magnet cost of 114 €/kg would be needed, which is considerable higher than the current magnet cost being a factor of about 4 lower due to production over capacity on the world marked.

A scenario study of the impact of future cost reductions of MgB_2 wire to 1 €/m or improved superconducting properties with a critical current being 4 times higher than the present values has also been conducted. It has been found that the iron cored topology will have a Levelized Cost of Energy (LCoE) very similar to other topologies with the potential to be more light weight. However the conclusion that the cost reductions of the cryostat and cooling machines are needed will also be valid for future more light weight designs.

The generator design and optimization has primarily been done by Delft University of Technology and DTU, whereas the integration into the INNWIND.EU nacelle has been done by DNV-GL. Contributions on the properties of power electronics tailored to the superconducting generators has been done by University of Strathclyde and Aalborg University.

A race track coil made of the high temperature superconducting $RBa_2Cu_3O_{6+x}$ coated conductor tape has been demonstrated by Siemens Wind Power. The philosophy of Siemens Wind Power was that the cooling system would contribute to a reduction of the reliability and an as high as possible operation temperature was therefore required. This is down selecting the high temperature superconductor as the only option with a resulting high cost of the coated conductor tape being about 100 €/m. The coil had an opening of 0.12 m and a straight section of 0.3 m and was made from 3 single pancake coils stacked into one race track coil. It was found that 5 out of 8 initial coils passed the test at liquid nitrogen temperature (77 K) and 3 coils were selected for testing at T = 30 K using liquid neon. It was found that one of the coils suffered from a damage during the first ramp up of the current and 69 % of the design current was reached. Test of AC losses where then performed in order not to burn the coils. It was conclude that the race track coil would be able to reach the design current if ramped further, but time did not allow that test to be performed after the AC loss test. Based on the RBCO coil demonstration it is concluded that the Technology Readiness Level is TRL = 4 (demonstrated in laboratory environment).

The properties of the coated conductor were used to design high temperature superconducting direct drive generators and different topologies with little and a lot of iron were investigated. For the 10 MW generator it was found that a diameter of D = 7 m and a length of L = 1.2 m was optimal. The active materials mass was estimated to be 150 tons and 5.3 km of 12 mm wide coated conductor tape is needed. The design has been scaled to 20 MW, where the diameter is found to be D = 11 m and the length is L = 1.2 m. The coated conductor needed is 10.5 km and the active mass is about 232 tons.

Based on the finding of Siemens Wind Power they conclude that the high temperature superconducting direct drive generators will first be cost competitive with the Permanent Magnet Direct Drive extrapolated to 2020 if the cost of the superconductor is reduced by a factor of 10. Secondly they conclude that the active materials mass will not become lower than for PMDD even if the cost of the superconductor is reduced. These two conclusions made Siemens Wind Power to terminate further work on the high temperature superconducting wind turbine generators and no attempts to construct the cryogenics or integrate the coil technology into a generator was done.

A potential study of partial superconducting direct drive generators has been done to indicate future developments of the superconducting wind turbines. It is suggested to use a target of 2 % loss in the generator with a shear force density twice as what is expected for a Permanent Magnet Direct Drive generator ~ 53 kPa. It is found that the iron cored topologies will be the most efficient method to achieve such a goal, but that more light weight topologies might be possible if high excitation current can be provided by the superconductors. The goal of 2 % loss and 106 kPA shear stress is mapped on to the critical current density plot of most commercial superconducting wires and it is concluded that MgB_2 is mainly suited for the iron cored generators, whereas the RBCO coated conductor can be used for more light weight deigns. Finally it is found that the low

(INNWIND.EU, Deliverable 3.11, Superconducting generators)

temperature superconductor like NbTi and Nb_3Sn can be used for almost all the topologies, but they will have to cooled to T = 4.2 K before they can be used. Since the cost of the cryostat and cooling system seem to be the bottle neck for making the superconducting generators economical feasible, the higher operating temperature are believed to be an advantage.

A roadmap of introducing 10 GW of superconducting wind turbine generators to the European offshore wind energy market is discussed at the end of the report. It is concluded that the production volume of both MgB_2 wire and RBCO tape worldwide is sufficient to fulfil the 10 GW demand. It will probably also be possible to get the cooling machines, which is currently being used in the Magneto Resonant Imaging (MRI) industry, but it is believed that an industrialization of the production of superconducting field coils is needed as well as the manufacturing of the cryostat for those coils. The INNWIND.EU MgB_2 generator topology calls for a cryostat with a warm magnetic pole piece. This is the same concept as the SUPRApower project and the modular cryostat of the SUPRApower project has been mapped onto the INNWIND.EU MgB_2 generators. These cryostats are modular and if they only hold one superconducting coil then there is a need for about 40000 cryostat. Who are going to make those? The wire manufacturer or the wind turbine manufacturer? This will probable depend on the intellectual properties associated with the cryostat, but eventually several independent cryostat manufacturers will probably be most beneficial for the cost reduction.

Finally it is discussed what the disruptive impact of the discovery of a new superconductor like a room temperature superconductor will be. It is argued that for the wind turbine generator application, where high magnetic fields will be present, then one will most likely have to cool the superconductor to about half of the critical temperature T_C in order to obtain a sufficient critical current of the superconductor. Thus even for a room temperature superconductor a cryostat to provide T = 150 K operation will be needed. It should however be said that constructing a cryostat for T = 150 K operation is much easier than for a T = 20 K operation. This means the any new superconductor with a high critical temperature will most likely improve the feasibility of the superconducting generators, but cryostats and cooling machines will still be involved.

(INNWIND.EU, Deliverable 3.11, Superconducting generators)

2 INTRODUCTION

2.1 Motivation for superconducting generators in wind turbine drive trains

Wind turbine drive trains have to supply a torque to the turbine blades in order to keep the rotation of the turbine rotor under control. This torque supply is increasing as the turbine rotor diameter D is scaled up, because the turbine power P is proportional to the turbine rotor diameter

$$P \sim D^2 \tag{2-1}$$

The torque T is related to the rotor rotations speed ω and the power by

$$P \sim T\omega \tag{2-2}$$

The tip speed v_{tip} of the blade however has to be maintained more or less constant in order not to create too much wear of the blade

$$v_{tip} \sim D_1\omega_1 \sim D_2\omega_2 \sim constant \tag{2-3}$$

and a consequence of that is that the larger the blade the slower the rotation speed. By combining these equations then the torque demand scales as

$$\frac{T_2}{T_1} = \frac{\frac{P_2}{\omega_2}}{\frac{P_1}{\omega_1}} = \left(\frac{P_2}{P_1}\right)^{3/2} \tag{2-4}$$

which is growing faster than linear with the power of the turbine. Thus upscaling of a turbine will result in an upscaling of the drive train torque demand where typical values for a 10 MW turbine will be in the order of 10 MNm at a rotation speed of 10 revolutions per minute (rpm).

This high torque demand can either be supplied by a gearbox combined with a medium to high speed generator rotating at 100-1500 rpm or by a direct drive generator connected directly to the turbine shaft. In the latter case of the direct drive generator then one can determine the volume of the generator from the shear force density F_d of the active material sitting in the air gap of a radial ring machine of diameter D_{gen} and length $L_{gen.}$

$$T \sim F_d D_{gen}^2 L_{gen} \tag{2-5}$$

For all radial electrical machines the shear force density F_d is proportional to the peak magnetic flux density in the air gap B_g provided by the field generating active materials and the current loading A_S in the armature windings

$$F_d \sim B_g A_S \tag{2-6}$$

These parameters are often limited for conventional machines, since the peak magnetic flux density B_g is limited to about 1 Tesla by either joule heating of the field windings, saturation of the magnetic steel or the strength of $Nd_2Fe_{14}B$ permanent magnets. The current loading A_S of the armature winding is limited to about 75-100 kA/m by the heating of the armature wires and forced air cooling of the lamination steel. Thus if the power rating of a conventional direct drive generator have to be scaled up by a factor of 2 then that is mostly possible by increasing the size of the machine. Since size is related to the amount of structural steel then this will also result in a larger mass.

Superconducting machines are often utilizing that magnetic flux can be generated in coils wound of superconducting wires without any Joule heating, since the superconductor is practically having a vanishing resistivity as long as the current density J running in the superconductor is below, what

is called the critical current density J_C. This is removing the limitation of the peak magnetic flux density B_g of the shear force density and therefore opens up for machines, which are considerable more compact than conventional machines.

A second possible application of superconducting wires is in the armature windings, whereby the current loading A_S can be increase and resulting in more compact machines. The superconductor will however be exposed to alternating currents and fields, and the superconductor will experience AC losses, which must be removed by a cooling machine connected to the superconducting generator. The challenge is then to ensure that the AC losses and associated cooling losses are low enough to provide a drive train with a total loss in the order of 3-5 % of the rated power of the turbine. AC losses will also be present in the superconducting field winding, but they are orders of magnitude lower.

Finally one can consider to use large blocks of superconducting material to trap magnetic flux providing magnetic flux densities of several Tesla. This will not be discussed any further, since a superconducting coil will be needed to magnetize the blocks as they are cold and then one can just as well build superconducting field winding.

2.2   Superconductor machine topologies

The major topologies of superconducting generators are

a.   Partial superconducting machines with only the field winding being wound of superconducting wires and the armature based on conventional winding at ambient temperature.
b.   Fully superconducting where both field and armature windings are made of superconducting wires.
c.   Bulk superconductors, where pieces of bulk superconductors are magnetized and used as very strong permanent magnets. These machines are challenged by the magnetization step, which must be done with a superconducting coil.

2.3   Types of superconductors

The superconductors needed for a superconducting wind turbine generators must be commercially available in long length up to the kilometre range. This is narrowing down the number of possibilities to the types mentioned in Table 2-1. The primary difference between the superconducting wires are the critical temperature T_C under which they become superconducting.

The low temperature superconductors (LTS) often refer to the two metal alloys NbTi and Nb_3Sn, which are used for Magneto Resonant Imaging (MRI) and high magnetic field magnets for research and accelerators. These wires are often cooled by immersing them in liquid helium (LHe) with a boiling temperature of T_{LHe} = 4.2 K or superfluid liquid helium at $T_{LHe,super}$ = 2.2 K.

The medium temperature superconductors (MTS) often refer to the metallic compound MgB_2 discovered in 2001, which is considered as a possible replacement for NbTi, but operating at a temperature of 10-20 K, where cryocooler machine can replace the liquid helium. MgB_2 wires for Magneto Resonant Imaging (MRI) are therefore being developed, because it might expand the usage of the MRI technique to hospitals in regions, where liquid helium is not easily supplied, but where a cooling machine can be supplied from the electricity grid. More recent types of medium temperature superconductor are the Fe based material family discovered in 2006, but they have not yet been introduced in commercial wires (Pallecchi, Eisterer, Malagoli, & Putti, 2015).

The high temperature superconductors (HTS) often refer to a series of ceramic compounds, which were first developed for the $Bi_2Sr_2Ca_2Cu_3O_{10+x}$ (Bi-2223) ceramic phase enclosed in tubes of silver and drawn into long round wires or rolled flat into tapes. The critical temperature of the Bi-2223 and Bi-2212 compounds are more than 4-5 times higher than the low temperature superconductors and one might think that is the origin of the name "high temperature". This is of

course true, but another more fundamental difference is that the mechanism responsible of making the electrons of the ceramic to pair up into superconducting electron pairs is not the same as for the low temperature superconductors. In the low temperature superconductor the coupling between the electrons in the superconducting electron pairs is provided by a distortion of the crystal lattice (phonon mediated), but for the high temperature superconductors the mechanism is speculated to be of magnet character and explaining this coupling is considered as one of the grand challenges of solid state physics. A consequence of the new pairing mechanism is a much higher critical temperature T_C and this is reflected in the name of the class "high temperature superconductors". It should be mentioned the critical temperature of the HTS are all higher than liquid nitrogen (LN_2), which is much cheaper then liquid helium used to cool the low temperature superconductors.

The development of the Bi-2212 and Bi-2223 wires and tapes is often called the first generation (1G) of high temperature superconductor (HTS), but the need of silver to encapsulate the ceramic turned out to put a limitation on how low a wire cost that can be reached.

The $RBa_2Cu_3O_{6+x}$ (RBCO) ceramic compound was suggested as an alternative to Bi-2223, because the superconducting properties are superior to the Bi-2223 compound. The R in the chemical formula for RBCO can be most of the rare earth elements or Y from the periodic table. The challenge of using RBCO is however that the crystalline grains of the ceramic phase must be aligned within a few degrees in order to allow the superconducting electron pairs to flow freely through the wire. This has been solved by making the coated conductor, where a flat metal substrate is covered by several nm-thin layers of ceramic buffer materials and then a RBCO layer of a few micro meters thickness is deposited. The entire tape is then covered with a micro meter thin silver layer and finally enclosed by a copper layer with thickness between 20-100 micro meter. The coated conductor is often called the second generator (2G) of the high temperature superconductor wires and is believed to hold the potential for large cost reduction as the production volume is scaled up.

The focus of the INNWIND.EU project is primarily on the MgB_2 and the RBCO superconductors, because they can be operated without the need of liquid helium and thereby by the use of cryogenic cooling machine. The NbTi low temperature superconductor is considered a baseline representing a very mature wire technology.

Superconductor class		Type	T_C [K]	Cost [€/m]
Low temperature		NbTi	10	0.4
		Nb_3Sn	18	3
Medium temperature		MgB_2	39	1-4
High temperature	(1G)	$Bi_2Sr_2Ca_1Cu_2O_{8+x}$ (Bi-2212)	90	20
	(1G)	$Bi_2Sr_2Ca_2Cu_3O_{10+x}$ (Bi-2223)	110	20
	(2G)*	$RBa_2Cu_3O_{6+x}$ (RBCO)	93	90-100

Table 2-1 Classes and types of commercial superconducting wires along with the critical temperature T_C provided in the Kelvin [K] temperature scale with the zero point of -273.15 °C. Costs are reproduced from (Jensen , Mijatovic, & Abrahamsen, Development of superconducting wind turbine generators, 2013) and updated with INNWIND.EU quotations (* based on 12 mm tape width).

(INNWIND.EU, Deliverable 3.11, Superconducting generators)

2.4 Types of cooling methods

Since the critical temperature of all the commercial superconductor wires are still considerable below ambient temperature then special cooling methods are needed.

Liquid cryogen in cryostat and refilling cryogen

The simplest cooling method is to immerse the superconductor wire into the liquid form of the gasses of the period table, with liquid helium (LHe, T_{LHe} = 4.2 K) and liquid nitrogen (LN$_2$, T_{LN2} = 77 K) being the most used. These liquids are often called cryogens, because the low boiling point temperature calls for a thermally insulated container called a cryostat. The superconductor can then be kept cold in the cryostat by allowing the cryogen to evaporate and then to refill the cryostat with new liquid cryogen produced by a separate machine called a liquefier. This calls for a lot of infrastructure and often manual work, which might be suitable for a lab, but not for a wind turbine generator, which must be operating with maintenance intervals of 1-2 years.

Liquid cryogen with zero boil off provided by a cooling machine

A solution to avoid the handling of refilling cryogen onto a cryostat is to place a cryocooler machine inside the compartment, where the evaporating gas is collected, and then to cool the gas back into the liquid state, whereby it will drop down into the liquid. This is the method that has been adopted by the Magneto Resonant Imaging (MRI) industry, where a cryocooler machine is often sitting at the top of the large donut shaped liquid helium cryostat holding the main superconducting coil surrounding the patient. This method is well established, but not very suited for a rotating application like the wind turbine if the cryostat is placed in the rotating frame.

Circulation of cold gas

Cooling of a superconducting coils can also be obtained by circulating a cold gas in tubes connected to the coil support and to a cooling machine removing the heat introduced by the coil or the surroundings. A cold fan is needed to provide the circulation and this result in a need for maintenance, which is not ideal for the wind turbine generator application. The coil can be mounted in a vacuum inside the cryostat and the cold gas is only present in the circulation tubes. Any leak of the cold gas from the circulation tubes and into the main vacuum will be problematic, since the thermal insulation of the cryostat will be reduced heavily.

Circulation of liquid cryogen

One can also circulate the liquid cryogen in tubes connected to superconducting coils at one end and connected to a cooling machine at the other end. Again a circulation fan is needed and result in the demand for maintenance. A challenge of this method is that large pressures will build up if the liquid cryogen is transferred to the gas phase due to a large inflow of heat in case of abnormal operation.

Conduction cooling in vacuum using cooling machines

Superconducting coils can be cooled in vacuum inside a cryostat by connecting highly thermally conduction material to the coil in one end and to a cryogenic cooling machine in the other end. The most used material for such a thermal bridge is high purity copper or even oxygen free copper sheets or plates, because it holds some of the largest thermal conductivities at low temperatures. The advantage of this method is that the superconducting coils will heat up slowly if the cooling machines are turned off, but there is no chance of building up large pressures caused by liquid cryogens turning into the gas phase as was the case above. A second method of providing high thermal conductivity between parts is to use heat pipes, where a gas- liquid phase transition is taking place inside a metal tube. Any leaking of the gas from the heat pipe will again decrease the main vacuum and result in poor thermal insulation.

2.5 State of the art superconducting wind turbine generators

During the last decade there have been several design proposals on superconducting wind turbine generators and the main trends will be outlined below in terms of the preferred superconductor of the different designs. Two comprehensive reviews of the superconducting generator have recently been provided as part of the INNWIND.EU project. The first is found in the report of the deliverable D.3.12 "Summary Report for Work Package 3.1.2 – Investigation of HTS Super-Conducting Direct Drive Generators" provided by Siemens Wind Power (Azar & Thomas, 2016) and the second is provided in the PhD thesis of Dong Liu as shown in Appendix A of this report (Liu D. , 2017).

2.5.1 Low temperature superconductors

NbTi is the most mature and well proven superconducting wire, which has also been proposed used for a 10 MW superconducting wind turbine generator by GE global research in 2012 (Fair, 2012). The advantage of the NbTi is the high peak magnetic air gap flux density reaching about 2.6 Tesla, which can provide a high shear force density of 179 kPa causing the generator to have dimensions of D_{gen} = 4.83 m and a length of L_{gen} = 1.88 m. This is about half the size of the permanent magnet direct drive wind turbine generator used for comparison in (Fair, 2012). The weight of the generator is 145 tons and the cost is estimated to be 2.2 M\$.

NbTi is the cheapest of the superconducting wires, as shown in Table 2-1, and will therefore not constitute a large portion of the generator cost. The main drawback of the 10 MW GE Global Research design is however the low operation temperature of the superconductors and the need for advanced cooling (Stautner, Fair, & et, 2013). A retractable cryocooler is intended to cooldown the generator to operations temperature of T = 4.2 K, whereas two smaller cryocooler will keep the generator at operation temperature with the help of a net of helium heat pipes distributed in the rotor support structure. Finally the design is proposing to have a superconducting field coil sitting stationary on the inner ring of the generator and then to have a rotating outer armature winding. This means that a slip ring system will have to pass all the current of the generator from the rotating blade frame and back to the stationary tower frame. Such slip rings are used in Double Fed Induction Generator (DFIG) wind turbines, where about 1/3 of the turbine power is supplied to the rotor windings. Such a slip ring arrangement will increased the need for maintenance.

The NbTi superconducting direct drive generators have also been investigated by the group of R. Qu in 2014 (Y. Liu, 2015). They have proposed a 13.2 MW machine with a diameter of D_{gen} = 7.3 m and L_{gen} = 0.98 m being larger than the GE global research design. The weight is 165 tons and the cost is 2.07 M\$.

There have been no major proposals of using Nb_3Sn wire for superconducting generators most likely due to the fact that coils made of Nb_3Sn are referred to as "wind and react". This means that the wire first have to be wound into the shape of the coil, the wires must then be heated to 600-700 °C for weeks in order to form the Nb_3Sn phase inside the wires and finally one will have to apply the insulation to the wires without breaking the brittle Nb_3Sn phase in the middle of the wire.

It should however be mentioned that Nb_3Sn is one of the primary wires for providing the magnetic confinement of the fusion plasma in the International Thermonuclear Experimental Reactor (ITER), which is under construction in France. A large global effort has been made to ramp up the Nb_3Sn wire production volume to deliver the 100000 km (500 tons) of wire for ITER and also to qualify the wires for the fusion application. This ramp up have changes the annual production from 15 tons/year before to 100 tons/year in the period from 2008 to 2015 and distributed among 9 strand manufactures (ITER, 2017).

2.5.2 Medium temperature superconductors

The advantage of increasing the operation temperature from T = 4.2 K of the Low Temperature Superconductors (LTS) to a temperature higher than T = 20 K is high, since the specific heat capacity of the most solids used for constructing the cold parts of the coil support is increasing considerable, whereby heat releases in the superconductor coils are causing less temperature changes. Secondly the heat conduction of most metals is peaking around T = 20 K making it easier to construct conduction cooled coil configurations avoiding the usage of helium heat pipes.

MgB_2 is seen as the enabling technology for using conduction cooled coils operated around T = 20 K for direct drive wind turbines.

This technology has been investigated as part of the INNWIND.EU project and the results will be outlined in the following sections. It has also been investigated by several other companies and universities and some of the main findings will be highlighted below.

The SUPRApower project funded under the European Union FP7 scheme has investigated MgB_2 coils in a modular cryostat that can be placed onto warm iron poles of an inner rotor for a 10 MW wind turbine generator (Suprapower, 2017). The operation temperature is T = 20 K and the armature winding is made of copper (Marino, et al., 2016). References to this type of cryostat will be made in this report under the discussion of the feasibility of different machine topologies of the superconducting wind turbine generators.

The machine designer S. Kalsi has proposed a 10 MW MgB_2 wind turbine generator based on a fully superconducting generator with both a superconducting rotor and armature winding (Kalsi, 2014). The generator will need twice the amount of cooling equipment of the partial superconducting generator and a cryostat for both field and armature part of the generator.

Finally American Magnetic Lab (AML) has proposed a 10 MW superconducting wind generator based on double helix winding of both rotor and armature (Advanced Magnet Lab, 2017).

2.5.3 High temperature superconductors

One might think that using high temperature superconductors for the wind turbine generators would allow cooling with liquid nitrogen and thereby simplifying the cooling system as well as reducing the cost of the generator. This is only partly true, because the critical current density J_C of the HTS wires is decreasing rapidly if the operation temperature $T_{operation}$ is approaching the critical temperature of the superconductor T_C. Thus one often have to cool the HTS well below about half of the critical temperature T_C, before the HTS are utilized, and $T_{operation}$ ~ 30-40 K is often proposed in the case of second generation coated conductors based on $RBa_2Cu_3O_{6+x}$ (RBCO) superconductors.

The first industrial proposal on using the high temperature superconductor for wind turbine was provided by American Superconductors in the form of the 10 MW Seatitan turbine (Snitchler, 2010). The design of the generator is ready to be licensed to wind turbine companies who has an interest of using it, but it seems that such a match has not materialized yet. AMSC is producing the second generation (2G) coated conductor based on RBCO and would be able to provide both the tape and wind generator technology. A recent joint venture between AMSC and BASF on the further development of the coated conductor technology is believed to hold the potential of cost reductions of the coated conductor and might enable the usage of high temperature superconductor for wind generators ((AMSC), 2016).

In the INNWIND.EU project the high temperature superconductor has been investigate for the direct drive generator application by Siemens Wind Power and the results can be found the deliverable report D3.12 of the INNWIND.EU project (Azar & Thomas, 2016). The main findings will be highlighted in this report.

The EU funded ECOswing project lead by the wind turbine company Envision is demonstrating the construction of a full size 4 MW direct drive high temperature superconductor generator with the intension of installation in the two bladed test turbine of Envision (ECOswing, 2017).

The construction and test of a coated conductor based armature winding for a fast rotating 2 MW DFIG wind turbine generator has recently been reported by Gamesa Innovation and Technology. The coated conductors are operated at T = 30 K and cooled by a combination of a liquid Nitrogen tank and a cryocooler (Muñoz, et al., 2017).

In the US there is also an industrial investigation of the high temperature superconducting direct drive wind generator by the University of Houston and Westinghouse as well as Brookhaven National Lab and American Superconductors (REACT, 2016). The collaborations have been funded by the ARPA-E REACT program under DOE and the consortium has reported that the critical current density of the coated conductors has been increased by a factor of 4 for the wind generator application.

(INNWIND.EU, Deliverable 3.11, Superconducting generators)

2.6 Specifications of the INNWIND.EU reference turbine and drive train design targets

One of the strengths of the INNWIND.EU project is that the entire turbine and offshore foundation are co-developed, whereby knowledge on the key performance indicators of the different components are available. This is particular useful for the development of new types of drive trains for the innovative INNWIND.EU turbines, because a base line design is provided as a starting point. Below the reference information for the drive train development is provided from the INNWIND.EU reference turbine.

2.6.1 Turbine

The INNWIND.EU reference turbine for 10 MW power rating and with a rotor diameter of $D_{blade, 10 MW}$ = 178 m has been defined in the deliverable report D1.21 (Bak, et al., 2013). The turbine is designed for an IEA wind class Ia. The important information in terms of drive train development is the mechanical power curve of the turbine rotor as function of wind speed as shown in Figure 2-1. The cut in rotation speed is 6 rpm, which is increased to 9.6 rpm at rated power. The torque at rated power thereby becomes T = 10.6 MNm, which must be supplied by the drive train. The 20 MW reference turbine with a rotor of $D_{blade, 20 MW}$ = 252 m has been defined much later in the INNWIND.EU project. For simplicity of the drive train development then the power curve of the 20 MW turbine is assumed to be a factor of two higher than what is shown in Figure 2-1 and with a rotation speed of 6.8 rpm scaled by the rotor turbine size.
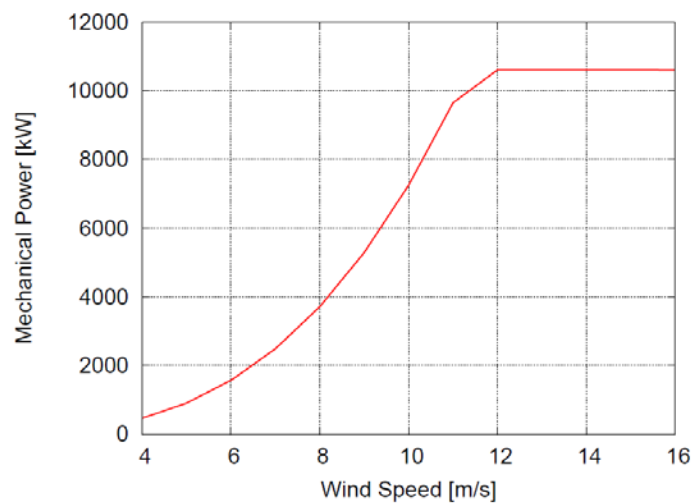
Figure 2-1 Mechanical power curve of 10 MW INNWIND.EU reference turbine. The rotation speed at rated power is 9.6 rpm and the drive train efficiency is assumed to be 94 %. Reproduced Figure 3.12 from (Bak, et al., 2013).

2.6.2 Foundation

The foundations developed as part of the INNWIND.EU project is targeted for a water depth of 50 m, which is relatively deep compared to the main stream offshore foundation used in European waters (10-30 m). The reference foundation for the 10 MW INNWIND.EU reference turbine is of the jacket type. In the design of the drive train only the cost of the foundation is taken into account in order to obtain an estimate of the impact of the drive train cost on the levelized cost of energy (LCoE). A more detailed analysis will also investigate the impact of the drive train mass on the resonances of the entire turbine and foundation structure in order to estimate the impact on Levelized Cost of Energy.

(INNWIND.EU, Deliverable 3.11, Superconducting generators)

2.6.3   Drive train

The reference drive train of the INNWIND.EU 10 MW reference turbine is a two stage gearbox followed by a medium speed synchronous generator. The properties of the reference drive train is shows in Table 2-2.

Rated Rotor Speed	9.6 rpm
Rated Generator Speed	480 rpm
Gearbox Ratio	50 : 1
Electrical Generator Efficiency	94
Generator Inertia about High-Speed Shaft	1500.5 kgm^2
Equivalent Drive-Shaft Torsional-Spring Constant	2,317,025,352 Nm/rad
Equivalent Drive-Shaft Torsional-Damping Constant	9,240,560 Nm/(rad/s)

Table 2-2 Properties of the drive train of the 10 MW reference turbine. Reproduced from Table 6.3 of (Bak, et al., 2013).

2.7   Organization of work on superconducting generators in INNWIND.EU

The task 3.1 on developing superconducting direct drive generators for the innovative INNWIND.EU turbines is organized into 3 sub-tasks:

1) Development of superconducting direct drive generators for wind turbines (D3.11)
2) Demonstration of a HTS pole pair and direct drive generator design (D3.12)
3) Demonstration of a scaled MgB$_2$ rotor field coil (D3.13)

The two last sub tasks are intended to provide the experimental properties of the HTS coated conductor tapes as well as the MgB$_2$ wire for the development of the superconducting direct drive generators in 1) targeted primarily for the 10 MW INNWIND.EU reference turbine. Once the designs for the 10 MW generators were established then they were scaled to the 20 MW INNWIND.EU turbine.

The tasks 1) and 3) were mainly conducted by the Technical University of Delft (TUD), SINTEF and the Technical University of Denmark (DTU) and with the focus only on MgB$_2$ generators. The second task was conducted by Siemens Wind Power with the focus only on high temperature superconducting (HTS) direct drive generators. The second task was originally intended to be "Confidential", but is was later decided that the research could be made publicly available as in the form of the deliverable D3.12 (Azar & Thomas, 2016).

The superconductor direct drive generator task 3.1 is part of the work package 3 electromechanical conversion, which consist of the following tasks:

3.1   Superconductor direct drive generator (SCDD)
3.2   Pseudo magnetic direct drive (PDD)
3.3   Power electronics for SCDD and PDD
3.4   Nacelle integration

The superconducting generator task has been interacting with task 3.3 on power electronics for superconducting direct drive generators and well as task 3.4 for the mechanical integration of the superconducting direct drive generator into the nacelle.

(INNWIND.EU, Deliverable 3.11, Superconducting generators)

2.8   Organization of task 3.1 Superconducting generators

This report provide the documentation of the work done in task 3.1 as part of the INNWIND.EU project. It will therefore outline the generator design philosophies developed and followed in the task as well as summarize the findings of the task on power electronics 3.3 and nacelle integration 3.4.

At the time of writing this report the task 3.12 Demonstration of a HTS pole pairs has been finished and reported in the deliverable report D3.12 (Azar & Thomas, 2016). These works will only be summarized and the main findings outlined.

The task 3.13 on demonstrating the scaled MgB_2 rotor field coil has almost been completed, with the construction and initial testing documented in the deliverable 3.13 (Magnusson, Hellesø, Paulsen, Eliassen, & Abrahamsen, 2016). The final measurements of the coil and the interpretations are however provided in this report and will be used to discuss the technical readiness level of the MgB_2 coil technology.

Finally it should be said that the details of the superconductor direct drive generator design method for MgB_2 has been reported by the PhD student Dong Liu from Delft University of Technology and is attached to this report as appendix A. References to the work of D. Liu will be provided and the main findings will be discussed.

Thus the intension of the this report is to document the information exchange between the tasks 3.1, 3.3 and 3.4 of the work package, to summarize and discuss the finding and finally draw the conclusion about the possible impact of superconducting direct drive generators on the Levelized cost of Energy (LCoE) of the INNWIND.EU innovative turbines.

(INNWIND.EU, Deliverable 3.11, Superconducting generators)

3 LEVELIZED COST OF ENERGY (LCOE)

The concept of Levelized Cost of Energy (LCoE) has been introduced to the wind energy sector in order to be able to compare different energy production technologies from the investment point of view as a society. Thus the question posed is often if a country should invest in a natural gas fired power plant or a wind farm in order provide an additional 1-5 TWh of electric energy the energy mix of a country (a 500 MW gas power plant and 1 GW offshore wind farm of 10 MW turbines will roughly provide around 4 TWh). At the end of life of a power producing unit (ex. Gas fired power plant or wind farm) one can ask how much was the total cost C for the producing all the energy E and then calculate the Cost of Energy (CoE) by

$$CoE = \frac{C}{E} \tag{3-1}$$

In the above definition in (3-1) of Cost of Energy provides a tool for analysing the historic production from a power producing technology, but it can also be used as a predictive tool if a model for the expected cost and energy production can be provided over time.

From an investor point of view one expect a certain interest rate w of an investment every year. This means that a cost that is first expected after several years do not need the full amount of money reserved at beginning of the invest, because a smaller amount is expected to grow before the payment is needed. So if we want to determine the cost reservation $C_{t,0}$ at the beginning of the investment due to a cost C_t at year t then this must be downscaled by the expected interest rate w by investing in other energy plants before the cost C_t will have to be payed

$$C_{t,0} = \frac{1}{(1+w)^t} C_t \tag{3-2}$$

The same consideration must be implemented in the evaluation of the energy production, because that is the source for generating income I, which will be proportional to the sales price S of the electricity. Therefore the income I_t in year t due to an energy production E_t will be worth less $I_{t,0}$ at the beginning of the investment, because it cannot be re-invested with an interest rate of w in the period in between.

$$I_{t,0} = \frac{1}{(1+w)^t} S_t E_t \tag{3-3}$$

In order to compare the ratio between cost and income for a power producing plant with a design life time of LT at the beginning of the investment one have to sum over all the cost contribution as given by (3-2) and the income given by (3-3), whereby the total levelized cost C_L and income I_L becomes

$$C_L = \sum_{t=0}^{LT} \frac{1}{(1+w)^t} C_t \tag{3-4}$$

$$I_L = \sum_{t=0}^{LT} \frac{1}{(1+w)^t} S_t E_t \tag{3-5}$$

It is however difficult to predict the electricity sales price as well as possible subsidy schemes for decades in the future, but if the sales price is considered a constant $S_t = S_0$, then one can write the ratio between cost and income

$$\frac{C_L}{I_L} = \frac{\sum_{t=0}^{LT} \frac{1}{(1+w)^t} C_t}{\sum_{t=0}^{LT} \frac{1}{(1+w)^t} S_t E_t} = \frac{1}{S_0} \frac{\sum_{t=0}^{LT} \frac{1}{(1+w)^t} C_t}{\sum_{t=0}^{LT} \frac{1}{(1+w)^t} E_t} = \frac{1}{S_0} LCoE \tag{3-6}$$

where the last factor is often referred to as the Levelized Cost of Energy (*LCoE*), because the ratio between levelized cost and income can be determined if one divide with the constant electricity sales price S_0. This is illustrating that the economic feasibility of two different energy producing

(INNWIND.EU, Deliverable 3.11, Superconducting generators)

technologies can be compared before an investment discussion is made, because if the same electricity sale price S_0 is assumed then the technology with the lowest Levelized Cost of Energy will provide the lowest ratio between cost and income.

Using the above concept and by looking at equation (3-6) one can see that a levelized energy production E_L can be defined

$$E_L = \sum_{t=0}^{LT} \frac{1}{(1+w)^t} E_t \qquad (3\text{-}7)$$

where E_t is the annual energy production in year t, w is the expected interest rate of investments in the energy sector and LT is the design life time of the energy producing technology. It should be noted that E_L is not indicating that less energy is produced physically, but that production and thereby income in the future cannot be reinvested before that have been produced.

The Levelized Cost of Energy (*LCoE*) can be defined by

$$LCoE = \frac{C_L}{E_L} = \frac{\sum_{t=0}^{LT} \frac{1}{(1+w)^t} C_t}{\sum_{t=0}^{LT} \frac{1}{(1+w)^t} E_t} \qquad (3\text{-}8)$$

where C_t and E_t are the cost and energy production in year t, w is the expected interest rate of investments in the energy sector and LT is the design life time of the energy producing technology. This definition of the Levelized Cost Of Energy (LCOE) is similar to the "developer – pre tax" version of the Levelized Cost Of Energy as defined by the MEGAVIND collaboration (MEGAvind, 2015).

3.1 Definition of Levelized Cost of Energy with focus on drive train

The concept of Levelized Cost of Energy (LCoE) will be applied to the evaluation of different superconducting direct drive generators designed in the INNWIND.EU project. In this chapter the costs associated with the INNWIND.EU wind turbine are presented in more detail in term of Capital Expenditure and Operational expenditures. The calculation of the annual energy production is outlined and based on the Weibull wind speed distribution of the INNWIND.EU reference turbine installed in the North Sea. Finally the specific materials cost of the generator parts are introduced and a simple sensitivity analysis of the impact of the drive train properties is performed.

3.1.1 CAPital EXpenditures (CAPEX)

The cost per year as introduced in equation (3-8) is often composed of 4 main contributions

$$C_t = C_{CAPEX,t} + C_{OPEX,t_t} + C_{DECOM,t} + C_{FUEL,t} \qquad (3\text{-}9)$$

where

$C_{CAPEX, t}$ is the CAPital EXpenditure needed in year t
$C_{OPEX, t}$ is the OPeration and maintenance Expenditure needed in year t
$C_{DECOM, t}$ is the DECOMmissioning expenditure needed in year t
$C_{FUEL, t}$ is the FUEL expenditure needed in year t

In the INNWIND.EU project we focus mainly on the CAPEX as influenced by different design choices and only consider the OPEX as being at the same order of magnitude as the current offshore projects. The impact of decommissioning is neglected, since it is believed to be the same for any project. Finally the wind power application is getting the wind for free, whereby the fuel cost is removed $C_{FUEL,t} = 0$.

(INNWIND.EU, Deliverable 3.11, Superconducting generators)

The CAPEX cost for the drive train analysis is split into the cost of the drive train C_D and the then the rest of the cost C_R of the INNWIND.EU reference turbine as well as the foundation. These costs have to be paid already at the installation whereby t = 0 is used.

$$C_{CAPEX,t} = C_{D,0} + C_{R,0} \qquad (3\text{-}10)$$

The analysis only considers the systems to the output of the power electronics of the turbine and the cost of the transformer, wind farm collection grid, transformer platform and main cable to land are neglected in the analysis, but can be included by adding a constant term to the LCoE.

By looking at eq. (3-8) and eq. (3-9), it can be seen that the impact of the CAPEX on the Levelized Cost of Energy (LCoE) can be determined separately from the OPEX contribution and one can thereby define a CAPEX part given by

$$LCoE_{CAPEX} = \frac{\sum_{t=0}^{LT} \frac{1}{(1+w)^t} C_{CAPEX,t}}{\sum_{t=0}^{LT} \frac{1}{(1+w)^t} E_t} = \frac{C_{D,0} + C_{R,0}}{\sum_{t=0}^{LT} \frac{1}{(1+w)^t} E_t} \qquad (3\text{-}11)$$

If the annual energy production E_t is assumed constant and given by E_{AEP} then the CAPEX contribution to LCoE can be simplified to

$$LCoE_{CAPEX} = \frac{C_{D,0} + C_{R,0}}{E_{AEP} \sum_{t=0}^{LT} \frac{1}{(1+w)^t}} = \frac{C_{D,0} + C_{R,0}}{E_{AEP} LT \left[\frac{1}{LT} \sum_{t=0}^{LT} \frac{1}{(1+w)^t} \right]} = \frac{C_{D,0} + C_{R,0}}{a \cdot E_{AEP} LT} \qquad (3\text{-}12)$$

where $C_{D,0}$ and $C_{R,0}$ is the CAPEX of the drive train and the rest of the turbine and foundation respectively, E_{AEP} is the average annual energy production and LT is the design life time. The factor a is levelizing the energy production and is given by

$$a = \frac{1}{LT} \sum_{t=0}^{LT} \frac{1}{(1+w)^t} = \frac{1}{LT} \frac{1+w}{w} \left[1 - \left(\frac{1}{1+w} \right)^{LT+1} \right] \qquad (3\text{-}13)$$

where w is the interest rate and LT is the design life time. The geometric series has been used to obtain the last expression.

Figure 3-1 shows the behaviour of the levelizing factor a as function of the interest rate w, but by plotting the inverse of a one obtains a factor indicating how much larger the CAPEX part of the LCoE is increased. This is termed the lift factor and is also shown in the figure.

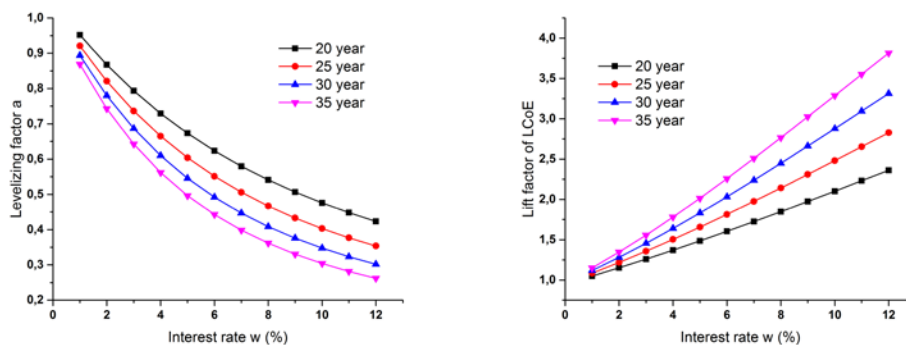Figure 3-1 Left: Levelizing factor *a* as function of the interest rate *w* and for different design life times *LT*. Right: Lift factor of CAPEX part of LCoE given as *1/a*. A lift factor of 2.0 for *w* = 8 % and *LT* = 25 years means that the LCoE CAPEX part is doubled compared to the case of no interest rate *w* = 0, which result in a lift factor of 1.

(INNWIND.EU, Deliverable 3.11, Superconducting generators)

3.1.2 OPerations and maintenance EXpenditures (OPEX)

The operation and maintenance expenses cover the daily operation such as changing wear parts of the turbine and foundations as well as both scheduled and unscheduled maintenance operations. The sum of these contributions are often called operation expenditures (OPEX) and if they are assumed constant per year $C_{OPEX,t} = C_{OPEX,C}$. then the contribution to the Levelized Cost of Energy (LCoE) will be

$$LCoE_{OPEX} = \frac{\sum_{t=0}^{LT}\frac{1}{(1+w)^t}C_{OPEX,t}}{\sum_{t=0}^{LT}\frac{1}{(1+w)^t}E_t} = \frac{C_{OPEX,C}\sum_{t=0}^{LT}\frac{1}{(1+w)^t}}{E_{AEP}\sum_{t=0}^{LT}\frac{1}{(1+w)^t}} = \frac{C_{OPEX,C}}{E_{AEP}} \tag{3-14}$$

which can be considered as a constant that can be added with eq. (3-12).

The Levelized cost of the INNWIND.EU wind turbine and foundation is then found as

$$LCoE = LCoE_{CAPEX} + LCoE_{OPEX} \tag{3-15}$$

3.1.3 Annual Energy Production (AEP)

The annual energy production of the INNWIND.EU wind turbine is determined from the mechanical power curve of the 10 MW 178 m rotor as shown on Figure 2-1. This is combined with the partial load efficiency of the drive train including the power electronics and also the wind speed distribution of the site, where the turbine is intended installed.

The wind speed distribution is described by the Weibull function given by

$$f(v, k, \lambda) = \frac{k}{\lambda}\left(\frac{v}{\lambda}\right)^{k-1} exp\left(-\left(\frac{v}{\lambda}\right)^k\right) \tag{3-16}$$

where v is the wind speed and λ and k are called the scale and shape parameters respectively.

The target position of the INNWIND.EU turbines is a position in the North Sea and the wind climate is characterized by IEC Class Ia with an average wind speed of V_{ave} = 10 m/s and a shape parameter of k = 2 giving a resulting Rayleigh wind distribution of

$$f(v, \sigma) = \frac{v}{\sigma^2} exp\left(-\frac{v^2}{2\sigma^2}\right) \tag{3-17}$$

where

$$\sigma = \frac{\lambda}{\sqrt{2}} \tag{3-18}$$

The average of the Rayleigh wind distribution function in eq. (3-17) is

$$v_{ave} = \sqrt{\frac{\pi}{2}}\sigma \tag{3-19}$$

whereby it is seen that the Class Ia corresponds to

$$\sigma = 7.98\frac{m}{s} \tag{3-20}$$

Figure 3-2 shows the mechanical power curve of the 10 MW reference turbine with a 178 m rotor as function of wind speed as well as the Rayleigh wind speed distribution of the INNWIND.EU reference installation site with wind Class Ia.

(INNWIND.EU, Deliverable 3.11, Superconducting generators)

The annual energy production is calculated by integrating the product of the mechanical power curve $P_{mech}(v)$, the partial load efficiency $\varepsilon(v)$ of the drive train and the wind distribution function $f(v,\sigma)$ over all wind speeds

$$E_{AEP} = \int_{v_{cut-in}}^{v_{cut-out}} P_{mech}(v)\ \varepsilon(v)\ f(v,\sigma)dv \qquad (3\text{-}21)$$

where $v_{cut\text{-}in}$ is the wind speed of startup and $v_{cut\text{-}out}$ is the wind speed at shutdown.

This calculation is however bias by the fact that the mechanical power curve is higher than the rated power above the rated wind speed in order to be able to subtract the assumed 6 % loss of the drive train and thereby provide the rated power at the output cable to the turbine. If different drive trains should be compared using the same mechanical power curve of the INNWIND.EU reference turbine, then it will more appropriate to integrate eq. (3-21) between the cut in wind speed and rated wind speed and then assume that the efficiency is adjusted to 100 % above rated wind speed, because the wind turbine controller will allow a slightly higher rated mechanical power.
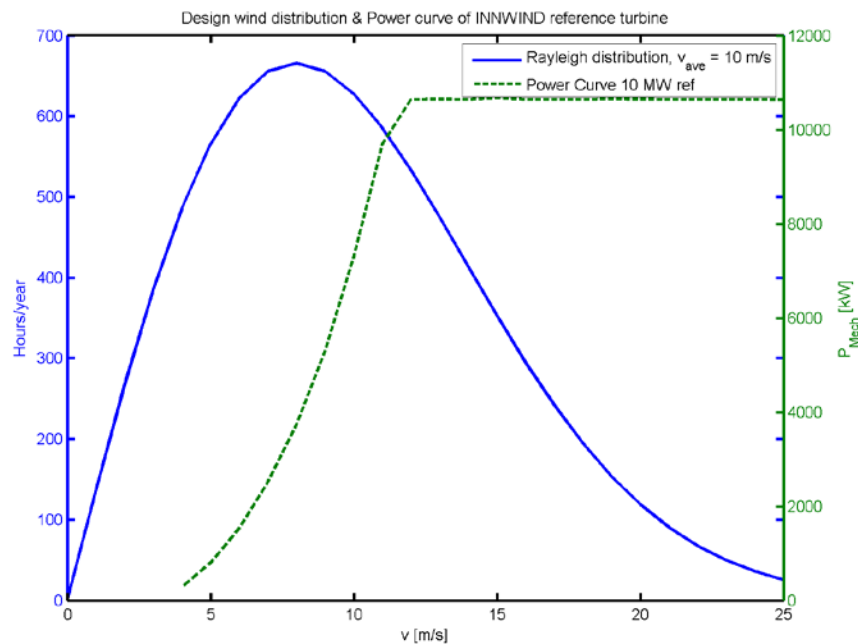
Figure 3-2 Power curve of the 10 MW INNWIND reference turbine and the Weibull wind speed distribution corresponding to a Class Ia wind site, The cut-in wind speed is $v_{cut\text{-}in}$ = 4 m/s, the rated wind speed is V_{rated} = 11.5 m/s and the cut-out wind speed is $v_{cut\text{-}out}$ = 25 m/s. Integrating the two curves result in an ideal annual energy production of E_{AEP} ~ 52 GWh/year

The partial load efficiency curve is given as the product between the generator and power electronics partial load efficiency curves, which are determined as part of the generator design in section 5 and in the deliverable 3.31 on power electronics (Chen, 2014).

For the superconducting generator one will probably have to keep the cooling system running when the wind speed is below the cut-in wind speed this energy consumption should be subtracted from the E_{AEP}. If the power for the cryogenic system is constant P_{Cryo} then this must be inserted in eq. (3-21) and integrated over the Weibull distribution when using an efficiency of 100 %.

(INNWIND.EU, Deliverable 3.11, Superconducting generators)

3.1.4 Design life time (LT)

The design lifetime of the INNWIND.EU turbine is chosen to be LT = 25 years.

This is in principle an arbitrary number, but the turbine and the foundation must be designed to be able to withstand both the extreme and fatigue loading during the design life time.

3.1.5 Cost of INNWIND.EU reference turbine components and OPEX

In order to determine the CAPEX of the rest of the turbine structure $C_{R,0}$ as specified in equation (3-12), the information about the cost of the different turbine components of the reference turbine should be taken from the cost model as provided in the deliverable D1.23 (P.K. Chaviaropoulos, 2014) .

Components	Cost [k€]
Wind turbine (excl. generator system)	7500
Balance of plant	17000
Power electronics	800
Cryogenic system	600[a]
Generator support structure	880[a]
Total cost $C_{R,0}$	26780

Table 3-1. Cost of component of the 10 MW INNWIND.EU reference turbine excluding the generator, which will be optimized by the choice of active materials such as superconductor wire length, Cu, laminates and glass fiber. The generator cost $C_{D,0}$ will be in the range of 1-2 M€ depending of the different designs. Reproduced from Liu *et. al.* (D. Liu, 2017) indicating that valued for [a] are obtained from a low temperature superconducting generator design as a starting point (Y. Liu, 2015)

The OPEX contribution to LCoE of the initial conceptual INNWIND.EU turbines has been estimated in deliverable 1.22 (Natarajan, 2014) and are shown in Table 3-2 together with the CAPEX for the turbine and balance of plant (foundations and cables). It should be noted that these reference turbines are not superconducting, but serves as a reference to give some indications of the expected cost levels of turbines up-scaled towards the 20 MW power range.

Operation & maintenance cost	Reference 5 MW	Classical upscale 10 MW	Innovative 10 MW	More Innovative 15 MW	More Innovative 20 MW
LCOE$_{TURBINE}$ [€/MWh]	31,58	41,54	31,11	35,83	40,77
LCOE$_{BOP}$ [€/MWh]	42,10	39,17	30,18	26,66	24,30
LCOE$_{opex}$ [€/MWh]	33,25	28,49	23,89	22,26	20,71
LCOE$_{TOTAL}$ [€/MWh]	106,93	109,19	85,18	84,75	85,77

Table 3-2. Predicted CAPEX and OPEX contribution to Levelized Cost of Energy (LCoE) for different size of conceptual INNWIND.EU turbines. These conceptual INNWIND.EU turbines were specified at an early stage in the project by upscaling a 5 MW reference turbine by using appropriate scaling exponents on determining the mass of the main components and thereby also the cost. Classical upscaling of blade mass of often scaled with the blade length raised to the power of 3. For more innovative scaling this is done with an exponent lower than 3. Thus the drive trains of the conceptual turbines shown here are not specified as superconducting, but rely on an up-scaled reference design being a two stage gearbox and a medium speed generator. Reproduced from Figure 5 in deliverable report D1.22 and also consult this for further information about the upscaling of the conceptual INNWIND.EU turbines (Natarajan, 2014).

One can now make an example calculation of the Levelized Cost of Energy of the INNWIND.EU 10 MW turbine based on the numbers of Table 3-1 and Table 3-2.

$$LCoE \sim \frac{C_{D,0}+C_{R,0}}{a \cdot E_{AEP}LT} + LCoE_{OPEX} = \frac{1\,M€+27\,M€}{0.55 \cdot 52\frac{GWh}{year} \cdot 25\,year} + 24\,\frac{€}{MWh} = 39\,\frac{€}{MWh} + 24\,\frac{€}{MWh} = 63\,\frac{€}{MWh} \quad (3\text{-}22)$$

This is considerable lower than what is seen for the Innovative 10 MW turbine in Table 3-2, because an interest rate of w = 5.75 % over a life time of LT = 25 years has been used to obtain a = 0.55 (see Figure 3-1). An interest rate of 5.75 % is however what is expected from a society point of view and is probably considerably higher as seen from a commercial point of view of a business sector. Thus if an interest rate of w = 12 % is assumed for LT = 25 years then a = 0.35, whereby the CAPEX part of LCoE is lifted

$$LCoE \sim \frac{C_{D,0} + C_{R,0}}{a \cdot E_{AEP} LT} + LCoE_{OPEX} = \frac{1\,M\text{€} + 27\,M\text{€}}{0.35 \cdot 52 \frac{GWh}{year} \cdot 25\,year} + 24\,\frac{\text{€}}{MWh} = 62\,\frac{\text{€}}{MWh} + 24\,\frac{\text{€}}{MWh} = 86\,\frac{\text{€}}{MWh} \quad (3\text{-}23)$$

which is matching the prediction of Table 3-2 for the innovative 10 MW turbine. It is however interesting that the large decline in the bids on offshore wind power in 2016 is indicating a LCoE ~ 56 €/MWh for the Kriegers Flak offshore wind farm with turbine sizes approaching 10 MW (DanskVindmølleIndustri, 2016).

In the following analysis of the superconducting drive trains then an interest rate of w = 5.75 % and a design life time of LT = 25 years resulting in a = 0.55 is used in order to target the lower LCoE. This means that any overhead of companies producing the superconducting drive trains is included in the materials cost used in the modeling of the generators.

3.1.6 Cost of generator manufactured materials

The cost of the superconducting generator designs will be determined from the mass of active materials $m_{mat,i}$ that they contain and by assuming unit weight cost $C_{mat,i}$ of the materials for the finished state when installed in the turbine. Thus any additional manufacturing cost and profits are included in the unit weigh cost, which will be considerably higher that the raw materials cost.

$$C_{D,0} = \sum C_{mat,i} m_{mat,i} \qquad (3\text{-}24)$$

where the materials that must be summed will typical be superconductor wires for the field windings, copper wires for the armature, silicon steel for the magnetic circuit of the generators, glass fiber composite material for support and steel for the structural support.

There are some differences in the cost of material values used by the partners in INNWIND.EU developing drive trains and the values reported below represent the assumptions behind the MgB$_2$ direct drive generator design.

Material	Unit weight cost of generator materials
MgB$_2$ wire [€/m] (potentially reaching 1€/m)	4
Copper wire in armature [€/kg]	15
Silicon iron laminates [€/kg]	3
Glass Fiber re-enforced composite [€/kg]	15
Structural steel [€/kg]	2

Table 3-3 Unit weight material cost of generator materials of the MgB$_2$ superconducting direct drive wind turbine design

(INNWIND.EU, Deliverable 3.11, Superconducting generators)

3.1.7 Sensitivity analysis of LCoE of the drive train

In order to guide the development of the superconductor generator design then the sensitivity of the Levelized Cost of Energy (LCoE) with respect to the parameters of eq. (3-15) will be provided. The following LCoE definition is used

$$LCoE = LCoE_{CAPEX} + LCoE_{OPEX} = \frac{C_{D,0} + C_{R,0}}{a \cdot E_{AEP} LT} + \frac{C_{OPEX,D} + C_{OPEX,R}}{E_{AEP}} \qquad (3\text{-}25)$$

where $C_{D,0}$ is the capital expenditure of the drive train as paid at the beginning of the investment (hence the index 0 referring to time $t = 0$), $C_{R,0}$ is the capital expenditure of the rest of the turbine and foundation (again paid at the beginning of the investment and with the index 0 to indicate that), a is the interest rate levelizing factor given by (3-13), the Annual Energy Production is E_{AEP}, LT is the design life time of the turbine and foundation, $C_{OPEX,D}$ the annual OPEX part related to the drive train and $C_{OPEX,R}$ is the part of the annual OPEX related to the rest of the turbine and foundation.

The sensitivity analysis is first applied to the CAPEX part by adding correction terms to the main parameters. In the case of the drive train cost $C_{D,0}$ then a variation term $\Delta C_{D,0}$ is added, which is representing the a change of the drive train cost in absolute cost compared to the initial cost, which is assigned with an index 0. Thus the following definition of $LCoE_{CAPEX}$ is obtained

$$
\begin{aligned}
LCoE_{CAPEX} \quad &= \frac{C_{D,0} + C_{R,0}}{a \cdot E_{AEP} LT} \\
&= \frac{C_{D,0} + \Delta C_{D,0} + C_{R,0} + \Delta C_{R,0}}{(a_0 + \Delta a) \cdot (E_{AEP0} + \Delta E_{AEP}) \cdot (LT_0 + \Delta LT)} \\
&= \frac{(C_{D,0} + C_{R,0}) \cdot \left(1 + \frac{\Delta C_{D,0}}{C_{D,0} + C_{R,0}} + \frac{\Delta C_{R,0}}{C_{D,0} + C_{R,0}}\right)}{a_0 \cdot E_{AEP0} \cdot LT_0 \left(1 + \frac{\Delta a}{a_0} + \frac{\Delta E_{AEP}}{E_{AEP0}} + \frac{\Delta LT}{LT_0}\right)} \\
&= LCoE_{CAPEX0} \left(1 + \frac{\Delta C_{D,0}}{C_{D,0} + C_{R,0}} + \frac{\Delta C_{R,0}}{C_{D,0} + C_{R,0}} - \frac{\Delta a}{a_0} - \frac{\Delta E_{AEP}}{E_{AEP0}} - \frac{\Delta LT}{LT_0}\right) \qquad (3\text{-}26)
\end{aligned}
$$

where $C_{D,0}$, $C_{R,0}$, a_0, E_{AEP0} and LT_0 are the initial drive trains cost, the initial cost of the rest of the turbine and foundation, the initial levelizing factor as given by (3-13), the initial Annual Energy Production and finally the initial design life time. The variation parameter $\Delta C_{D,0}$ is the absolute variation of the drive train cost, $\Delta C_{R,0}$ is the variation of the cost of the rest of the turbine and foundation, Δa is the variation of the levelizing factor, ΔE_{AEP} is the variation in the annual energy production and ΔLT is the variation of the design life time of the turbine and foundation. The last line of the above equation is obtained by omitting higher order terms and by relating the variations relative to the initial parameters. The factor LCOE_{CAPEX0} refer to the first line of the equation, where all variation terms are set to zero. The interpretation of the sensitivity equation is that a variation in the cost of either the drive train $\Delta C_{D,0}$ or the rest of the turbine and foundation $\Delta C_{R,0}$ must be analyzed relative to the entire cost of the system $C_{D,0} + C_{R,0}$. A consequence is that a change in the drive trains cost will have relatively small impact on LCOE, because the drive trains cost is relatively small compared to the total cost of the structure given by $C_{D,0} + C_{R,0}$. It can also be seen that a relative increase the levelizing factor $\Delta a / a_0$ will cause a similar relative decrease of LCOE. Similar is concluded on a relative change of the Annual Energy Production and the design life time.

A similar analysis is applied to OPEX part giving

$$
\begin{aligned}
LCoE_{OPEX} \quad &= \frac{C_{OPEX,D} + C_{OPEX,R}}{E_{AEP}} \\
&= \frac{C_{OPEX,D0} + \Delta C_{OPEX,D} + C_{OPEX,R0} + \Delta C_{OPEX,R}}{E_{AEP0} + \Delta E_{AEP}}
\end{aligned}
$$

(INNWIND.EU, Deliverable 3.11, Superconducting generators)

$$= \frac{\left(C_{OPEX,D0} + C_{OPEX,R0}\right) \cdot \left(1 + \frac{\Delta C_{OPEX,D}}{C_{OPEX,D0} + C_{OPEX,R0}} + \frac{\Delta C_{OPEX,R}}{C_{OPEX,D0} + C_{OPEX,R0}}\right)}{E_{AEP0}\left(1 + \frac{\Delta E_{AEP}}{E_{AEP0}}\right)}$$

$$= LCoE_{OPEX0} \cdot \left(1 + \frac{\Delta C_{OPEX,D}}{C_{OPEX,D0} + C_{OPEX,R0}} + \frac{\Delta C_{OPEX,R}}{C_{OPEX,D0} + C_{OPEX,R0}} - \frac{\Delta E_{AEP}}{E_{AEP0}}\right) \qquad \text{(3-27)}$$

where $C_{OPEX,D0}$ is the initial annual expenditure on the drive train operation and maintenance, $C_{OPEX,R0}$ is the initial annual expenditure on the rest of the turbine and foundation operation and maintenance and E_{AEP0} is the initial Annual Energy Production. The absolute variation of the drive trains O&M is given by $\Delta C_{OPEX,D}$, whereas the absolute variation of the O&M of the rest of the turbine and foundation is given by $\Delta C_{OPEX,R}$. The last line is obtained by omitting higher order terms and $LCOE_{OPEX0}$ refers to the initial line with all variations equal to zero. The interpretation of the result is that operation and maintenance part of the LCOE is determined by the variation in the O&M cost of the drive train $\Delta C_{OPEX,D}$ and the rest of the structure $\Delta C_{OPEX,R}$ relatively to the sum of the drive train annual costs $C_{OPEX,D0} + C_{OPEX,R0}$. Finally a variation of the annual energy production relative to the initial annual energy production $\Delta E_{AEP} / E_{AEP0}$ *will result in a similar relative change of the LCOE$_{OPEX}$ part.*

The combined sensitivity of the LCoE then becomes

$$LCoE = LCoE_{CAPEX0} + \Delta LCoE_{CAPEX} + LCoE_{OPEX0} + \Delta LCoE_{OPEX}$$

$$= \left(LCoE_{CAPEX0} + LCoE_{OPEX0}\right)\left(1 + \frac{\Delta LCoE_{CAPEX}}{LCoE_0} + \frac{\Delta LCoE_{OPEX}}{LCoE_0}\right)$$

$$= LCoE_0\left(1 + \frac{\Delta LCoE_{CAPEX}}{LCoE_0} + \frac{\Delta LCoE_{OPEX}}{LCoE_0}\right)$$

$$= LCoE_0\left(1 + \frac{LCoE_{CAPEX0}}{LCoE_0}\frac{\Delta LCoE_{CAPEX}}{LCoE_{CAPEX0}} + \frac{LCoE_{OPEX0}}{LCoE_0}\frac{\Delta LCoE_{OPEX}}{LCoE_{OPEX0}}\right) \qquad \text{(3-28)}$$

whereby the final sensitivity expression is obtained by inserting eq. (3-26) and eq. (3-27) to the above

$$\frac{\Delta LCoE}{LCoE_0} = \frac{LCoE_{CAPEX0}}{LCoE_0}\frac{\Delta LCoE_{CAPEX}}{LCoE_{CAPEX0}} + \frac{LCoE_{OPEX0}}{LCoE_0}\frac{\Delta LCoE_{OPEX}}{LCoE_{OPEX0}}$$

$$= \frac{LCoE_{CAPEX0}}{LCoE_0}\left(\frac{\Delta C_{D,0}}{C_{D,0} + C_{R,0}} + \frac{\Delta C_{R,0}}{C_{D,0} + C_{R,0}} - \frac{\Delta a}{a_0} - \frac{\Delta E_{AEP}}{E_{AEP0}} - \frac{\Delta LT}{LT_0}\right)$$

$$+ \frac{LCoE_{OPEX0}}{LCoE_0}\left(\frac{\Delta C_{OPEX,D}}{C_{OPEX,D0} + C_{OPEX,R0}} + \frac{\Delta C_{OPEX,R}}{C_{OPEX,D0} + C_{OPEX,R0}} - \frac{\Delta E_{AEP}}{E_{AEP0}}\right)$$

$$= -\frac{\Delta E_{AEP}}{E_{AEP0}} + \frac{LCoE_{CAPEX0}}{LCoE_0}\left(\frac{\Delta C_{D,0}}{C_{D,0} + C_{R,0}} + \frac{\Delta C_{R,0}}{C_{D,0} + C_{R,0}} - \frac{\Delta a}{a_0} - \frac{\Delta LT}{LT_0}\right) + \frac{LCoE_{OPEX0}}{LCoE_0}\left(\frac{\Delta C_{OPEX,D}}{C_{OPEX,D0} + C_{OPEX,R0}} + \frac{\Delta C_{OPEX,R}}{C_{OPEX,D0} + C_{OPEX,R0}}\right) \quad \text{(3-29)}$$

where $\Delta E_{AEP}/E_{AEP0}$ is the relative change of the annual energy production. $LCoE_{CAPEX0}$ is the CAPEX part of the levelized Cost of Energy $LCoE_0$. $\Delta C_{D,0}/(C_{D,0} + C_{R,0})$ is the change $\Delta C_{D,0}$ of the drive train cost relative to the sum of the drive train cost $C_{D,0}$ and the cost of the rest $C_{R,0}$ of the turbine and the foundation. $\Delta a/a_0$ is the relative change of the levelizing factor taking the interest rate into account. $\Delta LT/LT_0$ is the relative change of the deign life time of the structures. $LCoE_{OPEX0}$ is the OPEX part of the levelized Cost of Energy $LCoE_0$. $\Delta C_{OPEX,D}/(C_{OPEX,D} + C_{OPEX,R})$ is the change of the annual OPEX expenses of the drive train $\Delta C_{OPEX,D}$ in relations to the annual OPEX expenses of the drive train $C_{OPEX,D}$ and the annual OPEX expenses related to the rest of the turbine and foundation $C_{OPEX,R}$.

The interpretation of the above sensitivity analysis is that a relative increase of the Annual Energy Production $\Delta E_{AEP}/E_{AEP0}$ will result in an equal relative decrease of the LCOE. This is due to the presence of the Annual Energy Production E_{AEP} in the denominator in both the terms of the LCOE. It is also seen that a relative increase of either the drive trains cost or the cost of the rest of the structure relative to the entire cost of the structure must be weighted with the fraction of the CAPEX part of the LCOE with respect to the entire LCOE in order to determine the relative change

(INNWIND.EU, Deliverable 3.11, Superconducting generators)

of the LCOE. Similarly a relative increase of the O&M costs must be weighted by the OPEX part of LCOE relative to the LCOE in order to determine the impact of an O&M change.

3.1.8 Impact of the drive train on the LCoE

Using the sensitivity equation from the previous section one can estimate the possible impacts of the drive train on the LCoE of the INNWIND.EU turbine evaluating the terms individually. In the following approximate numbers obtained from the conceptual INNWIND.EU reference turbines will be discussed in relation to expected LCOE levels in order to obtain insight into the LCOE reduction that should be expected from possible drive train improvements.

Annual energy production

The sensitivity analysis shows that the relative change in the annual energy production will result in a similar relative change of the LCoE. Now how can one improve the annual energy production seen from the drive train point of view? The main influence comes from the partial load efficiency of the drive train. This is however already around 94 % as is the case for the INNWIND reference drive train as shown in Table 2-2, and one can estimate the maximum increase by the fact that the efficiency will be very hard to increase above 98-99%. Thus

$$\frac{\Delta E_{AEP}}{E_{AEP}} \sim +4\ \% \ \Rightarrow \ \frac{\Delta LCoE}{LCoE} \sim -4\ \% \tag{3-30}$$

It should be mentioned that if the annual energy production of the turbine is decreased by unforeseen downtime due to repairs then this will directly result in an equivalent increase of the levelized Cost of Energy LCoE. Thus - 10 % availability is expected to result in + 10 % LCoE. Indicating that the reliability of the drive train is very important.

Cost of the drive train

The largest impact of the drive train cost can be estimated by considering the drive train is obtained for half the cost of the present reference drive train, which cost about 2 M€ . In that case the change in the drive train cost $\Delta C_{D,0} = C_{D,0}/2$ will be half the cost of the drive train giving

$$\frac{\Delta C_{D,0}}{C_{D,0} + C_{R,0}} \sim \frac{-C_{D,0}/2}{C_{D,0} + C_{R,0}} \sim -\frac{1\ M€}{2M€ + 27\ M€} = -3.4\ \% \tag{3-31}$$

This must however be scaled with the ratio between the $LCoE_{CAPEX}$ and the full LCoE as obtained from Table 3-2 for the innovative 10 MW turbine giving

$$\frac{LCoE_{CAPEX}}{LCoE_0} \sim \frac{61.3\ €/MWh}{85.2\ €/MWh} \sim 0.72 \tag{3-32}$$

and

$$\frac{\Delta LCoE}{LCoE} = \frac{LCoE_{CAPEX}}{LCoE_0}\left(\frac{\Delta C_{D,0}}{C_{D,0} + C_{R,0}}\right) \sim -0.72 \cdot 3.4\% \sim -2.5\ \% \tag{3-33}$$

Levelizing factor caused by interest rate w

If the interest rate is changed of the sector then one have to evaluate the resulting relative change the levelizing factor a.

By expanding the expression for the levelizing factor a into the leading terms of the interest rate w then one get

(INNWIND.EU, Deliverable 3.11, Superconducting generators)

$$a = \frac{1}{LT}\frac{1+w}{w}\left[1 - \left(\frac{1}{1+w}\right)^{LT+1}\right] \sim \frac{1}{LT}\frac{1}{w} \sim \frac{1}{LT}\frac{1}{w_0\left(1+\frac{\Delta w}{w_0}\right)} \sim a_0\left(1 - \frac{\Delta w}{w_0}\right) \qquad (3\text{-}34)$$

where *LT* is the design life time of the structure.

Thus lowering the interest rate from *w* = 12 % to 6 % will result in

$$\frac{\Delta a}{a_0} \sim \frac{\Delta w}{w_0} = \frac{6\,\%}{12\,\%} = 50\,\% \qquad (3\text{-}35)$$

and the resulting impact on the LCoE is

$$\frac{\Delta LCoE}{LCoE} = \frac{LCoE_{CAPEX}}{LCoE_0}\left(-\frac{\Delta a}{a_0}\right) \sim 0.72 \cdot (-50\%) \sim -36\,\% \qquad (3\text{-}36)$$

This is illustrating that a change in the interest rate *w* can have a large impact in the Levelized Cost of Energy. The interest rate level is related to the risk of a project and with more experience of installing offshore turbines then one would expect the interest rate to approach the long term level of society being 5.75 %.

Design life time of structures

If the usual design life time of 25 years of offshore wind structures is increased by 1 or 5 years then the relative change of the LCoE will be

$$\frac{\Delta LT}{LT_0} = \frac{1}{25} \rightarrow \frac{5}{25} = +4\,\% \rightarrow 20\,\% \qquad (3\text{-}37)$$

and

$$\frac{\Delta LCoE}{LCoE} = \frac{LCoE_{CAPEX}}{LCoE_0}\left(-\frac{\Delta LT}{LT_0}\right) \sim 0.72 \cdot (-4\% \rightarrow -20\%) \sim -2.9\,\% \rightarrow -14.4\,\% \qquad (3\text{-}38)$$

In the INNWIND.EU project the design life time of the drive trains are assumed to be the same as the turbine and foundation, which is what is expected for different direct drive generator solutions. Care should however be taken when comparison to other drive trains with a substantial shorter life time such as gearboxes. It is not known what the lifetime of a 10-20 MW gearbox for a wind turbine will be, but if it turns out to be about half of the turbine life time as has been observed for many current offshore projects then one would have to reflect that into the O&M costs discussed below.

(INNWIND.EU, Deliverable 3.11, Superconducting generators)

Operation and maintenance expenses

As seen from the sensitivity equation (3-29) one have to estimate the ratio between $LCoE_{OPEX}$ and the total $LCoE$ from Table 3-2 which is

$$\frac{LCoE_{OPEX0}}{LCoE_0} \sim \frac{23.9 \,€/MWh}{85.2 \,€/MWh} \sim 0.28 \qquad (3-39)$$

In order to evaluate a change in the operation and maintenance expenses of the drive train one first must indicate the ratio between drive train OPEX expenses and OPEX for the rest of the turbine, foundation and cables. A guess on these numbers are hard to obtain, but some of the offshore experiences has been collected by the Crown Estate for their wind farm operation in the UK up to 2013 (Hassan, 2013). The OPEX number have been normalized by the energy production of a 500 MW wind farm by assuming a wind farm capacity factor of CF = 0.4. Figure 3-3 is showing the minimum and maximum estimates of the OPEX contributions to the Levelized Cost of Energy. These OPEX numbers represent gearbox drive trains in turbines with a power level lower than 4 MW. It is interesting to note that the cost associated to the spare parts is below 10 % of the total OPEX cost. This is clearly indicating that the first component installed initially at the turbine factory is very cheap compared to the replacement component that must be installed offshore.

The average OPEX contribution to LCoE from Figure 3-3 is 31.2 €/MWh, which is in good agreement with the number for the classically up scaled 10 MW turbine in
Table 3-2 and the final INNWIND.EU OPEX target is close the minimum of the Crown Estate study. The cost of the spare parts in average can be determined as 3.5 €/MWh, which for the 10 MW turbine will be equivalent to 3.5 €/MWh x 52 GWh/year = 182 k€/year or 4.6 M€ during the 25 year life time. The minimum amount of spare parts cost correspond to 2.3 €/MWh and one could assume that the average above the minimum is representing unscheduled replacement of parts. This would be 1.2 €/MWh x 52 GWh/year = 62 k€/year or 1.6 M€ during the 25 year life time. If about half of this is assumed to be associated with drive train issues, then it is of the same order as the cost of the drive train expected to cost around 1-2 M€ for the INNWIND.EU turbine. Thus the unscheduled spare part cost seems equivalent of replacing the entire drive train. It is therefore believed that changing from the gearbox solution and into the direct drive solution is needed to reduce the OPEX expenses for spare parts of the INNWIND.EU machines. This estimate is however only based on the direct expenses for the spare parts and did not include the expenses for crane barge service and offshore accommodation of Figure 3-3, which on average amount to 18 €/MWh. The difference between the average and the minimum scenario gives 7 €/MWh for the unscheduled repairs, whereby a drive train replacement making half of that would amount to 0.4 €/MWh + 3.5 €/MWh = 4 €/MWh or 208 k€/year or 5.2 M€ during the 25 year life time. This is about 2-3 times the cost of the expected cost of the superconducting drive trains and clearly indicates that there is a potential to allow for a more expensive direct drive generator if the offshore replacement can be avoided. The superconducting direct drive generator will however have to compete with other types of direct drive generators like the electrical excited and the permanent magnet direct drive generators.

The impact on the Levelized cost of energy by removing the unscheduled cost of drive train replacement amounting to 5.2 M€ can then be evaluated to be

$$\frac{\Delta C_{OPEX,D}}{C_{OPEX,D0} + C_{OPEX,R0}} = \frac{-5.2 \,M€}{\frac{24€}{MWh} \cdot 52 GWh/year \cdot 25 years} = -17 \,\% \qquad (3-40)$$
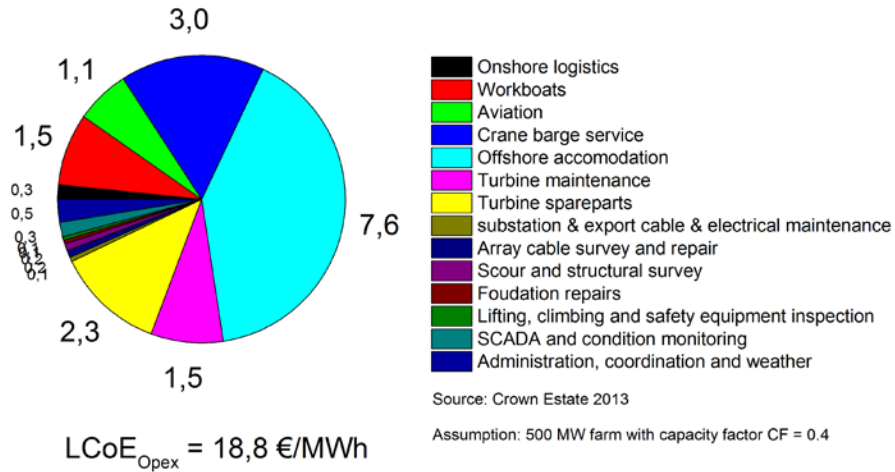
by also imposing the ratio between LCoE OPEX to the total gives

$$\frac{\Delta LCoE}{LCoE_0} = \frac{LCoE_{OPEX}}{LCoE_0} \frac{\Delta C_{OPEX,D}}{C_{OPEX,D0} + C_{OPEX,R0}} = 0.28 \cdot (-17 \,\%) = -4.8 \,\% \qquad (3-41)$$

(INNWIND.EU, Deliverable 3.11, Superconducting generators)

In conclusion it has been shown that the primary targets of the drive train development is to improve the efficiency, since the relative improvement will be directly reflected in the LCoE. The second priority is to remove any major unscheduled offshore drive train repairs and the change to the direct drive technology is believed to support that. A challenge of the superconducting direct drive generators is however not to introduce new major repairs involving crane and boat operation similar to the gearbox replacement of the reference drive train. The cost of the drive train is of less importance in reducing the LCoE, since the change of the drive train cost must be seen relative to the entire cost of the turbine and foundation.

Finally it has been shown that the impact of the drive train developments on the LCoE is limited to below a - 5% decrease. On the contrary it is very easy for the drive train to increase the LCoE, if the drive train suffers from possible new unforeseen failure modes like unscheduled maintenance of the cryogenic system. Major reductions of LCoE in the order of – 15 % might be obtained by increasing the life time of the entire turbine structure from 25 to 30 years. This will however call for a redesign of the foundation and turbine to comply with a longer fatigues life time. A -35 % decrease might be obtained by decreasing the interest rate w of the levelizing factor a of the LCoE from 12 % to 6 %. The latter seems to be the most plausible explanation of the sudden drop of the LCoE of offshore wind farm as seen for the Kriegers Flak farm (DanskVindmølleIndustri, 2016).

Minimum estimate of OPEX for 500 MW offshore wind in 2013

Legend:
- Onshore logistics
- Workboats
- Aviation
- Crane barge service
- Offshore accomodation
- Turbine maintenance
- Turbine spareparts
- substation & export cable & electrical maintenance
- Array cable survey and repair
- Scour and structural survey
- Foudation repairs
- Lifting, climbing and safety equipment inspection
- SCADA and condition monitoring
- Administration, coordination and weather

Source: Crown Estate 2013

Assumption: 500 MW farm with capacity factor CF = 0.4

Values shown: 3,0 1,1 1,5 0,3 0,5 0,3 7,6 1,5 2,3

$LCoE_{Opex} = 18,8 \text{ €/MWh}$

Maximum estimate of OPEX for 500 MW offshore wind in 2013

Legend:
- Onshore logistics
- Workboats
- Aviation
- Crane barge service
- Offshore accomodation
- Turbine maintenance
- Turbine spareparts
- substation & export cable & electrical maintenance
- Array cable survey and repair
- Scour and structural survey
- Foudation repairs
- Lifting, climbing and safety equipment inspection
- SCADA and condition monitoring
- Administration, coordination and weather

Source: Crown Estate 2013

Assumption: 500 MW farm with capacity factor CF = 0.4

Values shown: 9,1 2,3 2,3 0,5 1,1 0,6 15,2 6,1 4,6

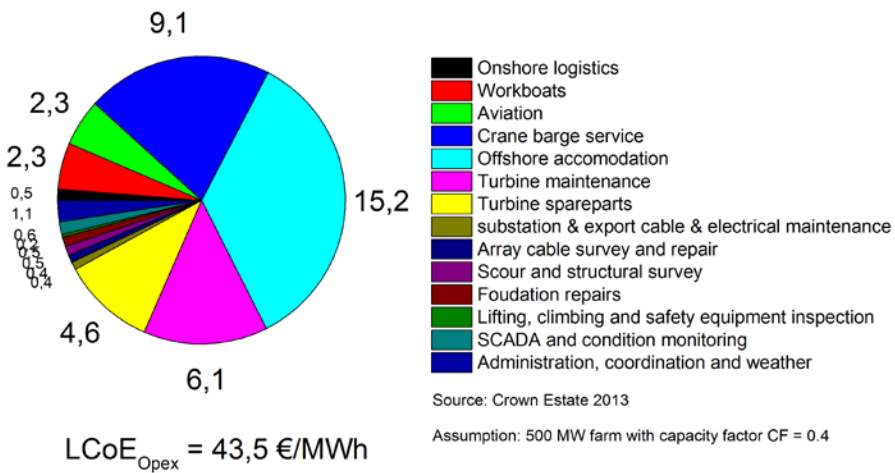$LCoE_{Opex} = 43,5 \text{ €/MWh}$

Figure 3-3 Estimate of the operation and maintenance contribution to the levelized cost of energy as determined from the study of The Crown Estate in 2013 (Hassan, 2013). The minimum and maximum are shown at top and bottom respectively.

(INNWIND.EU, Deliverable 3.11, Superconducting generators)

4 DESIGN PHILOSOPHIES OF INNWIND.EU SUPERCONDUCTING GENERATORS

4.1 "Light weight and not to expensive"

The initial INNWIND.EU philosophy on designing superconducting generators was to reduce the generator mass, whereby additional mass savings in the tower and foundation were believed to cause a cost reduction that would allow for a more expensive superconducting generator.

This philosophy has been termed "Light weight and not too expensive" and was investigated for a 10 MW MgB_2 direct drive generator (Abrahamsen, Magnusson, Jensen, Liu, & Polinder, 2014), (Abrahamsen, et al., 2014).

As part of the evaluation of the innovative INNWIND.EU concepts as performed in deliverable D1.24 (Chaviaropoulos, et al., 2015), there was an investigation of how much materials and cost saving in the tower and foundation that could be expected by reducing the turbine generator mass per ton. The conclusion was that this was very limited since the 10 MW INNWIND.EU reference turbine placed on a jacket foundation resulted in a crossing of the 3P excitation frequency of the turbine rotor with the first fore-aft and side-to-side resonance of the turbine – foundation structure as illustrated in Figure 4-1 (Berger, Sørensen, Gintautas, Kühn, & Kraft, 2015). The resonance frequency of the turbine- foundation structure can in a very simplified picture be seen as dictated by the structure stiffness k as well as the Rotor Nacelle Assembly (RNA) mass at the top of the tower

$$f_{res} \sim \sqrt{\frac{k}{m_{RNA}}} \tag{4-1}$$

Thus from a systems point of view it would be desirable to move the resonance frequency down below the 3P excitation (moving the red band of Figure 4-1 down). This can either be done by decreasing the stiffness constant k or by increasing the tower top mass m_{RNA}. The consequence of this conclusion on the generator design philosophy was that the one should not expect any coupling between a lower mass of the generator and a resulting lower cost of the rest of the system C_R in equation (3-25). A demand for increasing the m_{RNA} was even suggested at some point indicating that the usual motivation of superconducting generators being able to provide a light weight generator that can reduce coupled costs in the tower and foundation was not valid. The generator design philosophy was therefore changed to focus mainly on the impact of the generator efficiency and cost on the LCoE of the INNWIND.EU turbine and foundations.

It should be noted, that it was reported at the INNWIND.EU meeting in May 2017 that the deliverable 4.36 "Design solution for a support structure concept for future 20 MW" will contain an analysis of the resonances of the 20 MW INNWIND.EU turbine mounted on a jacket. This analysis is indicating that no crossing of the resonances and the excitations is expected at 20 MW, whereby a light weight generator will most likely become attractive again. Thus a warning to the designers of future superconducting generators for wind turbines is that the generator is such an integrated part of the turbine and that special combinations of external parameters such as turbine rotor size and water depth might result in system requirements not being feasible.

Future development of superconducting direct drive generators should most likely be focused at the power level of P = 13-15 MW as seen in the latest offer of DONG Energy for OWP West and Borkum Riffgrund West 2 with installation in 2024 (Dong Energy A/S, 2017).

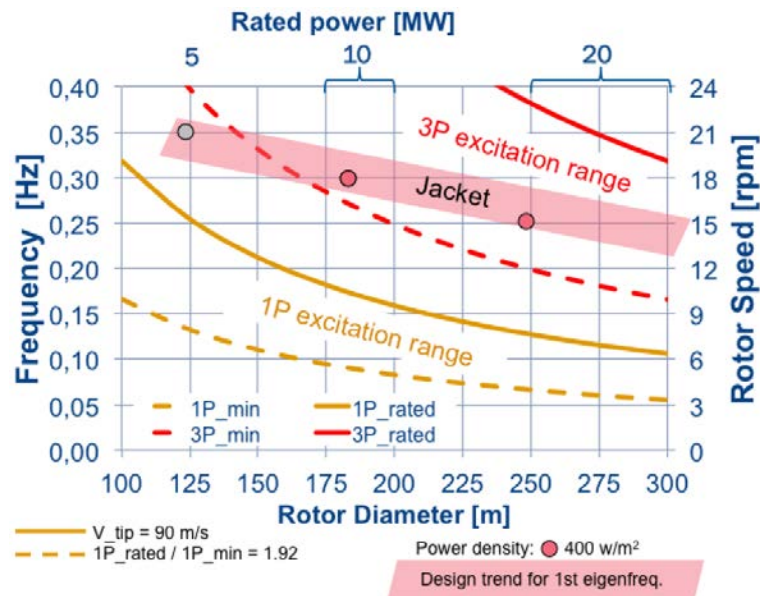*(INNWIND.EU, Deliverable 3.11, Superconducting generators)*

Figure 4-1. Illustration of the 1P and 3P excitations of the turbine rotor in comparison to the predicted resonances of jacket foundations at 10 MW and 20 MW (red points). It is seem that the jacket resonances are crossing right through the 3P excitation band resulting in severe reduction of the foundation life time. Reproduced from figure 3-1 of deliverable report 1.35 (Berger, Sørensen, Gintautas, Kühn, & Kraft, 2015).

4.2 "Cheap and not too heavy"

Since the generator design philosophy of "light weight and not too expensive" was found not to comply with the 10 MW INNWIND.EU offshore structure, because no premium of a small weight could be argued, then the philosophy was changed to "Cheap and not too heavy". The assumption behind this philosophy is that the drive train is only changing the cost $C_{D,0}$ in the expression for the levelized cost of Energy and that the term describing the cost of the rest of the structure $C_{R,0}$ is assumed as constant. The last assumption is only valid as long as the generator mass is not becoming too heavy, whereby it will start to have a large influence on the turbine and foundation loads. Thus this new design philosophy calls for the following two tasks

1) Investigate how to optimize the superconducting generator that will minimize the LCoE of the INNWIND.EU system
2) Determine a method of defining when the mass of the generator is "not too heavy"

The first task can be done by focusing purely on the construction of the generator, whereas the second task involves several iterative design loops, where the superconducting design of the generator is also integrated into the nacelle and then one can evaluate the loads on the turbine to address the questions if the generator turned out to be too heavy. The documentation of these steps are reported in the following chapters in the case of the MgB_2 generator.

(INNWIND.EU, Deliverable 3.11, Superconducting generators)

4.3 "As high superconducting operation temperature as possible"

The design philosophy chosen by Siemens Wind Power for investigating superconducting generators suitable for their direct drive turbines was focused on obtaining as high an operation temperature of the cooling system of the generator as possible (see D3.12). The reasoning behind this choice is that the cryogenic cooling system is seen as introducing a large uncertainty on the reliability of the turbine and with a potential risk of availability of the turbine and also increased maintenance costs. In general terms one can say that increasing the operation temperature from $T_{operation}$ ~ 4 K suitable for the Low Temperature Superconductors (LTS) and up to $T_{operation}$ ~ 20 K can simplify the design of the cryostat and the cooling system considerably. Such an operation temperature will however exclude the usage of both NbTi with $T_{c,NbTi}$ ~ 10 K and also Nb$_3$Sn with $T_{c,Nb3sn}$ ~ 18 K. If the operation temperature is increased even further to $T_{operation}$ ~ 30 K one can also improve the efficiency of the cooling system and possibly also use heat pipes based on the gas-liquid phase transition of neon at $T_{boilingpoint,LNe}$ ~ 24 K.

At such a high operation temperature of T = 30 K it is only the high temperature superconductors (HTS) of the first (1G Bi-2212 and Bi-2223) and second (2G RBa$_2$Cu$_3$O$_{6+x}$) generation that are applicable, since most superconductors must be cooled to about of half of their critical temperature T_C before they can support a suitable critical current density J_C. MgB$_2$ has a T_C ~ 39 K and would therefore not be applicable. The 1G HTS wires are enclosed in silver and are not believed to be able to provide a low cost wire even if scaling up the production volume. This leaves only the 2G coated conductor RBCO wire as the option for a $T_{operation}$ ~ 30 K operation system. The 2G coated conductor wire demonstrated for rotor coils and used for the generator design by Siemens Wind Power is state of the art wire with a width of 12 mm. The result of the work by Siemens Wind Power is described in deliverable D3.12 (Azar & Thomas, 2016) and the main results will be summarized in later chapters.

(INNWIND.EU, Deliverable 3.11, Superconducting generators)

5 OPTIMIZATION FOR LOWEST LCOE OF SUPERCONDUCTING GENERATORS

The methodology for investigating superconducting direct drive generators for the INNWIND.EU turbines will be briefly outlined in this chapter, whereas the details can be found the PhD thesis of Dong Liu (see appendix A and (Liu D. , 2017)). The main ideas of the methodology is explained in order to provide the background of how a series of generator designs were obtained and reported in later chapters.

Two demonstrations of scaled superconducting rotor field coils based on MgB_2 and the high temperature superconducting coated conductor tape $RBa_2Cu_3O_{6+x}$ are reported and used as input for the generator design.

5.1 Generator topologies

The main challenge of designing the superconducting generators for large offshore wind turbines is to determine the best combination of the active materials making up the electromagnetic circuit of the generator and the structural steel parts making sure that the active materials stay in position under all load conditions of the turbine.

A generator consist of a magnetic field generating part, which is moving relative to some coils called the armature, in which a voltages can be induced. The active materials of the field generating part are either coils wound around some magnetic steel poles or permanent magnets mounted onto magnetic steel poles. Similarly, the armature coils are often wound into a series of slots made in magnetic steel laminated plates.

If the active materials are arranged on the surfaces in between two cylinders which are rotating relative to each other then one calls that a radial machine, since the magnetic field in between the field and armature part is directed in the radial direction of the air gap between the two rings. In terms of the superconducting INNWIND.EU generators they are all considered to be radial direct drive generators, with superconducting field windings and conventional copper armature windings at ambient temperature. The major difference to a normal machine is that the superconducting coils have to be thermally isolated and cooled down to the operation temperature by a suitable cooling system. The thermal isolation is provided by placing the superconductors inside a cryostat, which must either enclose the superconducting coils, the coils and the pole pieces or the entire rotor structure. This choice have large consequences for the design of the cryostat and the cooling system, because the cold mass is different and the heat radiation onto the cold mass will be very different. Secondly one will have to decide if the pole of the field coils should be as cold as the superconductor or if it should remain at room temperature.

Thus a method for selecting the superconducting generator with the lowest Levelized Cost of Energy (LCoE) before designing a detailed cryostat design was formulated by specifying certain minimum amount of open space needed around the superconducting winding or in between the field winding and the armature. The cryostat wall is constructed from 5-10 mm of stainless steel, 10-20 mm vacuum space, some layers of structural support and space for Multi-Layer Insulation (MLI). This will roughly sum up to about 40 mm of space around the superconducting windings or extra space in the air gap of the machine.

Figure 5-1 shows how the active material of one pole of the direct drive generator can be specified as being either superconductor winding in the field coils or Cu in the armature and if the field pole is made of non-magnetic or magnetic material. These different configuration are referred to as the topologies T1 to T12. Secondly different field pole piece are extending half way through the field coil (T1 – T 3, T5 – T 7 and T9 to T11) or all the way through the field coil (T4, T8 and T12). In the last case then the pole piece is ending at the physical air gap between the field structure and the armature structure.

The physical air gap h_{gap} is chosen to be 0.1 % of the air gap diameter D_{gen}

(INNWIND.EU, Deliverable 3.11, Superconducting generators)
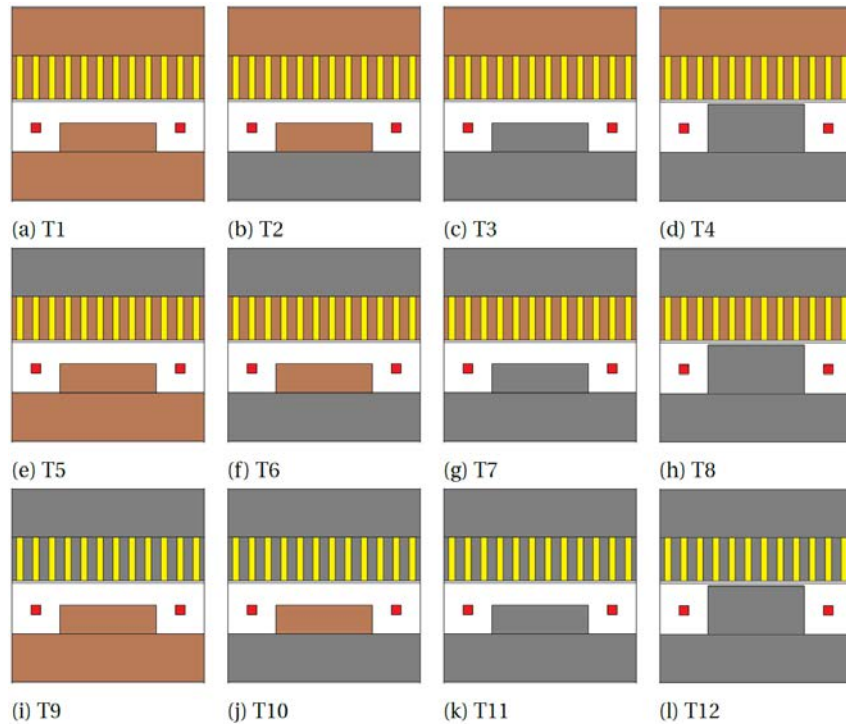
$$h_{gap} = 10^{-3} D_{gen} \tag{5-1}$$

Figure 5-1 Different topologies of superconducting generator pole, which will be placed onto the sides of two tubes rotating relative to one another. The lower part the topologies consist of the superconducting field winding (red), which is supported by either a non-magnetic pole piece (brown) or a magnetic pole piece (gray). Similarly the top part of the topology consist of the armature windings (yellow), which is either supported by non-magnetic material (brown) or by magnetic steel laminates(gray). The topologies T1 – T4 all have a non-magnetic armature winding. T1 also have a non-magnetic support of the superconducting winding and a large physical air gap of the field pole piece allowing a cryostat wall between the field winding and the armature. The topologies T2 and T3 are replacing the non-magnetic material of the field winding with magnetic steel laminates. The topology T4 have a magnetic pole piece of the field winding extending very close to the armature structure in order to close the magnetic circuit with as small an air gap as possible. The effect is this choice is that the cryostat holding the superconducting winding must have a hole in the center, which is at room temperature. The topologies T5 – T8 have a magnetic back iron of the armature and T9 to T12 also have magnetic teeth to support the armature windings. Reproduced from Figure A3.4 in appendix A.

The superconducting field coils are supplied by a DC current I_f, which result in a periodic magnetic field in the field structure with a peak field in the air gap of B_g. If the field and armature structure are rotating with a certain relative speed as specified by the turbine then one will have a certain voltage and current controlled by a back-to-back power electronic converter connected to the armature windings. The current in the armature windings result in a periodic current loading A_s in the armature structure and eventually the shear force density F_d acting between the surfaces of the field and armature structure will be given as

$$F_d \sim B_g A_s \tag{5-2}$$

The principle for optimizing the generator active material is then to change the dimensions of the field and armature coils, the types of materials in the pole pieces, evaluate the levelized cost of energy according to the framework of chapter 3 and to continue to change the dimensions until the lowest LCoE is obtained. Then one can compare the topologies T1 to T12 in order to understand the difference in LCoE between them.

5.2 Machine sizing and pole number

A direct drive generator is made of a large number of poles as illustrated in Figure 5-2 and the number of poles are related to the diameter of the generator D_{gen}, which is specified as an external fixed parameter being between 6 to 15 meters. Once the topology of the pole and the generator diameter are known then one can determine the torque per length of the machine from (5-2) and the generator diameter. The generator have to be able to provide the rated torque T_R as dictated by the turbine and this can be used to determine the length of the generator L_{gen} by

$$L_{gen} = \frac{2T_R}{\pi D_{gen}^2 F_d} \tag{5-3}$$

From this the generator dimensions are known and the active masses can be calculated from the specification of the pole topology.

Different generator diameters are investigated in separate studies, because the diameter of the INNWIND.EU generators are attempted limited in order to be able to mount the generator in front of the turbine blades taking advantage of the Kingpin nacelle configuration of the INNWIND.EU nacelle configuration as illustrated in Figure 5-2.
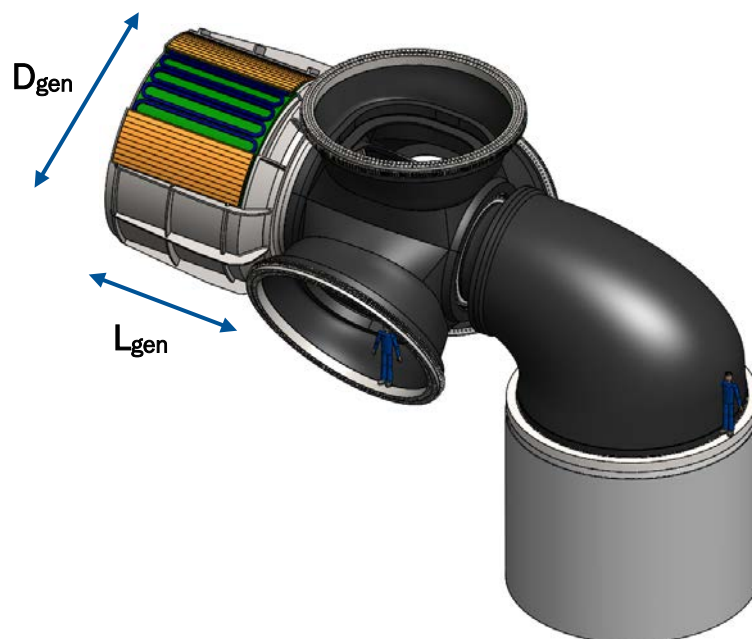

Figure 5-2 Illustration of superconducting direct drive generator with the armature winding (yellow) mounted on the outer tube sitting in front of the turbine hub and the superconducting field coils (blue) sitting on the inner tube attached to the Kingpin of the nacelle (Abrahamsen, et al., 2014).

5.3 Critical current of superconductor and load line

The DC current of the field winding I_f can pass through the superconducting coil with a very small voltage drop per length E as long as the coil current is not approaching what is known as the critical current I_C of the superconducting wire

$$E = E_0 \left(\frac{I_f}{I_C(B,T)}\right)^{n(B,T)} \tag{5-4}$$

where the $E_0 = 10^{-4}$ V/m and the exponent of the power-law is called the n-value often in the range of $n = 20\text{-}30$. Both the critical current and the *n*-value are non-linear functions of the local magnetic flux density $\boldsymbol{B}$ as well as the local temperature T along the superconducting wire. The critical surface of I_C as function of $\boldsymbol{B}$ and T is often provided by the manufacturer of the superconducting wire or is determined on small pieces of the wires. The physical meaning of the power law stated above is that the power dissipation per length of the superconducting wire P is given by the product of the electric field of (5-4) and the coil current

$$P = EI_f = E_0 I_f \left(\frac{I_f}{I_C(B,T)}\right)^{n(B,T)} \tag{5-5}$$

Thus if the coil current I_f is reaching the critical current I_C then a power dissipation per length becomes $P_C = E_0\, I_C$. In the case of a wire with an $I_C = 200$ A this gives $P_C = 10^{-4}$ V/m $\cdot$ 200 A = 20 mW/m. This might seem as a small power dissipation, but a consequence of the power-law is that if the power dissipation causes local heating of the wire then I_C will decrease and the coil current might exceed the critical current. If the coil current i_f becomes 20 % higher than the critical current I_C the power dissipation increases by a factor $(I_f/I_C)^n = (1.2)^{20} = 38$, whereas if it is 20 % lower than the critical current the dissipation become $(I_f/I_C)^n = (0.8)^{20} = 10^{-2}$.

The operational current I_{coil} of a superconducting field coil is determined from what is known as the load line of the coil. The field produced by the superconducting coil is proportional to the current in the coil and by using the finite element method one can determine the maximum field position of a superconducting field coil as it is combined with the active materials of the generator. A complication is if the active material are govern by non-linear materials characteristics, such as the magnetization curve of the steel laminates (see Figure A3.7). By plotting the current of the coil as function of the maximum field B_{max} on can combine that with a plot of the critical current I_C of the superconductor wire used as shown in Figure 5-3. The operation current I_{coil} of the coil is found by imposing a 25 % current margin between the operational point of the coil and the critical current $I_C(B,T)$ of the superconductor. The 25 % safety margin is seen as a reasonable conservative starting point of a design of a superconducting generator, but in the final design one will have to determine the maximum temperature of the superconducting wire in the case that the coil is pushed out of the superconducting state. Such an event is called a quench and result from the coupled feedback of an increased local heat, which will result in lower local critical current density and thereby an even higher local heat. Eventually the superconductor will locally turn normal conducting and this zone will then spread to the rest of the coil, unless sufficient cooling is provided to the coil.
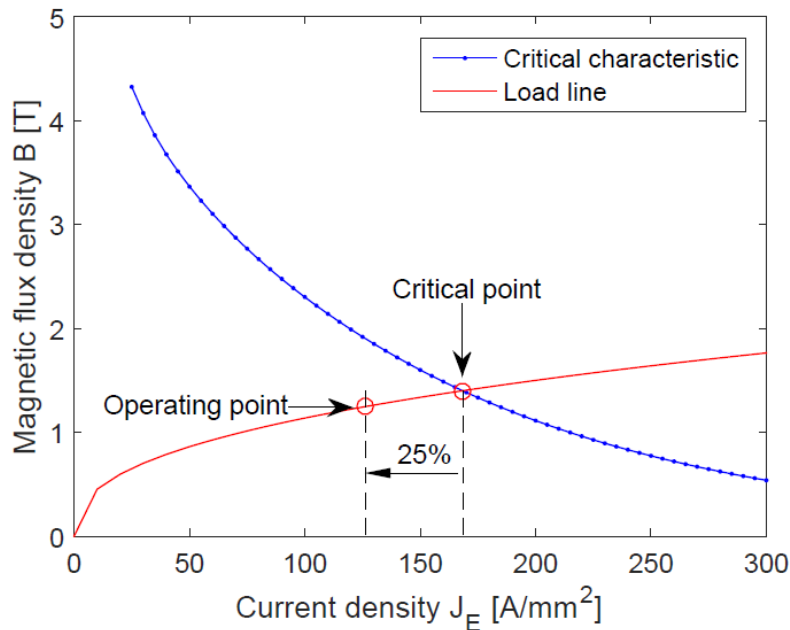
(INNWIND.EU, Deliverable 3.11, Superconducting generators)

Figure 5-3 Load line of MgB$_2$ wire in 10 MW generator. The critical current density of the MgB$_2$ wire (blue) at T = 20 K is reached by the operation current in the coil (red) at J = 170 A/mm^2. A safety margin of 25 % is imposed to ensure safe operation at the operation point of the coil. Reproduced from Figure A3.8.

The DC voltage drop U_{SC} of the superconducting field winding coil is given by the integral of the electric field of (5-4) along the superconducting wire

$$U_{SC,DC} = \int_{l=0}^{L} E(l)\,dl = \int_{l=0}^{L} E_0 \left(\frac{I_f}{I_C(l,B(l),T(l))}\right)^{n(l,B(l),T(l))} dl \qquad (5\text{-}6)$$

where l is the local position and L is the total wire length. The critical current I_C is now depending on the local properties of the superconducting material at position l as well as the local magnetic field $B(l)$ in the superconducting material and also the local temperature $T(l)$ of the material at position l. The local material properties depend on the local chemistry of the superconductor, where the ratio between magnesium and boron in MgB$_2$ might not be the stoichiometric 1:2, or in the high temperature superconductors RBa$_2$Cu$_3$O$_{6+x}$, which is not superconducting if the oxygen concentration is x < 0.5. Secondly the local superconducting properties will also depend on local mechanical strain, which can destroy the connection at the grain boundaries of the superconducting crystalline grains. Thus when winding a superconducting wire into a superconductor coil one must ensure that the wire is not exposed to stresses and strains above the critical levels. This also means that a critical bending diameter D_C is assigned to superconducting wires in order to ensure that the local I_C is not decreased during the winding and subsequent impregnation. For the MgB$_2$ and RBCO the values are D$_{C,MgB2}$ ~150 mm and D$_{C,RBCO}$ ~11 mm. Thus MgB$_2$ can only be used for large coils with an inner diameter of 15 cm, whereas RBCO can be used for small coils with a diameter down to 1.1 cm.

The detection of a quench of a superconductor coils is often detected by measuring the voltage drop U across the coil and then to compare that with a certain threshold value. In order to remove the energy of the coil during a quench a dump resistor will be switched in across the superconducting coil to discharge the coil. Such a system is call the quench detection and protection system and have to be designed for a specific superconducting generator. In the INNWIND.EU project a quench protection system was made for the MgB$_2$ coil demonstrator and it is believe that this can be transferred to a generator system with some adaptation.

The operation point obtained from the load line is used in the generator optimization process to determine how much superconductor wire that is needed in combination with the magnetic steel laminates in order to provide a certain peak magnetic flux density B_g in the air gap of the superconductor generator as given by (5-2).

5.3.1 Critical current of superconductors as input of INNWIND.EU generator designs

Two superconductor field coil demonstrations have been constructed and tested as part of the INNWIND.EU project in order to obtain state-of-the-art input on the critical current for the generator design in task 3.11 as well as 3.12 (Azar & Thomas, 2016). A MgB_2 superconductor race track coil made up of 10 double pan cake coils have been designed and tested in the Task 3.13 (Magnusson, Hellesø, Paulsen, Eliassen, & Abrahamsen, 2016). A high temperature superconducting 2G coated conductor coil has been designed and tested as part of task 3.12 (Azar & Thomas, 2016).

The critical current characteristics as obtained from the superconductor tape manufactures were used as a first input for the generator design. The critical current obtained in the field coil demonstrations were then compared to the initial values and the Technology Readiness Level of the coil manufacturing was evaluated.

MgB_2 critical current input for the design

The MgB_2 wire consist of 19 filament of MgB_2 inside a matrix of Ni, which is rolled into a tape like shape with a width of 3 mm and a thickness of 0.5 mm. A copper strip of width 3 mm and thickness of 0.2 mm was soldered onto the Ni matrix in order to provide a stabilizing materiel with high electrical as well as thermal conductivity. 5 km of wire was delivered from Columbus Superconductor at a cost of about 4 €/m (Columbus Superconductors SpA, 2017). It was discussed with Columbus superconductor if the wire cost could be reduced by ordering larger quantities (2-3 orders of magnitude more than the INNWIND.EU order) and it was believed that a cost of 1 €/m could be realistic. It was also discussed if a wire with a better critical current I_c in high magnetic field in the range of B = 2-4 Tesla could be supplied. It was believed that it would be possible, but with the relative small quantity of wire ordered by INNWIND.EU then only standard production wire could be supplied, since a large cost would be associated to optimizing a production line for a custom wire.

The cost ranges outlined above will be used in the evaluation of the MgB_2 generator costs.

Figure 5-4 is showing a plot of the critical current specification of the MgB_2 wire as well magnetization measurement of the expected scaling of the critical current at magnetic flux densities higher than 2 Tesla (Magnusson, Hellesø, Paulsen, Eliassen, & Abrahamsen, 2016). The critical current is lower at magnetic flux densities above B = 2 T compared to the original critical current data supplied for the MgB_2 wire. Some future scenarios of the wire development has therefore also been investigated in order to determine, which will be most beneficial for the feasibility of the MgB_2 generator technology. The MgB_2 wire development scenarios are

1) Standard: MgB_2 cost = 4 €/m   Critical current $I_C(B) = I_{C,INNWIND}(B)$ at T = 20 K

2) Low cost: MgB_2 cost → 1 €/m   Critical current $I_C(B) = I_{C,INNWIND}(B)$ at T = 20 K

3) Better wire: MgB_2 cost = 4 €/m   Critical current $I_C(B) →$ 4 x $I_{C,INNWIND}(B)$ at T = 20 K

4) Both: MgB_2 cost → 1 €/m   Critical current $I_C(B) →$ 4 x $I_{C,INNWIND}(B)$ at T = 20 K

Figure 5-5 is showing the present design critical current density of MgB_2 at T = 20 K as well as the future scenario of an improved critical current of a factor of 4. These two curves were used for evaluating the topologies T1 to T12 of the MgB_2 generators.
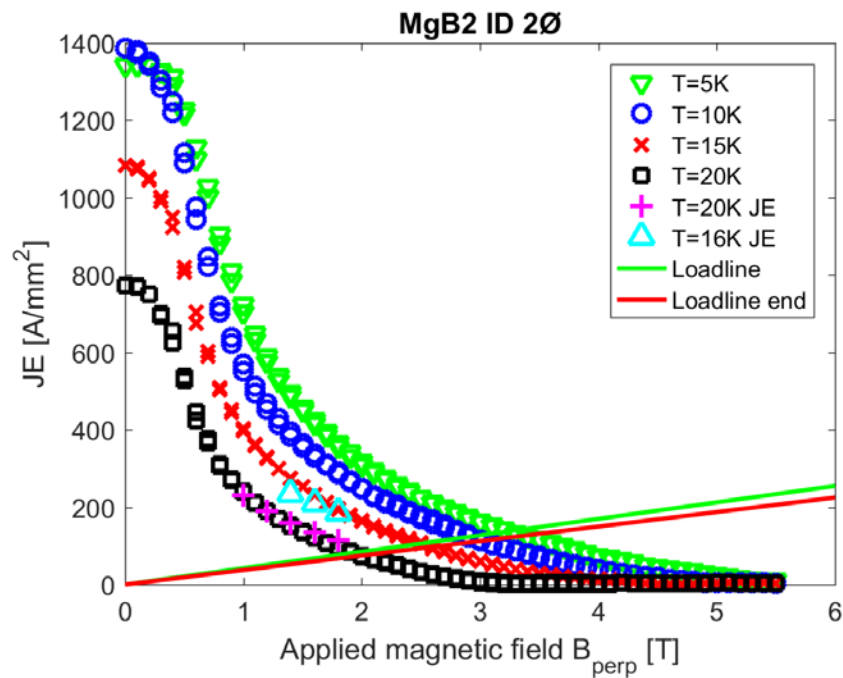
(INNWIND.EU, Deliverable 3.11, Superconducting generators)

Figure 5-4 Engineering critical current density $J_E(B)$ of the MgB$_2$ wire delivered from Columbus Superconductors as function of applied magnetic flux density. The data with the label $T = 20$ K JE and $T = 16$ K JE are the transport critical current measurements supplied from Columbus Superconductors on the different batches of wire. The remaining data was obtained from magnetization measurements on pieces of the MgB$_2$ wire and then scaled to the $B = 1$ T and $T = 20$ K transport measurement. Reproduced from Figure 1.15 of D3.13 (Magnusson, Hellesø, Paulsen, Eliassen, & Abrahamsen, 2016).
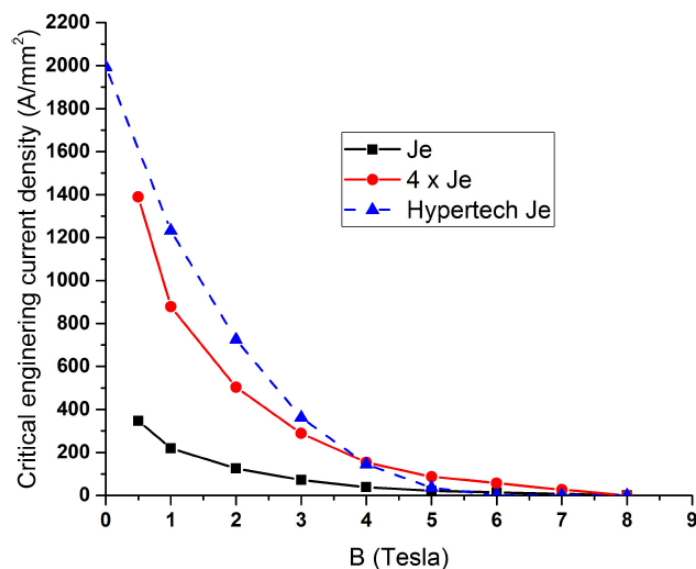

Figure 5-5 Design engineering critical current density of $J_E(B)$ of the MgB$_2$ wire at $T = 20$ K wire with current properties as well as a future scenario of a 4 times better critical current. Reproduced from Figure A3.16.

RBCO coated conductor tape critical current input for generator design

A high temperature superconducting 2G coated conductor race track coil has been constructed and tested as part of task 3.12 (Azar & Thomas, 2016). The RBCO coated conductor tape used for the coil demonstration is of the Gadolinium based type with the rare earth element R = Gd in the $RBa_2Cu_3O_{6+x}$ chemical formula. The manufacture of the tape in unknown due to confidentially concerns in task 3.12 (Azar & Thomas, 2016). The critical current density of the RBCO tape used for the generator design with an operation temperature of T = 30 K is shown in Figure 5-6 together with the load line.
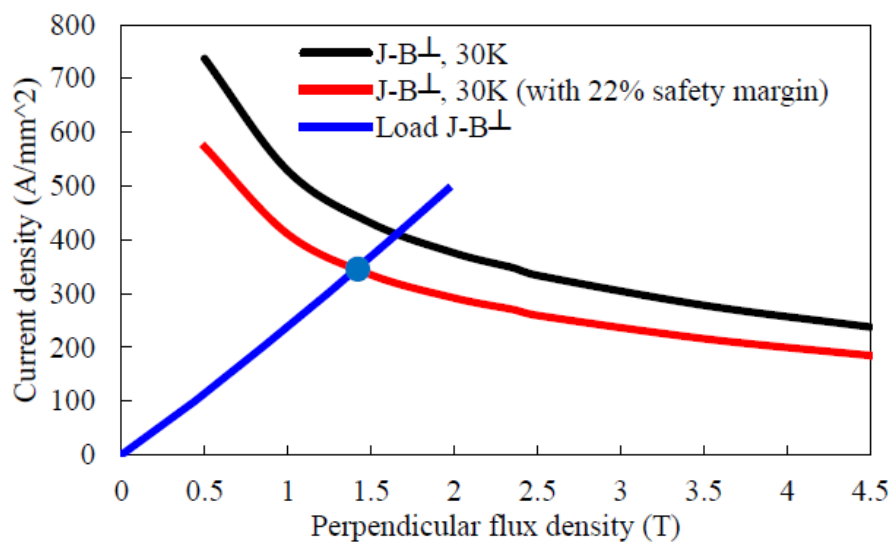

Figure 5-6 Critical current density of the coated conductor used for the design of the high temperature superconducting direct drive generators. The load line and a critical current density imposing a 22 % safety margin are also shown. Reproduced from Figure 22 of D3.12 (Azar & Thomas, 2016).

5.3.2 Critical current and Technology Readiness Level of INNWIND.EU MgB₂ coil demonstration

The Technology Readiness Level (TRL) of the MgB_2 wire for wind turbine coils manufacturing has been investigated in task 3.13 by the construction of a scaled rotor field coil demonstration (Magnusson, Hellesø, Paulsen, Eliassen, & Abrahamsen, 2016).

Approximately 500 m of MgB_2 wire were wound into double pan cake coils with an inner opening of 0.3 m and a straight section of 0.5 m using wet winding into a low temperature Stycast 2850. The total length of the coils were about 1 m and the width 0.5 m. 10 pan cake coils were stacked into the final race track coil with a height of 8 cm. Each double pan-cake coil was cured individually and 10 pan cakes were then glued together with Stycast 2850 into a race track coil resembling a short version of a high field MgB_2 10 MW wind turbine generator design (Abrahamsen, Magnusson, Jensen, Liu, & Polinder, 2014). The opening of 0.3 m of the race track coil was chosen as double the critical bending diameter D_C = 0.15 m as specified by Columbus Superconductor (Columbus Superconductors SpA, 2017).

The initial testing of the race track coil is reported in deliverable report 3.13 (Magnusson, Hellesø, Paulsen, Eliassen, & Abrahamsen, 2016) and it was found that the initial coil test was suffering from a problem in providing enough cooling from the 1 stage of the cold head to the radiation shield of the cryostat.

A coil temperature of T = 18 K at both ends of the coil was reached after 7 days, but it was found that the Bi-2223 high temperature superconductor tapes used as current leads from the radiation shield and to the coil were not superconducting. This was due to the insufficient cooling of the radiation shield, which ended up having a temperature of 140 K instead of the design target of 70 K.

A low current test of the MgB_2 race track coil was conducted to investigate the IV - curves of the 10 double pancake coils of the race track demonstrator. Large voltage drops in the range of 20-45 µV across the two outer pancake coils no. 1 and no. 10 as well as coil no. 6 were observed at a coil current of only 16 A as shown in Figure 5-7. The remaining coils showed a voltage drop corresponding to the noise level ~ 1-3 µV of the measurements. This indicated that 7 out of 10 coils were showing the expected superconducting characteristics.

The cold head connection to the radiation shield was fixed and a second cool down of the coil was performed. This resulted in a coil temperature of 11 K and 14 K at the two ends of the coil. The radiation shield reached a temperature of 53 - 54 K and the high temperature current leads were superconducting. Figure 5-7 is showing the voltage drop across the pancake coils 1-10 during the second test where the coil current was ramped up to 130 A and stabilized, whereby the inductive voltage contribution from the coil inductances have decayed. The temperature of the coil increased to 14 K and 17 K during the ramp due to the additional heating of the current leads.

The voltage drop of the pan-cake coils are expected to follow the power law dependence and the critical voltage drop is given as $U_0 = E_0 \cdot L$, where $E_0 = 10^{-4}$ V/m and L is the length of the wire reaching the critical current. For the pan-cake coil then the two inner most turns will be exposed to the highest magnetic flux density and will therefore reach the critical current first. Thus by choosing L = 4 m one can obtain an estimate of the critical voltage drop

$$U_0 = E_0 L = 10^{-4} \frac{V}{m} \cdot 4\, m = 4 \cdot 10^{-4}\, V = 400\, \mu V \qquad (5\text{-}7)$$

This voltage drop criteria has been included in Figure 5-7 as a horizontal line. It is seen that several coils are passing this criteria even at I = 50 A due to the development of a voltage drop even at low currents. Thus the superconductors seem to contain damaged segments, which will

make the determination of the critical current difficult and also make the detection of quenches of the coil difficult. It was decided to perform a third test in which the coil current was ramped to I = 146 A. This resulted in a quench of the race track coil and a burnout of the soldering connections between pan-cake coil 9 and 10. The jump of the voltages at the critical current in most of the pan-cake coils can be seen by the last point of the third test in Figure 5-7.

The cryostat was opened after the quench and a series connection of coil 1 to 8 was re-established before the race track coil was cooled down again. A fourth test, where the race track coil current was ramped to I = 50 A, was performed while the voltage drop across coil 1 to 8 was measured. It was found that the IV curve of coils were unchanged after the quench except for coil no 7 as shown in Figure 5-8. This is indicating that the thermal properties of the race track coil are quite good and the quench is most likely associated with the damaged and weak segments of the wires in the pan-cake coils.

Discussion of MgB$_2$ race track results

It is clear from Figure 5-7 that coil 4 and 5 are looking perfectly superconducting with a constant voltage drop corresponding basically to the noise floor of the measurement all the way up to I = 140 A after which a sharp increase of the voltage is observed. In deliverable 3.13 (Magnusson, Hellesø, Paulsen, Eliassen, & Abrahamsen, 2016) is was predicted in table 6 that that the operational current $I_{operation, 20 K}$ = 130 A @ 20 K and $I_{operation, 15 K}$ = 183 A @ 15 K for the race track coil taking into account the critical current scaling measure by Vibrating Sample Magnetometer (VSM) on the actual wire used in the coil. Thus the measurements on coil 4 and 5 confirm the superconductor properties of the MgB$_2$ wire for the application as a generator field race track coil.

It is however also clear from Figure 5-7 that the rest of the coils are showing a gradually increasing voltage drop already from coil currents much lower than the critical current I_c, which was predicted as $I_{c, 20 K}$ = 173 A @ 20 K and $I_{c, 15 K}$ = 244 A @ 15 K (Magnusson, Hellesø, Paulsen, Eliassen, & Abrahamsen, 2016). This is indicating that a fraction of the 500 m of wire in these pan-cake coils is damaged and has lower superconducting properties. Qualitatively what happen is that the current will be shared between the weak superconducting section and the Ni matrix and the Cu strip connected in parallel with the superconducting filaments. Thus at low current the superconducting filaments will carry all the current, but as the critical current of the weak section is exceeded then current is forced into the normal metal.

The voltage drop across coil 2, 3, 7, 8 and 9 is increasing gradually above the noise floor at about I = 50 A, whereas coil 1, 2 and 10 shows a gradually increasing voltage above the noise floor already above I = 10 A. There seem to be some systematic pattern with the pan-cake coils facing the Cu cooling support plates showing the worst behaviour, the coils in position 3 and 4 being slightly better and the middle coils basically perfect. This could be reflecting thermal stresses building up due to the mis-match in the thermal expansion coefficients of Cu and the MgB$_2$ wire or mechanical stresses due to the winding and mounting procedure. It is also worth noting that the outer coils will experience the largest magnetic flux density, whereby any weak sections of the wires will have a further reduction of the critical current. But the fact that the voltage drop is observed at I/I_c ~ 10 A / 173 A = 5 % for 3 of the coils is indicating a physical damage of the wires.

(INNWIND.EU, Deliverable 3.11, Superconducting generators)

IV curves of INNWIND.EU MgB$_2$ Race track coil
Double pancake coils from no. 1-10 in series

T_1 = 11.0 K -> 14.0 K
T_2 = 14.2 K -> 17.0 K

I_c criteria

Dashed lines: First cool down
Closed symbols: Test 4.1 16/12-2016
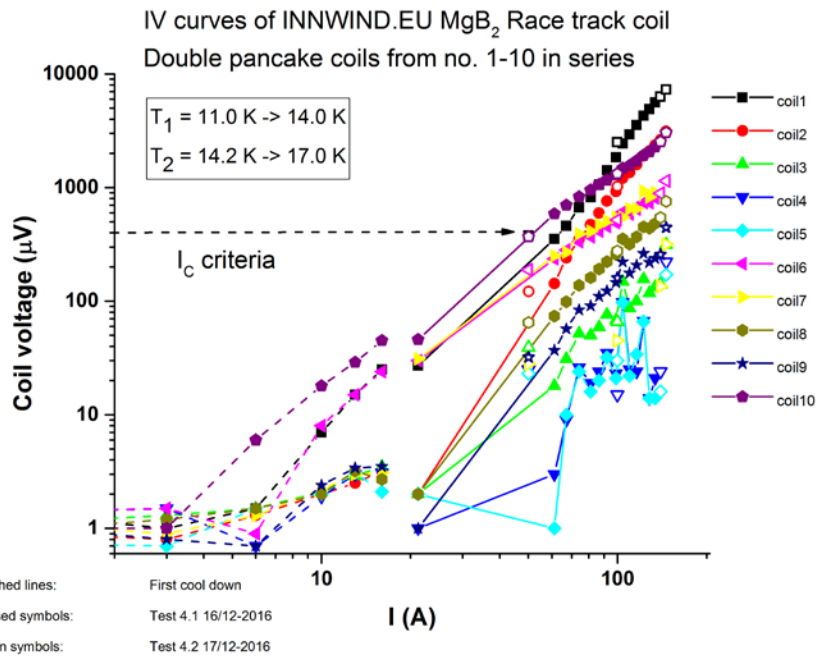Open symbols: Test 4.2 17/12-2016

Figure 5-7 Voltage drop across the 10 pan-cake coils making up the INNWIND.EU MgB$_2$ race track field coil demonstrator as function of the coil current. Each pan-cake coil holds about 500 m of MgB$_2$ wire. The pan-cake coils are stacked in order from 1-10 and series connected resulting in 5 km of wire in the race-track coil. The race track was cooled to T = 18 K in the first test (dashed lines) and only tested to I = 16 A due to insufficient cooling of the radiation shield of the cryostat. The coil current was ramped to I = 130 A in the second test (closed symbols) where the race track end temperatures changed from 11 → 14 K and 14 → 17 K due to heating of the current leads. The coil current was increased to I = 146 A in the third test (open symbols), which resulted in a quench and a destruction of coil 9 and 10 as well as the series connection between the coils. The expected voltage drop corresponding to the inner two turns reaching the critical current is shown as a horizontal dashed line.
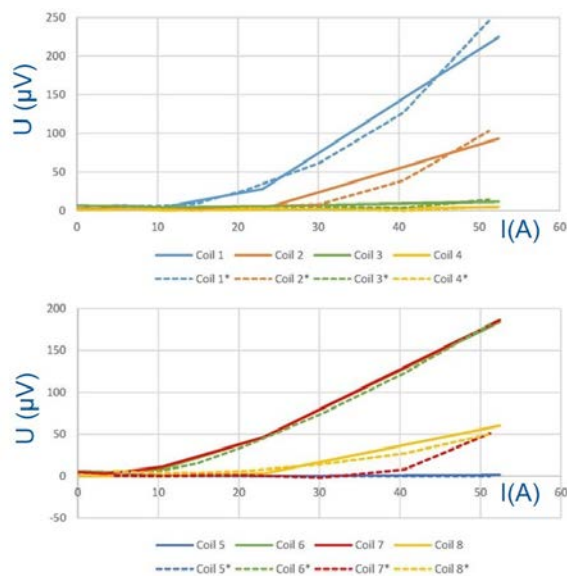

Figure 5-8 IV curves of pan-cake coils before (dashed) and after (full) quench of the INNWIND.EU Race Track coil. It is seen that all coils but coil no. 7 show the same IV curves after the quench, which is indicating very good thermal properties of the race track coil. Coil no 9 and 10 burned during the quench and was disconnected in the fourth test of the Race track coil.

(INNWIND.EU, Deliverable 3.11, Superconducting generators)

Voltage drop model of MgB₂ wire with weak sections

In order to extract more detailed information about the damaged section then a model of the current sharing in the pan-cake coils is formulated. Figure 5-9 is showing a circuit diagram of how a superconducting wire can be considered as a parallel coupling of a superconductor sections and a normal resistor sections. The voltage drop of a superconductor section is

$$U_{sc} = E_0 L \left(\frac{i_{sc}}{i_C}\right)^n \Rightarrow i_{sc} = i_C \left(\frac{U_{sc}}{E_0 L}\right)^{\frac{1}{n}} \tag{5-8}$$

where E_0 is the electric field at the critical current i_C, L is the length of the superconducting section under evaluation, n is the n-value of the power law for the section and i_{sc} is the supercurrent running in the filaments.

The voltage drop across the normal resistor is equal to the superconductor voltage drop

$$U_{sc} = R_N i_N \Rightarrow i_N = \frac{U_{sc}}{R_N} = \frac{U_{sc}}{\frac{\rho_N}{A_N} L} \tag{5-9}$$

where i_N is the current running in the normal metal, R_N is the normal metal resistance of the section, which can also be expressed from the normal metal resistivity ρ_N, the cross section area of the normal metal A_N and the length of the section L. A value of $\rho_N = 1.4 \cdot 10^{-9}$ Ωm at $T = 20$ K and $A_N = 1.19$ mm² have been estimated from data provided from Columbus Superconductor.

The total current running through the wire section then becomes

$$i = i_{sc} + i_N = i_C \left(\frac{U_{sc}}{E_0 L}\right)^{\frac{1}{n}} + \frac{U_{sc}}{\frac{\rho_N}{A_N} L} \tag{5-10}$$

The above equation is valid for each section of the wire, but the voltage U measured by the voltmeter in Figure 5-9 consist of the sum of 3 sections $U = U_{sc2} + U_{sc3} + U_{sc4}$. If however the critical current of section 2 is much larger that for section 3 ($i_{c2} \gg i_{c3}$) then U_{Sc2} is basically zero and can almost be neglected from the sum even though L_2 is several hundreds of meters of wire. Similarly, if the superconductor in section U_{SC4} is completely destroyed then only the normal resistor R_{N4} will appear in the circuit diagram as shown in Figure 5-9 b.

A 3 segment model of the wire can then be formulated as

$$U_{3segment\,model} = U_{SC2} + U_{SC3} + R_N i + U_{noise} \tag{5-11}$$

where U_{SC2} is the good superconductor segment, U_{SC3} is the weak superconductor segment, R_N is the resistance of the segment where no superconductor is present and finally a constant noise voltage U_{noise} as given by the measuring method is added. For small currents in the 3 segment model then little current sharing is present and the voltage drop U_{SC} is reasonable described by just the power-law, since most of the current is running in the superconductor, $i_{SC} \sim i$.

Figure 5-10 is showing the response of the 3 segment model when the good superconducting section is assumed to have $i_{c2} = 140$ A and an *n*-value of $n_2 = 20$. The length of the good segment is assumed to have a length equivalent to the two inner most turns of the pan-cake coil giving $L_2 = 4$ m. The weak section is assumed to have $i_{c3} = 40$ A, $n_3 = 4$ and a length of $L_3 = 0.1$ m. The normal resistor R_N is determined from the initial slope of the IV curves of coil 1, 6 and 10 of Figure 5-7 and a value of $R_N \sim 2$ μΩ obtained. Figure 5-10 is showing the ideal expected voltage drop U_{ideal} of the wire as the sum of the noise floor and the good superconductor, but also the full 3 segment model including the weak superconductor section as well as the normal resistive voltage

(INNWIND.EU, Deliverable 3.11, Superconducting generators)

drop. Thus the 3 segment model seems to provide a reasonable description of the observed voltage drop of coil 1, 6 and 10 in Figure 5-7.

The 3 segment model can be used to quantify the properties of the weak superconducting segment by subtracting of the normal resistance voltage drop as well as the voltage drop of the good superconductor segment giving

$$U_{SC3} = U_{measured} - U_R - U_{SC2} - U_{noise} \qquad (5\text{-}12)$$

The simplest way to describe the weak superconductor section U_{SC3} is to assume that it is given by a power-law

$$U_{SC3,simple} \sim E_0 L_3 \left(\frac{i_{sc}}{i_{c3}} \right)^{n_3} \qquad (5\text{-}13)$$

Figure 5-11 is showing the voltage drop of the weak segment of coil no. 1 after subtracting the normal resistance voltage drop and the expected voltage drop of the good superconductor section. It is seen that U_{SC3} is falling on a straight line in the Log-Log plot, which is confirming that the power-law description is reasonable. The power law (5-13) has been fitted to the upper part of U_{SC3}, whereby the n-value is determined to be $n_3 = 3.7$ being considerable lower than the expected 20. The fit can however not provide information about both the critical current i_{c3} and the length of the weak segment L_3, because only the ratio

$$\left(\frac{L_3}{i_{c3}} \right)^{n_3} = \left(\frac{L_3{}'}{i_{c3}{}'} \right)^{n_3} \qquad (5\text{-}14)$$

is obtained as a fitting parameter. This means that a many combination of critical currents and lengths will be able to describe the observed voltage drop of the weak section. The power law fit was therefore done by assuming that the length of the weak segment can be fixed to $L_3 = 1$ m and the equivalent $i_{c3} = 45.2$ A was then determined. Figure 5-12 is showing how these parameters can equally well be obtained by other combinations such as $L_3 = 0.02$ m and $i_{c3} = 20$ A or $L_3 = 10$ m and $i_{c3} = 100$ A. If the critical current is assumed to be the same as for the good superconductor $i_{c3} = 140$ A then the length of the weak segment of a small n-value will have a length of $L_3 = 50$ m.

Figure 5-13 is showing the superconducting parameters of the power-law fitted to the weak segments of the INNWIND.EU pan-cake coils when the length of the weak sections are assumed fixed at $L = 1$ m as described above. It is seen that the n-values are in the range between 2-4, which is considerable smaller than 20 as expected for the good superconducting segments represented by coil 4 and 5. The critical currents of the weak segments are found to be in the range of 26 – 110 A, which is considerable lower than the expected critical current of 140 A of the good segments.

For the coils showing a large voltage drop of the weak segment then the current sharing model of equation (5-10) can be used to obtain further information about the length of the weak segment, because the normal resistance will scale with the segment length. Figure 5-14 is showing a fit of the current sharing model to the U_{CS3} voltage of coil no. 1 and it can be seen that the current increases linearly with the voltage for large voltages indicating the current sharing between the superconductor and the normal metal. An n-value of $n = 4.5$ is obtained from the fit. The critical current is found to be $I_c = 39.9$ A and the length of the weak segment is $L = 36$ cm. Figure 5-15 shows the properties of the weak segments as obtained by fitting the current sharing model to the measurements of the coils, where a sufficient current sharing was present in order to make a reasonable fit. This is shown together with the properties obtained by the power-law fit. It is seen that both models agree that the n-values are in the range between 2-5. The critical current of the weak segment of coils no. 1 is found to have decreased from $I_{c,powerlaw} = 45$ A to $I_{c,current\ share} = 40$ A obtained from the power-law to the current sharing model fit. The length of the weak segment is found to be $L = 36$ cm for the current sharing model. A similar result is obtained for coil no. 2

where $I_{c,powerlaw}$ = 48 A to $I_{c,current\ share}$ = 31 A, but the length is decreased to L = 6 cm. In case of coil 6 and coil 10 then a considerable reduction of the critical current to I_C = 7-8 A is observed and the length of the weak section is decreasing towards L = 1-3 cm.

It can be concluded that weak superconducting segments have been identified in 8 out of 10 pan-cake coils of the INNWIND.EU race track coil demonstrator. The superconducting properties of the weak sections show n-values in the range of 2-5, which is considerable lower than the expected value of 20 for the good segments of the wire. The critical current is reduced to $I_{C,\ weak}$ = 26-110 A and should be compared to I_C = 140 A for the good segment of the wire. The length of the weak segments have been determined to be in the range L = 1-36 cm, which is a very small fraction of the total wire length of 500 m in each double pan-cake coil. Additionally 3 out of 10 coils showed a small segment of no superconductivity, which cause a normal resistance in series with the wire. The non-superconducting and weak superconducting segments are believe to be the reason for the destructive quench of the race track coil.

It therefore remains a questions if the weak segments were introduced by the winding technique or if such weak segment were present in the wire already after the wire manufacturing. The fact that weak segments are observed in most of the pan-cake coil is indicating that either they are quite likely to be found in each 500 m wire piece or the winding method is introducing them consistently. A wire qualification test has been proposed, where the remaining 20 – 50 m pieces of the wires from the INNWIND.EU pan-cake coils are wound onto a coil former with an opening of only 15 cm equivalent to the critical bending diameter and then tested at T = 20 K by measuring the voltage drop up to I = 100 A. This should reveal if any weak segment are found in a wire piece of about 1/10 of the 500 m piece length used for the winding. Such an experiment will also indicate if it should be recommended to test up to 1 km of wire on the spool of the manufacturer in the future by cooling it down to T = 20 K and pass a current of I < 50 A. If the wire is good then it will show a flat IV curve, but if it is bad one will be able to see the weak segments and the wire can be discarded before winding. Eventually such a test will have to be not needed in order to bring the wire cost towards the 1 €/m, but it might be useful in the work on scaling up the wire production volume in order to improve the quality.

Based on the findings above the Technology Readiness Level of the MgB_2 field coil technology has been raise from TRL = 3 (characteristic proof of concept) to about TRL = 4 (component validation in laboratory environment).
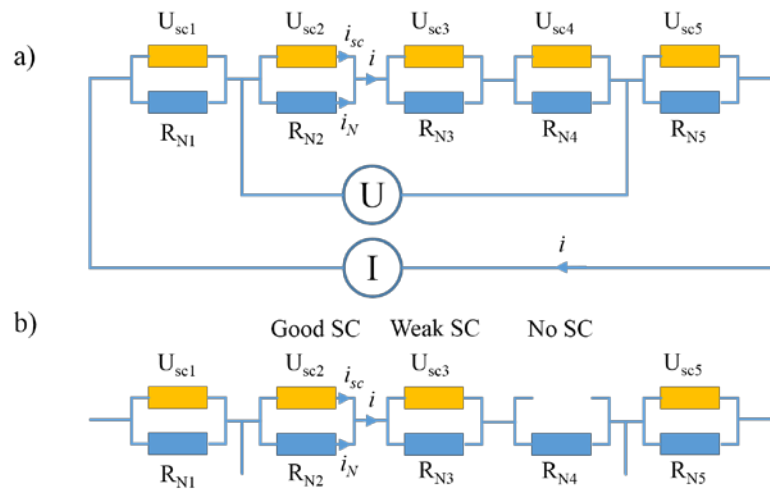
(INNWIND.EU, Deliverable 3.11, Superconducting generators)

Figure 5-9 Circuit model for current sharing of a superconducting wire with a normal resistor in parallel for stabilization. a) A current i is supplied by a power supply to the ends of the wire, which is divided into 5 sections. A voltmeter U is measuring the voltage drop across the 3 middle sections in a 4 point measurement setup. The normal resistance of the sections are denoted R_{N1} to R_{N5} and the voltage drop across the superconducting sections are denoted U_{sc1} to U_{sc5}. The current sharing result in $i = i_{sc} + i_N$ for each section, where i_{sc} is the current running in the superconducting filaments of the wire and i_N is the current running in the metal matrix and copper strip around the filaments. b) Illustration that the voltage drop measured by U can be composed of a good U_{SC2} and a weak U_{SC3} superconducting section with the critical current as current $I_{C2} \gg I_{C3}$. In the case that superconductivity is almost completely suppressed in section 4 then only the voltage drop across the normal resistor R_{N4} is observed.
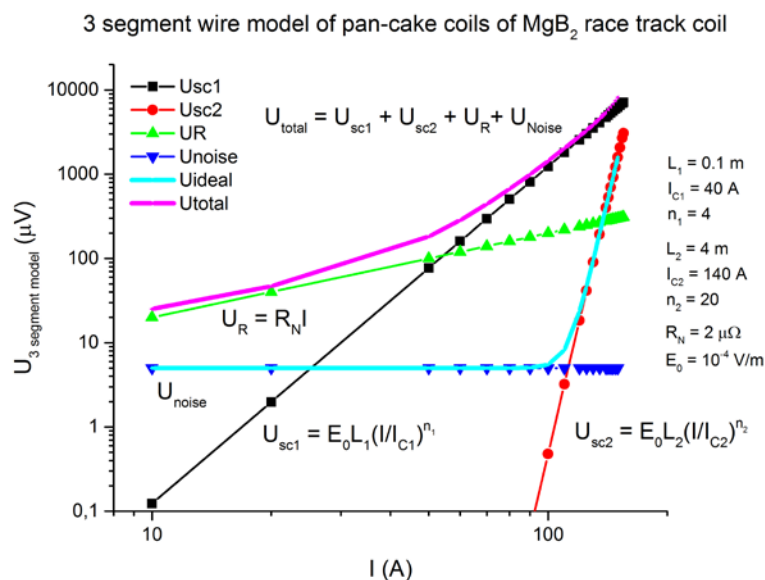

Figure 5-10 Prediction of a 3 segment model of the voltage drop of the pan-cake coils of the INNWIND.EU Race track coils. The ideal response of the coil U_{Ideal} would be a combination of a noise floor U_{noise} and the power law of the good superconductor U_{SC1}, with a critical current of $I_c = 140$ A and a n-value of 20. The observed measurement are however also showing a resistive voltage drop U_R and the voltage drop corresponding to a weak superconductor section U_{SC2} with a critical current of only $I_{C2} = 40$ A and a n-value of only 4. The total voltage drop is the combination of the four contributions.

Power law fit to weak section of pan-cake coil no. 1

Model	PowerSuperconductor (User)
Equation	E0*L*(x/IC)^n + U0
Plot	coil1Usc2
E0	100 ± 0
L	1 ± 0
IC	45,15433 ± 1,48461
n	3,67908 ± 0,11878
U0	2 ± 0
Reduced Chi-Sqr	18927,25363
R-Square(COD)	0,9941
Adj. R-Square	0,99357

$T_{\text{Race track coil}} = 14\text{-}18\ K$

U_{sc2}
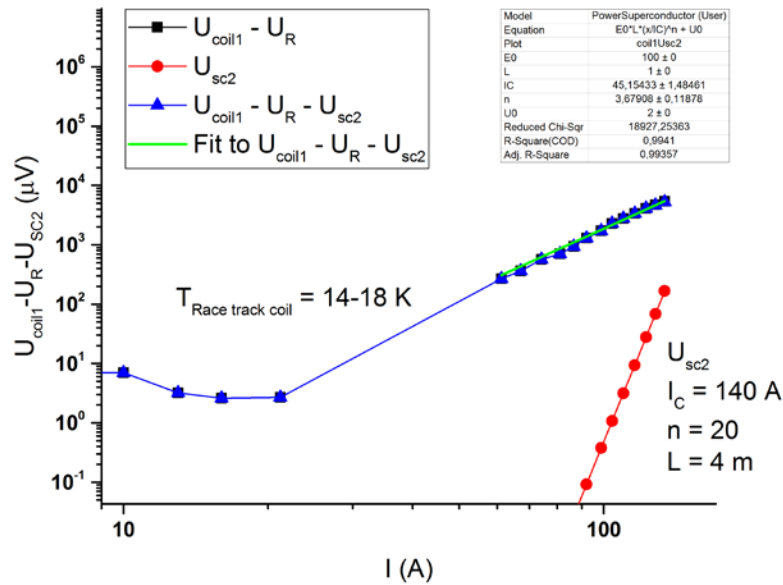$I_C = 140\ A$
$n = 20$
$L = 4\ m$

Figure 5-11 Voltage drop of pan-cake coil no. 1 after subtracting the normal resistor R_{N4} and also the contribution of the expected voltage-e drop of the good section denoted U_{sc2} in Figure 5-9. A power law of the form $U = E_0 L (I/I_C)^n$ has been fitted to the resulting voltage drop of pan-cake coil no. 1. The slope of the curve is given by the *n*-value and it can be seen that the obtained $n \sim 3{,}7$ is considerable smaller than the $n \sim 20$ expected for the good superconducting section U_{sc2}. The fit is obtained by fixing the length of the weak superconducting section to $L = 1$ m.

Inter dependency of weak section lenght and weak critical current

$L_2 = (I_{c2}\,/\,I_{c1})^n\,L_1$

Pan-cake coil no. 1 weak section
$n = 3.68$
$I_{c1} = 45.2\ A$
$L_1 = 1\ m$
$T_{\text{Race track}} = 14\text{-}18\ K$
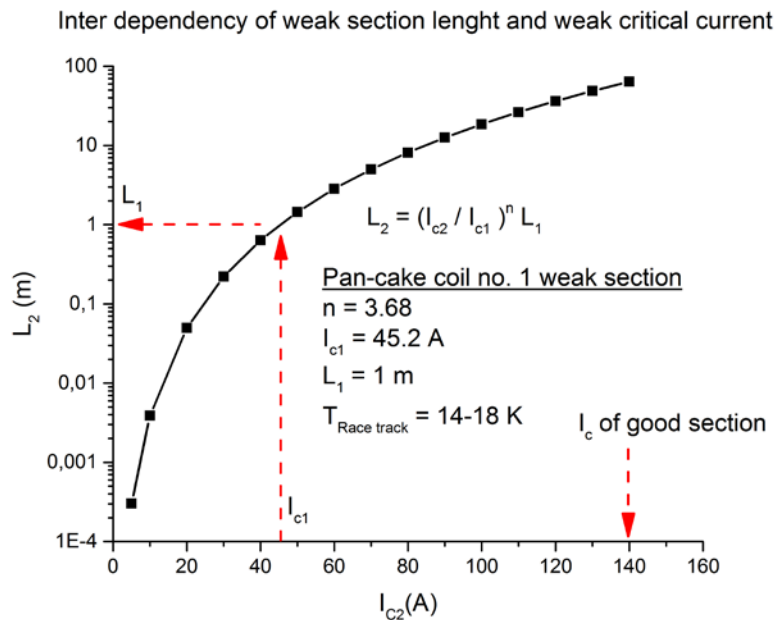
I_c of good section

Figure 5-12 Interdependency between the critical current I_c and the length L of the weak section of the pan-cake coil no. 1 as obtained from the power law fit. The value of I_c obtained by fixing $L = 1$ m is indicated by arrows, but any combination of I_c and L on the curve will produce the observed voltage drop of the weak superconducting section.

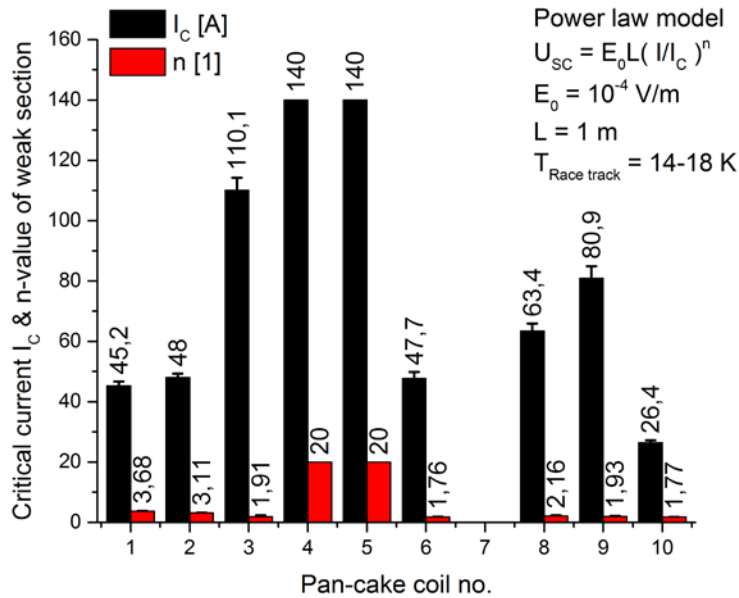*(INNWIND.EU, Deliverable 3.11, Superconducting generators)*

Figure 5-13 Critical current and *n*-values of the weak section of pan-cake coils of the INNWIND.EU race track coil obtained by fitting a power law to the voltage drop of the pan-cake coils. The values for coil 4 and 5 are indicating expected values of the two perfectly working coils.
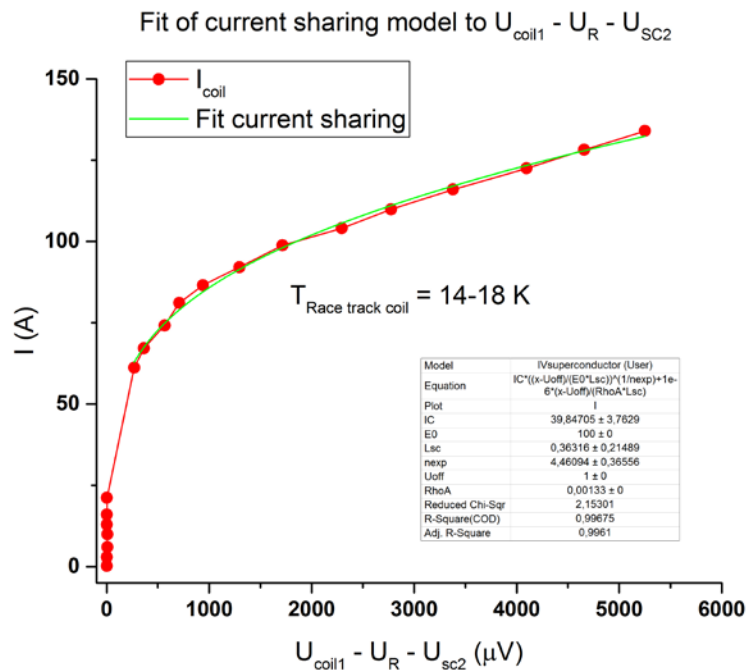

Figure 5-14 Fitting of current sharing model to the voltage drop of the weak section of pan-cake coil no.1 after correcting for the section without superconductivity and the section with good superconducting properties.

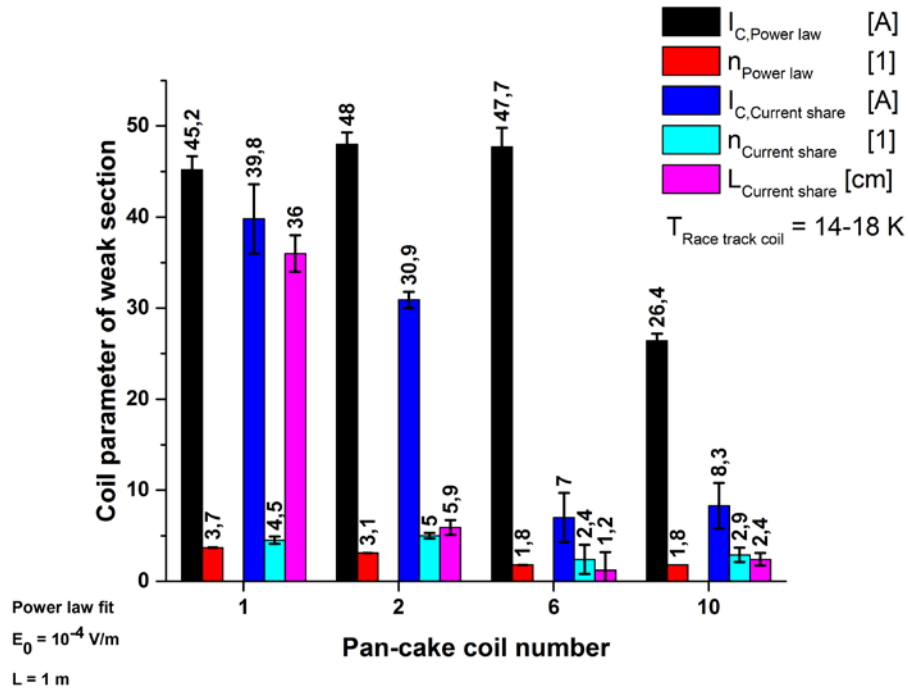*(INNWIND.EU, Deliverable 3.11, Superconducting generators)*

Figure 5-15 Superconducting characteristics of weak sections of the pan-cake coils no. 1, 2, 6 and 10 obtained from both the power-law model fit and the current sharing model fit to the measurements.

(INNWIND.EU, Deliverable 3.11, Superconducting generators)

5.3.3 Critical current and Technology Readiness Level of INNWIND.EU RBCO coil demonstration

A high temperature superconducting second generation (2G) coated conductor race track coil has been constructed and tested as part of task 3.12 (Azar & Thomas, 2016). The critical current of the coil has been used for the generator design of Siemens Wind Power in phase B of task 3.12.

The RBCO tape used for the coil demonstration is of the Gadolinium based type with the rare earth element R = Gd in the $RBa_2Cu_3O_{6+x}$ chemical formula. The tape consist of a 75 µm Hastelloy substrate, a 2 µm GdBCO high temperature superconducting film and a 100 µm copper stabilizer layer. The width of the tape is 12 mm and the unit length cost is stated as 100 €/m, but future wire costs of 60 €/m and 20 €/m have been suggested. The manufacture of the tape in unknown due to confidentially concerns of task 3.12 (Azar & Thomas, 2016).

The critical current of the RBCO tape has been measured as function of applied magnetic flux density and temperatures as shown in Figure 5-16. The GdBCO coated conductor was wound into 8 single race track coils with an opening of 120 mm and a straight section of 300 mm using a wet winding technique. Each coil holds about 102 turns resulting in a winding thickness of 22 mm. The opening of the coil is similar to the pole size of current permanent magnet direct drive (PMDD) wind turbine generators, but the length of the coil is down scaled compared to the PMDD generators to reduce the cost of the demonstration. The coils were equipped with an outer and inner current connection block, whereby several coils could be stacked in series connected into a race track field coil. The 8 single winding coils were first tested by cooling in liquid nitrogen to T = 77 K and measuring the voltage drop across the coils as the current was ramped up. It was found that 3 out of 8 coils were showing non-superconducting behaviour at low current, whereas the rest were superconducting up to the design current I_c = 180 A at T = 77 K. The damages of 3 of the coils are believed to be caused by a too fast cooling rate from 300 K to 77 K in 10-15 minutes using the liquid nitrogen, since the last coils were cooled at a considerable slower rate and resulted in no observed damage.

The race track field coil was constructed by combining 3 of the best performing coil from the T = 77 K test and Figure 5-17 a) is showing the test of the full race track coil at T = 77 K. The race track coil was then tested at T = 30 K using a cooling circuit of liquid neon. Figure 5-17 b) is showing the voltage drop across the individual coils and it is seen that two of the coils were fully superconducting up to I = 450 A. One coil showed a faster increasing voltage drop at I = 450 A during the first ramp and this resulted in a permanent change of the IV- curve in subsequent IV curve measurements. Thus it was concluded that 2 out of 3 coils were proving the superconducting properties up to 69 % of the design current of 650 A and then AC loss measurements were performed before any burn out of the race track coil would happen if the coil current was increased further towards the 650 A design target. No further tests were done to measure the properties of the two coil, because that would need a re-design of the current leads or a replacement of the damaged coil.

The Technology Readiness Level (TRL) of the high temperature superconducting coated conductor race track coil demonstration of the INNWIND.EU project must be concluded to have shown an increase from TRL = 3 (characteristic proof of concept) to about TRL = 4 (component validation in laboratory environment). Further work on industrializing the coil manufacturing with a high success rate is needed before the technology is attempted lifted to TRL = 5 (component validation in a relevant environment).

It should be mentioned that second generation coated conductor tape for wind turbine generators is also investigated in the ECOswing project (ECOswing, 2017) as well as the HTS-Gen project (Song, et al., 2017). In those project functional field coils have been produced, but no information about the success rate is available.

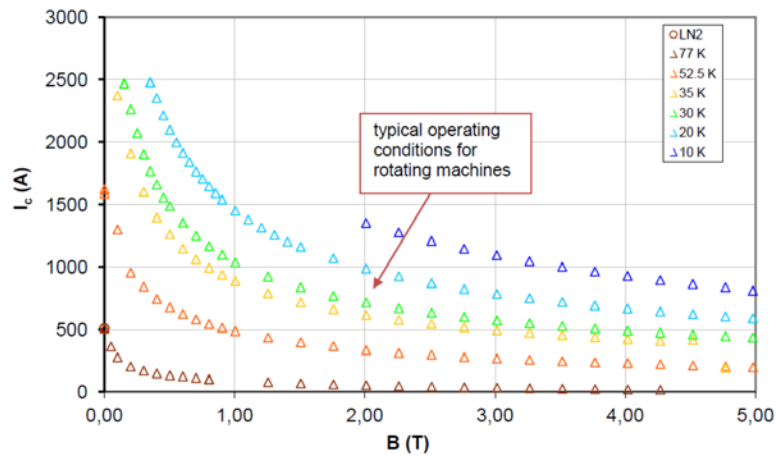*(INNWIND.EU, Deliverable 3.11, Superconducting generators)*

Figure 5-16 Critical current of the high temperature superconducting GdBCO coated conductor tape used for the field coil demonstration of task 3.12. Reproduced from Figure 3 (Azar & Thomas, 2016).
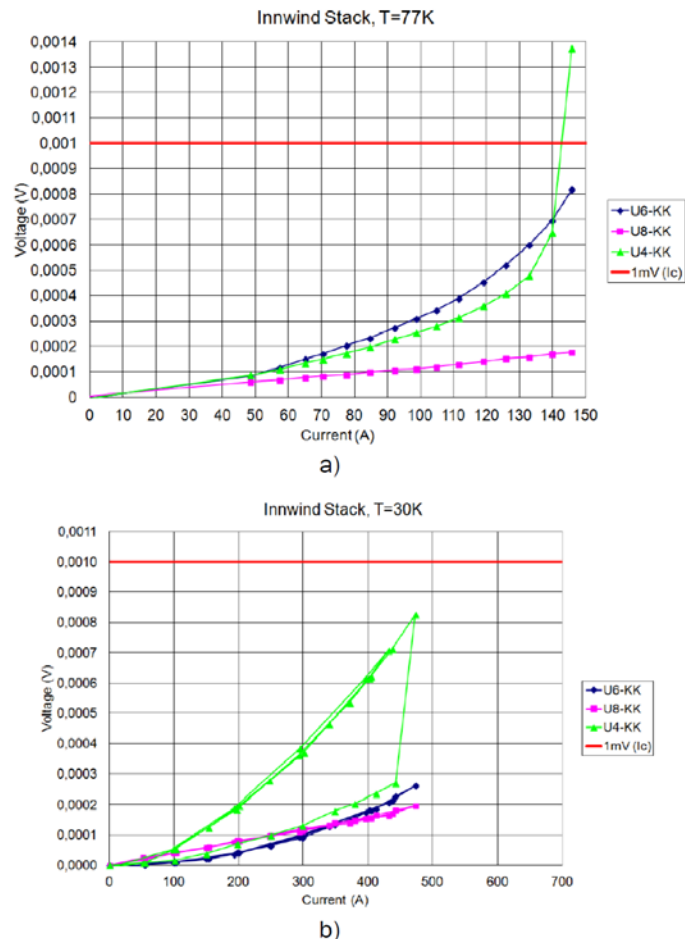

a)

b)

Figure 5-17 Voltage drop across the coated conductor high temperature superconducting single race track coils U4, U6 and U8 combined into the final demonstration race track coil. a) Measured after cooling down the coils in liquid nitrogen (LN2) to T = 77 K and b) after cooling down to T = 30 K using a liquid neon cooling setup. A critical current criteria of 1 mV is indicated by the horizonthal line. Coil U4 showed a steep increase of the voltage at I = 450 A and T = 30 K. A subsequent increased voltage drop at low currents indicates the appearance of a weak segment in the tape of coil U4, but coil U6 and coil U8 are expected to be able to comply with the target current of $I_{operation}$ = 650 A. Reproduced from Figure 11 (Azar & Thomas, 2016).

(INNWIND.EU, Deliverable 3.11, Superconducting generators)

5.4   Losses and efficiency

The losses of the superconducting generator are mainly associated with

1) The joule heating of the armature wires due to the phase currents.
2) Hysteresis losses of the magnetic steel laminates when exposed to AC magnetic field.
3) Eddy current losses in conducting material exposed to time varying magnetic fields.
4) Losses in the superconductors due to the DC coil current as well as the AC magnetic field from the armature.
5) Losses of the power electronics controlling the currents in the armature windings.
6) Power consumption of the cryogenic cooling machines.

The items 1-3 are described in chapter 3 "Topology comparison based on currently available MgB_2 superconductors" page A71 (Liu D. , 2017). Item 4 is examined in chapter 4 "Ripple field AC losses in MgB_2 superconducting field windings" page A89 (Liu D. , 2017). Item 5 is examined in the deliverable report "Converter Designs tailored to SC and PDD concepts" of the task 3.31 (Chen, 2014).

The power consumption of the cryogenic cooling system is assumed to be maximum 1 % of the full rated power of the turbine in order to maintain an efficiency of the system higher than 90 %. In chapter 3 of (Liu D. , 2017) a constant cooling power of 50 kW is assumed and that is twice the loss specified in the work of GE global research in NbTi (Fair, 2012).

All the loss terms outlined above are determined as function of the wind speed and subtracted from the mechanical power curve of the turbine when the annual energy production is calculated for the evaluation of the Levelized Cost of Energy (LCoE).

5.5   Genetic algorithm for optimization

The method used to search for the most optimal generator design is called the genetic algorithm, since a number of initial generator designs are created and evaluated in terms of the lowest levelized cost of energy after which a new generation of designs are created from the ones with the lowest cost of energy (see page A73 of (Liu D. , 2017)) . This loop of selecting and generating new designs are repeated until the levelized cost of energy is converging towards a minimum as illustrated in Figure 5-18.

It is only the CAPEX part of the Levelized Cost of Energy given by (3-12) that is implement in the genetic algorithm for the optimization, because the OPEX contribution to the LCoE is assumed to be added as described in chapter 3.

A series of constraint ranges are imposed on the optimization parameters in order to limit the design space from approaching unrealistic dimensions as described in table A3.4 on page A74 of (Liu D. , 2017).

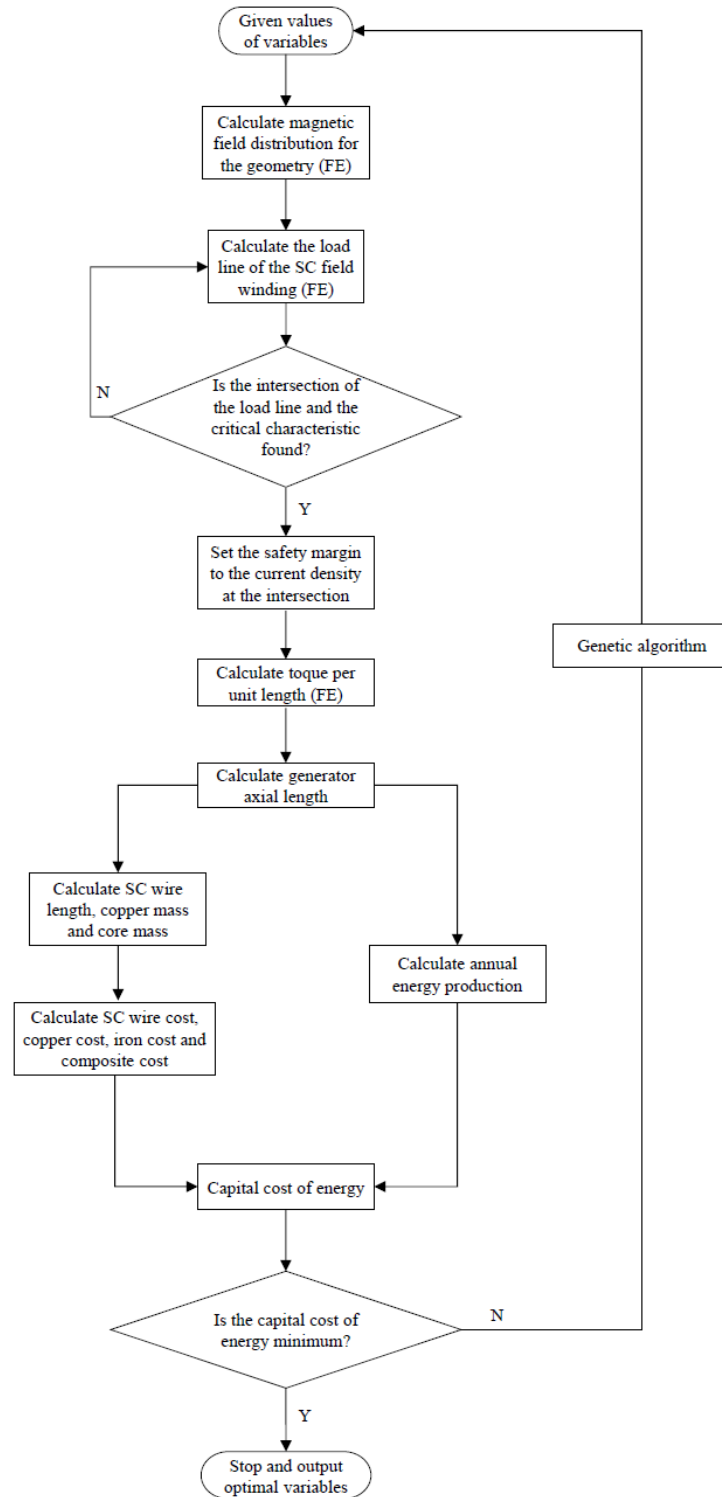*(INNWIND.EU, Deliverable 3.11, Superconducting generators)*

Figure 5-18 Illustration of the flow diagram of the generator design optimization method based on the genetic algorithm. Reproduced from Figure A3.5 of (Liu D. , 2017).

(INNWIND.EU, Deliverable 3.11, Superconducting generators)

5.6   Results for 10 MW MgB₂ generators

The 12 topologies T1 to T12 outlined in Figure 5-1 have been optimized for the lowest CAPEX contribution to the Levelized Cost of Energy (LCoE) as given by equation (3-12) for the 10 MW INNWIND.EU turbine with the 4 scenarios of the MgB₂ wire development as outlines in 5.3.1.

Figure 5-19 shows the magnetic flux density of the topologies for the original scenario of the present current density J_E of MgB₂ wire and a cost of 4 €/m. The number of pole pair range between 12 and 22 (see table A3.5) and it can be seen that qualitatively very different generators are obtained with very different magnetic flux densities at the superconducting windings.

(a) T1   (b) T2   (c) T3   (d) T4

(e) T5   (f) T6   (g) T7   (h) T8
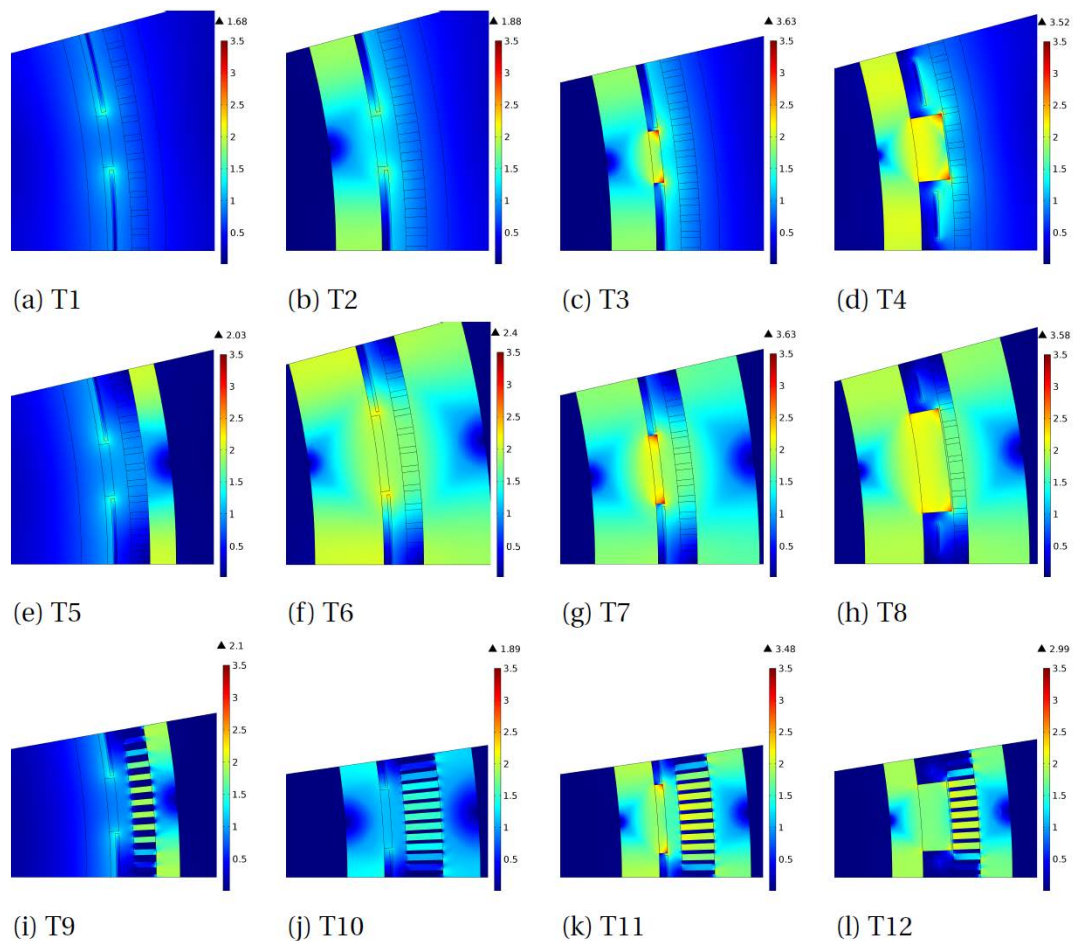
(i) T9   (j) T10   (k) T11   (l) T12

Figure 5-19 Magnetic flux density distribution in the unit of [T] of 10 MW generator topologies T1 to T12 after optimization for the lowest CAPAX contribution to the Levelized Cost of Energy (LCoE) and operated at T = 20 K. T1 contains no magnetic steel laminates and constitute a "light weight, but expensive" generator. T12 includes magnetic steel in field back iron, field pole, armature teeth and armature back iron, and thereby constitute a "cheap, but heavy" design. The diameter of the air gap is fixed to D_{gen} = 6 m for all the topologies. Reproduced from A79 of (Liu D. , 2017).

Figure 5-20 shows the active length of the generators as obtained from equation (5-3) for the optimized 10 MW topologies and Figure 5-21 is showing the resulting amount of MgB₂ superconductor needed. The masses of the active materials can then be determined as shown in Figure 5-22 as well as the cost of the active materials as shown in Figure 5-23. In order to calculate the CAPEX part of the LCoE as given by (3-12) then the annual energy production is

determined as in Figure 5-24 by subtracting the losses of the different topologies. Finally the CAPEX contribution to the LCoE is obtained as shown in Figure 5-25.
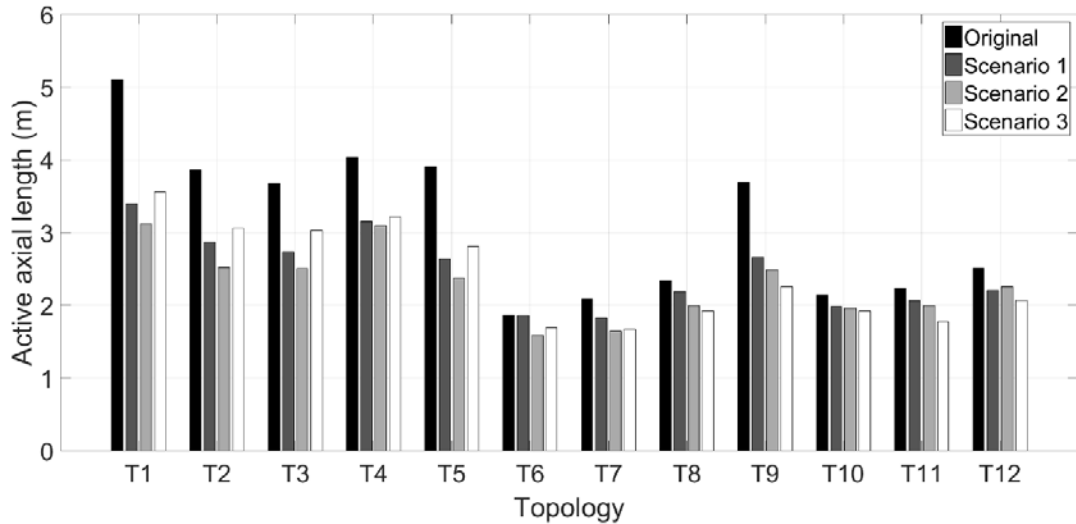

Figure 5-20 Active generator length L_{gen} of the optimized topologies T1 to T12 for the 10 MW MgB$_2$ wind turbine generators with a diameter of the air gap of D_{gen} = 6 m. The scenarios refer to: Original is present critical current density J_E and a cost of 4 €/m. Scenario 1: Cost reduced to 1 €/m. Scenario 2: Critical current density J_E increased by a factor of 4. Scenario 3: Both 1 and 2. Reproduced from Figure A3.21.

Figure 5-21 Length of MgB$_2$ superconductor wire needed for the optimized topologies T1 to T12 when operated at T = 20 K in a 10 MW generator with an air gap diameter of D_{gen} = 6 m. The scenarios refer to: Original is present critical current density J_E and a cost of 4 €/m. Scenario 1: Cost reduced to 1 €/m. Scenario 2: Critical current density J_E increased by a factor of 4. Scenario 3: Both 1 and 2. Reproduced from Figure A3.22
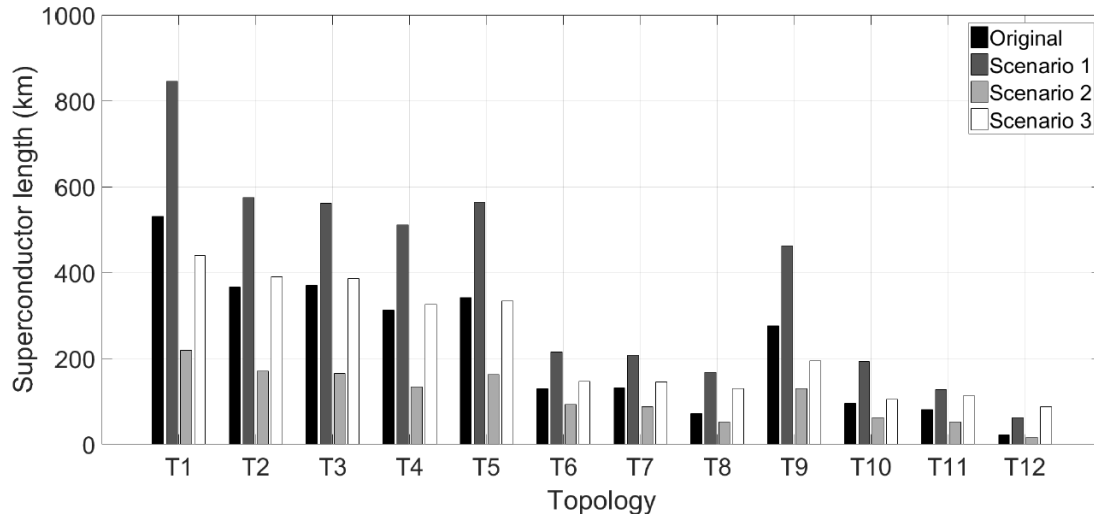
(INNWIND.EU, Deliverable 3.11, Superconducting generators)

Figure 5-22 Active material mass of optimized topologies T1 to T12 when operated at T = 20 K in a 10 MW generator with an air gap diameter of D_{gen} = 6 m. The scenarios refer to: Original is present critical current density J_E and a cost of 4 €/m. Scenario 1: Cost reduced to 1 €/m. Scenario 2: Critical current density J_E increased by a factor of 4. Scenario 3: Both 1 and 2. Horizontal lines indicate expected active mass of 10 MW Permanent Magnet Direct Drive (PMDD) generator. Reproduced from Figure A3.23.

Figure 5-23 Active materials cost of optimized topologies T1 to T12 when operated at T = 20 K in a 10 MW generator with an air gap diameter of D_{gen} = 6 m. The scenarios refer to: Original is present critical current density J_E and a cost of 4 €/m. Scenario 1: Cost reduced to 1 €/m. Scenario 2: Critical current density J_E increased by a factor of 4. Scenario 3: Both 1 and 2. Reproduced from Figure A3.20.
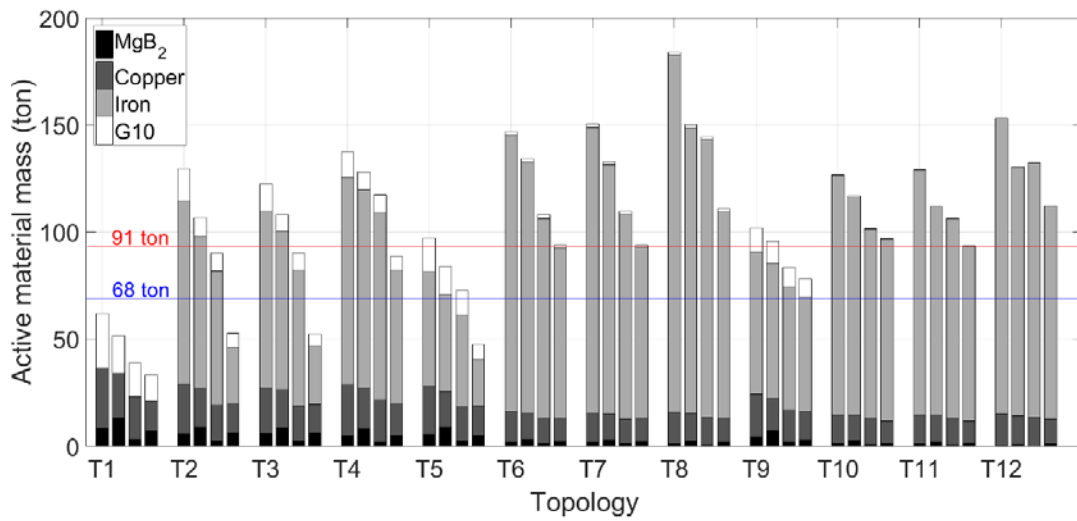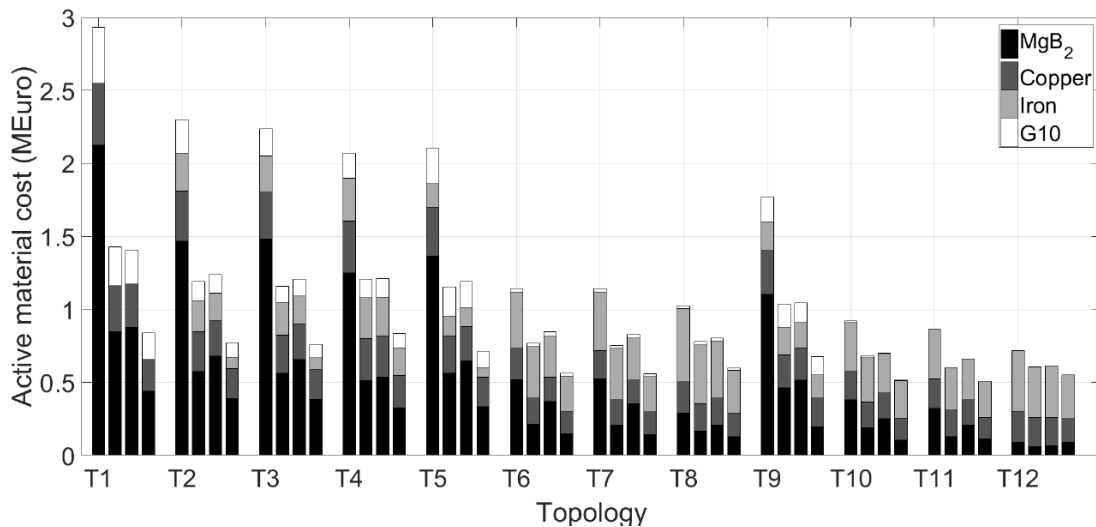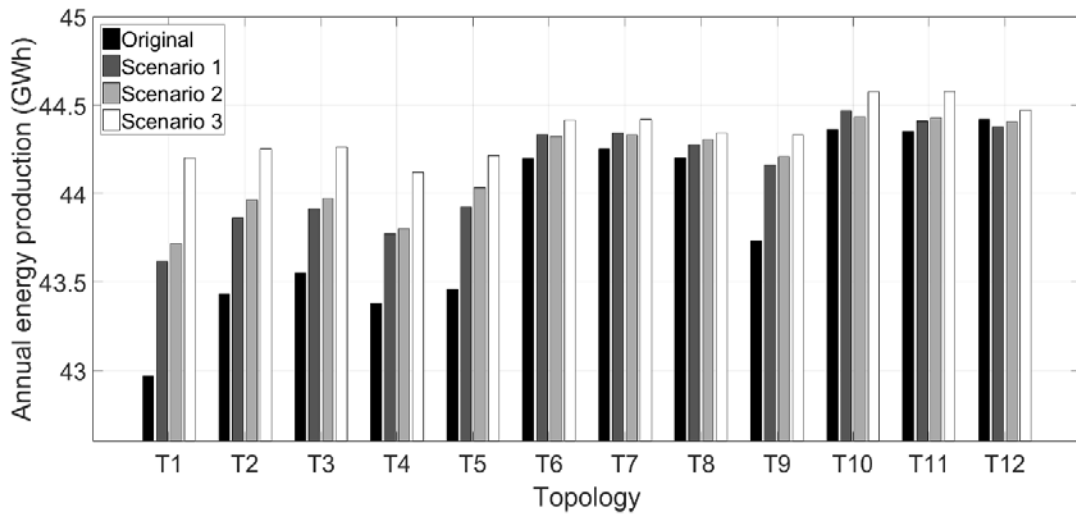
Figure 5-24 Annual energy production of optimized topologies T1 to T12 when operated at T = 20 K in a 10 MW generator with an air gap diameter of D_{gen} = 6 m. The scenarios refer to: Original is present critical current density J_E and a cost of 4 €/m. Scenario 1: Cost reduced to 1 €/m. Scenario 2: Critical current density J_E increased by a factor of 4. Scenario 3: Both 1 and 2. Reproduced from Figure A3.19.
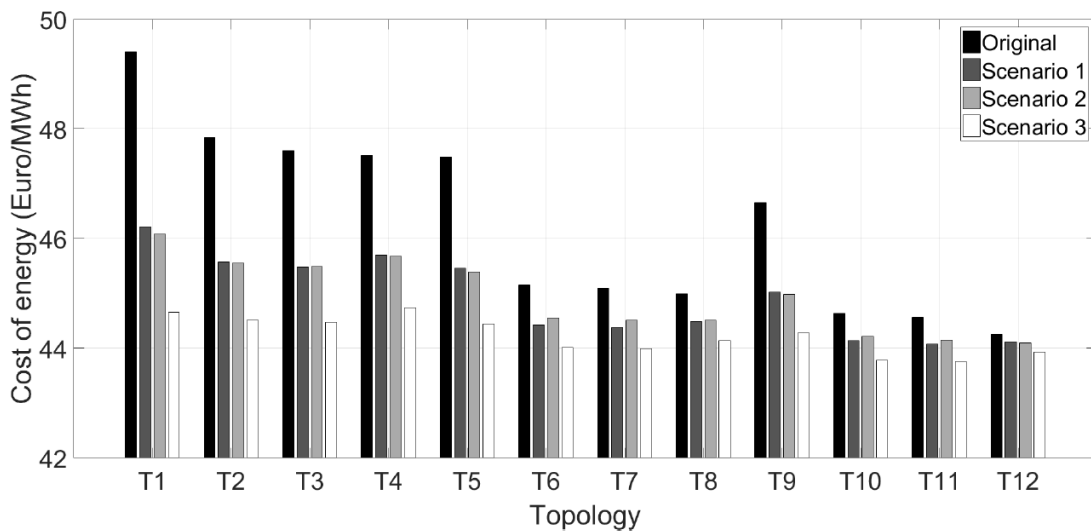

Figure 5-25 CAPEX contribution to Levelized Cost of Energy (LCoE) of the topologies T1 to T12 when operated at T = 20 K in a 10 MW generator with an air gap diameter of D_{gen} = 6 m. The scenarios refer to: Original is present critical current density J_E and a cost of 4 €/m. Scenario 1: Cost reduced to 1 €/m. Scenario 2: Critical current density J_E increased by a factor of 4. Scenario 3: Both 1 and 2. Reproduced from Figure A3.18.

5.6.1 Discussion of 10 MW MgB$_2$ optimization

From Figure 5-25 it is concluded that the light weight topology T1 is also the least economical feasible due to the high amount of MgB$_2$ superconductor needed to create the magnetic flux density in the generator when the present cost and properties of the MgB$_2$ is used for the optimization. The topology T12 based on steel laminates to close the magnetic circuit is the most economical feasible when using the present MgB$_2$ properties.

This result is not too surprising, since replacing expensive superconductor with cheap steel laminates is reducing the cost of the generator considerably. The question is however what is the weight of these topologies?

(INNWIND.EU, Deliverable 3.11, Superconducting generators)

By looking at Figure 5-22 it is seen that T1 holds the potential of providing an active mass of only 60 tons, which is lower than the active mass of 68 – 91 tons expected for a 10 MW Permanent Magnet Direct Drive (PMDD) generator as marked by the horizontal lines. Thus T1 has been identified as "light weight, but expensive". It is also seen that the cheap topology T12 will have an active mass of the order 155 tons, which is considerable higher than what is expected for the PMDD. Thus T12 is cheap, but probably also too heavy to be competitive to the PMDD.

Based in the current properties of the MgB_2 wire one will conclude that introducing magnetic steel laminates in the generator topology is the best way to improve the economic feasibility of superconducting direct drive generators based on MgB_2. It is however also shown that the weight of the active materials of such a generator will most likely not be competitive with the permanent magnets direct drive generators. This is showing that it is important to also analyze how the feasibility of the topologies T1 to T12 will develop in case the MgB_2 is improving in the future as specified by the scenarios: Original, scenario 1 with ¼ cost of the wire, scenario 2 with 4 times higher critical current density and scenario 3 being both 1 and 2.

The topology T1 will benefit a lot from better MgB_2 wires and the LCoE will approach the other topologies in the scenario 3 in Figure 5-25. Secondly the weight of the active materials could be reduced to about 30 tons in Figure 5-22. This is however not the case for topology T12 which is only expected to show a small reduction in the LCoE in Figure 5-25 and also a reduction of the active materials mass from 155 tons to about 115 tons. This is still higher than what is expected for the PMDD and is illustrating that T12 is limited for future development, since it resembles a conventional electrically excited generator, where the field windings are "just" replaced by a superconducting winding used to magnetize a magnetic steel structure.

In scenario 3 one can see that the LCoE of most of the topologies in Figure 5-25 are approaching the same level and one can therefore look for topologies with a better weight performance than T12 in Figure 5-22. It is seen that the topologies T1 to T5 and also T9 holds this potential, but it should be said that these topologies will need torque transferring elements connecting the superconducting coils mechanically to the room temperature part of the generator.

Following the INNWIND.EU design philosophies it is clear that the T1 with the current MgB_2 properties is indeed lightweight, but also too expensive. Especially with the INNWIND.EU conclusion on the 10 MW turbine and foundation that a more heavy nacelle would be beneficial in order to avoid the crossing of the fundamental resonance of the jacket foundation and the 3P excitation of the turbine rotor then the T12 was chosen as the preferred topology in order to comply with the design of "Cheap and not too heavy" In the following design of the INNWIND.EU nacelle and the integration of the superconducting generator then the T12 topology is used, because this will provide the highest generator weight and any future improvements by obtaining better superconductors or better design will only improve the feasibility and not compromise the turbine and foundation design by increasing the loads.

Finally it must be concluded that it has not been possible to identify a clear winner among the 12 topologies in terms of LCoE and also generator weight with the current properties of MgB_2. The future scenarios are indicating that the cheap T12 topology is too heavy to compete with the Permanent Magnet Direct Drive (PMDD) and other topologies like T1 to T5 and T9 should be considered. The topology choice has a large influence on the design of the cryostat holding the superconducting coils and since no clear winner could be identified the ambition of the INNWIND.EU cryostat design has been downscaled. It should however be said that the cryostat needed for the T12 topology is the same as has been developed by the SUPRAPOWER consortium (Suprapower, 2017). No further work on that cryostat concept will be done in INNWIND.EU in order not to duplicate the work of SUPRAPOWER. The INNWIND.EU MgB_2 coil demonstrator was however designed in accordance with the T5 topology and from the analysis above it is clear that an improved MgB_2 wire is needed before the T5 topology can compete with the permanent magnet direct drive technology.

(INNWIND.EU, Deliverable 3.11, Superconducting generators)

5.7   Results for 10 MW RBCO generators

The design optimization of generators based on the high temperature superconducting coated conductors have involved topologies with a reduced as well as a large quantity of magnetic steel laminates in the magnetic circuit. Figure 5-26 is showing 3 topologies changing from both air-cored rotor and stator to both iron-cored rotor and stator. In Figure 5-27 the torque per generator length is shown as function of the superconductor winding cross sectional area for the 3 topologies. It is clearly seen that the iron-cored topology will be economically most feasible, because the usage of the expensive RBCO coated conductor is reduced considerable. Thus only the iron-cored topology was investigated further in task 3.1.2.

A series of topology parameter studies were performed in order to determine the optimal combinations of generator properties such as pole number, superconductor cross sectional area, losses and pole width. Figure 5-28 shows the final design of the 10 MW generator based on the iron-cored topology and Table 5-1 contains the generator properties.

(a) Air-core stator, air-core rotor
(b) Iron-core stator, air-core rotor
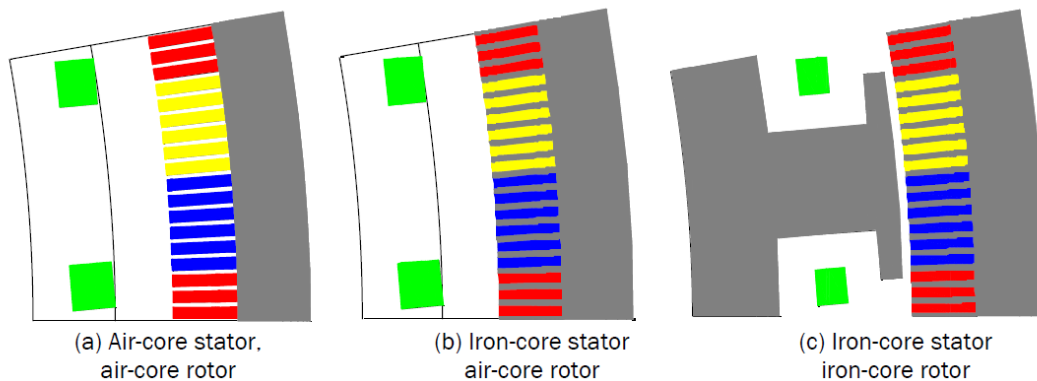(c) Iron-core stator, iron-core rotor

Figure 5-26 Topologies of generator pole suggested for the optimization of the high temperature coated conductor based generators. a) The rotor holding the superconducting winding (green) contains no magnetic steel laminates and is termed air cored. Similarly the stator is termed air-core, since the teeth are made of non-magnetic material. b) The teeth of the stator are made of magnetic steel laminated and the stator is termed iron-core. c) The rotor is equipped with a magnetic steel laminated core and the rotor is termed iron core. Reproduced from Figure 19 in (Azar & Thomas, 2016).
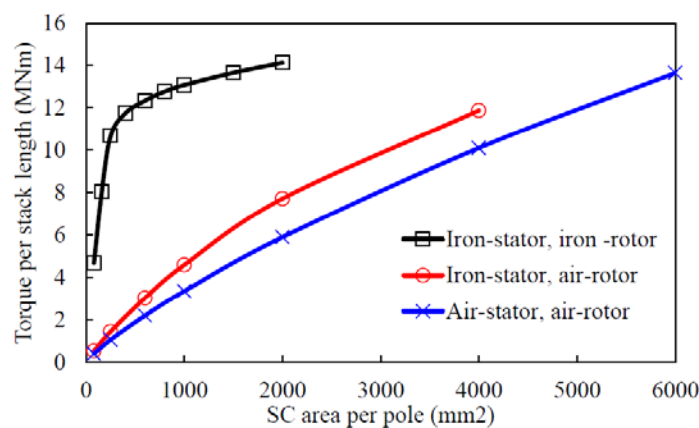
Figure 5-27 Generator torque per generator length plotted as function of the superconductor winding cross sectional area per pole for the topologies with iron-core stator and rotor, iron-core stator and air-core rotor and air-core rotor and stator. The air gap diameter of the generator is D_{gen} = 7 m, the length is L_{gen} = 1 m, the stator current density is J_a = 3.5 A/mm² and the copper loss is P_{cu}/L_{gen} = 274 kW. The iron-core rotor and stator topology result in a much lower usage of the expensive coated conductor and indicates a higher economic feasibility of this topology, which was chosen for the design of the RBCO based generators. Reproduced from Figure 20 in (Azar & Thomas, 2016).

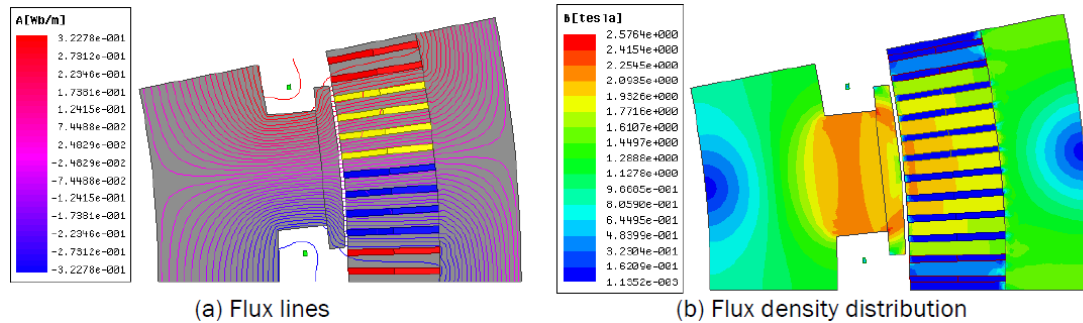|	
(a) Flux lines	(b) Flux density distribution

Figure 5-28 Final layout of iron cored high temperature superconducting coated conductor generator for 10 MW with D_{gen} = 7m and L_{gen} = 1.2 m. a) Flux lines under no-load and b) magnetic flux density distribution. Reproduced from Figure 45 in (Azar & Thomas, 2016).

Stator outer diameter D	7m
Stack length L	1.2m
Speed n	9.6rpm
Torque T_{em}	10.5MNm
Line voltage U_{ab} (no load)	3,130Vrms
Stator phase current I_a	2200Arms
Stator current density J_s	3.5A/mm²
Stator phase resistance R_s	0.0313Ω
Copper loss P_{Cu} (DC loss)	454Kw
Stator slot packing factor	0.6
Number of poles $2p$	32
Number of stator slots Q	384
Air gap length g	9mm
SC current density J_{SC}	340A/mm²
SC area per pole	200mm²
Length of SC wire	5.348km
Dimensions of cross section of SC coil	12.65mm×7.9mm
Stator yoke thickness h_{yi}	210mm
Stator slot dimension	16mm×238.7mm
Ampere turns of SC per pole	34,000AT
Max. $B\perp$ in SC	1.348T
Torque ripple (peak to peak)	2.8%
Type of stator core	Iron-core
Type of rotor core	Iron-core
Cost of SC (million €)	0.534
Cost of Cu (million €)	0.117
Cost of iron (million €)	0.112
Cost of total (million €)	0.764

Table 5-1 Properties of 10 MW coated conductor high temperature superconducting generator. Reproduced from Table 10 of (Azar & Thomas, 2016).

5.7.1 Discussion of 10 MW RBCO optimization

From Figure 5-27 it is seen that the iron-cored topology is found to be the most economical design when considering the current cost and properties of the coated conductors used in the RBCO coil demonstration. The generator obtained has an outer diameter of D_{gen} = 7 m and an active length of L_{gen} = 1.2 m. Thus the findings of the RBCO generators are very similar to the MgB₂ finding and the iron-cored topology for the RBCO generators is basically the same as the T12 for the MgB₂ study. The cost of the RBCO generator is shown in Table 5-1 to be around 0.8 M€, which is the same order of magnitude obtained in Figure 5-23 for the T12 of the MgB₂ generator, but using different unit cost of the copper and laminates. The weight of the iron in the RBCO generator is

estimated to be around 141 tons and the copper to about 15 tons, whereby a total mass around 160 tons is expected. Again this is quite similar to the weight of the active materials as found for the MgB$_2$ generator in Figure 5-22.

In conclusion then the 10 MW RBCO generator is found to be most economical by choosing an iron cored rotor and stator, but similarly as for the 10 MW MgB$_2$ generators it is found that the weight of the active materials are high and will not be competitive with the expected weight from the Permanent Magnet Direct Drive (PMDD) generators.

(INNWIND.EU, Deliverable 3.11, Superconducting generators)

6 ELECTRICAL SPECIFICATIONS OF SUPERCONDUCTING GENERATORS

In year 2 and 3 of the project (2014 & 2015), the power electronics designers from task 3.3 needed indicative values for the superconducting (SC) generator parameters. In that stage of the project, the SC generator design was far from finalised. Therefore, it was decided to calculate the SC generator parameters for a number of different possible SC generator designs to give the power electronics designers the possibility to proceed. These parameters are outline in this chapter in section 6.1.

The main question of the work were the following.

- Does the relatively low frequency of the SC generator (in the order of a few Hz) make it necessary to overrate the power electronics converter when compared to more common frequencies (in the order of 50 Hz)?

- Would it be possible to split the power electronics into four parallel converters to reduce short-circuit torques without significantly increasing the cost of the power electronics?

In deliverable 3.31 "Power electronics tailored for SC and PDD generators" (Chen, 2014) it was concluded that the superconducting generators would fit to conventional power converters without major concerns and that the cost of the converters are in the order of 80 k€/MW. Also the influence of segmenting the generator into 4 was investigated and it was concluded that no major effect on the power electronics would result.

Furthermore, the concern about the high short circuit torque of superconducting generators approaching 10 times the rated torque of the turbine is discussed in section 6.2.

It has been found that segmentation of the armature windings can solve this issue without a large increase of the cost of the power electronics.

The superconductor generator properties used in the work of deliverable D3.31 has not yet been reported as part of the INNNWIND.EU project and we have decided to include this information here in order to provide the complete information used for previous work. The main conclusions of the D3.31 on power electronics have been found as being representative also for the superconducting direct drive generators obtained in the optimization studies obtained later in the INNWIND.EU project and also for the designs presented in this report.

6.1 Superconductor generator properties for power electronics design

The following two sections hold a series of electrical specifications of the 10 MW and 20 MW superconducting MgB$_2$ generator that was provided to the design of power electronics tailored for the superconducting generators in task 3.3. The content was compiled quite early in the INNWIND.EU project and the generator topologies are therefore not directly connected the superconducting direct drive topologies presented in chapter 5. The generator topologies presented in the next chapters have been renamed into Generator G5-9 for the 10 MW generators and G10-G11 for the 20 MW generators. The relation to the topologies are explained in the text. Finally the G5-G11 topologies outlines in the following two sections provide the input for the power electronics evaluation as reported in deliverable D3.31 and which is described in chapter 6.1.3.

(INNWIND.EU, Deliverable 3.11, Superconducting generators)

6.1.1 Synchronous Inductances, Reactances and Phase Resistances of 10 MW Superconducting Generators (written by D. Liu in 2014 as internal working document of INNWIND.EU on defining the superconducting direct drive generators for designing power electronics in deliverable report D3.31)

I. INTRODUCTION

This report aims at providing the synchronous inductances, reactances and phase resistances of four 10 MW superconducting generator designs to the power electronic converter designers. Each generator design has two configurations. One is not segmented in the armature and the other has the armature divided into four identical segments. The synchronous inductances have two components. One is direct axis (d-axis) synchronous inductance and the other is quadrature axis (q-axis) synchronous inductance, corresponding to the d- and q- axis of a synchronous generator. Four sets of synchronous inductances, reactances and resistance are provided from the non-segmented generators and four sets are provided from the segmented generators, corresponding to the four different generator designs.

II. GENERATOR DESCRIPTION

Based on an optimization result, four superconducting generator designs have been selected as promising candidates, resulting in four different designs:

- G5: iron field yoke, iron armature yoke, non-magnetic field pole core and non-magnetic armature tooth (a non-optimised version of topology T6 from Figure 5-1).
- G6: iron field yoke, iron armature yoke, iron field pole core and non-magnetic armature tooth (a non-optimised version of topology T7 from Figure 5-1).
- G8: iron field yoke, iron armature yoke, non-magnetic field pole core and iron armature tooth (a non-optimised version of topology T10 from Figure 5-1).
- G9: iron field yoke, iron armature yoke, iron field pole core and iron armature tooth (a non-optimised version of topology T11 from Figure 5-1).

These designs have been selected because they are topologies with a significant amount of iron, resulting in a low LCoE.

Each generator design from G5 to G9 has two configurations:

- One is not segmented in the armature.
- The other has the armature divided into four identical segments.

Armature segmentation

The armature segmentation is realised by dividing the armature into four identical segments. Each segment has an integer multiple number of pole pairs. The three phase winding of each segment can be distributed in two ways according to how the phase terminals are connected with the power electronic converters (an example with 12 pole pairs is illustrated in Fig. 1):

- One power electronic converter is connected with one segment of the generator. Each segment is connected with only one converter. This way allows an individual converter to be connected to the armature segment prior to the assembly of the

whole armature. But during a short circuit of the terminal of one converter, the whole connected segment will be shorted and a severe asymmetry of the generator will occur.

- One power electronic converter is connected with multiple segments. Each segment is connected with multiple converters. This way needs the connection between the converters and the armature segments during assembly of the armature segments. However, during a short circuit of the terminal of one converter, none of the segments will completely be lost and symmetry of the generator remains.

Which way of segmentation is employed does not influence the inductances and the resistances at all. Therefore, the detailed design of segmentation will not be introduced in this report. In this report, however, the first way of segmentation will be used as the definition of segmentation, as shown in Fig. 1(a). This is to avoid misunderstandings and confusions for the use of the term "segment". One should thus keep in mind that this is not the only way of segmentation.
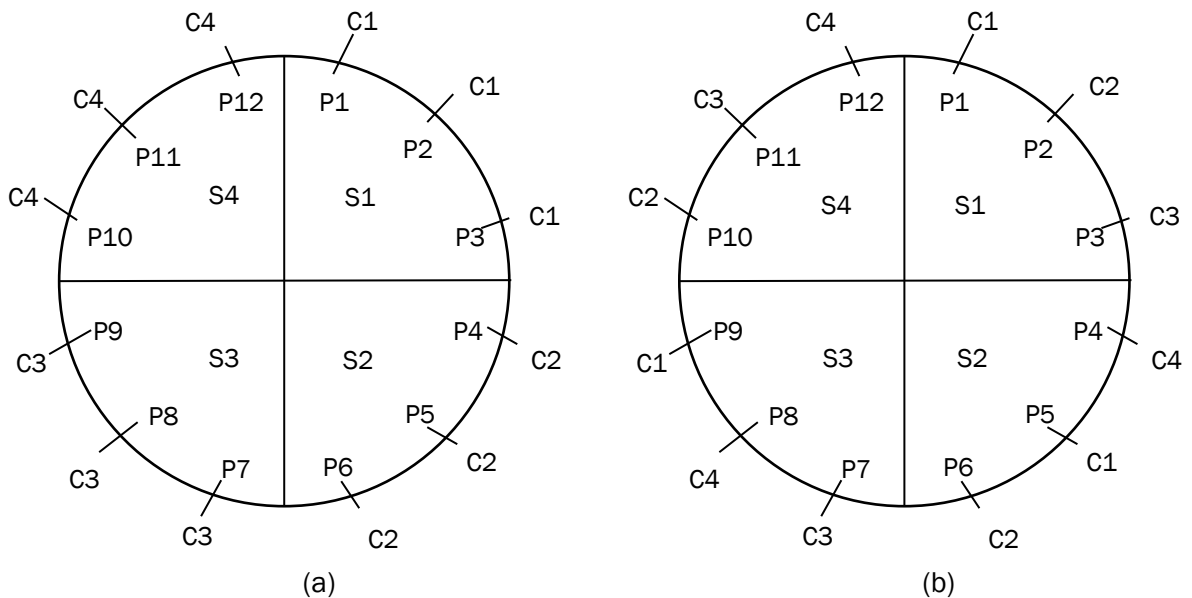

(a)　　　　　　　　　　　　　(b)

Fig. 1. Schematics of the connection between power electronic converters and armature segments with 12 pole pairs. (a) One power electronic converter is connected with one segment and each segment is connected with only one converter. (b) One power electronic converter is connected with all the four segments and each segment is connected with multiple converters. (Sx – segment numbering, Px – pole pair numbering, Cx – converter numbering)

Generator designs

The four generator designs with a whole piece of non-segmented armature are summarized in Table I. The four generator designs with the armature segmented into four identical parts are summarized in Table II. The generator designs are plotted in Fig. 2 with their magnetic flux density distributions. These plots are not changed by the way of armature segmentation.

(INNWIND.EU, Deliverable 3.11, Superconducting generators)

Table I: Parameters of the four generator designs (non-segmented)

	G5	G6	G8	G9
Number of pole pairs p	12	12	20	20
Electrical frequency f [Hz]	1.93	1.93	3.22	3.22
Generator axial length l_s [m]	3.05	2.66	2.98	2.85
Field current density J_f [A/mm²]	93.34	107.2	117.7	121.6
Number of conductors per slot n_s	2.71	2.82	1.71	1.70
Air gap radius r_s [m]				3
Armature current density $J_{s,rms}$ [A/mm²]				3
Rated generator power [MW]				10
Rated line-to-line generator voltage [V]				3300
Rated phase current if not segmented [A]				1750
Rated speed [rpm]				9.65

In this stage of conceptual design of the SC generator, the number of conductors per slot is not an integer. It is assumed that in a later stage, the number of conductors per slot can be made an integer by fine-tuning the design and by using higher numbers of conductors per slot and connecting coils in parallel.

The designs for the non-segmented generator will be used for the power electronic converter connected to the generator terminal, which has a power of 10 MW and a line-to-line voltage of 3300 V. The designs for the segmented generator will be used for the power electronic converter connected to one segment of the generator, which has a power of 2.5 MW and a line-to-line voltage of 3300 V.

Table II: Parameters of the four generator designs (with four segments)

	G5	G6	G8	G9
Number of pole pairs p	12	12	20	20
Number of segments		4		
Number of pole pairs per segment	3	3	5	5
Electrical frequency f [Hz]	1.93	1.93	3.22	3.22
Generator axial length l_s [m]	3.05	2.66	2.98	2.85
Field current density J_f [A/mm²]	93.34	107.2	117.7	121.6
Number of conductors per slot n_s if segmented	10.83	11.28	6.84	6.79
Air gap radius r_s [m]				3
Armature current density $J_{s,rms}$ [A/mm²]				3
Rated power per segment[MW]				2.5
Rated line-to-line voltage per segment [V]				3300
Rated phase current if segmented [A]				437.4
Rated speed [rpm]				9.65

III. SYNCHRONOUS INDUCTANCE

The synchronous inductance must be separated into d-axis synchronous inductance L_d and q-axis inductance L_q, due to saliency originating from iron field pole cores and/or magnetic saturation. In the four generator designs, the relation $L_d = L_q$ is not true. In G5 and G8, even though the field pole is non-magnetic, the high saturation in the d-axis due to the superconducting field winding excitation will make the relative permeability not equal between d-axis and q-axis. In G6 and G9, besides the saturation effect, the iron salient poles will result in more inequality between d- and q-axis synchronous inductances.

(INNWIND.EU, Deliverable 3.11, Superconducting generators)

The calculation of synchronous inductances L_d and L_q follows:

$$\lambda_d = \frac{2}{3}\left[\lambda_a \cos\vartheta + \lambda_b \cos\left(\vartheta - \frac{2}{3}\pi\right) + \lambda_c \cos\left(\vartheta + \frac{2}{3}\pi\right)\right]$$

$$\lambda_q = -\frac{2}{3}\left[\lambda_a \sin\vartheta + \lambda_b \sin\left(\vartheta - \frac{2}{3}\pi\right) + \lambda_c \sin\left(\vartheta + \frac{2}{3}\pi\right)\right] \qquad (1)$$

$$I_d = \frac{2}{3}\left[I_a \cos\vartheta + I_b \cos\left(\vartheta - \frac{2}{3}\pi\right) + I_c \cos\left(\vartheta + \frac{2}{3}\pi\right)\right]$$

$$I_q = -\frac{2}{3}\left[I_a \sin\vartheta + I_b \sin\left(\vartheta - \frac{2}{3}\pi\right) + I_c \sin\left(\vartheta + \frac{2}{3}\pi\right)\right] \qquad (2)$$

$$L_d = \frac{\lambda_d}{I_d}$$

$$L_q = \frac{\lambda_q}{I_q} \qquad (3)$$

where λ is the flux linkage, I is the armature current, d/q represents the direct and quadrature axis, a/b/c represents the three phases, and ϑ is the electrical angle between the d-axis and the axis of phase a.
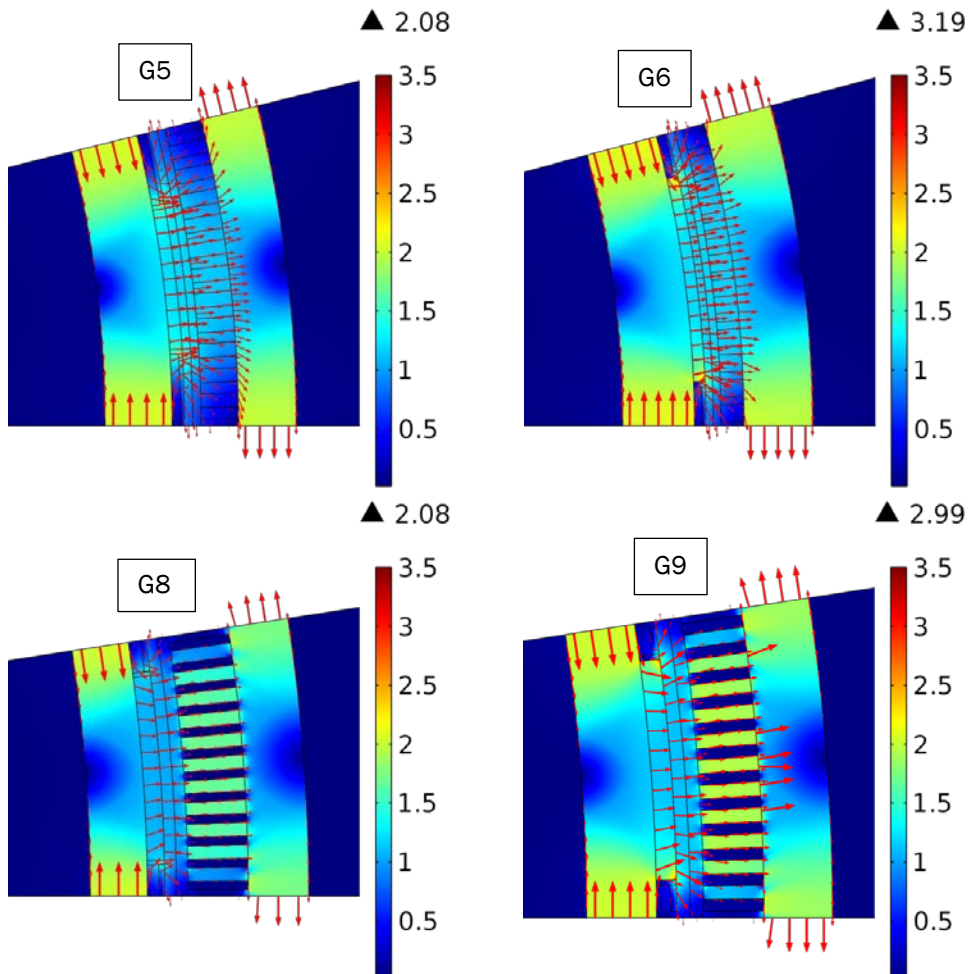

Fig. 2: Generator designs plotted with their magnetic flux density distribution in [T] (color)

(INNWIND.EU, Deliverable 3.11, Superconducting generators)

For the non-segmented generator, the base impedance Z_{B1} for calculating per unit values is defined as

$$Z_{B1} = \frac{U_{B1}^2}{P_{B1}} = \frac{U_{abN1}^2}{P_{N1}} = 1.089 \ \Omega \tag{4}$$

where $U_{abN\ 1}$ = 3300 V is the rated line-to-line voltage of the generator terminal and P_{N1} = 10 MW is the rated power of the generator.

For the segmented generator, the base impedance Z_{B4} for calculating per unit values is defined as

$$Z_{B4} = \frac{U_{B4}^2}{P_{B4}} = \frac{U_{abN4}^2}{P_{N4}} = 4.356 \ \Omega \tag{5}$$

where U_{abN4} = 3300 V is the rated line-to-line voltage of one segment of the generator, and P_{N4} = 2.5 MW is the rated power of one segment of the generator.

The synchronous inductances of the four designs with non-segmented armature are given in Table III. These parameters are used for the 10-MW-3300-V power electronic converter connected to the generator terminal. The synchronous inductances of the four designs with segmented armature are given in Table IV. These parameters are used for the 2.5-MW-3300-V power electronic converter connected to the terminal of one segment of the generator. All the inductance calculations are done in 2-D finite element programs. The saturated inductances are obtained when the field current density is set according to Table I and Table II. The saturated values will be used for evaluating the generator performance and for the design of the power electronic converter. Due to the fact that the armature reaction is weak in such superconducting generators, it is assumed that the saturated inductances remain the same at all rotational speeds (electrical frequencies) of the generator. Accordingly, the synchronous reactances are proportional to the rotational speeds (electrical frequencies). In Table III and Table IV, the values of synchronous reactance are obtained at the rated speed (rated electrical frequency).

Since these inductances are obtained in 2-D finite element simulations, it is needed to take the end winding inductance into account by appropriate means. Here Kalsi's model [1] is used as correction factors to estimate the effect of end winding dimensions on the total inductance. The correction factor AL_{CF} is defined by

$$AL_{CF} = 1 + \frac{L_{EndTurn}}{3 \cdot l_s} \tag{6}$$

where $L_{EndTurn}$ is the length of an end turn beyond the end of a stator slot and l_s is the active axial length of the machine. This correction factor is modelled for air-core machines, so it is an extreme case. For the four designs G5, G6, G8, and G9, the correction factors cannot be so large due to the presence of iron cores. In order to estimate the inductance with the end winding but not to overestimate the inductance values, the end winding inductance correction factor is averaged between 1 and AL_{CF} calculated by (6) for the four designs here by

$$AL'_{CF} = \frac{1 + AL_{CF}}{2} \tag{7}$$

(INNWIND.EU, Deliverable 3.11, Superconducting generators)

Table III and Table IV also give the correction factors AL_{CF} calculated by (6) and the resulting synchronous inductances and reactances with the correction factors AL'_{CF}. The power electronic converter should use the corrected synchronous inductances and reactances.

<div align="center">IV. PHASE RESISTANCE</div>

The resistance per phase of the armature winding is calculated for 100 °C, at which the resistivity of copper is $\rho_{Cu} = 2.2 \times 10^{-8}\,\Omega m$. The resistance is calculated simply by

$$R_s = \rho_{Cu} \frac{l_{Cu}}{A_{Cu}} \tag{5}$$

l_{Cu} is the total length of copper conductors per phase, including the end winding length, and A_{Cu} is the cross-sectional area per copper conductor. It is noted that for the segmented generator, the resistance is the phase resistance of a single segment and used for a single converter connected to this segment.

The resistances and the inductances of the segmented machines expressed in Ω and H are 4 times as high as the resistances and the inductances of the non-segmented machines. Expressed in per unit values, they are equal.

Table III: Synchronous inductance, synchronous reactance and phase resistance (non-segmented)

		G5	G6	G8	G9
Saturated (with field winding excitation)	L_{d2D} [mH]	7.49	11.84	11.85	9.44
	L_{q2D} [mH]	13.53	18.56	15.31	14.64
	X_{d2D} [p.u.]	0.083	0.132	0.220	0.175
	X_{q2D} [p.u.]	0.151	0.207	0.284	0.272
End winding inductance correction factor	AL'_{CF}	1.174	1.199	1.107	1.112
Saturated (**used for converter**, with field winding excitation and end winding inductance)	L_d [mH]	8.79	14.20	13.12	10.50
	L_q [mH]	15.88	22.25	16.95	16.28
	X_d [p.u.]	0.097	0.158	0.244	0.195
	X_q [p.u.]	0.177	0.248	0.314	0.302
Resistance per phase R_s (mΩ)		45.52	43.34	40.73	38.99
Resistance per phase R_s (p.u.)		0.0418	0.0398	0.0374	0.0358

Table IV: Synchronous inductance, synchronous reactance and phase resistance (with four segments)

		G5	G6	G8	G9
Saturated (with field winding excitation)	L_{d2D} [mH]	29.89	47.34	47.39	37.67
	L_{q2D} [mH]	54.01	74.25	61.24	58.39
	X_{d2D} [p.u.]	0.083	0.132	0.220	0.175
	X_{q2D} [p.u.]	0.150	0.207	0.284	0.271
End winding inductance correction factor	AL'_{CF}	1.174	1.199	1.107	1.112
Saturated (**used for converter**, with field winding excitation and end winding inductance)	L_d [mH]	35.09	56.76	52.46	41.89
	L_q [mH]	63.41	89.03	67.79	64.93
	X_d [p.u.]	0.097	0.158	0.244	0.195
	X_q [p.u.]	0.176	0.248	0.314	0.301
Resistance per phase R_s (mΩ)		182.08	173.37	162.91	155.94
Resistance per phase R_s (p.u.)		0.0418	0.0398	0.0374	0.0358

(INNWIND.EU, Deliverable 3.11, Superconducting generators)

V. CONCLUSION

The synchronous inductance, the synchronous reactance and the resistance have been calculated and shown in Table III for an armature phase of the non-segmented generator designs and in Table IV for an armature phase of one segment of the segmented generator designs. The inductances were calculated with saturation due to field excitation. The saturated inductances and reactances with end winding correction factors are used for evaluating the generator performance and for the design of the power electronic converter. Both values and per-unit values of synchronous reactance are provided. The parameters in Table III will be used for calculation and simulation of currents with respect to time in the power electronic converter which is connected to the 10-MW-3300-V non-segmented superconducting generator terminal. The parameters in Table IV will be used for calculation and simulation of currents with respect to time in the power electronic converter which is connected to a 2.5-MW-3300-V segment of the generator.

REFERENCES

[1] S. S. Kalsi, Application of High Temperature Superconductors to Electric Power Equipment, John Wiley & Sons. New Jersey, 2011, pp. 100-101.

(INNWIND.EU, Deliverable 3.11, Superconducting generators)

6.1.2 Synchronous Inductances, Reactances and Phase Resistances of 20 MW Superconducting Generators (written by D. Liu in 2015 as internal working document of INNWIND.EU on defining the superconducting direct drive generators for designing power electronics in deliverable report D3.31)

I. INTRODUCTION

This report aims at providing the synchronous inductances, reactances and phase resistances of two 20 MW superconducting generator designs to the power electronic converter designers. Each generator design has two configurations. One is not segmented in the armature and the other has the armature divided into four identical segments. The synchronous inductances have two components. One is direct axis (d-axis) synchronous inductance and the other is quadrature axis (q-axis) synchronous inductance, corresponding to the d- and q- axis of a synchronous generator. Two sets of synchronous inductances, reactances and resistance are provided from the non-segmented generators and two sets are provided from the segmented generators, corresponding to the two different generator designs.

II. GENERATOR DESCRIPTION

Based on an optimization result, two superconducting generator designs have been selected as promising candidates, resulting in two different designs:

- G10: iron field yoke, iron armature yoke, iron field pole core and iron armature tooth (a non-optimised version of topology T12 from Figure 5-1).

- G11: iron field yoke, iron armature yoke, iron field pole core and non-magnetic armature tooth (a non-optimised version of topology T8 from Figure 5-1).

Because the generator diameter becomes large with 20 MW power, modular cryostats [1] are employed to avoid a thin-large tube-shape cryostat [2] which accommodates all the superconducting coils. Salient iron poles can then be used to shorten the distance between the rotor and the stator, significantly reducing the active material cost and the generator length [3]. The generator designs are plotted in Fig. 1 with their magnetic flux density distributions for G10 and G11. These plots are not changed by the way of armature segmentation.

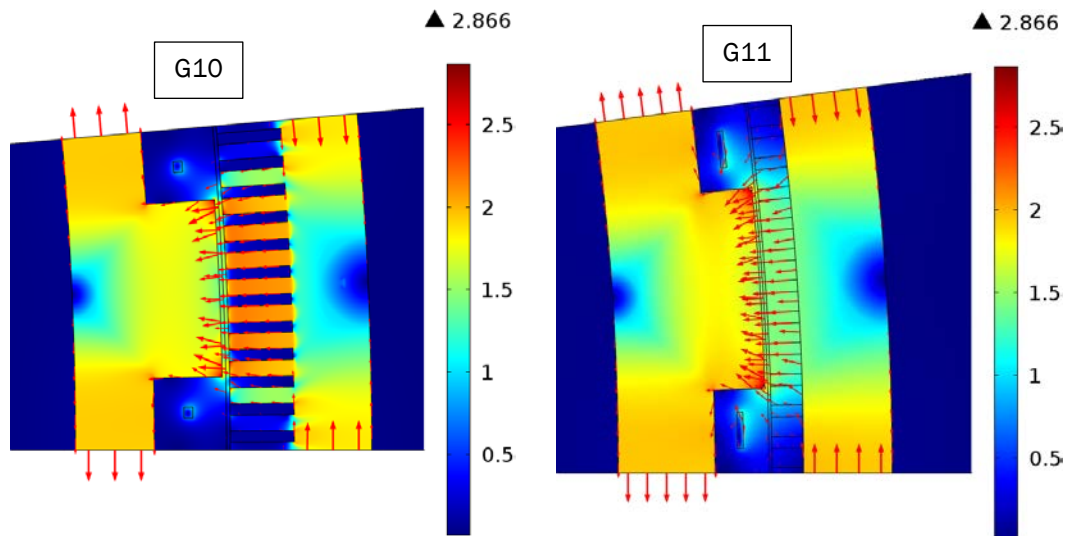*(INNWIND.EU, Deliverable 3.11, Superconducting generators)*

Fig. 1: Generator designs plotted with their magnetic flux density distribution in [T] (color)

G10 and G11 have two configurations respectively:

- One is not segmented in the armature.

- The other has the armature divided into four identical segments.

The way of how the armature is segmented does not influence the inductances and the resistances for the power electronic converter design.

Generator designs

The two generator designs with a whole piece of non-segmented armature are summarized in Table I. The two generator designs with the armature segmented into four identical parts are summarized in Table II. The generator designs are plotted in Fig. 2 with their magnetic flux density distributions. These plots are not changed by the way of armature segmentation.

In this stage of conceptual design of the SC generator, the number of conductors per slot is not an integer. It is assumed that in a later stage, the number of conductors per slot can be made an integer by fine-tuning the design and by using higher numbers of conductors per slot and connecting coils in parallel.

Table I: Parameters of the two generator designs (non-segmented)

	G10	G11
Number of pole pairs p	36	24
Electrical frequency f [H$_z$]	4.09	2.73
Generator axial length l_s [m]	2.61	2.49
Number of conductors per slot n_s	1.55	2.32
Air gap radius r_s [m]		5
Armature current density $J_{s,rms}$ [A/mm^2]		3
Rated generator power [MW]		20
Rated line-to-line generator voltage [V]		6600
Rated phase current if not segmented [A]		1750
Rated speed [rpm]		6.82

Table II: Parameters of the two generator designs (with four segments)

	G10	G11
Number of pole pairs p	36	24
Number of segments		4
Number of pole pairs per segment	9	6
Electrical frequency f [H$_z$]	4.09	2.73
Generator axial length l_s [m]	2.61	2.49
Number of conductors per slot n_s if segmented	3.10	4.64
Air gap radius r_s [m]		5
Armature current density $J_{s,rms}$ [A/mm^2]		3
Rated power per segment[MW]		5
Rated line-to-line voltage per segment [V]		3300
Rated phase current if segmented [A]		875
Rated speed [rpm]		6.82

The designs for the non-segmented segmented generator will be used for the power electronic converter connected to the generator terminal, which has a power of 20 MW and a line-to-line voltage of 6600 V. The designs for the segmented generator will be used for the power electronic converter connected to one segment of the generator, which has a power of 5 MW and a line-to-line voltage of 3300 V.

If only one design can be chosen for the power electronic converter design, generator design G10 will be recommended because generator design G10 (fully iron cored) results in the lowest LCoE.

III. SYNCHRONOUS INDUCTANCE

The synchronous inductance must be separated into d-axis synchronous inductance L_d and q-axis inductance L_q, due to saliency originating from iron field pole cores and/or magnetic saturation. In the two generator designs, the relation $L_d = L_q$ is not true. Without heavy saturation, L_d should be larger than L_q. With heavy saturation due to the superconducting field winding excitation, however, the d-axis becomes quite saturated in G10 and G11 and L_q becomes larger than L_d.

The calculation of synchronous inductances L_d and L_q follows:

$$\lambda_d = \frac{2}{3}\left[\lambda_a \cos\vartheta + \lambda_b \cos\left(\vartheta - \frac{2}{3}\pi\right) + \lambda_c \cos\left(\vartheta + \frac{2}{3}\pi\right)\right]$$

$$\lambda_q = -\frac{2}{3}\left[\lambda_a \sin\vartheta + \lambda_b \sin\left(\vartheta - \frac{2}{3}\pi\right) + \lambda_c \sin\left(\vartheta + \frac{2}{3}\pi\right)\right]$$

(1)

$$I_d = \frac{2}{3}\left[I_a \cos\vartheta + I_b \cos\left(\vartheta - \frac{2}{3}\pi\right) + I_c \cos\left(\vartheta + \frac{2}{3}\pi\right)\right]$$

$$I_q = -\frac{2}{3}\left[I_a \sin\vartheta + I_b \sin\left(\vartheta - \frac{2}{3}\pi\right) + I_c \sin\left(\vartheta + \frac{2}{3}\pi\right)\right]$$

(2)

$$L_d = \frac{\lambda_d}{I_d}$$

$$L_q = \frac{\lambda_q}{I_q}$$

(3)

(INNWIND.EU, Deliverable 3.11, Superconducting generators)

where λ is the flux linkage, I is the armature current, d/q represents the direct and quadrature axis, a/b/c represents the three phases, and ϑ is the electrical angle between the d-axis and the axis of phase a.

For the non-segmented generator, the base impedance Z_{B1} for calculating per unit values is defined as

$$Z_{B1} = \frac{U_{B1}^2}{P_{B1}} = \frac{U_{abN1}^2}{P_{N1}} = 2.178 \ \Omega \tag{4}$$

where $U_{abN\,1}$ = 6600 V is the rated line-to-line voltage of the generator terminal and P_{N1} = 20 MW is the rated power of the generator.

For the segmented generator, the base impedance Z_{B4} for calculating per unit values is defined as

$$Z_{B4} = \frac{U_{B4}^2}{P_{B4}} = \frac{U_{abN4}^2}{P_{N4}} = 2.178 \ \Omega \tag{5}$$

where U_{abN4} = 3300 V is the rated line-to-line voltage of one segment of the generator, and P_{N4} = 5 MW is the rated power of one segment of the generator.

The synchronous inductances of the two designs with non-segmented armature are given in Table III. These parameters are used for the 20-MW-6600-V power electronic converter connected to the generator terminal. The synchronous inductances of the two designs with segmented armature are given in Table IV. These parameters are used for the 5-MW-3300-V power electronic converter connected to the terminal of one segment of the generator. All the inductance calculations are done in 2-D finite element programs. The saturated inductances are obtained when the field current density is set according to Table I and Table II. The saturated values will be used for evaluating the generator performance and for the design of the power electronic converter. Due to the fact that the armature reaction is weak in such superconducting generators, it is assumed that the saturated inductances remain the same at all rotational speeds (electrical frequencies) of the generator. Accordingly, the synchronous reactances are proportional to the rotational speeds (electrical frequencies). In Table III and Table IV, the values of synchronous reactance are obtained at the rated speed (rated electrical frequency).

Since these inductances are obtained in 2-D finite element simulations, it is needed to take into the end winding inductance into account by appropriate means. Here Kalsi's model [4] is used as correction factors to estimate the effect of end winding dimensions on the total inductance. The correction factor AL_{CF} is defined by

$$AL_{CF} = 1 + \frac{L_{EndTurn}}{3 \cdot l_s} \tag{6}$$

where $L_{EndTurn}$ is the length of an end turn beyond the end of a stator slot and l_s is the active axial length of the machine. This correction factor is modelled for air-core machines, so it is an extreme case. For the two designs G10 and G11, the correction factors cannot be so large due to the presence of iron cores. In order to estimate the inductance with the end winding but not to overestimate the inductance values, the end winding inductance correction factor is averaged between 1 and AL_{CF} calculated by (6) for the two designs here by

(INNWIND.EU, Deliverable 3.11, Superconducting generators)

$$AL_{CF}^{'} = \frac{1 + AL_{CF}}{2} \tag{7}$$

Table III and Table IV also indicate the correction factors AL_{CF} calculated by (6) and the resulting synchronous inductances and reactances with the correction factors $AL_{CF}^{'}$. The power electronic converter should use the corrected synchronous inductances and reactances.

The resistances and the inductances of the segmented machines expressed in Ω and H are equal to the resistances and the inductances of the non-segmented machines because the voltage level of the non-segmented generator is double the voltage level of the segmented generator. Also expressed in per unit values, they are equal.

IV. PHASE RESISTANCE

The resistance per phase of the armature winding is calculated for 100 °C, at which the resistivity of copper is $\rho_{Cu} = 2.2 \times 10^{-8}$ Ωm. The resistance is calculated simply by

$$R_s = \rho_{Cu} \frac{l_{Cu}}{A_{Cu}} \tag{8}$$

l_{Cu} is the total length of copper conductors per phase, including the end winding length, and A_{Cu} is the cross-sectional area per copper conductor. It is noted that for the segmented generator, the resistance is the phase resistance a single segment and used for a single converter connected to this segment.

Table III: Synchronous inductance, synchronous reactance and phase resistance (non-segmented)

		G10	G11
Saturated (with field winding excitation)	L_{d2D} [mH]	14.600	16.616
	L_{q2D} [mH]	19.707	18.990
	X_{d2D} [p.u.]	0.172	0.131
	X_{q2D} [p.u.]	0.233	0.149
End winding inductance correction factor	AL'_{CF}	1.106	1.172
Saturated (**used for converter**, with field winding excitation and end winding inductance)	L_d [mH]	16.148	19.474
	L_q [mH]	21.796	22.256
	X_d [p.u.]	0.190	0.154
	X_q [p.u.]	0.258	0.175
Resistance per phase R_s (mΩ)		58.73	63.89
Resistance per phase R_s (p.u.)		0.0270	0.0293

Table IV: Synchronous inductance, synchronous reactance and phase resistance (with 4 segments)

		G10	G11
Saturated (with field winding excitation)	L_{d2D} [mH]	14.600	16.616
	L_{q2D} [mH]	19.707	18.990
	X_{d2D} [p.u.]	0.172	0.131
	X_{q2D} [p.u.]	0.233	0.149
End winding inductance correction factor	AL'_{CF}	1.106	1.172
Saturated (**used for converter**, with field winding excitation and end winding inductance)	L_d [mH]	16.148	19.474
	L_q [mH]	21.796	22.256
	X_d [p.u.]	0.190	0.154
	X_q [p.u.]	0.258	0.175
Resistance per phase R_s (mΩ)		58.73	63.89
Resistance per phase R_s (p.u.)		0.0270	0.0293

(INNWIND.EU, Deliverable 3.11, Superconducting generators)

V. CONCLUSION

The synchronous inductance, the synchronous reactance and the resistance have been calculated and shown in Table III for an armature phase of the non-segmented generator designs and in Table IV for an armature phase of one segment of the segmented generator designs. The inductances were calculated with saturation due to field excitation. The saturated inductances and reactances with end winding correction factors are used for evaluating the generator performance and for the design of the power electronic converter. Both values and per-unit values of synchronous reactance are provided. The parameters in Table III will be used for calculation and simulation of currents with respect to time in the power electronic converter which is connected to the 20-MW-6600-V non-segmented superconducting generator terminal. The parameters in Table IV will be used for calculation and simulation of currents with respect to time in the power electronic converter which is connected to a 5-MW-3300-V segment of the generator.

REFERENCES

[1] Ainhoa Pujana, "Design, optimization and integration of a direct drive, superconducting generator for large wind turbines", EWEA 2014, Barcelona, Spain.

[2] J. He, Y. Tang, J. Li, L. Ren, J. Shi, J. Wang, R. Qu, L. Su, X. Li, Y. Xu, and Z. Zhu, "Conceptual design of the cryogenic system for a 12 MW superconducting wind turbine generator," *IEEE Trans. Appl. Supercond.*, vol. 24, no. 3, pp. 1–5, 2014.

[3] H. Karmaker, M. Ho, and D. Kulkarni, "Comparison between different design topologies for multi-megawatt direct drive wind generators using improved second generation high temperature superconductors," *IEEE Trans. Appl. Supercond.*, vol. 25, no. 3, pp. 1–1, 2015.

[4] S. S. Kalsi, Application of High Temperature Superconductors to Electric Power Equipment, John Wiley & Sons. New Jersey, 2011, pp. 100-101.

(INNWIND.EU, Deliverable 3.11, Superconducting generators)

6.1.3   Power electronics tailored to Superconducting Generators

The two main types of power converters tailored to the MgB_2 superconducting generators are the current industrial standard back-to-back converter and a current source inverter with active filters as shown in Figure 6-1 and reported in task 3.3 (Chen, 2014).

The generator specification of initial superconducting direct drive generator designs as outlined in chapter 6.1.1 and chapter 6.1.2 were passed on to the power electronics development task 3.3. The generators termed G5-G9 (10 MW SC generators in 6.1.1) and G10-G11 (20 MW superconducting generators in 6.1.2) are handled in the deliverable report D3.31 of task 3.3 as generator type T5-T9 and T10-T11. The relation to the previous topology definition of chapter 5 is given in the introduction of chapter 6.1.1 and chapter 6.1.2.

The back-to-back converter is well established and the only challenge imposed by the superconducting generators is the possible low frequency down to only a few Hz. Such a low generator frequency could open up for different power converter and the Current Source Inverter with active filter is based on thyristors with a very low switching frequency and therefore much higher reliability than the IGBT semiconductors used in the standard back-to-back converter. It was found that the CSI might be cheaper than the back-to-back converter, but more work is needed to clarify if the low voltage ride through characteristics can comply with the grid code specification.

It was therefore concluded that the most suitable converter for the superconducting generators is the back-to-back converter and it was also found that the low frequency of a few Hz would not result in higher losses and thereby a more expensive converter. In order to investigate the possibility to segment the superconducting generator electrically then the cost of a 4 segmented power converter was also evaluated as illustrated in Figure 6-2. This means that instead of using one 20 MW power converter, the generator is wound into 4 machines on the same ring and then 4 x 5 MW power converters are used to operate the wind turbine. The conclusion in terms of the cost for the different power converted are listed in Table 6-1 and it is seen that the cost for the segmented and non-segmented are very similar around 0.8 M€/MW. It should be noted that the translation of generator G5-G11 into generator type T5 to T11 should be applied to the results of deliverable D3.31 as reported in Table 6-1.
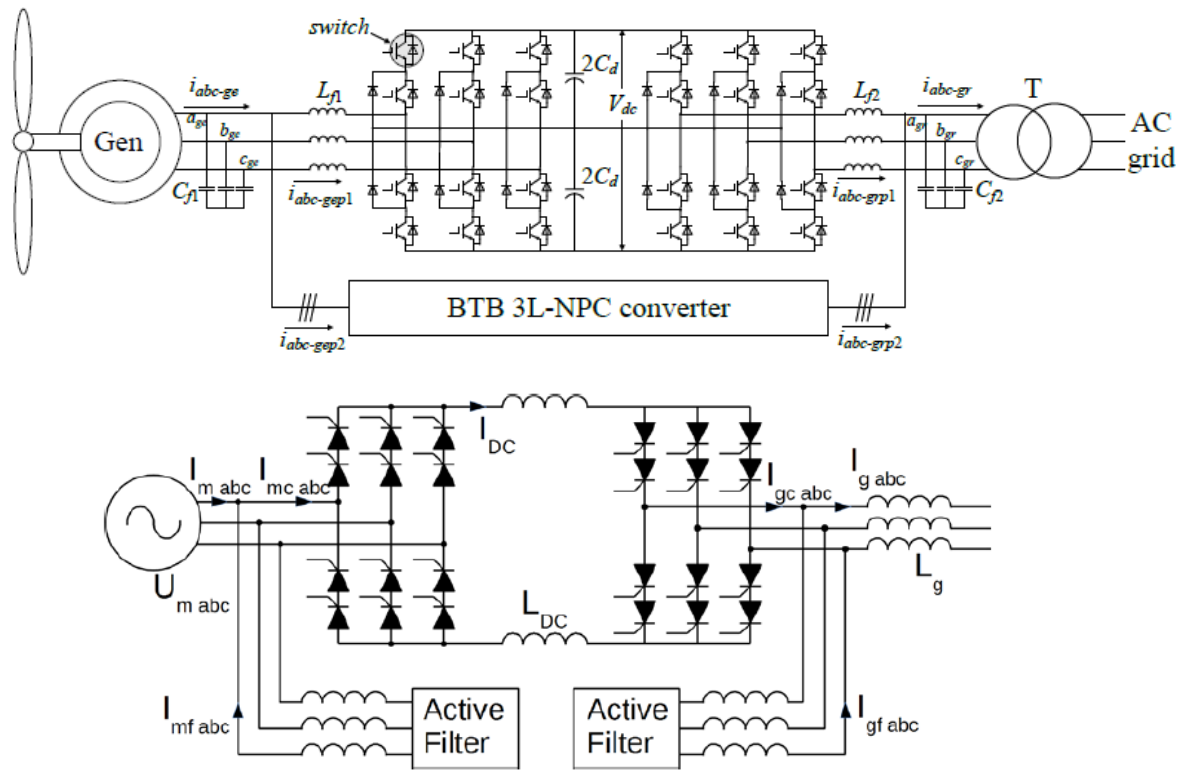
(INNWIND.EU, Deliverable 3.11, Superconducting generators)

Figure 6-1 Two main power converters tailored for the MgB$_2$ superconducting generators. Top: Back-to-Back converter based on IGBT semiconductors. Bottom: Current Source Inverter with active filters based on thyristors. Reproduced from Figure 1.2 in deliverable 3.31 (Chen, 2014).
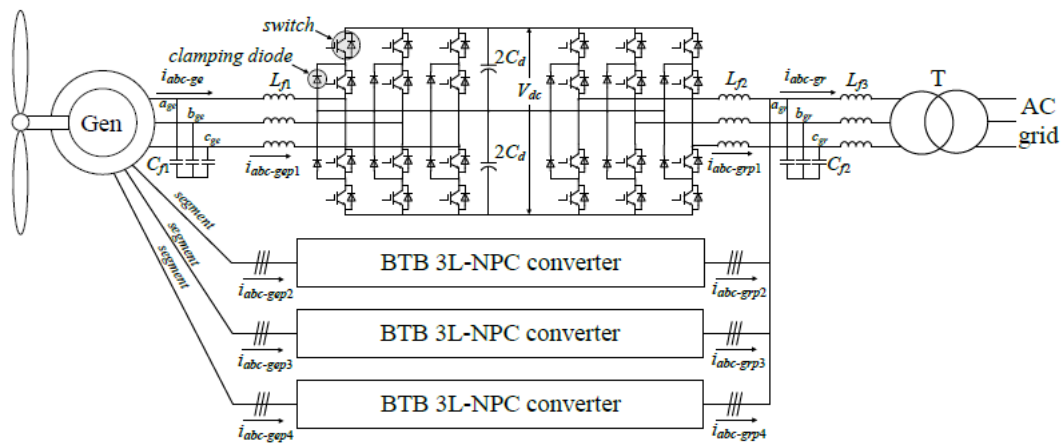

Figure 6-2 Back-to-back power converters connected to a generator wound into 4 segmented armature windings. This configuration is seen as a means to reduce the short circuit torque level of MgB$_2$ superconducting generators. Reproduced from Figure 2.2 in deliverable D3.31 (Chen, 2014).

Power Converter	Gen.	Power (MW)	Seg.	Gen. type	Total cost (k€)	Size (m³)	Weight (kg)	AEP (MWh)	CoE (€/MWh)
VSC	SCG	10	non-seg.	T8	841.9	30.4	10710	47588	0.71
			Seg.	T8	861.1	46.4	19308	47423	0.73
		20	non-seg.	T10	1508.7	34.3	12822	95171	0.63
			Seg.	T10	1595	60.8	21420	95018	0.67
	PDDG	10	non-seg.		859	26,69	8550	47020	0.731
		20	Seg.		1823	59.37	17100	93799	0.777
CSI	SCG	10	non-seg.	T5,6	499	23.8	7040	47,668	0.419
				T8,9	452	20.3	6040	47,635	0.380
			Seg.	T5,6	376	20.7	5820	47,611	0.316
				T8,9	384	20.7	5590	47,464	0.323
		20	non-seg.	T10	760	30.7	9880	95,580	0.318
				T11	824	34.7	11100	95,607	0.345
			Seg.	T10	711	30.0	9680	95,335	0.298
				T11	777	33.0	10800	95,370	0.326
	PDDG	10	non-seg.		402	17.8	7590	47,436	0.339
			Seg.		376	19.9	7780	47,524	0.317
		20	non-seg.		619	26.7	11100	95,388	0.259
			Seg.		601	26.7	11100	95,458	0.252

Table 6-1 Cost of power converters for the MgB$_2$ superconducting generators as well as the Magnetic Pseudo Direct Drive (PDD) for 10 MW and 20 MW wind turbine systems as reported in deliverable D3.31 (Chen, 2014). The generator type T5-T11 in the table are the generators G5-G9 specified in chapter 6.1.1 and the generators G10-G11 specified in chapter 6.1.2. The Voltage Source Converters (VSC) are the chosen technology for the superconducting generators, because some questions remain if the Current Source Inverters (CSI) can comply with the low voltage ride trough. It should however be noted that the CSI has the potential for a cost reduction. Reproduced from Table 5-1 in Deliverable report D3.31 (Chen, 2014).

(INNWIND.EU, Deliverable 3.11, Superconducting generators)

6.2 Short circuit torque considerations

Superconducting generators generally have small inductances compared to conventional synchronous generators due to the large air gap resulting from the space needed for the cryostat to provide thermal insulation to the superconducting field winding. A result of the low inductances is that a very high torque in the order of 10 times the rated torque of the generator will result if the generator terminals are shorted (see chapter 5 on page A101 in (Liu D. , 2017)).

The rated torques of the INNWIND.EU turbines T_R = 10 MNm and 30 MNm for the 10 MW and 20 MW respectively will therefore result in detrimental short circuit torques if a factor of 10 must be applied. Usual design procedures for wind turbine nacelles is to assume that the short circuit torque is limited to 3 times the rated torque and methods to reduce the short circuit torque of superconducting machines have therefore been investigated.

The two main ideas on reducing the short circuit tore are examined

1) Provide an electromagnetic shield between the field winding and armature winding

2) Segment the generator into several electrically independent machine connected to separate boxes of power electronics.

I has been found that option 1) is not solving the problem, but that option 2) holds the potential of a solution (chapter 5 on page A101 in (Liu D. , 2017)).

The short circuit peak torque can in a simple model be described as

$$T_{e,peak} = \frac{E_f^2}{X_l}$$
(6-1)

where E_f is the no load voltage of the generator and X_l is the leakage reactance. If however the generator is segmented into N_{seg} segments then both E_f and X_l is reduced by the number of segments whereby

$$T_{e,peak\ seg} = \frac{T_{e,peak}}{N_{seg}}$$
(6-2)

Thus the 10 times rated short circuit torque can be reduced to the design criteria of 3 times rated torque by introducing a segmentation into N_{seg} = 4 segments.

This hypotheses has been investigated for 4 of the topologies of the 10 MW MgB$_2$ generators, namely design A to D as shown in Figure 6-3. The designs were defined as follows

Design A:	Based on an air cored superconducting field pole and armature windings without magnetic teeth, but a magnetic back iron. This design is similar to the topology T5 as specified in section 5.1.
Design B:	Based on an air cored superconducting field pole and armature windings with magnetic teeth and a magnetic back iron. This design is similar to the topology T9 as specified in section 5.1.
Design C:	Based on a superconducting field winding supported by a magnetic pole and armature windings without magnetic teeth, but a magnetic back iron. This design is similar to the topology T8 as specified in section 5.1.
Design D:	Based on a superconducting field winding supported by a magnetic pole and armature windings with both magnetic teeth and a magnetic back iron. This design is similar to the topology T12 as specified in section 5.1.

(INNWIND.EU, Deliverable 3.11, Superconducting generators)

Figure 6-4 shown that the peak short circuit torque of all 4 designs can be reduced below 3 times rated torque by segmentation. No major increase of the cost of the power converter supporting such a configuration is expected, but future studies will have to determine if the torque reduction is weaker if the full details of the armature winding configuration is taken into account.

We did not separately study short circuits in the 20 MW generator because we are convinced that the problem and the solution at 20 MW is the same as at 10 MW.

(a) Design A (T5) (b) Design B (T9)

(c) Design C (T8) (d) Design D (T12)
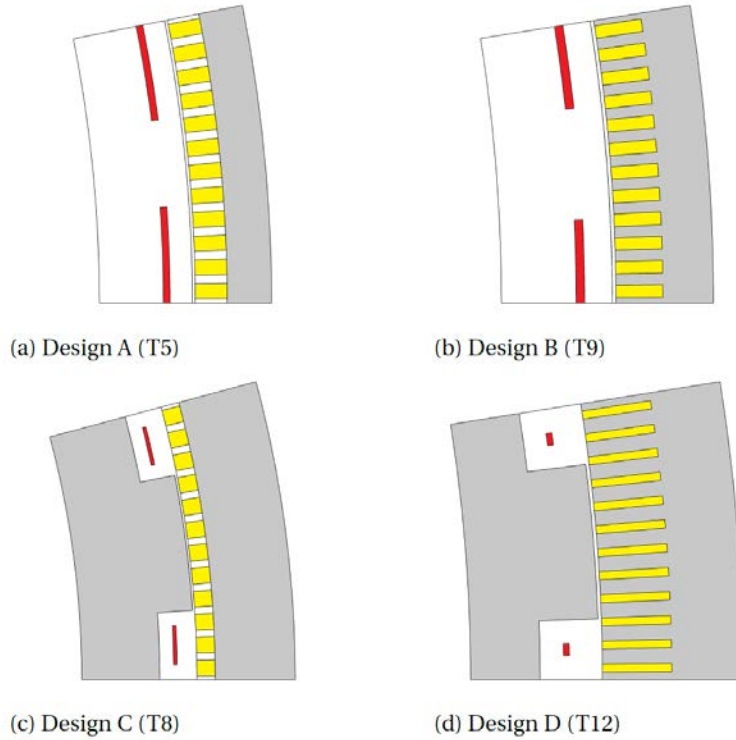
Figure 6-3. MgB$_2$ generator topologies used for examination of the short circuit torque and segmentation of the generators. Reproduced from Figure A5.2 (Liu D. , 2017).
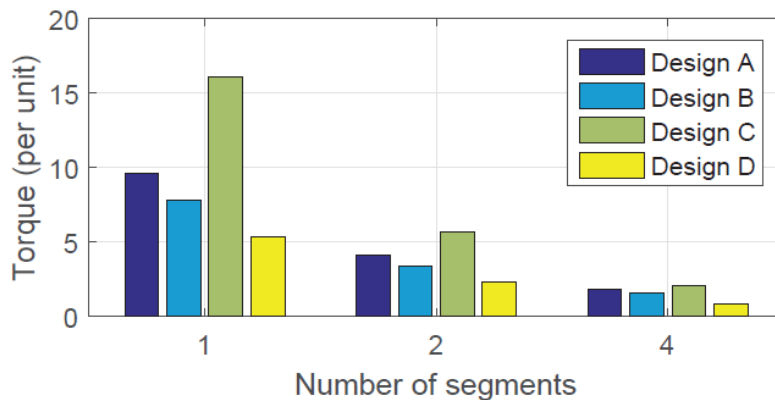
Figure 6-4 Short circuit peak torque of the MgB$_2$ generator topologies shown in Figure 6-3 as function of the number of segment by which the generators are split. Reproduced from Figure A5.4 (Liu D. , 2017).

(INNWIND.EU, Deliverable 3.11, Superconducting generators)

7 SIZE SPECIFICATIONS OF SUPERCONDUCTING GENERATORS

The optimization methods outlined for the MgB_2 and the RBCO generators have been used to specify the active materials and dimensions of the machines at 10 MW and 20 MW. The properties of the active materials of the MgB_2 generators have been used as input for the integration into the nacelle in of the INNWIND.EU turbines, whereas the results of the RBCO design was used to evaluate the feasibility of the coated conductor superconductor technology for direct drive wind turbine generators.

7.1 MgB_2 generators

The following section contain the generator designs obtained from the MgB_2 optimization and is reported in the original form as passed onto the task 3.4 Nacelle integration. The results of the nacelle integration has been reported in deliverable report D3.41 (Stehouwer, van Zinderen, & Hossain, 2017) and the main result will be summarized in the following chapter 8.

7.1.1 Electromagnetic Design of 10 and 20 MW Superconducting Generators (written by D. Liu 2016 as input for the Nacelle integration task as reported in deliverable D3.41).

I. INTRODUCTION

This report describes the electromagnetic design of the 10 MW and 20 MW superconducting generators for the stage of the mechanical construction design. The electromagnetic design is given with three diameters for the 10 MW generator and with one diameter for the 20 MW generator. This report provides the general parameters, the dimensioning parameters and the schematic of the individual pole of the generator. In addition, the physical and mechanical properties of the used electromagnetic materials are provided.

II. GENERAL PARAMETERS

This superconducting generator is designed for a 10 MW and a 20 MW direct drive wind turbines. The generator is a synchronous machine with a rated rotational speed of 9.60 rpm (10 MW) and 7.13 rpm (20 MW). The field winding is superconducting which is achieved by using superconducting MgB_2 wires to carry the DC excitation current in the rotor. The operating temperature for the superconducting field winding is T = 20 K. The 3-phase armature winding located in the stator is made from conventional copper conductors working with AC currents and AC fields. The rated line-to-line voltage from the stator winding is 3300 V (10 MW) and 6600 V (20 MW)

Table 1. General parameters of the electromagnetic design

Nominal power	10 MW	20 MW
Rated speed	9.60 rpm	7.13 rpm
Drive train type	Direct drive	
Generator type	Synchronous machine	
Field winding type	Superconducting DC (MgB_2)	
Cryogenic temperature	20 K	
Stator winding type	Copper AC	
Rated line-to-line voltage	3300 V	6600 V
Rotor core type	Salient iron poles with iron core back	
Stator core type	Iron teeth with iron yoke	
Cryostat type	Modular racetrack	
Stator winding cooling method	Forced-air cooling	
Specific electrical loading	A = 75 kA/m	
Field current density in coil	$J_{f,coil}$ = 111 A/mm^2	115 A/mm^2
Field current density in tape	$J_{f,wire}$ = 178 A/mm^2	184 A/mm^2

Both the stator yoke and the stator teeth are made from silicon steel laminates. In the rotor, silicon steel laminates are also used in the field pole shoe to reduce the eddy current losses caused by the stator teeth. The core back and the field pole core are made from cast iron. Generally speaking, the generator employs iron cores in the stator and the rotor.

(INNWIND.EU, Deliverable 3.11, Superconducting generators)

The cryostat is modular and in the shape of racetrack. The superconducting field coils are individually accommodated in the modular cryostats. The stator winding is cooled by forced air so that the electrical loading of the generator is limited at A = 75 kA/m (RMS value). The operating field current density in the superconducting field winding is limited around $J_{f,coil}$ = 113 A/mm² in the coil and $J_{f,wire}$ = 181 A/mm² in the wire, considering a filling factor of 62.5%. All the general parameters of the electromagnetic design are summarized in Table 1.

III. DIMENSIONING PARAMETERS

The generator has a structure with an inner stator and an outer rotor as sketched in Fig. 1. The inner stator is connected to the "kingpin" axle (the stationary supporting shaft). The outer rotor is connected to the rotating hub of the wind turbine and rotates via a bearing on the "kingpin" axle.
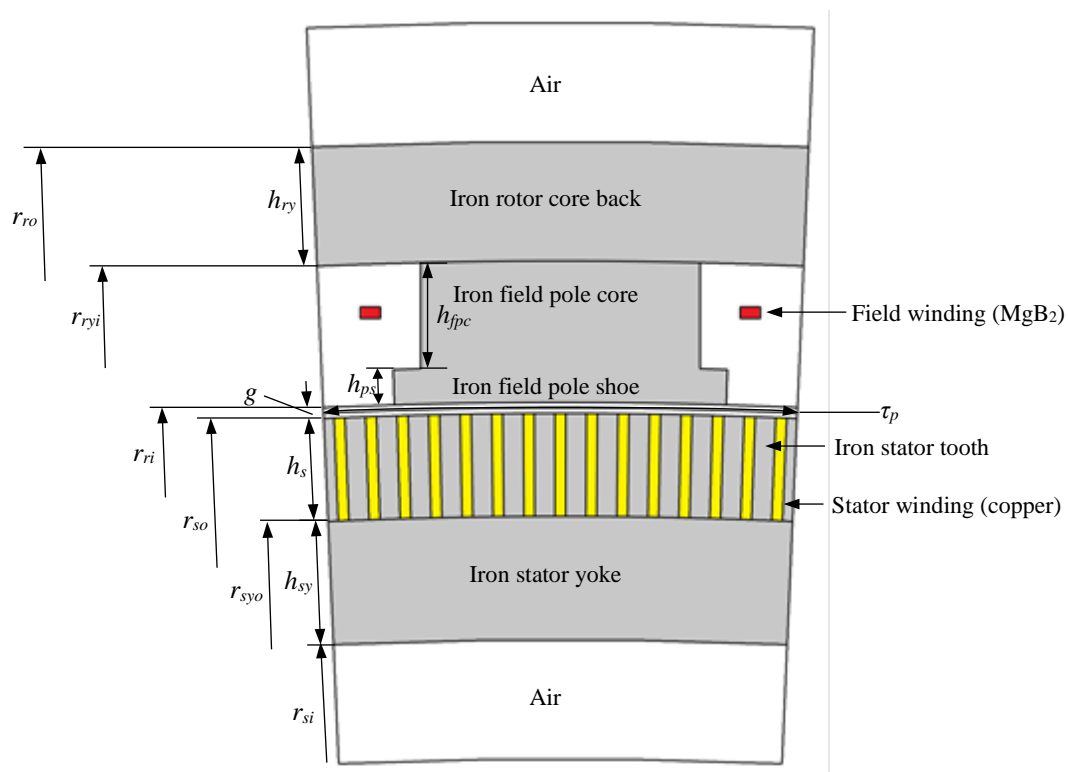
Fig. 1. Schematic of one pole of the superconducting generator design

Based on this structure, the dimensioning parameters of the generator are designed for three air gap diameters and summarized in Table 2. The air gap diameter D_s is defined as the diameter of the outer boundary of the stator (the air gap radius is r_s). The air gap length g is set to 0.1% of the air gap diameter D_s. The generator design with D_s = 6.0 m is obtained through an optimization, from which the generator designs with D_s = 8.4 m and D_s = 10.8 m are scaled up by keeping the same pole pitch τ_p = 471 mm. With the same pole pitch, the number of pole pairs for the three diameters can be obtained. Here one pole of the generator can be seen as a unit. The increase of the diameter is just to increase the number of the unit.

Table 2. Dimensioning parameters of the electromagnetic design

Power (MW)		10		20
Stator outer diameter D_s (m)	6.0	8.4	10.8	10.8
Number of phases m	3			
Number of slots per pole per phase q	5			
Pole pitch τ_p (mm)	471			
Stator slot height h_s (mm)	102			
Stator yoke height h_{sy} (mm)	122			
Stator tooth width b_t (mm)	20.2			
Stator slot width b_s (mm)	10.9			
Extension of stator end winding in axial length $L_{sw,ext}$ (mm)	408			
Rotor core back height h_{ry} (mm)	118			
Field pole core height h_{fpc} (mm)	105			
Field pole core width w_{fpc} (mm)	278			
Field pole shoe height h_{ps} (mm)	35			
Field pole shoe width w_{ps} (mm)	332			
Field coil height h_{coil} (mm)	11.4			
Field coil side width w_{coil} (mm)	20.2			
Extension of field end winding in axial length $L_{fw,ext}$ (mm)	200			
Distance between two field coil sides of one coil d_{coil} (mm)	358			
Cryostat height h_{cr} (mm)	91			
Cryostat side width w_{cr} (mm)	100			
Cryostat outer width $d_{cr,o}$ (mm)	478			
Cryostat inner width $d_{cr,i}$ (mm)	278			
Extension of cryostat in axial length $L_{cr,ext}$ (mm)	240			
Number of pole pairs p	20	28	36	36
Frequency f_e (Hz)	3.22	4.50	5.79	4.23
Axial stack length L_s (m)	2.44	1.31	0.80	2.25
Aspect ratio k_{asp}	0.41	0.16	0.07	0.21
Shear stress σ_t (kPa)	76.1	72.3	71.6	71.6
Normal stress σ_r (kPa)	513.8	486.0	459.9	459.9
$D_s^2 L_s$ (m³)	87.8	92.4	93.3	262.4
Air gap length g (mm)	6	8.4	10.8	10.8

The shear stress in the air gap is 71.6-76.1 kPa. The normal stress is 459.9-513.8 kPa. The slight decrease with the increased diameter is caused by the increase of the air gap length. The mass of each active material is indicated in Table 2 as an input to the mechanical construction design.

For mechanical construction design, the radius of each part of the generator is of importance. Table 4 summarizes the radii of the stator and the rotor in case of that the mechanical design needs to simplify the machine geometry to concentric rings. The generator size is illustrated in Fig. 2 for the three diameters.

One pole unit

Ds=6 m
Ls=2.44 m

Ds=8.4 m
Ls=1.31 m
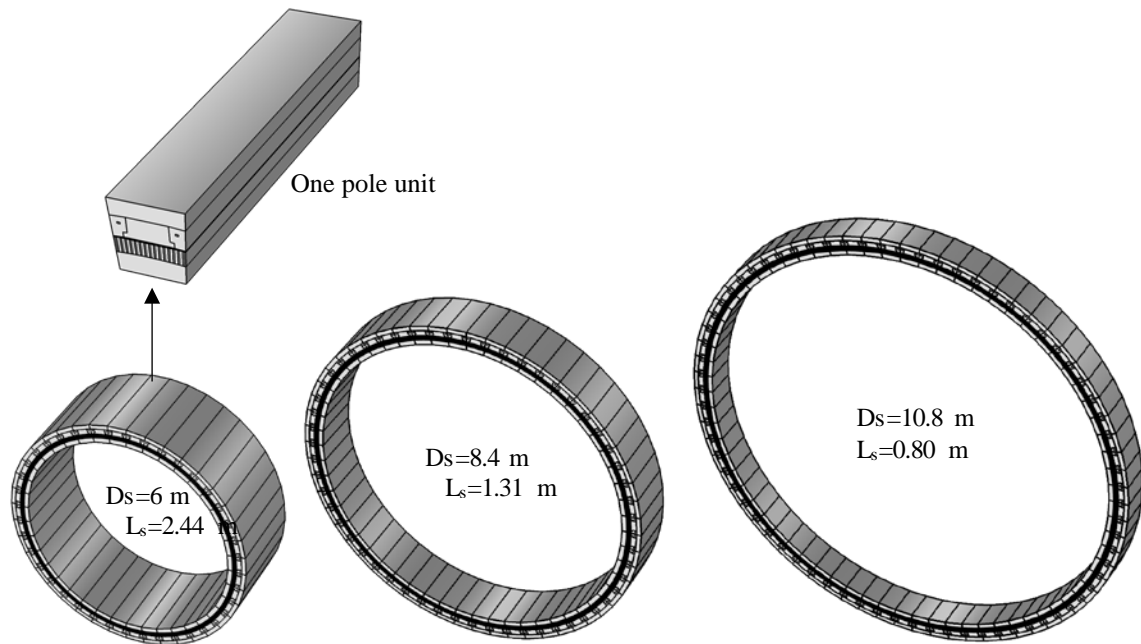
Ds=10.8 m
Ls=0.80 m

Fig. 2. Size comparison for the designed 10 MW superconducting generator with three different diameters D_s = 6.0 m, D_s = 8.4 m and D_s = 10.8 m. The 20 MW generator looks similar to the 10.8 m 10 MW generator but with a stack length of 2.25 m instead.

The cryostat follows the shape of field coils (racetrack) as sketched in Fig. 3. The dimensioning parameters are all indicated. The end winding extension length in the axial direction is also defined. The value of these parameters is listed in Table 2.

Table 3. Radii of the stator and the rotor

Power (MW)	10			20
Stator outer diameter D_s (m)	6.0	8.4	10.8	10.8
Outer diameter of the generator D_{so} (m)	6.528	8.933	11.338	11.338
Radius of the outer boundary of the rotor r_{ro} (m)	3.264	4.467	5.669	5.669
Radius of the inner boundary of the rotor yoke r_{ryi} (m)	3.146	4.348	5.551	5.551
Radius of the inner boundary of the rotor r_{ri} (m)	3.006	4.208	5.411	5.411
Radius of the outer boundary of the stator $r_{so}=0.5D_s$ (m)	3.000	4.200	5.400	5.400
Radius of the outer boundary of the stator yoke r_{syo} (m)	2.898	4.098	5.298	5.298
Radius of the inner boundary of the stator r_{si} (m)	2.776	3.976	5.176	5.176
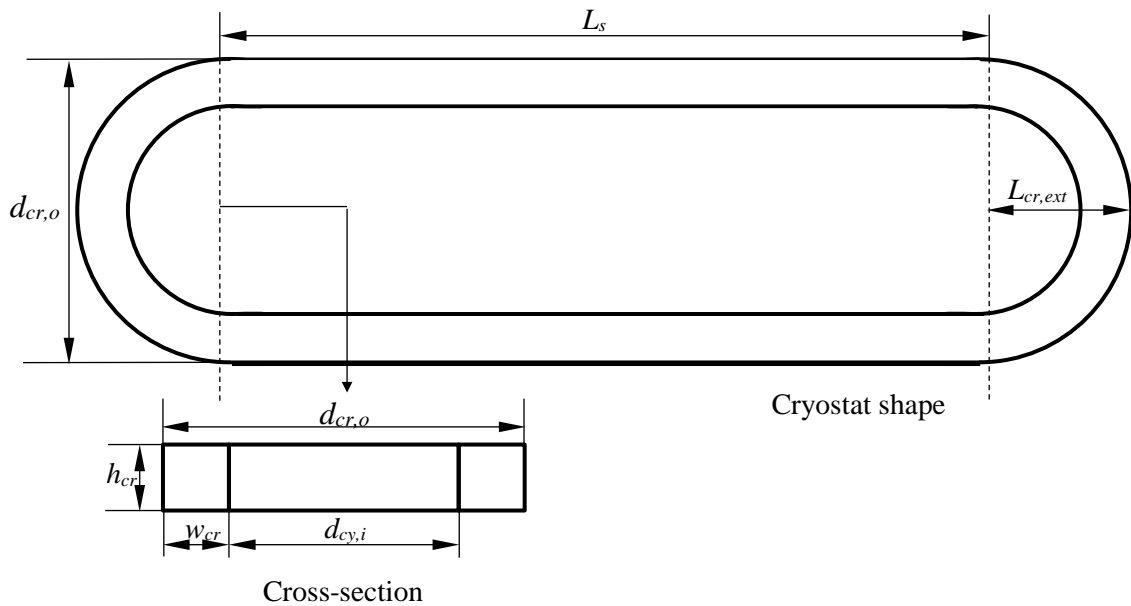
Fig. 3. Sketch of the cryostat shape and its dimensioning parameters
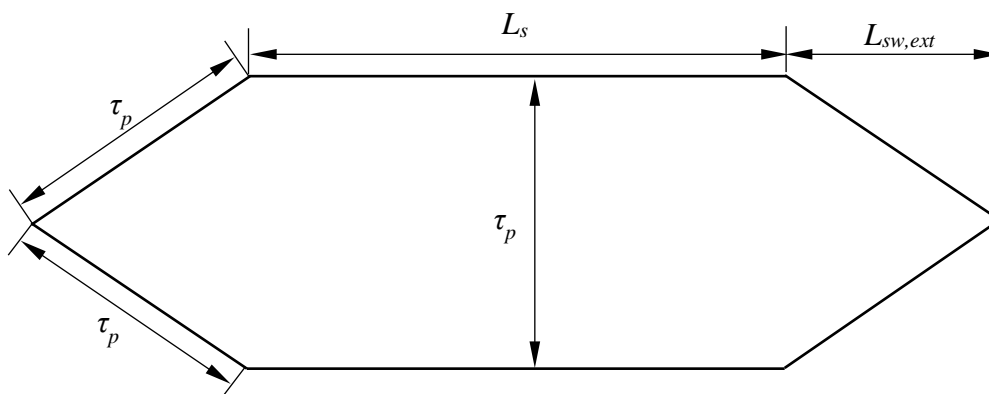
Fig. 4. Sketch of the shape of a stator winding turn and its dimensioning parameters

One turn of the stator winding follows the shape sketched in Fig. 4. The dimensioning parameters are all indicated. The end winding extension length in the axial direction is also defined. The value of these parameters is listed in Table 2. The end winding forms an equilateral triangle with each side of the length equal to a pole pitch τ_p.

IV. MATERIAL PROPERTIES

The properties of the materials used in the electromagnetic design are summarized in Table 4. The unit cost of these materials is also estimated and given in this table. The mechanical properties of the electrical steels for the core are indicated in Table 5. The grade of the silicon steel laminate is chosen for low iron losses. AISI M15 is a typical silicon steel for large electrical machines. In the rotor the steel laminates are used in the

(INNWIND.EU, Deliverable 3.11, Superconducting generators)

pole shoe to reduce the iron losses near the stator teeth. Solid cast iron EN-GJS-400-15 is used in the pole core and the rotor core back, where the iron losses are very small.

The mass and the cost of the active materials can be calculated based on the selected materials. Table 6 shows the masses and Table 7 shows the costs. The cryostat masses are also estimated for the diameters D_s = 6.0 m, D_s = 8.4 m and D_s = 10.8 m respectively. The cryostat cost has not been estimated yet.

Table 4. Choice of the electromagnetic materials

	Grade or type	Mass density [kg/m³]	Unit Cost* [€/kg]
Silicon steel laminate for the stator core	M15 (250-35-A5)	7650	3
Silicon steel laminate for the rotor pole shoes	M15 (250-35-A5)	7650	3
Solid cast iron for the rotor pole core and core back	EN-GJS-400-15	7200	3
Copper conductor for the stator winding	No standard	8900	15
Superconducting wire for the field winding (raw wires)	Columbus MgB2	0.015 kg/m	4 €/m
Superconducting field winding (racetrack coils)	Homemade	6500	NA

* These unit costs are only for the MgB2 generators of work package (WP3).

Table 5. Mechanical properties of the silicon steel for the stator and rotor cores

EU IEC grade	Yield strength (MPa)	Tensile strength (MPa)	Elongation (% in 50 mm)
250-35-A5 (AISI M15) [1]	358	490	23
EN-GJS-400-15 (ISO 1083 400-15) [2]	250	370-390	15

Table 6. Masses of the electromagnetic design

Power (MW)		10			20
	Stator outer diameter D_s (m)	6.0	8.4	10.8	10.8
Rotor	Field winding mass, including end winding (ton)	0.36	0.32	0.30	0.52
	Rotor iron mass (ton)	70.78	51.77	40.59	111.5
	Cryostat mass (ton)	3.87	3.38	3.16	8.89
Stator	Stator iron mass (ton)	63.99	49.37	38.86	106.7
	Copper mass, including end winding (ton)	13.93	13.06	13.02	24.27
Total rotor mass (ton)		75.00	55.46	44.04	120.39
Total stator mass (ton)		77.92	62.43	51.88	130.97
Total mass (ton)		153	118	96	251

(INNWIND.EU, Deliverable 3.11, Superconducting generators)

Table 7. Costs of the electromagnetic design

Power (MW)	10			20
Diameter (m)	6.0	8.4	10.8	10.8
Superconducting wires (k€)	93	80	75	140
Copper conductors (k€)	209	196	195	364
Rotor iron (k€)	212	155	122	334
Stator iron (k€)	192	148	117	321
Total cost (k€)	706	579	509	1159

V. SUMMARY

The electromagnetic design of the 10 and 20 MW superconducting generators has been described. Its diameters, lengths, shear stresses, dimensions and masses have been provided as input to the mechanical construction design. The type of each electromagnetic material has been indicated. The mechanical properties of the silicon steel and the cast iron have been provided so that they can be incorporated to the mechanical construction design.

REFERENCES

[1] AK Steel, Nonoriented Electrical Steels Product Data Bulletin, pp. 9. Online Available [2015]: http://www.aksteel.com/pdf/markets_products/electrical/non_oriented_bulletin.pdf

[2] Online Available [2015]: http://www.steelnumber.com/en/steel_composition_eu.php?name_id=1520

(INNWIND.EU, Deliverable 3.11, Superconducting generators)

7.2 High temperature superconducting generator design

The 10 MW high temperature superconducting Rare Earth-Barium-Copper-Oxide (RBCO) coated conductor based generator design was up-scaled in task 3.1.2 to 20 MW by following two methods

1) Keep the diameter of the 10 MW generator and optimize to obtain the rated torque of the 20 MW turbine

2) Optimize the 20 MW generator with the diameter as a free parameter

The parameters of the resulting generators are outlined below and have been reported in the deliverable report D3.12 (Azar & Thomas, 2016).

7.2.1 RBCO generators at 10 MW and 20 MW

The properties of the 10 MW and 20 MW RBCO coated conductor high temperature superconductor generators are shown in table Table 7-1. It is clearly seen that it is economical most feasible to increase the diameter of the 20 MW generator to D_{gen} = 11 m, whereby the cost of the generator is only increased by a factor of 2 when upscaling from 10 MW to 20 MW. Figure 7-1 shows the final designs of the RBCO coated conductor generators.

	10MW	20MW-I	20MW-II
Stator outer diameter D (m)	7	7	11
Stack length L (m)	1.2	1.95	1.16
Speed n (rpm)	9.6	6.8	6.8
Torque T_{em} (MNm)	10.5	30	30
Stator current density J_s(A/mm2)	3.5	3.5	3.5
Stator slot packing factor	0.6	0.6	0.6
Number of poles 2p	32	32	64
Number of stator slots Q	384	384	768
Air gap length g (mm)	9	9	13
SC current density J_{SC} (A/mm2)	340	273	340
SC area per pole (mm2)	200	1000	200
Length of SC wire (km)	5.35	39.2	10.54
Ampere turns of SC per pole (AT)	34,000	136,500	34,000
Type of stator core	Iron-core	Iron-core	Iron-core
Type of rotor core	Iron-core	Iron-core	Iron-core
Volume of generator (m³)	42.3	68.7	100.5
Mass of Iron (t)	141	271.9	208
Cost of SC (million €)	0.543	3.92	1.054
Cost of Cu (million €)	0.117	0.215	0.192
Cost of iron (million €)	0.112	0.217	0.166
Cost of total (million €)	0.764	4.35	1.412

Table 7-1 Properties of RBCO coated conductor high temperature superconducting generators for 10 MW and 20 MW. Reproduced from Table 14 of (Azar & Thomas, 2016).

(INNWIND.EU, Deliverable 3.11, Superconducting generators)

(a) 10MW, D=7m, 2p=32.   (b) 20MW, D=7m, 2p=32.   (c) 20MW, D=11m, 2p=64.
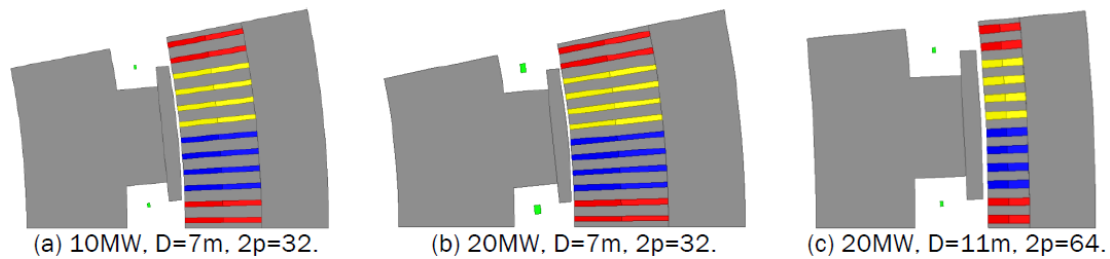
Figure 7-1 Final design of RBCO high temperature superconducting pole for 10 MW and 20 MW turbines. Reproduced from Figure 80 of (Azar & Thomas, 2016).

7.2.2 Topology and price sensitivity of high temperature superconducting generators

The impact of different generator topologies termed Iron-cored stator & iron cored rotor topology (ISIRT), Iron-cored stator & air-cored rotor topology (ISART) and Air-cored stator & air cored rotor topology (ASART) have recently been investigated for a 10 MW coated conductor based direct drive generator (Guan, et al., 2017). It was found that the amount of coated conductor was increased from 5.3 km to 81.7 km and finally 156.4 km for the iron cored going towards the air cored topologies as shown in Table 7-2. Thus the iron-cored topology was clearly preferred with the current cost of the coated conductor quoted to be 100 €/m. It was however also examined what the impact of a cost reduction of the coated conductor to 20 €/m would have on the topologies and this is also shown in Table 7-2. The total active materials cost is found to be about 0.8 M€ for 100 €/m and this could be reduced to 0.33 M€ if the cost of the coated conductor is reduced to 20 €/m. It should be noted that the cryogenic cooling system cost is not included.

(INNWIND.EU, Deliverable 3.11, Superconducting generators)

TABLE I
SPECIFICATIONS OF SC GENERATORS

	Iron-stator Iron-rotor	Iron-stator Air-rotor	Air-stator Air-rotor
Power (MW)	10		
Speed (rpm)	9.6		
Line voltage (Vrms)	3300		
Torque, based on efficiency=95% (MNm)	10.5		
Stator outer diameter D (m)	7		
Stack length L (m)	1.16	1.06	0.95
Number of poles	32		
Number of slots	384		
h_y (mm)	210	210	175
h_s (mm)	238	231	92.5
b_s (mm)	16	17.5	40
g (mm)	7	82	82
b_p (mm)	300	517	529
Area of SC coil per pole (mm²)	200	3000	6000
Dimensions of SC coil (mm)	7.9×12.65	30.6×49	43.3×69.3
Dimensions of SC wire (mm)	9.99×0.225		
Stator current density J_a (A/mm²)	3.5		
SC coil current density J_{SC} (A/mm²)	345	217	194
Maximum normal flux density / corresponding critical current density of SC coil @30K	1.34T / 430A/mm²	3.22T / 272A/mm²	4.09T / 241A/mm²
Packing factor	0.6		
Length of SC wire (km)	5.348	81.66	156.4
Weight of iron (t)	136.3	64.6	29.2
Weight of stator winding (t)	14.8	14.8	14.8
Type of SC material	YBCO		
Cost of SC (million €), quotation=100(or 20)€/m	0.534 (0.107)	8.166 (1.63)	15.64 (3.13)
Cost of copper (million €), quotation=7.5€/kg	0.111	0.111	0.111
Cost of iron (million €), based on quotation=0.8€/kg	0.108	0.0517	0.0233
Cost of total active material (million €), with SC quotation=100(or 20)€/m	0.764 (0.327)	8.328 (1.795)	15.77 (3.26)

Table 7-2 Properties of 10 MW coated conductor high temperature superconducting direct drive generators based on different generator topologies. Reproduced from Guan et. al. (Guan, et al., 2017).

7.2.3 Conclusion on RBCO generators based on the active materials

Based on the obtained specification of the active materials of the RBCO direct drive generators as outlined in Table 7-1 and Table 7-2 it has been estimated how large a cost reduction of the RBCO tape that is needed for the RBCO coated conductor direct drive generator to be economical competitive with the Permanent Magnet Direct Drive (PMDD) generator technology of Siemens Wind Power when extrapolated to 2020. The result is shown in Figure 7-2 and it is seen that the cost of the RBCO tape must be reduced to about 10 % in order to be competitive. In absolute numbers this is from 100 €/m and down to 10 €/m for 12 mm tape high temperature superconducting coated conductor tape. An analysis showing the impact of tapes with improved superconducting properties have not been performed, but it expected to result in a lower usage of tape.

Secondly it has been evaluated what the total mass of the active materials are for the RBCO coated conductor direct drive generator in comparison to the PMDD of Siemens Wind Power as extrapolated to 2020. This is shown in Figure 7-3 and shows that the RBCO coated conductor

(INNWIND.EU, Deliverable 3.11, Superconducting generators)

direct drive active materials are expected to remain heavier that the PMDD active materials even if the superconductors were obtained for free. This is a consequence of the iron-cored topology and reflects that the magnetic circuit of the PMDD is closed more effectively than for the RBCO coated conductor generator.

This above analysis resulted in a conclusion from Siemens Wind Power that the high temperature superconducting direct drive generator technology will not be competitive with the PMDD by 2020 and no further development was done in the INNWIND.EU project.
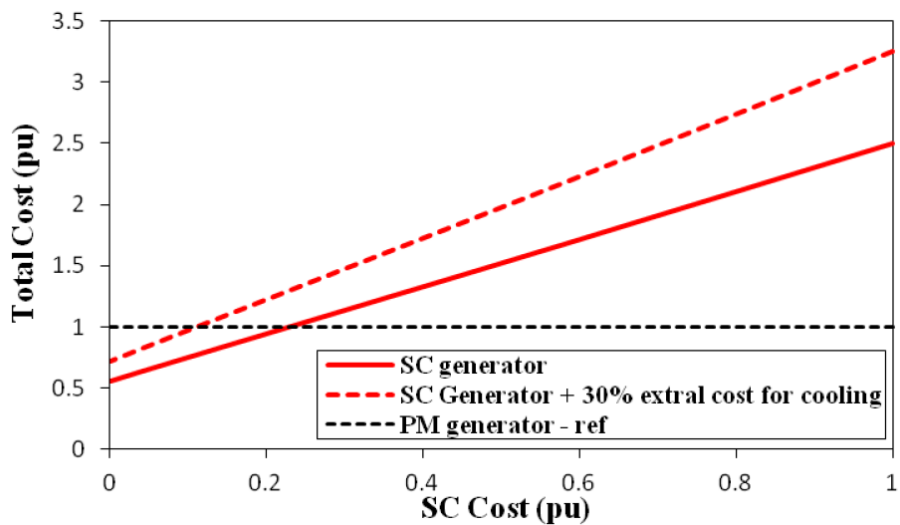
Figure 7-2 Evaluation of the economic feasibility of the RBCO superconducting direct drive generator in comparison to the Permanent Magnet Direct Drive generator technology of Siemens Wind Power as extrapolated to 2020. It is estimated that 30 % of the active materials cost must be added to account for the cooling system. Reproduced from Figure 3 of (Azar & Thomas, 2016).
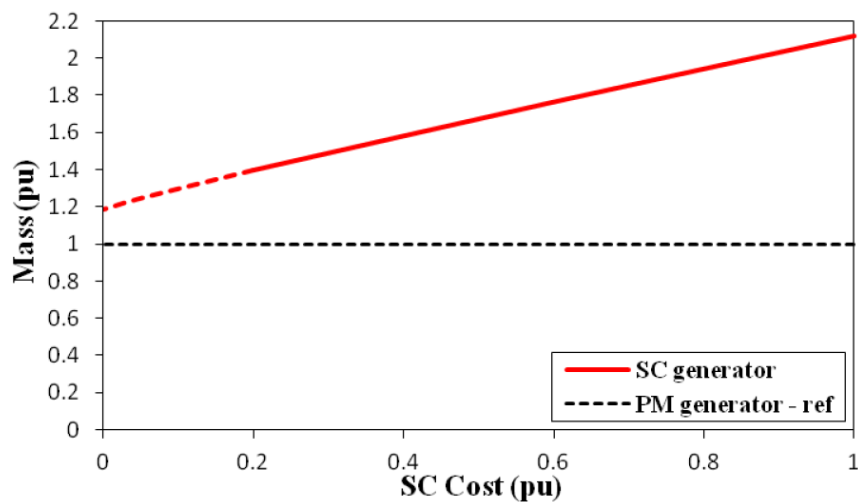
Figure 7-3 Evaluation of the active material mass of the RBCO coated conductor generator in comparison with the Permanent Magnet Direct Drive (PMDD) generator of Siemens Wind Power extrapolated to 2020. Reproduced from Figure 4 of (Azar & Thomas, 2016).

(INNWIND.EU, Deliverable 3.11, Superconducting generators)

8 NACELLE INTEGRATION

The integration of direct drive generators into large offshore turbines has such a large impact on the turbine design that it is difficult not to consider a direct drive generator as a component tailored to a specific turbine.

In the INNWIND.EU project it was suggested at an early stage to use the so called kingpin design from DNV-GL as template for the nacelle layout. The motivation for the kingpin nacelle is that it is believe that the only way to support the hub of a 20 MW turbine is to have two main bearings positioned at each side of the hub and a stationary pin going through the hub. This configuration has been described in details in deliverable D3.41 (Stehouwer, van Zinderen, & Hossain, 2017). The main question associated with the integration of a superconducting direct drive generator was if it should be positioned down-wind from the turbine rotor, as what is done with most permanent magnet direct drive generators today, or if the generator should be positioned in front of the turbine rotor. In the INNWIND.EU project it was decided to place the superconducting generator in front of the turbine rotor due to the following arguments:

1) The superconducting direct drive (SCDD) generators hold the potential to be light weight, which is an advantage to reduce the overhang mass of a front mounted generator.
2) A front mounted generator can be replaced without changing the rest of the turbine, which will allow a comparison between the superconducting direct drive generator and also the Magnetic Pseudo direct drive PDD studied in the INNWIND.EU project.
3) A front mounted SCDD can be removed from the turbine without dismounting the turbine rotor blades, whereby maintenance cost might be reduced in case of the need for major repairs.
4) A front mounted SCDD will allow space inside the centre of the generator for installation of cryogenic cooling equipment.

The following sections will outline the design of the generator support and the integration into the INNWIND.EU nacelle.

8.1 Front mounted MgB$_2$ generators

The dimensions of the active materials of the 10 MW MgB$_2$ generators specified in section 7.1 has been used as input for the design support structures of the generators and for the integration into the INNWIND.EU nacelle. Figure 8-1 is showing the cross sectional view of a front mounted 10 MW generator and the kingpin nacelle layout, where a stationary kingpin is supporting the turbine hub using two separated tapered roller bearings. The kingpin is connected to the tower by the mainframe.

The front mounted generators has been denoted as concept-1 and are shown for the generator diameters D_{gen} = 6.0 m, 8.4 and 10.8 m in Figure 8-2. It is however a questions if the front mounted generators have any advantages over a back mounted generator superconducting generator, which has been denoted concept-2 and are shown in Figure 8-3.

From a geometric point of view one can see that the D_{gen} = 8.4 m is matching the dimensions of the nacelle structure quite well, whereas the D_{gen} = 10.8 m is getting close to the blade root due to the 2.5 degree cone angle of the hub. Thus the D_{gen} = 8.4 m seems the most feasible from an integration point of view for the front mounted generator. This problem is not present for the back mounted generator and one could easily integrate the D_{gen} = 10.8 m generator.

In the following sections the difference in mass and cost of the two concepts are reviewed.

(INNWIND.EU, Deliverable 3.11, Superconducting generators)
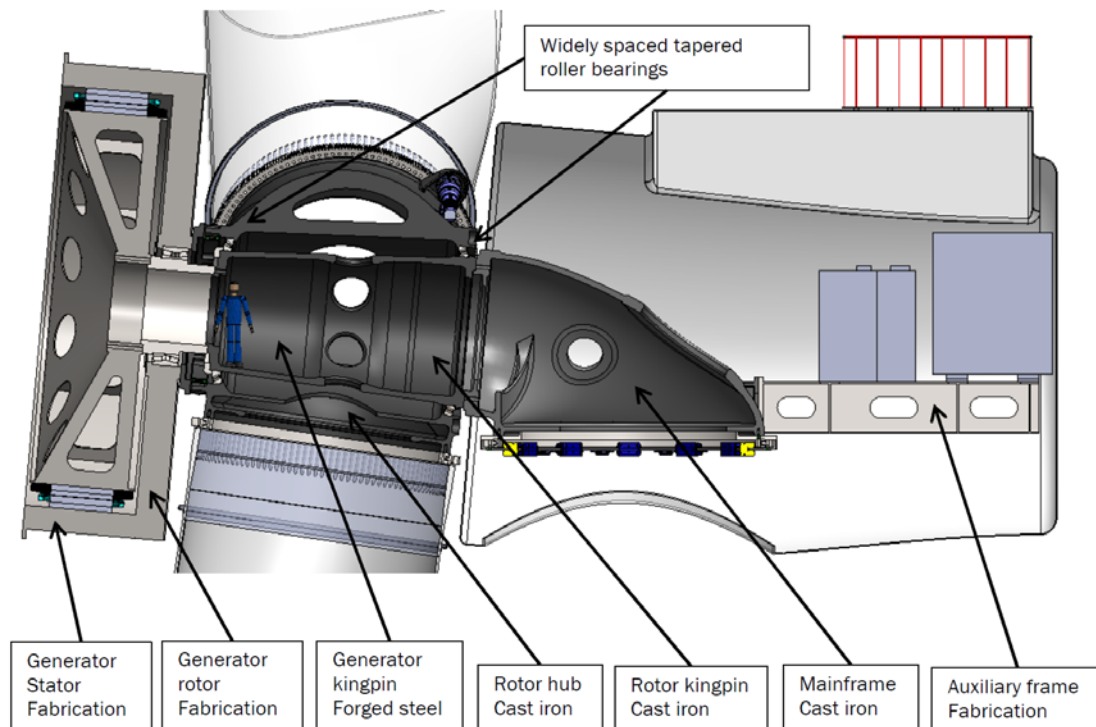
Figure 8-1 Cross section view of the INNWIND.EU nacelle with the D_{gen} = 8.4 m 10 MW MgB$_2$ generator mounted in front of the turbine blades. The inner and stationary structure of the generator is attached to the stationary kingpin going all the way through the rotor hub and connected to the main frame. The turbine rotor hub is supported by two separated tapered roller bearings and the generator rotor structure is attached to the turbine hub using hydraulic pads. The generator rotor structure is supported by a set of generator bearing allowing the dismounting of the entire generator from the nacelle. Reproduced from Figure 4-4 in (Stehouwer, van Zinderen, & Hossain, 2017).

(INNWIND.EU, Deliverable 3.11, Superconducting generators)
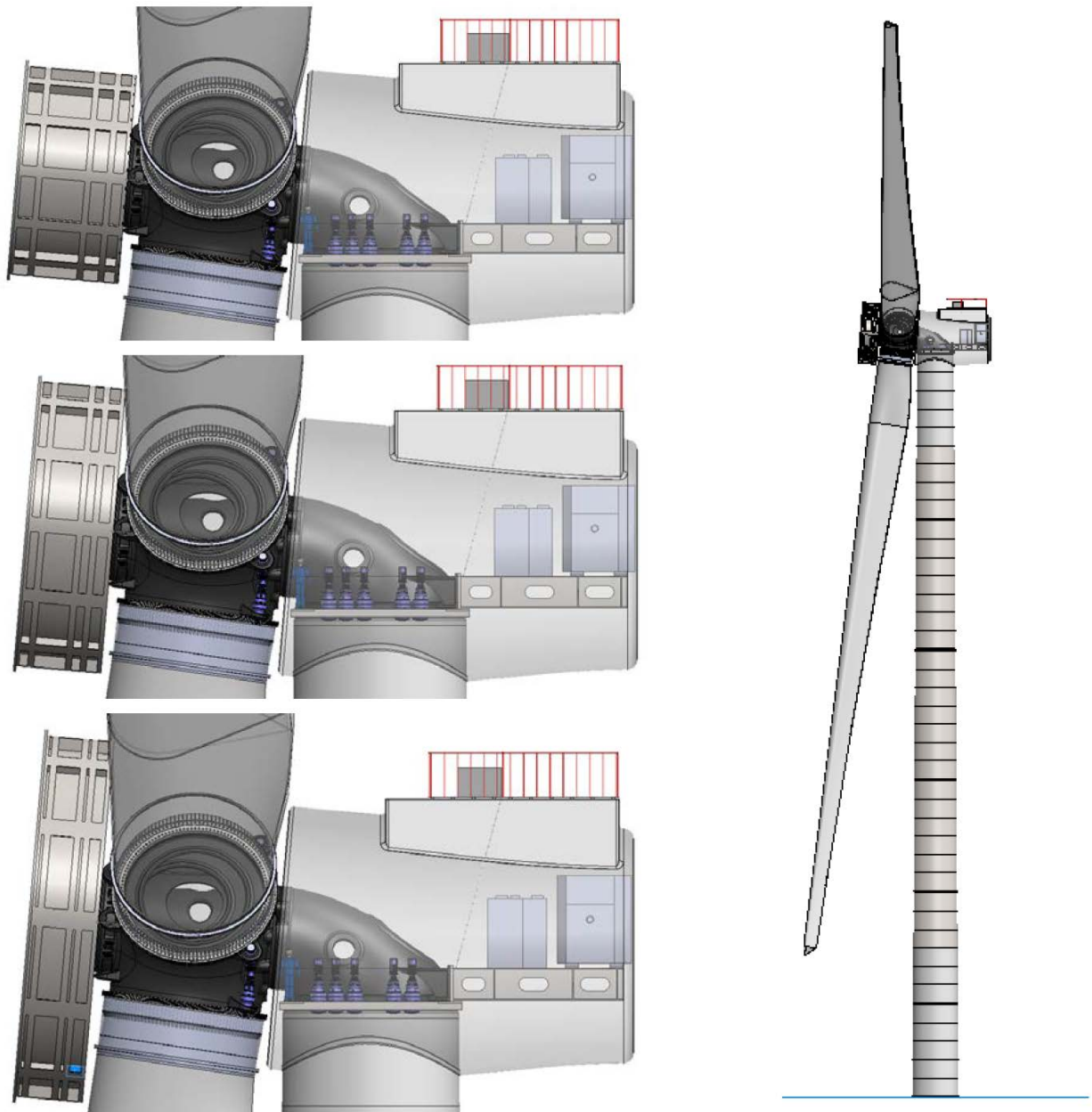
Figure 8-2. Left: Front mounted 10 MW MgB$_2$ generators with generator diameters of D_{gen} = 6.0 m , 8.4 m and 10.8 m. This configuration has been termed concept-1. Right: illustration of D_{gen} = 8.4 m generator mounted in front of the INNWIND.EU nacelle and on the D = 178 m INNWIND.EU reference turbine. Reproduced from Figure 4-3 in (Stehouwer, van Zinderen, & Hossain, 2017).
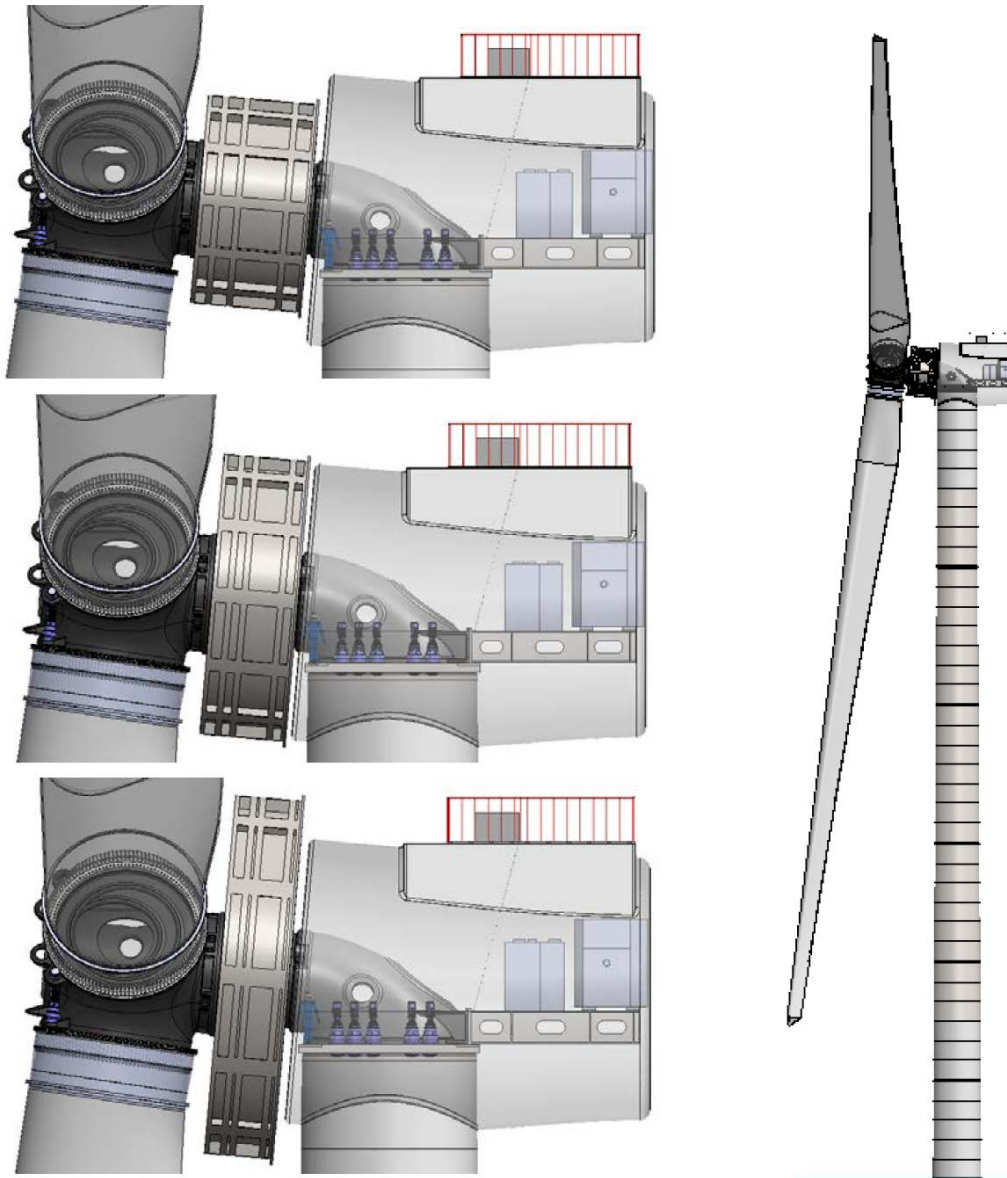
Figure 8-3 Left: Back mounted 10 MW MgB$_2$ generators with generator diameters of D_{gen} = 6.0 m , 8.4 m and 10.8 m. This configuration has been termed concept-2. Right: Illustration of D_{gen} = 8.4 m generator mounted behind the rotor blades of the INNWIND.EU nacelle and on the D = 178 m INNWIND.EU reference turbine. Reproduced from Figure 4-5 in (Stehouwer, van Zinderen, & Hossain, 2017).

(INNWIND.EU, Deliverable 3.11, Superconducting generators)

8.1.1   Structural support of generator

The structural support for the active materials are provided by a stationary inner part and a rotating outer part as illustrated in Figure 8-4. A set of generator roller bearings keep the position of the two support parts, whereby the generator can be dismounted from the nacelle in case repairs are needed. The generator rotor support part is connected to the turbine hub using a torque connection based on hydraulic pads as shown in Figure 8-5. The hydraulic pads are depressurized in case the generator must be removed from the turbine. Figure 8-6 and Figure 8-7 are showing the assembled generator as well as the inner and out structural support of the generator.

The final structure of the generator is shown in Figure 8-8, where the superconducting coils are mounted inside modular cryostats allowing a warm magnetic steel laminate pole piece to go right through the cryostat in order to realize the T12 topology introduced in chapter 5.1. This cryostat design is basically similar to the cryostat developed of the SUPRApower project and it is assumed that their concept can be transferred to the INNWIND.EU generator (Suprapower, 2017).

Finite element simulation of the deflection of the generator parts during different load situations have been performed as part of the task 3.4 and been reported in deliverable D3.41 (Stehouwer, van Zinderen, & Hossain, 2017). It has been found that gravity forces are the largest contribution to the deflection of the air gap of 35 % between the rotor and stator. Secondly it was found that when the short circuit torque was added to the gravitational forces then the mechanical air gap deflections of 42 % were larger than the 10 % target, but there were no closure of the air gap.

It was judged that an air gap deflection of only 10 % can be obtained with further engineering and by possibly adding a second generator bearing. Taken the uncertainties of the generator specifications into account then it was concluded that the structural generator concept is technically possible to realize, but considerable industrial work is needed before it can be manufactured.
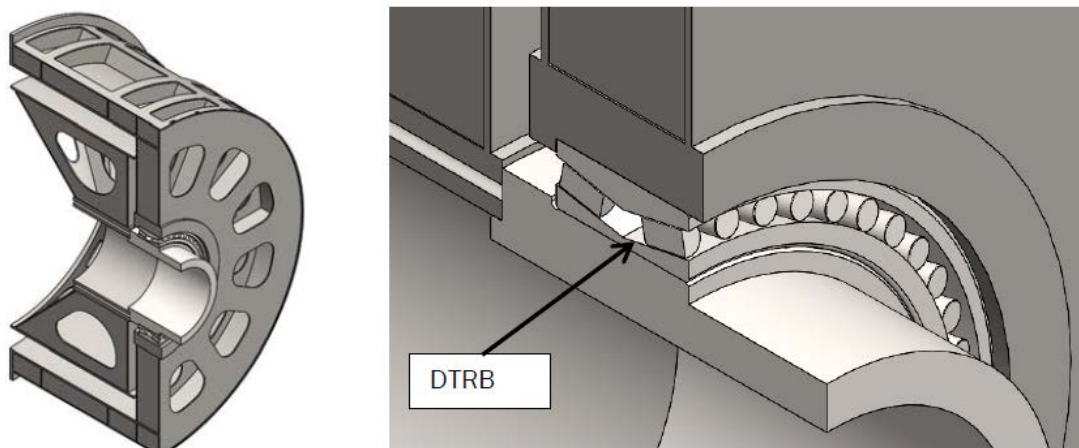
Figure 8-4 Structural support for the active materials of the 10 MW MgB$_2$ generators. The inner structural generator part is stationary and connected to the kingpin, whereas the outer structural generator part is rotating and is supported by a set of generator bearings. Reproduced from Figure 3-1 in (Stehouwer, van Zinderen, & Hossain, 2017).

(INNWIND.EU, Deliverable 3.11, Superconducting generators)
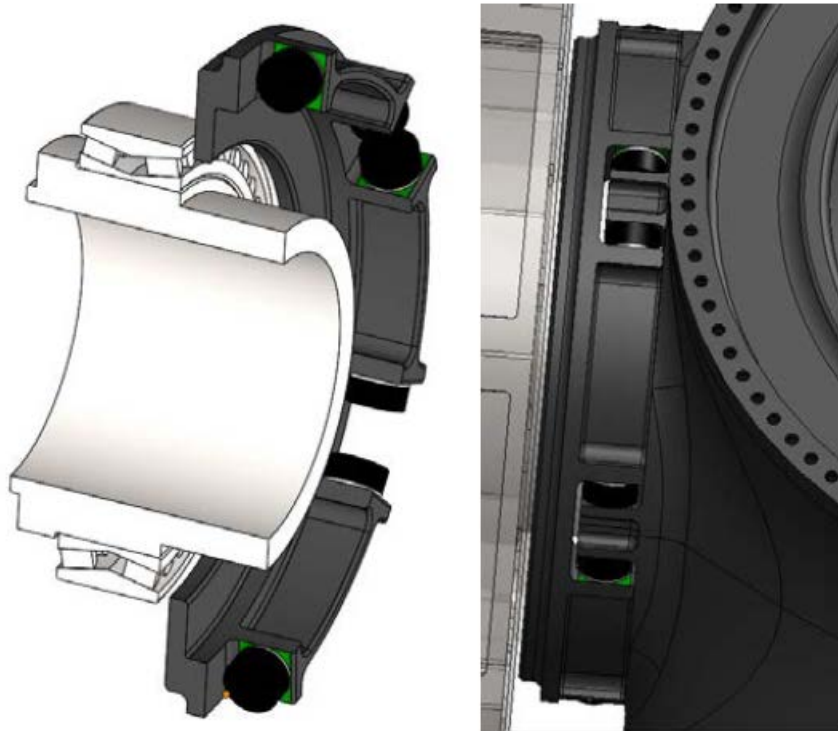
Figure 8-5 Torque coupling between generator rotor structural part and the turbine hub based on hydraulic pads. Reproduced from Figure 3-2 in (Stehouwer, van Zinderen, & Hossain, 2017).
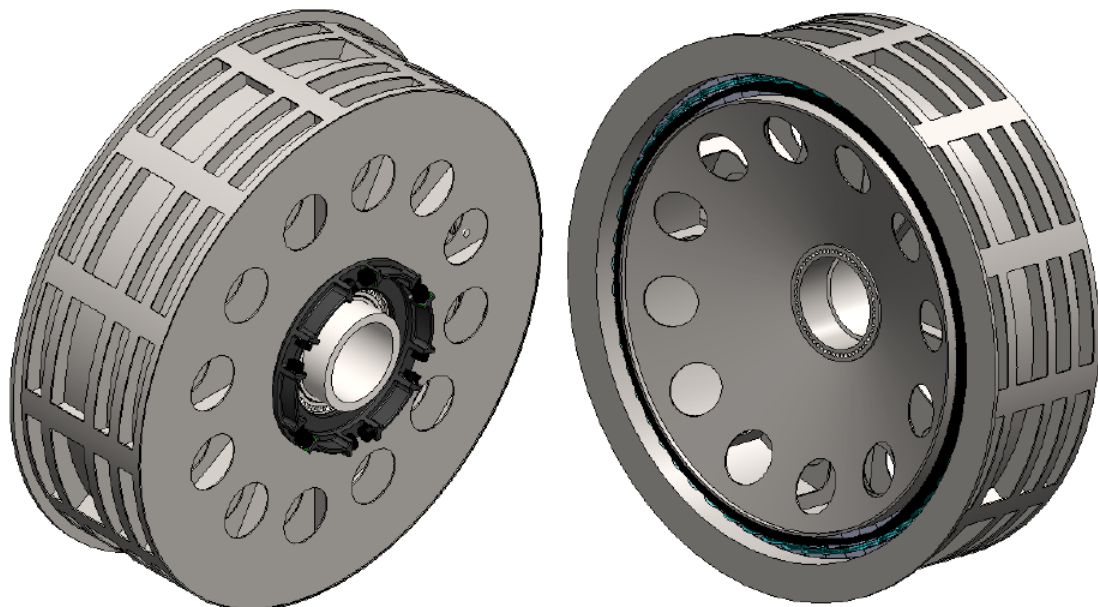
Figure 8-6. Front mounted 10 MW MgB$_2$ generator with D_{gen} = 8.4 m. Left: Seen from the back where the center tube is connected to the stationary kingpin and the back parts provide the torque coupling using hydraulic pads. Right: Seen from the front. The inner part is stationary and the outer part is rotating. Reproduced from Figure 3-3 in (Stehouwer, van Zinderen, & Hossain, 2017).

(INNWIND.EU, Deliverable 3.11, Superconducting generators)
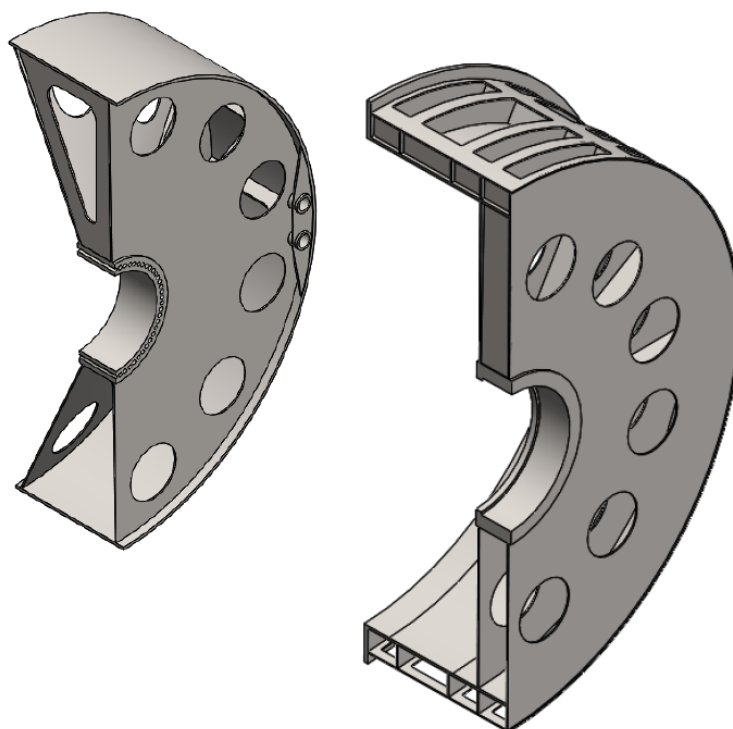
Figure 8-7 Structural generator support parts for the 10 MW MgB₂ generators. Left: Stationary inner part. Right: Rotating outer part. Reproduced from Figure 3-4 in (Stehouwer, van Zinderen, & Hossain, 2017).
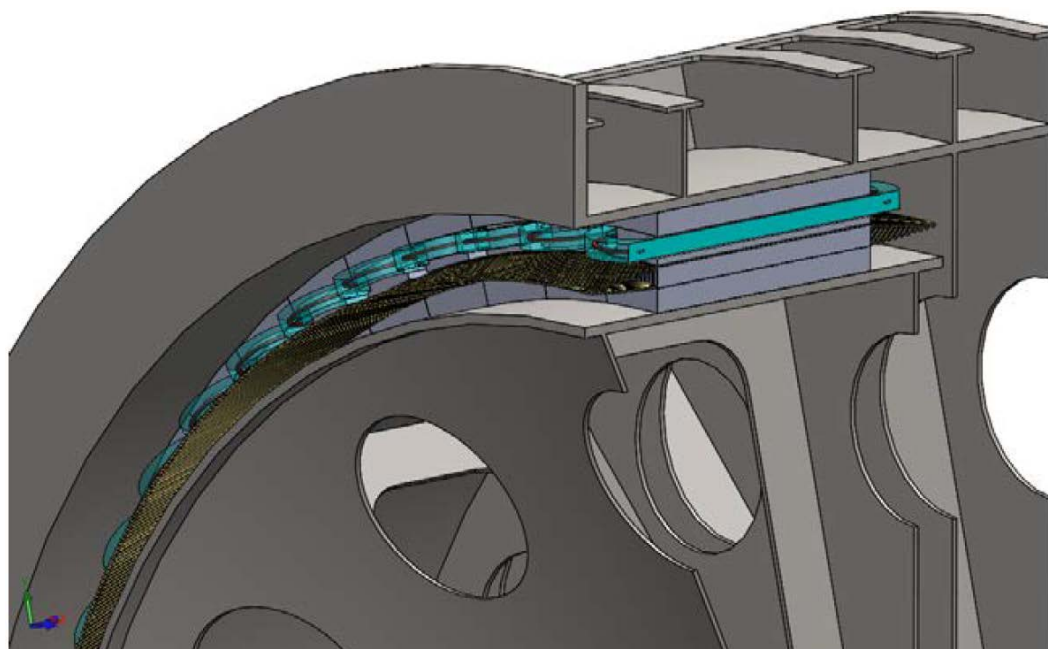
Figure 8-8 Assembled 10 MW MgB₂ generator where the active material of the generator is shown mounted onto the generator support structures, In this case the superconducting coils inserted in modular cryostats (cyan) are mounted on the outer rotating support part for the generator topology T12, where a warm magnetic steel laminate pole piece is going through the cryostat all the way to the armature surface expect for a 8 mm air gap. The armature windings are placed on the inner stationary generator support structure again corresponding to the topology T12. Reproduced from Figure 3-5 in (Stehouwer, van Zinderen, & Hossain, 2017).

(INNWIND.EU, Deliverable 3.11, Superconducting generators)

8.1.2 Weight and cost of superconducting generator including support structure

The weight and cost of the 10 MW MgB_2 generator support structures and nacelle components of both the front (concept-1) and the back mounted generator (concept-2) have been evaluated. The results are shown in Table 8-1 and Table 8-2 for the two concepts.

It is seen in Table 8-1, that the structural mass of 152 tons is starting out as equal to the mass of the active materials of 153 tons for the 6.0 m front mounted generator, but that the structural mass is increasing to 191 tons whereas the active material mass is decreasing to 96 tons for the 10.8 m generator. The total mass of the generator is therefore about 286 tons and the same for both the 8.4 m and the 10.8 m generator. The cost of the structural mass is only 392 k€ compared to the cost of the active mass being 706 k€ for the 6.0 m generator, but for the 10.8 m generator then the cost of the structural and active mass are about the same resulting in a generator cost of about 1.0 M€. It should be noted that this cost does not include the cooling system or the power electronics, which is added later in the determination of the Levelized Cost of Energy (LCoE).

A similar trend is observed for the back mounted generator in Table 8-2. By comparing the masses of the front and back mounted generators then it can be seen that the front mounted generator solutions has a lower weight by 39 tons, 29 tons and 23 tons when increasing the generator diameter from 6.0 to 10.8 m. Similar one observe that the cost difference of the front mounted generator is 95 k€, 73 k€ and 58 k€ lower than the back mounted generator when increasing the generator diameter from 6.0 to 10.8 m. The relative difference between the front and back mounted superconducting generator is thereby below 11 % for the mass and below 8 % for the cost.

Thus it is concluded that the front mounted superconducting generator seems to have a small advantage in terms of weight of about 30 tons and cost of about 70 k€. The front mounted generator with the lowest weight are either the 8.4 m or 10.8 m generator. The front mounted D_{gen} = 8.4 m is chosen as the most feasible, because that diameter is equal to the equivalent size of the nacelle. This generator have a weight of 286 tons and a cost of 1.01 M€ excluding the cryogenics and power converter.

	SCDD1	SCDD2	SCDD3	CC	Unit price	SCDD1	HTSC2	SCDD3
	[kg]	[kg]	[kg]	[-]	[€/kg]	[€]	[€]	[€]
Torque transmission	8,000	8,000	8,000	CC2	4	32,000	32,000	32,000
Generator kingpin	13,000	13,000	13,000	CC1	3	32,500	32,500	32,500
Generator Rotor Structure	82,000	98,000	112,000	FC2	3	205,000	245,000	280,000
Generator Stator Structure	49,000	49,000	58,000	FC2	3	122,500	122,500	145,000
Total Structure	152,000	168,000	191,000			392,000	432,000	489,500
Generator active parts mass [4]:	153,000	118,000	96,000		-	706,000	579,000	509,000
Total	305,000	286,000	287,000			1,098,000	1,011,000	998,500

Table 8-1 Weigh and cost of the front mounted (Concept-1) superconducting 10 MW MgB_2 generators with D_{gen} = 6.0 m (SDDD1), 8.4 m (SCDD2) and 10.8 m (SCDD3) as shown in Figure 8-2 . The generator active mass and cost are coming from chapter 6.1. Reproduced from Table 3-2 in (Stehouwer, van Zinderen, & Hossain, 2017).

	SCDD1	SCDD2	SCDD3	CC	Unit price	SCDD1	SCDD2	SCDD3
	[kg]	[kg]	[kg]	[-]	[€/kg]	[€]	[€]	[€]
Torque transmission	8,000	8,000	8,000	CC2	4	32,000	32,000	32,000
Generator Kingpin	60,000	46,000	39,000	CC1	3	150,000	115,000	97,500
Generator Rotor structure	84,000	100,000	116,000	FC2	3	210,000	250,000	290,000
Generator Stator Structure	38,000	43,000	51,000	FC2	3	95,000	107,500	127,500
Total Structure	190,000	197,000	214,000			487,000	504,500	547,000
Generator active parts mass [4]:	153,000	118,000	96,000		-	706,000	579,000	509,000
Total	343,000	315,000	310,000			1,193,000	1,083,500	1,056,000

Table 8-2 Weight and cost of the back mounted (Concept-2) superconducting 10 MW MgB$_2$ generators with D_{gen} = 6.0 m (SDDD1), 8.4 m (SCDD2) and 10.8 m (SCDD3) as shown in Figure 8-3. The generator active mass and cost are coming from chapter 6.1. Reproduced from Table 3-3 in (Stehouwer, van Zinderen, & Hossain, 2017).

8.2 Initial load simulation of 10 MW MgB$_2$ front mounted direct drive generator

Initial turbine load simulations including a 10 MW MgB$_2$ direct drive front mounted generator have been performed by formulating an aero-elastic-model of the kingpin nacelle holding an early version of the 10 MW MgB$_2$ generator (Abrahamsen & Natarajan, 2016). The starting point was a 10 MW MgB$_2$ generator with a diameter of D_{gen} = 6.6 m and a length of L_{gen} = 2.44 m, which is similar to the small diameter generator discussed in section 8.1. The total weight of active and structural mass was estimated to be m_{gen} = 363 tons, which is somewhat larger than what was presented in section 8.1, because the hub extenders holding the pitch bearings are more heavy in the configuration shown in Figure 8-9 than the configuration of section 8.1.

In order to understand if the front mounted generator was "too heavy" then a series of generators with a shorter length and thereby lower mass were also investigated. It was assumed that that the initial torque could be provided with the shorter generators by replacing the generator active materials with more advanced superconductors resulting in a higher shear force density. The 10 MW low temperature superconductor NbTi direct drive wind turbine design of GE Global research with a total mass of 142 tons (Fair, 2012) was used as end mass target of the shorter MgB$_2$ generators. The shorter MgB$_2$ generators investigated therefore had a length of 75 %, 50 % and 40 % of the original design. The MgB$_2$ generator of 40% length had a weight of 145 tons being quite close to the mass of the GE NbTi generator (Fair, 2012).

The code HAWC2 was used to perform the aero elastic simulations of the nacelle integrated with the INNWIND.EU 10 MW onshore reference turbine in order to investigate both extreme and fatigued loads of the main and yaw bearings of the nacelle. Figure 8-10 is showing the extreme loads on the main bearing, the low speed shaft (LSS) and the thrust for the reference geared drive train as well as for the Direct Drive kingpin (DDK) with 100 %, 75 %, 50 % and 40 % of the initial design mass. Similarly Figure 8-11 is showing the extreme loads of the yaw bearing for the same configurations. Figure 8-12 is showing the fatigue damage equivalent loads of the main and yaw bearing for a life time of 20 years.

One way to determine if the front mounted 10 MW MgB$_2$ generator is "too heavy" is to estimate when the loads of the front mounted generator is similar to the loads obtained from the reference drive train. Using this criteria it can be seen from Figure 8-10 that the main bearing loads of the DDK-75 configuration will have the same loads as the reference. Thus a 75 % reduction of the

generator mass to 0.75 x 363 tons ~ 272 tons would be needed. From Figure 8-11 it is seen that the front mounted generator will increase the yaw bearing load even for the 40 % configuration. It should however be noted that the 70 MNm moment indicated is observed for other load cases of the reference drive train. Finally the fatigue loads on the yaw bearing is seen to be quite similar for the geared and front mounted generators in Figure 8-12, but the fatigue loads of the main bearing are considerable higher for the front mounted generator. The aero elastic simulation of the front mounted generator is however only representing one main bearing and it is believed that the two separated main bearings will be able to comply with this higher fatigue loads.

It was concluded from the aero elastic simulations that if the mass of the front mounted generator was reduced to about 75 % of the initial design mass of 363 tons then one could claim that the loads due to the front mounted generator mass would not exceed that loads already observed for the reference drive train. By comparing the mass of the D_{gen} = 8.4 m generator of section 8.1 m which is m_{gen} = 286 tons, then one can see that the final generator mass is quite close to fulfil this criteria and it is concluded that the front mounted generator design is not violating the design of the INNWIND.EU reference turbine.
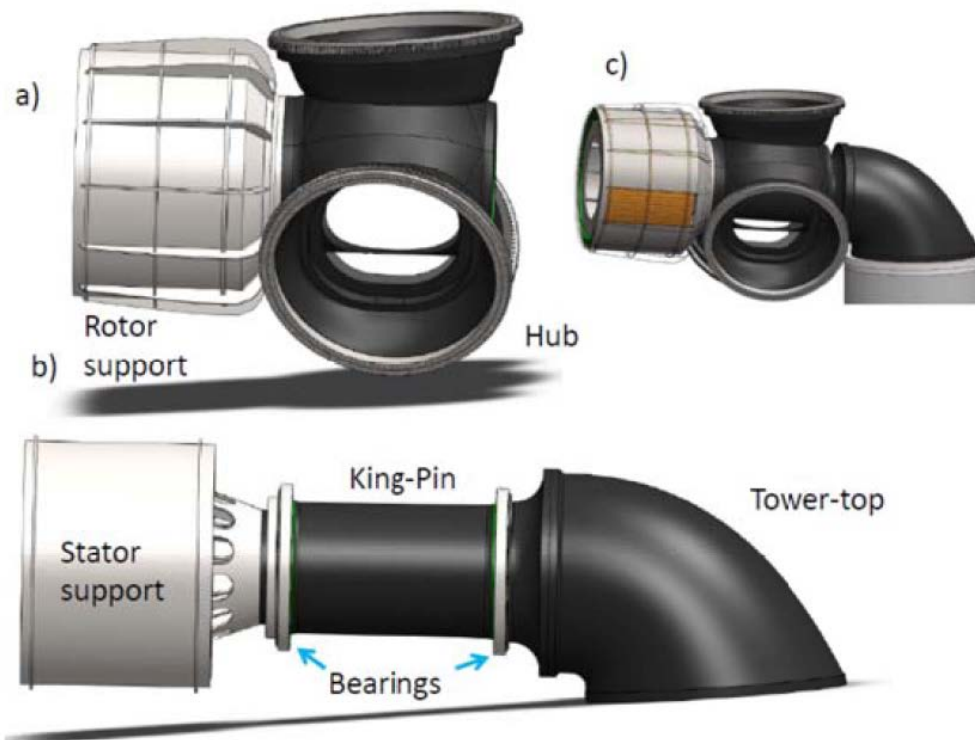
Figure 8-9 Front mounted 10 MW MgB₂ superconducting generator integrated into the kingpin nacelle layout. a) Rotating parts of the nacelle. b) Stationary parts of the nacelle. Inset: full assembly of the turbine nacelle. Reproduced from (Abrahamsen & Natarajan, 2016).

(INNWIND.EU, Deliverable 3.11, Superconducting generators)
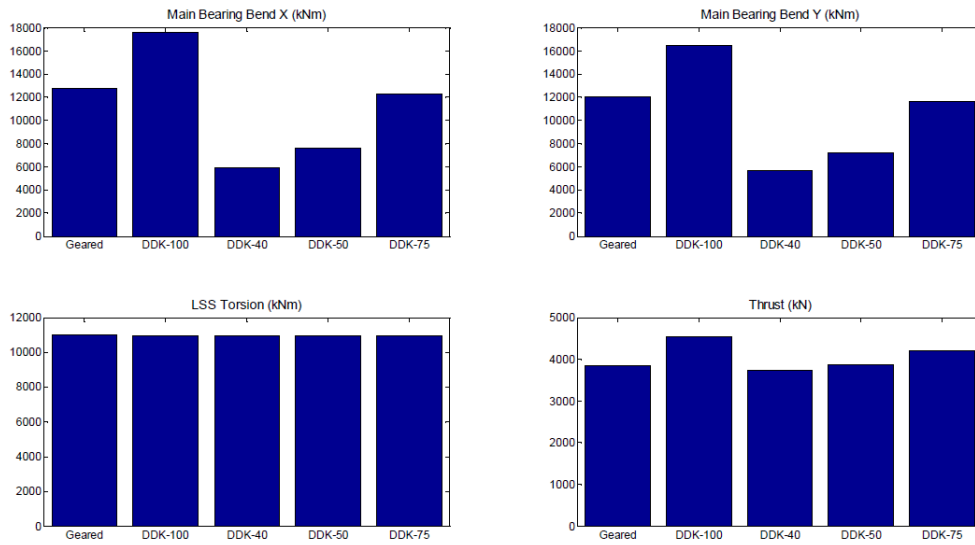
Figure 8-10 Variation in the extreme load under Design Load Case (DLC) 2.3 for different nacelle configurations: Geared is the gearbox drive train of the INNWIND.EU reference turbine and the Direct Drive kingpin is denoted DDK with the number indicating the percentage of the original length or mass. Reproduced from (Abrahamsen & Natarajan, 2016).
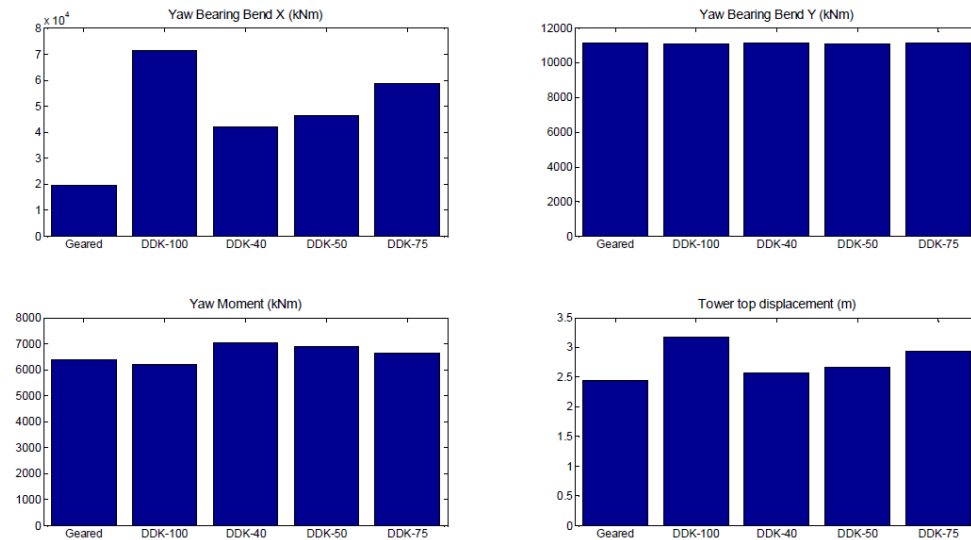
Figure 8-11 Extreme loads on the yaw bearing along with the peak tower top displacement for the geared and the Direct Drive kingpin configurations. Reproduced from (Abrahamsen & Natarajan, 2016).

(INNWIND.EU, Deliverable 3.11, Superconducting generators)
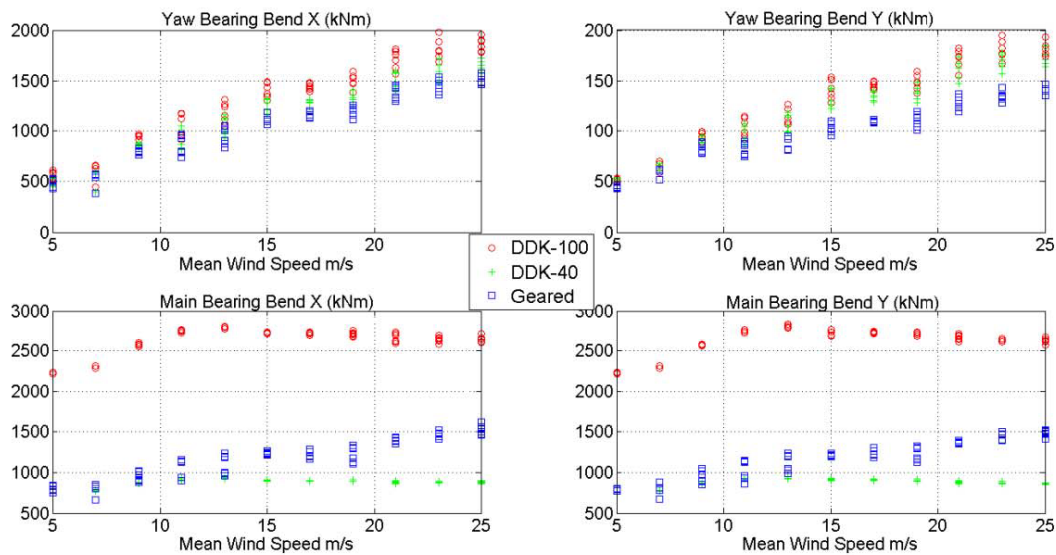
Figure 8-12 Variation of the damage equivalent moments over a 20 year lifetime for the geared drive train of the reference turbine and the Direct Drive kingpin with 100 % and 40 % of the initial design length or mass. Reproduced from (Abrahamsen & Natarajan, 2016).

8.3 Nacelle integration of high temperature superconducting generator

The initial thinking of integrating the coated conductor high temperature superconducting coils into the direct drive wind turbines of Siemens Wind Power was to replace the outer permanent magnet rotor with a superconducting version as illustrated on Figure 8-13. The priorities were to have as high an operation temperature of the coils resulting in the choice of the High Temperature superconductors and secondly to have all cooling machines sitting in the nacelle in a position where they could be serviced by a technician entering the turbine as part of the normal maintenance. Such a solution call for a cryogenic rotating coupling by which a cold gas or cryogenic liquid can be transferred into the rotating frame which is cooled by a gas or liquid flow. The company Stirling Cryogenics is providing this technology for rotating electrical machines and was considered as a starting point for design of the cryogenic system (Stirling Cryogenics, 2018).

In the formulation of the description of work on the high temperature superconducting generator task of INNWIND.EU there were however a series of phases with go/no go criteria between them. The first phase A was the demonstration of the coated conductor coil technology, Phase B was generator design based on the superconductor properties obtained from the coils, Phase C was cryostat design and Phase D was demonstration in a rotating frame. The criteria between phase B and the remaining phases was that the RBCO direct drive generator would be more feasible than the permanent magnet direct drive of Siemens Wind Power in 2020. This turned out not to be the case and the work of designing the cryostat and demonstrating it was not performed.
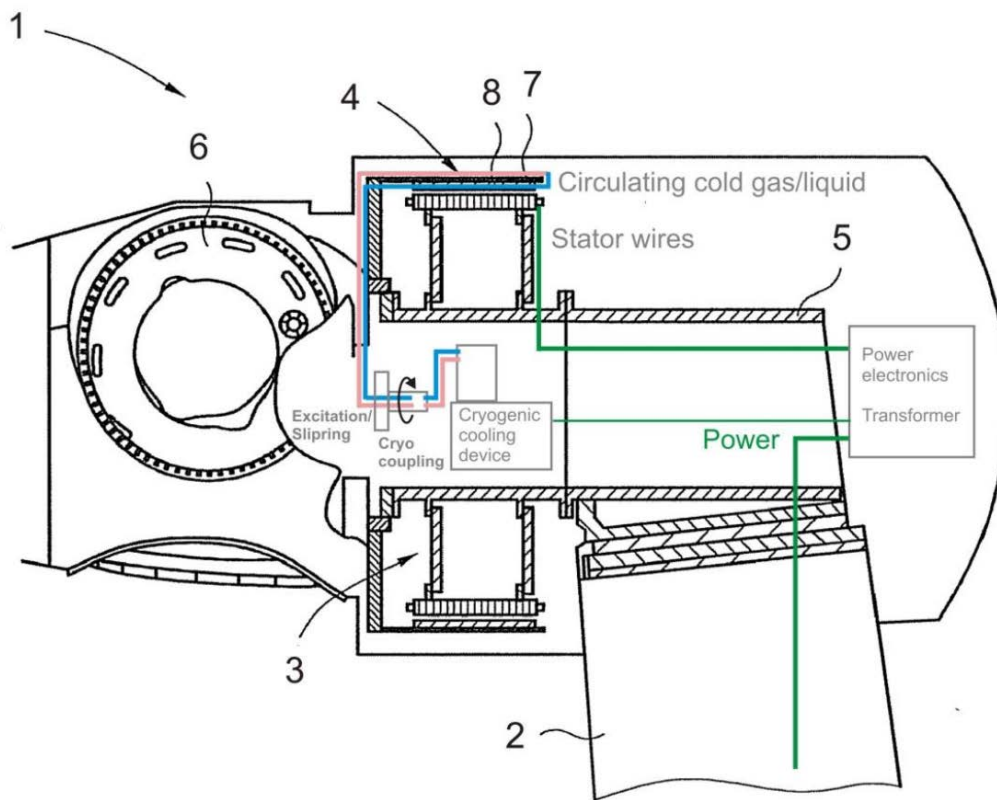
Figure 8-13 Initial proposal on integration of high temperature superconducting coated conductor coils into the direct drive turbine of Siemens Wind Power. The permanent magnet outer rotor is replaced by high temperature superconducting coils. The cooling of the superconducting coils is provided from a cooling device placed central in the nacelle in order to be able to perform maintenance on the cooling device.

(INNWIND.EU, Deliverable 3.11, Superconducting generators)

9 INNWIND.EU SUPERCONDUCTING GENERATORS

9.1 MgB$_2$

The INNWIND.EU 10 MW MgB$_2$ superconducting direct drive generator has a diameter of D_{gen} = 8.4 m and an active length of L_{gen} = 1.3 m as shown in Figure 9-1. It is based on the T12 generator topology, where the field winding pole is made of magnetic steel laminates kept at ambient temperature and the MgB$_2$ winding is positioned in a cryostat wrapped around the pole piece. The number of field winding poles is 56 and the pole pitch is 0.47 m. The cross sectional area of the MgB$_2$ coil is 20 mm x 12 mm holding a current density of 113 A/mm^2 at a temperature of T = 20 K as specified in section 7.1.1.

The T12 topology calls for a cryostat, which has a hole in the middle, and the superconducting winding is placed around the warm pole piece being a part of the magnetic circuit of the generator rotor. This cryostat is of the same type as has been demonstrated in the SUPRApower project (Suprapower, 2017) as illustrated in Figure 9-2. In the SUPRApower design a series of cryocooler cold heads are placed on the superconducting rotor windings and a rotating gas connection is placed in the centre of the hub, whereby the helium gas compressor running the cold heads can be placed in the static frame of the turbine as shown in Figure 9-3. It is believed that the SUPRApower technology can be transferred directly to the INNWIND.EU design and no further detailed design of the cryostat have been done in order not to replicate the work of the SUPRApower project. It is however assumed that the cost of the INNWIND.EU cryostats and cooling system should be in the order of 600 k€ and that a constant power consumption of 50 kW is possible as indicated for a low temperature superconducting (LTS) wind turbine generator design in (Y. Liu, 2015). The cost comparison of the SUPRApower cryostat is done in the next section.

The INNWIND.EU 10 MW MgB$_2$ generator is placed in front of the kingpin nacelle and the generator weight is estimated to be 286 tons. The T12 generator topology is chosen, because it is found, to provide the lowest Levelized Cost of Energy (LCoE) with the current MgB$_2$ properties. It is however also found that the 10 MW MgB$_2$ generator is most likely not going to be competitive with the Permanent Magnet Direct Drive (PMDD) generator technology in terms of mass, because magnetic steel laminates are added to the generator in order to reduce the amount of MgB$_2$ used. Thus it is argued that with future better and cheaper MgB$_2$ wires then other and lighter weight generator topologies might be feasible compared to the PMDD. In this sense the 10 MW INNWIND.EU MgB$_2$ generator is seen as a reference for comparison of future designs.

(INNWIND.EU, Deliverable 3.11, Superconducting generators)
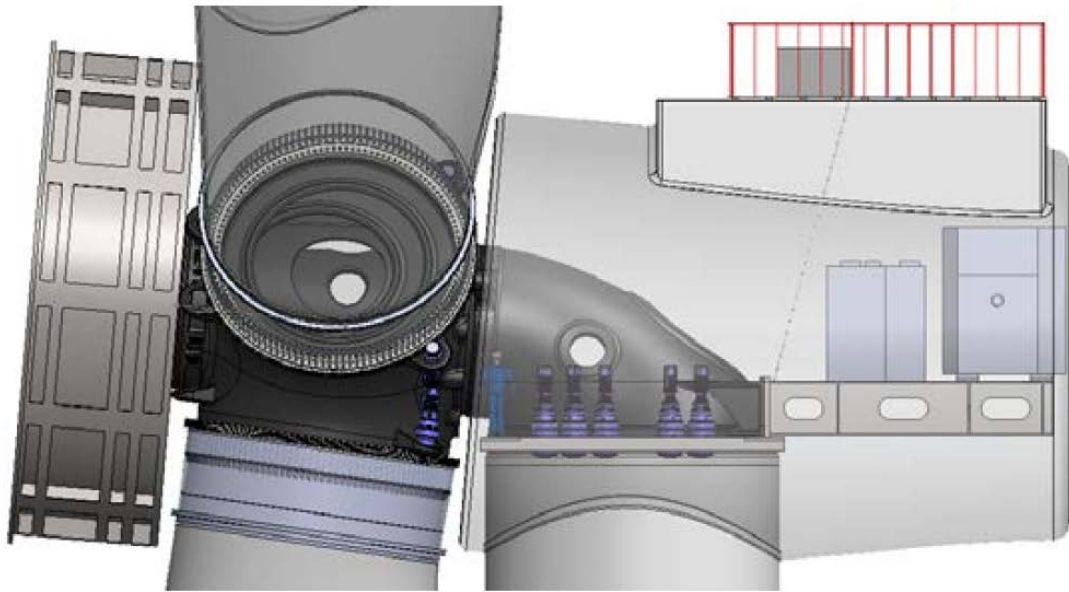
Figure 9-1 INNWIND.EU 10 MW MgB₂ superconducting direct drive wind turbine generator with a diameter of D_{gen} = 8.4 m, an active length of L_{gen} = 1.3 m and a weight of m_{gen} ~ 286 tons mounted in front of the kingpin nacelle.
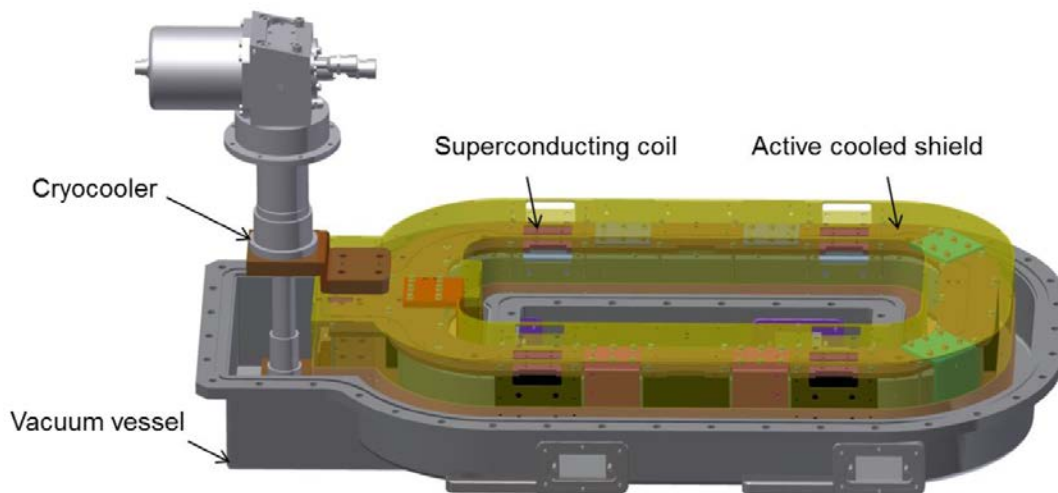
Figure 9-2 Illustration of modular cryostat for operating a superconducting MgB₂ field winding at T = 20 K in a wind turbine generator developed as part of the SUPRApower project (Suprapower, 2017). The MgB₂ coil is placed inside a radiation shield, which is connected to a cryocooler coldhead. All the cold part are placed in a stainless steel vacuum vessel in order to provide thermal insulation. The coldhead is supplied with high pressure helium lines connected to a compressor. Reproduced from (Sun, Sanz, & Neumann, 2015)

(INNWIND.EU, Deliverable 3.11, Superconducting generators)
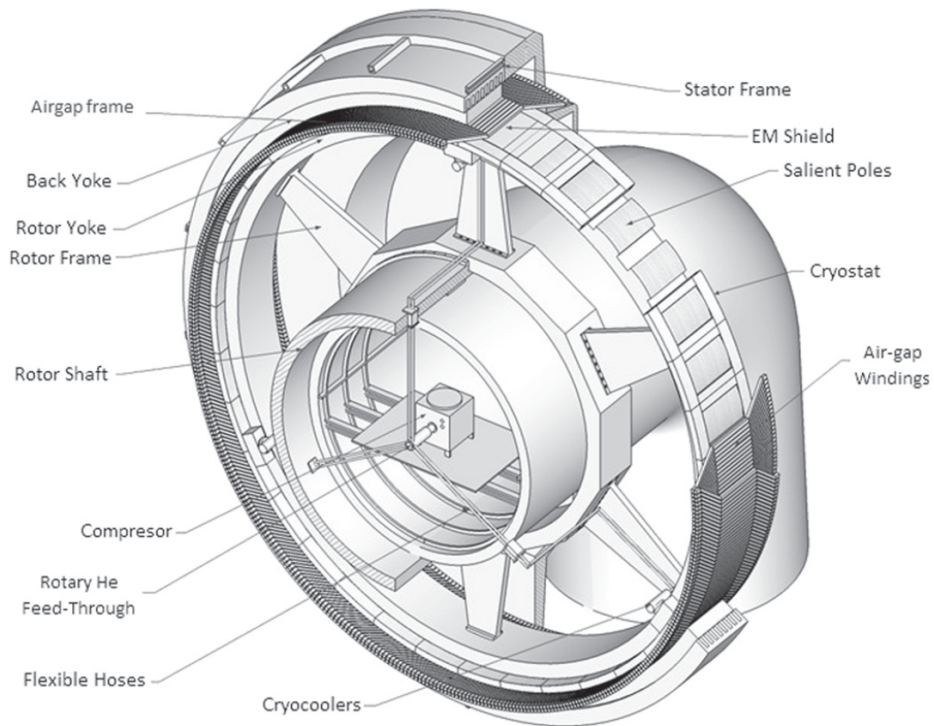
Figure 9-3 Illustration of the SUPRApower project integration of the cryocooler cold heads in the superconducting field windings and how the coldheads are supplied with high pressure helium gas lines through a rotating gas coupling connected to helium compressors in the static frame of the turbine. Reproduced from (Marino, et al., 2016).

(INNWIND.EU, Deliverable 3.11, Superconducting generators)

9.1.2 Mapping SUPRApower cryostats and cooling system to INNWIND.EU generator

The cold heads used in the SUPRApower project are the COOLPOWER 10 MD from Oelikon Leybold connected to the COOLPAK 6000 HMD/6200 HMD helium compressors (Oerlikon, 2017). This cold head can provide a cooling power of 18 W at T = 20 K on the 2 stage of the cold head with an electrical power input of 7 kW to the compressor. The heat load into the SUPRApower cryostat can be used to estimate the equivalent heat load of the INNWIND.EU generators, by scaling the heat radiation and heat conduction through the coil support with the stack length ratio of the two generators, and by scaling the heat load associated with the current leads with the coil current. The stack length of the SUPRApower cryostat is $L_{SUPRAcryo}$ = 0.52 m and the INNWIND.EU 10 MW 8.4 m generator has $L_{INNWIND\ 8.4\ m}$ = 1.13 m. Table 9-2 is showing how the SUPRApower cryostat (Sun, Sanz, & Neumann, 2015) and cooling system is mapped onto the INNWIND.EU generators. This is done by estimating the heat load per cryostat and then assuming that each pole is equipped with an individual cryostat. The number of poles is $n_{pole,\ 10MW}$ = 56 and $n_{pole,\ 20MW}$ = 72 for the INNWIND.EU 10 MW and 20 MW generator respectively. The SUPRApower project has investigated a method of sharing the cryocooler cold heads between several cryostats and this method is assumed transferred to the INNWIND.EU generators as well. The number of cold heads needed to provide the cooling of the generator is thereby estimated from the heat load at T = 20 K on all the poles of the generator divided by the cooling capacity of the coldhead as shown in Table 9-1. The total power consumption of the generators is then determined from the power consumption of the compressors. Also the cost, weight and volume of the cold heads and compressors are estimated in Table 9-2.

It is concluded that the power consumption for the cooling of the INNWIND.EU turbines are found to be $P_{cooling}$ = 104 kW and 263 kW for the 10 MW and 20 MW generators. This is equivalent to 1.0 % and 1.3 % of the rated power of the generators and about twice as high as the initial design target of 50 kW for the 10 MW INNWIND.EU generator. It should however be noticed that the largest heat load contribution at T = 20 K in Table 9-2 is the AC losses of the superconducting coil Q_{AC}. The AC losses of a preliminary INNWIND.EU 10 MW generator has been investigated in section A4 and it was found to be in the order of 2.5 W for the iron-cored design with 40 poles and an air gap diameter of 6 m (see figure A4.6). This is indicating that the INNWIND.EU AC losses are expected to be smaller, whereby the number of cold heads needed could be reduced. The AC losses are however highly non-linear and future work should determine the loss level more accurately as an industrial design is available. It is however seen that a loss lower than about 1% should be possible.

(INNWIND.EU, Deliverable 3.11, Superconducting generators)

The cost of the cryocooler cold heads and the compressors needed for the INNWIND.EU generators have also been estimated in Table 9-2. The cost is estimated to be about 223 k€ and 563 k€ for the 10 MW and 20 MW generators respectively. In the initial design target of the cooling cost 600 k€ was assumed for the 10 MW. This will mean that the cryostats can be built for 600 k€ - 223 k€ = 377 k€ or 7 k€ per cryostat. This is probably quite low compared the research environment used for the current development, but could serve as in indication of the level needed after an industrialization. Thus the cost of the INNWIND.EU cryostats are assumed to be a factor of 1.7 times the cost of the cold heads. This result in a cryostat cost of 1.0 M€ for the 20 MW INNWIND.EU generator and a total expenses on cold heads, compressors and cryostats of 1.51 M€, which is included in the next section.

Coldhead 10 MD & compressor	
Cooling power @ 2 stage T = 20 K [W]	18
Cooling power @ 1 stage T = 80 K [W]	110
Maintenance interval [Years]	5-10
Weight per cold head [kg]	20
Compressor power consumption [W]	7000
Maintenance interval [Years]	3-5
Weight per compressor [kg]	104
Compressor volume [m^3]	0.114
Compressor & Cold head cost est. [k€]*	15

Table 9-1 Properties of Oerlikon Leybold coldhead COOLPOWER 10 MD and helium compressor COOLPAK 6000 HMD / 6200 HMD used in the SUPRApower cryostat.* This cost includes an assumed discount of 50 % due to large number of units as compared to current cost (Oerlikon, 2017).

(INNWIND.EU, Deliverable 3.11, Superconducting generators)

		Q_s [W]	Q_r [W]	Q_{AC} [W]	Q_{cl} [W]	Q_a [W]	T_a [K]	L_{stack} [m]	I_{coil} [A]	Q_{Total} [W]	Cold head	Comp power [kW]	Coldhead Compres [k€]	Weight [kg]	Volume [m³]
SUPRApower	Shield	5,11	1,07	0	3	9,2	80	0,52	95						
	Coil	0,79	0,1	1,25	0,03	2,2	20	0,52	95						
INNWIND 10 MW	Shield	11,1	2,3	0,0	11,8	25,2	80	1,13	374	1413	13				
	Coil	1,7	0,2	2,7	0,1	4,8	20	1,13	374	267	15	103,8	222,5	1840	1,7
INNWIND 20 MW	Shield	22,1	4,6	0,0	12,2	38,9	80	2,25	386	2803	25				
	Coil	3,4	0,4	5,4	0,1	9,4	20	2,25	386	676	38	262,7	562,9	4653	4,3

Table 9-2 The heat load contributions for the SUPRApower modular cryostat (Sun, Sanz, & Neumann, 2015) are projected onto the INNWIND.EU MgB$_2$ generators by scaling with the stack length L_{stack} and the coil current I_{coil}. The heat contributions are: Support Q_s, Radiation Q_r, AC losses in superconductor Q_{AC}, Current lead heat load Q_{cl}. The total heat load per cryostat is Q_a and the total heat load of the generator at the temperatures T_a is given by Q_{Total}. The number of coldheads needed is used to determine the compressors power consumption and the cost, weigh and volume.

(INNWIND.EU, Deliverable 3.11, Superconducting generators)

9.1.3 Scaling MgB$_2$ generator to 20 MW

The design of the MgB$_2$ superconducting generator has been scaled to 20 MW using the specification of the active materials for the 20 MW generator as outlines in section 7.1 and the scaling of the structural support as specified in delivery 3.41 (Stehouwer, van Zinderen, & Hossain, 2017). The results are shown in table Table 9-3 where the input parameter is the turbine rotor diameter, because the mass scaling of the nacelle components is determined by

$$\frac{M_1}{M_0} = \left(\frac{D_1}{D_0}\right)^{CSF} \tag{9-1}$$

where the reference design has a diameter of D_0 and a weight of m_0, whereas the up-scaled design has a diameter D_1 and weight m_1. The scaling is governed by the Cubic Scaling Factor CFS. The input design for the nacelle components are based on a D = 210 m turbine rotor, which is considered as the current limit in terms of nacelle components of what can be constructed with today's technology (See D3.41 for a discussion of Technology Readiness Levels (Stehouwer, van Zinderen, & Hossain, 2017)). The active materials for the MgB$_2$ generators have been obtained at P = 10 MW corresponding to a D = 178 m turbine and at P = 20 MW corresponding to a D = 252 m turbine rotor. The scaling factor of the MgB$_2$ active materials has been determined between at the two turbine diameters and is combined with the structural generator support, which is scaled according to D3.41. The equivalent turbine power is estimated in Table 9-3 by assuming a wind power density of 400 W/m^2.

Figure 9-4 is showing the mass scaling of the main components of the turbine holding the MgB$_2$ superconducting generators from Table 9-3. Two more points has been added for a D = 154 m and D = 164 m rotor obtained by down scaling the INNWIND.EU nacelle design. The D = 154 m rotor is similar to the Siemens Wind Power SWP 6.0-154 turbine with a power of 6 MW (Siemens, 2016) and the D = 164 m is similar to the Vestas V-164 turbine (de Vries, 2013). The active materials mass of the generator is plotted along with the total generator mass. By adding the blade and nacelle mass then the Rotor Nacelle Assembly (RNA) mass is shown as function of turbine rotor diameter. The RNA mass of the INNWIND.EU reference turbines are shown for comparison as well as the RNA of the Vestas V-164. The expected total generator mass of a 10 MW Permanent Magnet Direct Drive generator designed by Polinder in 2007 is also marked (Polinder, Bang, van Rooij, McDonald, & Mueller, 2007).

It is concluded that the MgB$_2$ superconducting direct drive generator provide a mass which is quite similar to the reference drive train at D = 178 m and 10 MW, but it is scaling slightly better than the reference at D = 252 m and 20 MW. Similarly it is seen that down scaling the RNA to a D = 164 m rotor is giving a MgB$_2$ RNA mass similar to the Vestas V-164. Thus even though the MgB$_2$ superconducting generators were design by the philosophy of "cheap and not too heavy" then the mass scaling does turn out to be slightly better than the INNWIND.EU reference generators.

Table 9-4 is summarizing the mass and estimated cost of the 10 MW and 20 MW MgB$_2$ superconducting direct drive turbine components by applying an assumption of some unit cost for the different materials. These unit cost include manufacturing and are therefore larger than just the raw materials cost. The cost and mass breakdown is illustrated in Figure 9-5 for the 10 MW MgB$_2$ generator turbine. This is instructive for discussing the cost contribution to the superconducting drive train. First of all one sees that the cost of the MgB$_2$ superconductors is only 85 k€ compared to 223 k€ for the cooling system and 377 k€ for the cryostats. This should be compared to the total generator cost of 1.7 M€ and the superconductors therefore only correspond to 5 % of the generator cost. However if the cooling system and cryostat is added to the superconductor cost then that is about 40 % of the generator cost. It is therefore clear that future cost reductions of superconducting direct drive generators will most likely be related to the cooling system and the cryostat manufacturing.

In order to compare the cost of the 10 MW MgB$_2$ generator to a permanent magnet direct drive generator then the 10 MW PMDD generator paper from 2007 of Henk Polinder is used (Polinder,

(INNWIND.EU, Deliverable 3.11, Superconducting generators)

Bang, van Rooij, McDonald, & Mueller, 2007). This is of course an old design, which is reflected in the unit cost of the $R_2Fe_{14}B$ permanent magnet materials being quoted at $C_{PM,2007}$ = 25 €/kg. People working in the field of permanent magnets will most likely recall the price peak of the rare earth elements in 2011 and the resulting jump of the $R_2Fe_{14}B$ magnet price. PM magnet materials cost higher than $C_{PM,2011}$ > 100 €/kg were reported in 2011, but since then several major companies have decreased the usage of $R_2Fe_{14}B$ magnets and the world market has an overcapacity, which has resulted in a decreasing price development since 2011. Today it seems that the magnet cost is back down to the level used in the Polinder paper from 2007 and we will therefore use this PM cost level for the comparison. It was found by Polinder that 6 tons of $R_2Fe_{14}B$ magnets will be needed for a 10 MW PMDD with a diameter of D_{gen} = 10 m and a stack length of L_{gen} = 1.6 m. The cost of the permanent magnets is $C_{PM,total}$ = 6 ton x 25 €/kg = 150 k€ and the total generator cost is 1.24 M€. Thus the SCDD is about 37 % higher than for the PMDD of Polinder. This is indicating that the INNWIND.EU generator is still too expensive, but also that there is not several orders or magnitude in difference. The INNWIND.EU generator is based in the iron-cored technology and is therefore quite similar to the PMDD of Polinder. So one method for evaluating the competition between the SCDD and the PMDD could be to directly compare the cost of the PM magnet material to the cost of the superconductors, the cooling system and the cryostats.

$$C_{PM}m_{PM} > C_{SC}m_{SC} + C_{cooling} + C_{cryostat} \qquad (9\text{-}2)$$

where C_{PM} is the unit cost of the $R_2Fe_{14}B$ magnets, m_{PM} is the mass of magnets expected to be around 0.6 ton/MW, C_{SC} is the unit cost of the superconductors, m_{sc} is the mass (or length) of the superconductors, $C_{cooling}$ is the cost of the cooling system and $C_{cryostat}$ is the cost of the cryostat(s).

This can be used to determine at what PM magnet cost the superconducting direct drive generator will become competitive and by inserting the numbers outlined above for MgB_2 one gets C_{PM} > 114 €/kg. Thus at the beginning of the INNWIND.EU project the SCDD was basically providing a similar cost as the PMDD, but in the period until now the cost of the $R_2Fe_{14}B$ material has decreased by a factor of 4 moving the competitive advantage back to the PMDD.

The above analysis is however not taking into account the added loss due to the cryogenic cooling nor the reduced availability due to the maintenance of the cooling system.

(INNWIND.EU, Deliverable 3.11, Superconducting generators)

Concept 1-SCDD2	D$_{rotor}$[m]	210	178	198	210	252	280
	CSF	Component mass [t]	Mass [t]	Mass [t]	Mass [t]	Mass [t]	Mass [t]
Hub	2,8	110	69,2	93,3	110,0	183,3	246,2
Blade	2,7	200	128,0	170,6	200,0	327,2	434,9
Pitch Bearings	2,5	28	18,5	24,2	28,0	44,2	57,5
Other Rotor parts	2,6	18	11,7	15,4	18,0	28,9	38,0
Main Bearings	3	5	3,0	4,2	5,0	8,6	11,9
Kingpin	2,8	50	31,5	42,4	50,0	83,3	111,9
Main shaft	2,8	0	0,0	0,0	0,0	0,0	0,0
Mainframe	2	73	52,4	64,9	73,0	105,1	129,8
Yaw bearing	2,3	9	6,2	7,9	9,0	13,7	17,4
Lantern	2	0	0,0	0,0	0,0	0,0	0,0
Main bearing housing	3	0	0,0	0,0	0,0	0,0	0,0
Other nacelle parts	2,5	35	23,2	30,2	35,0	55,2	71,8
Generator kingpin	2	13	9,3	11,6	13,0	18,7	23,1
Total nacelle		541	353,1	464,7	541,0	868,2	1142,5
Generator SCDD2	D$_{rotor}$[m]	178					
	CSF	Component mass [t]	Mass [t]	Mass [t]	Mass [t]	Mass [t]	Mass [t]
Active materials	2,17	118	118,0	148,7	168,9	250,9	315,4
Structural support	2,75	168	168,0	225,2	264,7	437,0	583,9
Total mass	2,75	286	286,0	373,8	433,6	687,9	899,3
RNA mass [t]			639,1	838,5	974,6	1556,2	2041,7
Rotor area [m²]			24872	30775	34619	49851	61544
Turbine Power [MW] 400 W/m²			9,9	12,3	13,8	19,9	24,6
Rotation speed [rpm]			9,6			7,13	
Rotation speed calculated [rpm]	0,85		9,6	8,8	8,3	7,1	6,5
Rotation speed [rad/sec]			1,00	0,92	0,87	0,75	0,68
Torque [MNm]			9,9	13,4	15,9	26,7	36,0

Table 9-3 Properties of the MgB$_2$ superconducting direct drive generator nacelle scaled as function of the turbine rotor diameter ranging from D = 178 m to D = 280 m using the Cubic Scaling Factors (CSF) as specified in deliverable D3.41 (Stehouwer, van Zinderen, & Hossain, 2017). The scaling factor of the MgB$_2$ generator active materials are determined from the MgB$_2$ generator designs obtained at 10 MW and 20 MW in section 7.1. The scaling of the nacelle components are obtained from the D = 210 m reference design. The power rating of the turbines are determined by assuming a wind power density of 400 W/m².

(INNWIND.EU, Deliverable 3.11, Superconducting generators)

Concept 1-SCDD2	10 MW	20 MW		10 MW	20 MW
	Mass [t]	Mass [t]	Mass cost [€/kg]	Cost [k€]	Cost [k€]
Hub	69,2	183,3	2,5	173	458
Blade	128,0	327,2	6,5	832	2130
Pitch Bearings	18,5	44,2	15,0	278	663
Other Rotor parts	11,7	28,9	2,5	29	72
Main Bearings	3,0	8,6	30,0	90	258
Kingpin	31,5	83,3	2,5	79	208
Main shaft	0,0	0,0	2,5	0	0
Mainframe	52,4	105,1	4,0	210	420
Yaw bearing	6,2	13,7	15,0	93	206
Lantern	0,0	0,0	4,0	0	0
Main bearing housing	0,0	0,0	4,0	0	0
Other nacelle parts	23,2	55,2	10,0	232	552
Generator kingpin	9,3	18,7	2,4	22	45
Total nacelle	353,1	868,2		2038	5012
Generator SCDD2					
Copper armature	13,1	24,3	15	197	365
Iron armature	49,4	106,7	3	148	320
MgB$_2$ rotor 4€/m	0,32	0,52	267	85	139
Iron rotor	51,8	111,5	3	155	335
Gen. Structural support	168	437	3	504	1311
Coldh & compres	1,8	4,7		223	563
Cryostats	3,4	8,9		377	951
Power converter	19,3	21,4		861	1595
Total	660	1583		4588	7558
Rotor area [m²]	24872	49851			
Turbine Power [MW] 400 W/m²	9,9	19,9			

Table 9-4 Mass and cost of components in 10 MW and 20 MW MgB$_2$ superconducting direct drive wind turbines.

(INNWIND.EU, Deliverable 3.11, Superconducting generators)

Rotor Nacelle Assembly mass scaling of MgB$_2$ Direct Drive generator
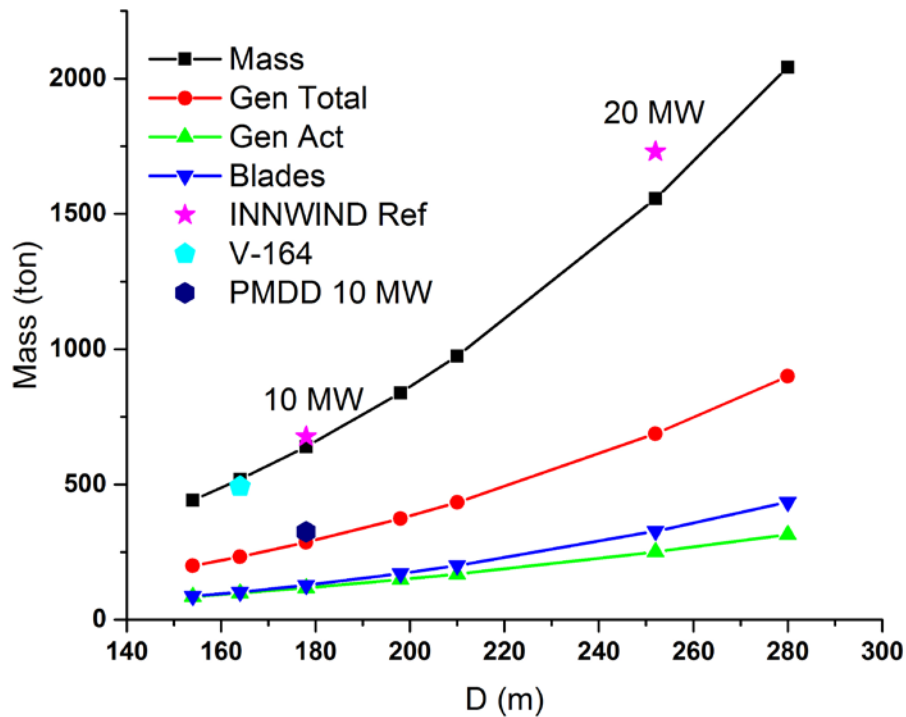
Figure 9-4 Mass scaling of the main components of the front mounted MgB$_2$ superconducting direct drive generator as function of the turbine diameter. The MgB$_2$ generator active materials mass (green) is added to the structural generator mass whereby the total generator mass (red) is obtained. By adding also the blade mass (blue) and the nacelle mass then the Rotor Nacelle Assembly (RNA) mass (black) is obtained. The RNA of the INNWIND.EU reference designs for P = 10 MW and 20 MW are shown (stars) as well as the RNA of the Vestas V-164 (de Vries, 2013) and the total generator mass of a 10 MW permanent magnet direct drive (PMDD) generator design by Polinder (Polinder, Bang, van Rooij, McDonald, & Mueller, 2007) .
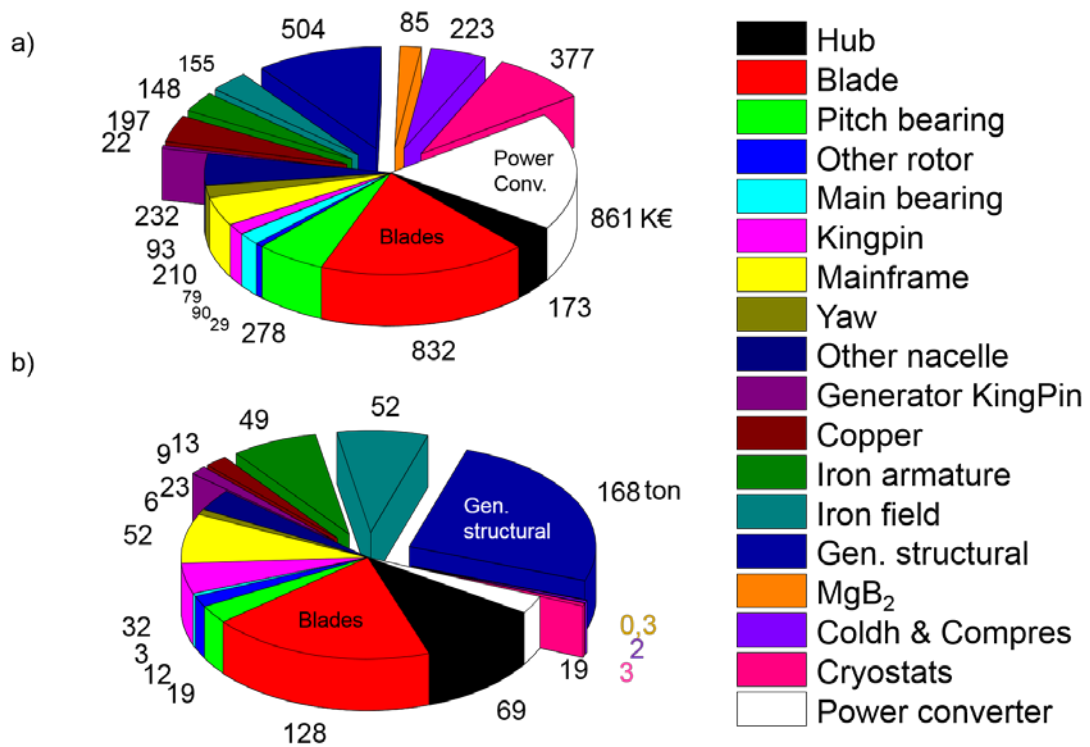
Figure 9-5 10 MW MgB$_2$ superconducting direct drive wind turbine rotor, generator and nacelles component cost and weight breakdown. a) Component cost in [k€] and b) component weight in [ton] according to the components outlined in Table 9-4. The components associated with the superconducting drive train have been displaced from the center.

10 ROADMAP OF SUPERCONDUCTING WIND GENERATORS AND FUTURE DEVELOPMENT

From the analysis of the superconducting generators of INNWIND.EU it is seen that neither the MgB_2 nor the RBCO direct drive generators with iron cored field and armature windings will be economical feasible with the current cost of the superconducting MgB_2 or RBCO wires. In this chapter it is discussed if that can change by upscaling the wire production volume or by further improvement of the superconducting properties of the wires.

10.1 Roadmap for superconducting wind turbine generators

In order to discuss the potential upscaling of the superconductor wire production imposed by a demand from the offshore wind turbine sector then it is instructive to formulate a potential roadmap for the introduction of the superconducting wind turbine generator technology. Figure 10-1 is showing a proposal on the introduction of superconducting wind turbine generator in comparison to the present European as well as worldwide wind capacity. The intention of the road map is to indicate that a 10 MW superconducting direct drive could from a technical point be installed in a few years from now. After the initial test of the first two turbines it will however be preferable to scale up the production considerable in order to attain about 1 % of the world market or 10 % of the European offshore market by 2030. This will correspond to 1000 turbines of 10 MW installed by 2030 and can be used to estimate the needed amount of superconducting wire.

In case of the MgB_2 direct drive then it was found in section 7.1 that L_{MgB2} = 20 km of 3 .0 x 0.7 mm MgB_2 wire is needed for the 10 MW generator if the current wire is operated at T = 20 K. Similarly section 7.2 showed that L_{RBCO} = 5.4 km of the 12 mm coated conductor tape is needed for the 10 MW high temperature superconducting direct drive generator if it is operated at T = 30 K. It should be noted that the INNWIND.EU MgB_2 coil demonstrator was based on 5 km of MgB_2 wire, which is equivalent to about 20 % of the wire needed for the iron cored 10 MW generator. Thus the MgB_2 wire is available in quantities that is needed for the first demonstration turbine indicated in the roadmap of Figure 10-1. The RBCO coated conductor demonstration coil was based on 250 m of RBCO tape, which is in the order of 5 % of the tape needed to build one 10 MW iron cored high temperature superconducting generator. Thus considerable higher quantities of RBCO tape will be needed to demonstrate the first 10 MW turbine as indicated in Figure 10-1.

It is interesting to compare the superconducting generator roadmap in Figure 10-1 with the wire production capacity of the companies producing both MgB_2 and also RBCO. Table 10-1 is listing the different major superconductor wire companies as well as the estimated maximum production capacity and the usual length of the superconducting wire produced. From the superconductor wind generator scenario it is seen that 20.000 km of MgB_2 and 6000 km of RBCO tape over a period of about 10 years is needed. For the MgB_2 wire then the wind imposed demand corresponds to about 15 % of the expected production capacity of the two main manufactures. For the RBCO tape then the wind imposed demand corresponds to the production of one of the main manufactures or about 15 % of the world marked production. This is a remarkable change from the earlier discussions of using superconductors for wind turbine generator. In 2010 it was concluded that the worldwide production of coated conductors would have to be scale up by a factor of 36 in order to provide about 10 GW of offshore wind power capacity (Abrahamsen, et al., 2010). The difference to the present scenario is a considerable smaller usage of the superconductor due to the better understanding of the impact on the generator cost and that the number of RBCO coated conductor manufactures have increased from 2 to more than 10 as seen below.

Thus the INNWIND.EU iron-cored based superconducting wind turbine generators can be supplied from the main manufactures of the wires in order to provide 10 GW of superconducting offshore wind. In case a more light weight generator topology is needed then the wire demand will increase

to about 50-200 km of MgB$_2$ wire per 10 MW generator as shown in Figure 5-21. In that case the 10 GW offshore superconducting wind power demand will exceed the current MgB$_2$ production volume by 65 %, which can most likely be solved by gradual upscaling and there is therefore no need of orders of magnitude scale upscaling. A similar conclusion is reached for the coated conductors if the tape demand per 10 MW turbine in increased by a factor of 10, but scenario studies of the coated conductor high temperature superconductor generators will have to be performed in order to determine how much more wire is needed for other topologies.

It can be concluded that the amount of wire needed to provide about 10 GW of offshore wind capacity is available for both MgB$_2$ and RBCO, but a remaining questions is if the coils manufacturing, cryostat manufacturing and cooling system manufacturing is available?

Both the MgB$_2$ and the RBCO coil demonstrations have shown that it is not easy to construct superconducting field coils that retain the superconducting properties under the operation condition of the wind turbine generator. In order to produce the 10 GW of superconducting offshore turbines holding about 32-40 field coils per 10 MW generator then a production of 32000 – 40000 superconducting coils must be manufactures over 10 years. This number is orders of magnitude from the current level and clearly calls for initiative of an industrialization. The question is if the turbine manufacturer is to take this task as part of the turbine company or if subcontracting to a sector of superconductor coil manufactures would be needed. The first approach is probably what is preferred if the coil manufacturing holds crucial intellectual properties (IP), but the last approach is probably what is needed in order to drive down the cost by competition.

A second question is if the superconducting coils can be considered as independent from the cryostat and cooling system where they must be installed? Again one can ask if the turbine company will have to manufacture the cryostats them self or if that should be subcontracted? The conclusion is probably the same as for the coils manufacturing that it will be related to IP. There is however a large difference between the cryostats needed for the iron cored topology, where the modular cryostat concept as introduced by SUPRApower (Suprapower, 2017) and the concept of ECOswing (ECOswing, 2017) or GE Global research (Fair, 2012) with one large cryostat holding all superconducting coils. The first could be considered as a serial produced product that will fit different turbine manufactures, whereas the latter is tailored to a specific turbine dictating the cryostat diameter and length. If each superconducting field coil must be placed in individual cryostats then one would again need 32000 – 40000 cryostats to make the 10 GW, which should be compared to the other case of 1000 large cryostats. A more ideal situation is most likely that many superconducting field coils are placed in a segmented cryostats that can be combined into the generator field structure. In order to reduce the segmented cryostat size below the generator diameter then one will have to segment the generator field structure into at least 3 segments and by most 6 in order to reduce the number of cryostat connections.

It should also be asked how the cooling system is connected to the cryostat(s) in order to keep the superconducting field windings at the operation temperature? The modular cryostats proposed by SUPRApower contains one cold head per 4 superconducting coils, whereby about 10000 cold heads will be needed for the 10 GW superconducting generator scenario. This number is quite high, since there were about 22000 Magneto Resonance Imaging (MRI) scanners working globally at hospitals in 2008 with one cold head in about half of them to re-condense the helium inside the cryostat back into liquid helium (zero-boil off) (Radebaugh, 2009). Thus the 10 GW superconducting generator scenario corresponds in numbers of cold heads to the MRI industry. Cold heads are however also use for cryopumps at the same scale as the MRI industry and it therefore seems possible to scale up the production to meet the superconductor wind turbine demand. The cost of the cryocoolers must however be reduced compared to the MRI application before the superconducting wind turbine generators will be feasible. Another issue with the cryocoolers is a usual maintenance interval of about 3-5 years, where regular replacement procedures must be implemented.

An alternative to the cold head solution is to use larger size cooling machines like the Stirling cooler or Turbo Brayton coolers, whereby one might be able to reduce the number of devices to 1 machines per turbine or 2 in order to have redundancy. This is the methods outlined for the INNWIND.EU high temperature superconductor solution in section 8.3. In the case of the front mounted INNWIND.EU superconductor generator one could consider to place the entire cryogenic system inside the armature structure and for the Turbo Brayton it might be possible to place it in a rotating frame, whereby only power have to be transferred into the rotating frame. The advantage of the Turbo Brayton cooling machine is also the very low requirement for maintenance, since the machine is based on magnetic bearings. The cost is however a challenge.

Finally the critical material usage of the superconducting generator should be compared to the alternatives such as the permanent magnet direct drive (PMDD) generator. The RBCO coated conductor high temperature superconducting $RBa_2Cu_3O_{6+x}$ tapes are based on rare earth elements with R = Gadolinium (Gd) or Yttrium (Y) as the preferred choices. The strong $R_2Fe_{14}B$ permanent magnets used for the PMDD generator are often based R = Neodymium (Nd) and Praseodymium (Pr) with addition of R = Dysprosium (Dy) in order to increase the coercivity of the magnets at the relative high operation temperature around 100-120 ^{o}C of PMDD generators. Thus the critical material of the two technologies are different segments of the rare earth elements and will therefore be decoupled. Secondly the amount of rare element materials that is needed for the two technologies is very different. The coated conductor holds a 1 micrometer thin layer of the high temperature superconductor, which gives a RBCO volume of $V_{RBCO} \sim 10^{-6}$ m x $1.2 \cdot 10^{-2}$ m x 5350 m = $6.4 \cdot 10^{-5}$ m$^3 \sim$ 64 cm^3 for the entire 10 MW high temperature superconducting generator outlined in section 7.2. The mass of the critical material is therefore less than 1 kg for the entire 10 MW generator, since the mass density of RBCO is about 5 g/cm^3 (Abrahamsen, et al., 2010). The mass of $R_2Fe_{14}B$ magnets needed for the PMDD is in the order of 0.6 ton/MW (Polinder, Bang, van Rooij, McDonald, & Mueller, 2007). This amount to 6000 tons of $R_2Fe_{14}B$ needed to provide 10 GW of offshore wind power as shown in Figure 10-1 and should be compared to a demand of 1 ton of RBCO high temperature superconductor (not plotted). In case of the MgB$_2$ wire then the raw materials magnesium and boron are not considered as critical materials, but larger quantities are needed as indicated in the figure for an air-cored as well as for an iron-cored 10 MW MgB$_2$ generator. The reason that the Rare Earth elements are considered critical for Europe is that mining and processing of the heavy rare earth elements are completely dominated by Chinese sources (Kooroshy, Tiess, Tukker, & Walton , 2015).

Based on the road map analysis it is concluded that the superconducting wire production volume is sufficient to provide 10 GW of superconducting wind turbine generators, but an industrialization of the coil and cryostat manufacturing is needed. Secondly it is still an open question, which cooling system is the best for the superconducting wind turbine generators and this will have to be linked to the down-selection of the generator topology as well as the maintenance contribution to the Levelized Cost of Energy (LCoE).

(INNWIND.EU, Deliverable 3.11, Superconducting generators)

Material	Company	Capacity [km/year]	Wire length [m]
MgB$_2$	Columbus Superconductors (Italy)	3000	5000
	HyperTech (USA)	10000	4000
RBCO	American Superconductors (USA)	1000	1000
	Superpower (USA/Japan)	1000	1000
	STI (USA)	750	1000
	METOX (USA)		
	SuperOX (Russia)		500
	Theva (Germany)	150	600
	Bruker (Germany)	25	600
	Deutche Nanoschict / BASF (Germany)	200	100
	SUNAM (Korea)	1000	500
	Fujikura (Japan)		500
	Shanghai Superconductor technology (China)		

Table 10-1 List of manufactures of MgB$_2$ wire and RBa$_2$Cu$_3$O$_{6+x}$ (RBCO) high temperature superconducting coated conductor tapes (Noe, 2016). The approximate wire production capacity and wire piece length by 2016 is listed (collected from contribution to CCA2016 (CCA2016, 2016)).
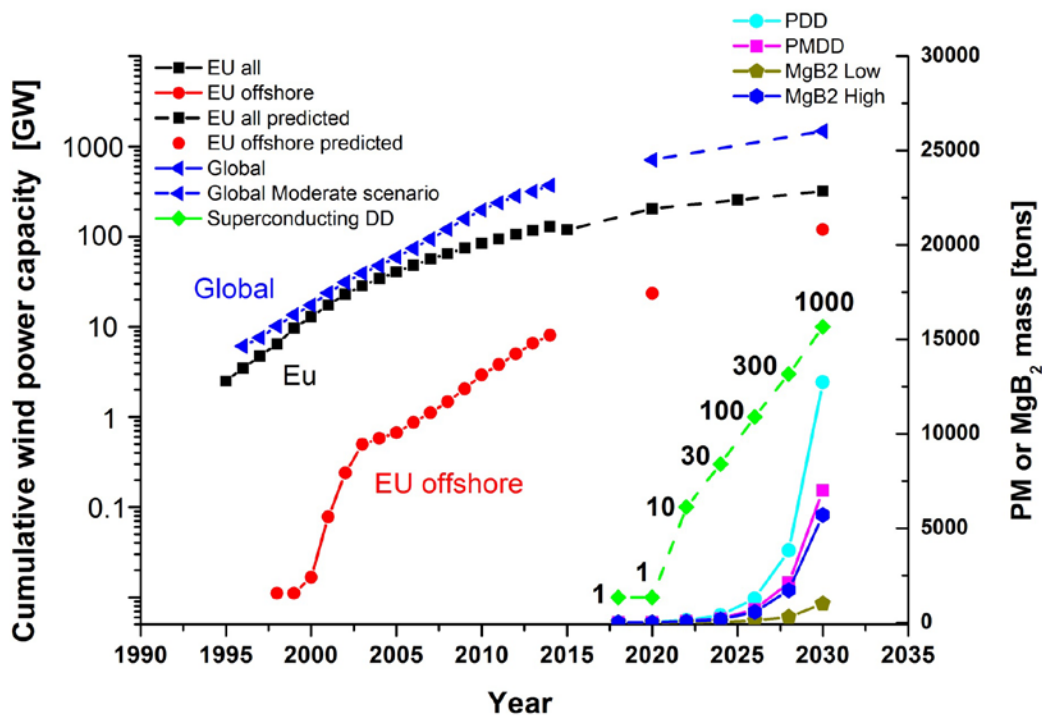
Figure 10-1 Historic wind power capacity of Europe and the world as well as predicted development until 2030. A scenario of the introduction of superconducting direct drive (SCDD) has been added by assuming the first 10 MW SCDD is installed in 2018 (green), the next in 2020, then 10 turbines by 2022, 100 turbines by 2026 and finally 1000 turbines by 2030. The mass of active materials needed for the MgB$_2$ generators is shown on the right hand axis and is also compared to the mass of Nd$_2$Fe$_{14}$B permanent magnets needed for the equivalent magnetic Pseudo Direct Drive (PDD) and the Permanent Magnet Direct Drive (PMDD) generators. Reproduced from (Abrahamsen, Liu, Magnusson, & Polinder, 2015).

(INNWIND.EU, Deliverable 3.11, Superconducting generators)

10.2 Philosophy of twice shear force density of Permanent Magnet Direct Drive (PMDD)

In the previous section it was shown that superconducting wind turbine generators can be built with the current superconducting wire and tape technology, but as also indicated in section 5.6 and 7.2, then the iron-cored generators targeting the lowest Levelized Cost of Energy (LCoE) will most likely not be light weight enough to outperform the Permanent Magnet Direct Drive (PMDD) generators. There is no question that superconductors can provide very light weight generators as shown in 5.6, but they are currently too expensive for the wind turbine application.

What will it take for the superconducting direct drive generators to become competitive with the PMDD?

Well the SCDD will probably have to provide something that is currently hard to obtain with the PMDD, but at the same cost.

The main property to target is the generator efficiency, but here the design of the cryogenic system can have a large impact.

The second property is probably the shear force density of the generator, because the superconducting field winding can be used to increase the magnetic flux density in the air gap beyond the saturation flux density of the magnetic steel laminates used in the iron-cored topology proposed for the INNWIND.EU superconducting generators. The shear force density will be related to the size of the active material of the generator and thereby also to the mass.

This design philosophy of increasing the magnetic flux density in an electrical machine is quite different from what is usually done, because full saturation of the magnetic steel laminates is often avoided by all means. In order to understand how the different topologies outlined in section 5.1 would behave in case of more powerful superconductors then a study was conducted, where it was asked how to obtain twice the shear force density in the SCDD as compared to the PMDD by increasing the current carrying capacity of the superconductors (Liu, polinder, Abrahamsen, & Ferreira, 2017) and (Appendix A). The current carrying capacity of the superconducting field winding were specified by the total excitation current of the field winding being the product of the number of windings and the current in each wire (often called the ampere-turns of the winding). This quantity was increased for a typical pole configuration with a pole pitch of 0.4 m without considering the choice of the superconductor nor the operation temperature. The impact on the shear stress of the different topologies could be obtained as shown in Figure 10-2. It is seen that iron-cored topology T12 is providing the largest shear stress with the least excitation current and is reaching twice the shear stress of the Permanent Magnet Direct Drive (PMDD) at I_{EX} = 200 kA-turns. Similarly the air cored technology T1 is first reaching twice the shear stress of the PMDD at I_{EX} = 750 kA-turns, which is indicating a need of 4 times as much wire, 4 times as much current in each wire or 2 times as much current and 2 times more wire. The shear stress is plotted up to extremely high and also unrealistic values in order to investigate the limit of fully saturated iron machines. It is seen that the iron-cored topologies are showing an un-linear increase of the shear stress at low excitations due to the saturation of the iron, whereas the air-cored topology is linear in the response.

The obtained shear stresses of the topologies were used to determine the performance of 10 MW superconducting direct drive generators with different diameters and length by fixing the pole pitch, but just increasing the pole pair number to match the diameter. Figure 10-3 shows the generator loss as function of the field excitation and the vertical dashes lines indicate a loss level of 2 % (200 kW) and 3 % (300 kW). It is seen that the losses can be decreased with higher field winding excitation, because the superconductor is producing more magnetic flux and the amount of current in the armature can be reduced. The loss limit of 3 % can be reached for all topologies based on an armature current density of 3 A/mm², but the 2 % loss limit cannot be met by all. Decreasing the armature current density to 2 A/mm² is however opening up for that. Based on this map of losses one can link the different topologies to the excitation demand. It should be

(INNWIND.EU, Deliverable 3.11, Superconducting generators)

noted that the cryogenic cooling losses should be added to the values of Figure 10-3. Figure 10-4 is showing how the stack length is scaling with excitation current for the different topologies and Figure 10-5 is showing how the active mass of the 10 MW generator topologies are scaling. Here it is seen that the iron-cored topology T12 is showing the lowest active mass for field excitation currents up to I_{EX} = 200 kA. At I_{EX} = 300 kA then the active material mass for all topologies are equal $m_{SC, 6m}$ = 70 ton for D = 6 m, $m_{SC, 10m}$ = 50 ton for D = 10 m and, $m_{SC, 14m}$ = 40 ton for D = 14 m. The permanent magnet direct drive in (Polinder, Bang, van Rooij, McDonald, & Mueller, 2007) is indicating m_{PMDD} = 65 ton for a D_{gen} = 10 m and L_{stack} = 1.6 m. Thus the active mass is decreasing below the equivalent PMDD and the shorter generator length of for instance the T12 with $L_{gen, T12}$ ~ 0.5 m showing the result of the higher shear stress. For higher excitation currents then the more air-cored generators have lower weight, but it is seen that the weight reduction is relatively small.

With the above analysis one can see that twice the shear force density is possible to a loss level of 2 %. Tracking these generator properties one can determine the properties that is demanded from the superconducting winding and whereby the possible selection of the different superconductors available. This is done by choosing a proper cross sectional area of the field winding being either 20 mm x 20 mm or 40 mm x 40 mm and then determining the magnetic flux density at the edge of the superconducting winding. From that the current density of the field winding can be plotted along with the operating magnetic flux density on top of the engineering current density of commercial available superconductors. This analysis is shown on Figure 10-6, where the operations points of the T12, T9, T8 and T5 are indicated with ellipses for a 40 mm x 40 mm field winding cross section. The span along the field axis is indicating the perpendicular magnetic flux density as the lower limit and the average magnetic flux density as the upper limit.

It is seen that the iron-cored topology T12 can be realized using all the types of superconductor, but moving for more air cored type like T8 then MgB_2 will have to provide improved superconducting properties. The MgB_2 engineering critical current density as obtained for the INNWIND.EU demonstration coil is shown as well as some short length wire properties of the experimental samples. Here the experimental values of MgB_2 are corresponding to the 4 x J_E scenario discussed in 5.3, but such values were not available in long length at the time of the INNWIND.EU wire purchase. It is also noticed that the T9 and T5 topologies with a loss level of 2 % and shear force density of twice the Permanent Magnet Direct Drive (PMDD) generator level cannot be obtained even with the experimental MgB_2 wire.
The RBCO coated conductor can be used to realize both the T12 and the T8 topology with the present superconducting properties, but it should be noticed that recent work have resulted in a 4 x times improved RBCO tape, which will also allow the realization of the T9 and T5 topology (REACT, 2016). Finally it is seen that the low temperature superconductor NbTi and Nb_3Sn have no problem in realizing all the topologies.

Based on the above analysis then it is concluded that MgB_2 is most suited for the iron cored topologies, whereas the RBCO coated conductor opens up for a larger design space. Based on the current cost of the superconductors then it is also seen that MgB_2 will probably be the cheapest wire technology to realize the superconducting wind turbine generators now, but that the RBCO coated conductor hold a large potential if the tape cost is reduced in the future.

(INNWIND.EU, Deliverable 3.11, Superconducting generators)
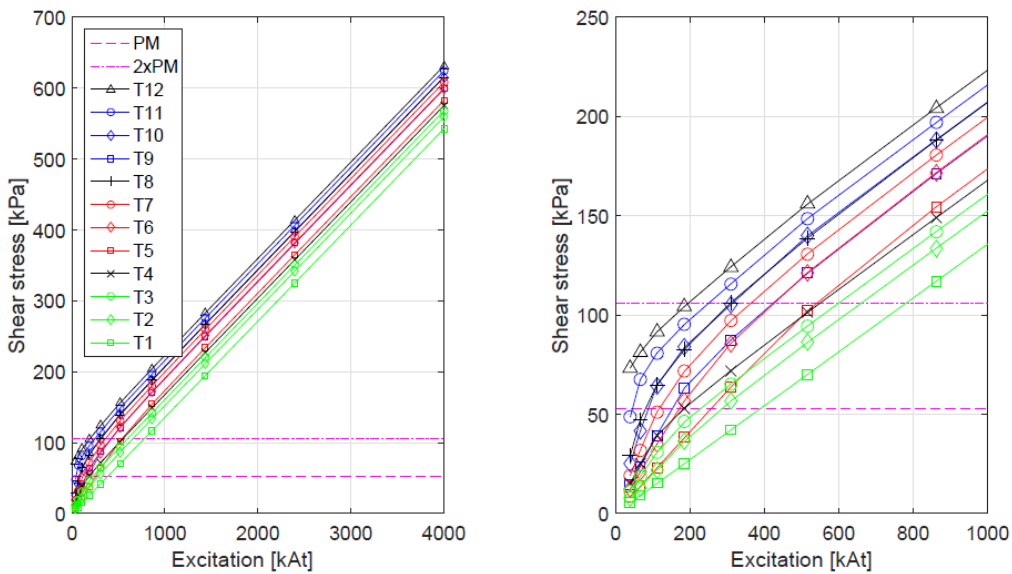
Figure 10-2 Shear stress evaluation of superconducting topologies T1 (fully air cored) to T12 (fully iron-cored) as function of the excitation current of the field winding quantified by the Ampere-turns. The two horizontal lines indicate the usual shear stress level of a permanent magnet direct drive generator (PM) as well as the target of the superconducting direct drive being twice the shear stress level of the PMDD (2 x PM). Reproduced from A7.3 (Liu D. , 2017).

(a) 3 A/mm^2, 6.11 m   (b) 3 A/mm^2, 10.19 m   (c) 3 A/mm^2, 14.26 m

(d) 2 A/mm^2, 6.11 m   (e) 2 A/mm^2, 10.19 m   (f) 2 A/mm^2, 14.26 m
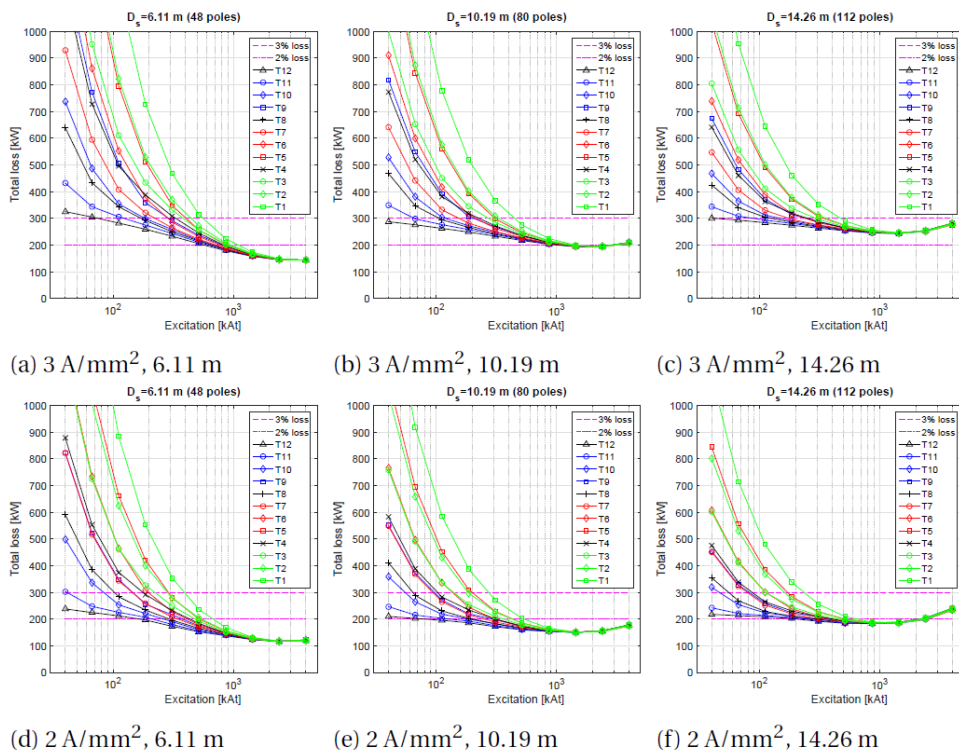
Figure 10-3 Evaluation of the superconducting direct drive generator loss as function of the field winding excitation current for 10 MW generators with a diameter of D_{gen} = 6.1 m, 10.2 m and 14.3 m as well as armature winding current densities of J_S = 2 A/mm² and 3 A/mm². The two horizontal lines indicate a 2 % and 3 % generator loss. Reproduced from A7.6 (Liu D. , 2017).

(INNWIND.EU, Deliverable 3.11, Superconducting generators)

(a) 6.11 m   (b) 10.19 m   (c) 14.26 m
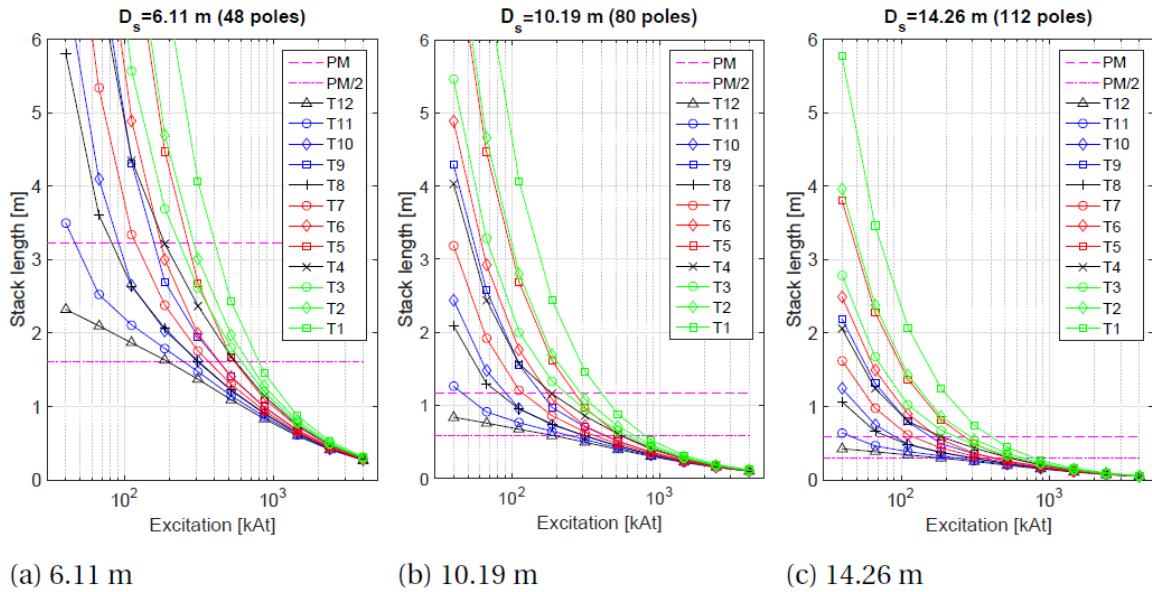
Figure 10-4 Stack length of 10 MW superconducting direct drive generator with topologies T1 to T12 as function of excitation current of the field windings. The two horizontal lines indicate the usual permanent magnet direct drive generator length as well as half of that. Reproduced from A7.8 (Liu D. , 2017).

(a) 6.11 m   (b) 10.19 m   (c) 14.26 m
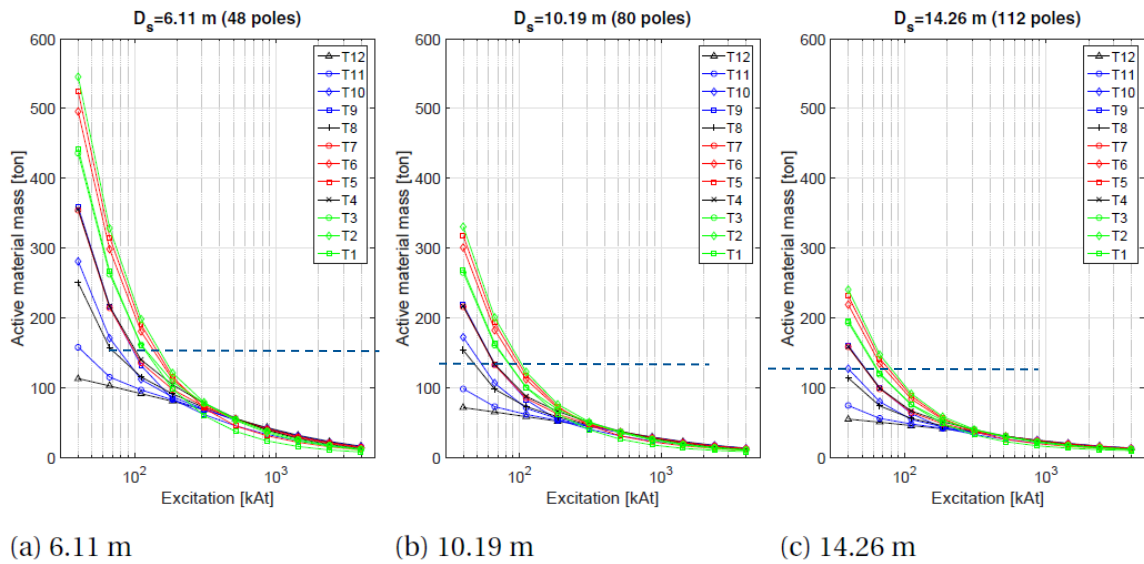
Figure 10-5 Active material mass for 10 MW superconducting direct drive generators with topologies T1 to T12 as function of the excitation current of the field winding. Dashes horizontal lines indicate when the topologies show the same active mass. Reproduced from A7.9 (Liu D. , 2017).

(INNWIND.EU, Deliverable 3.11, Superconducting generators)
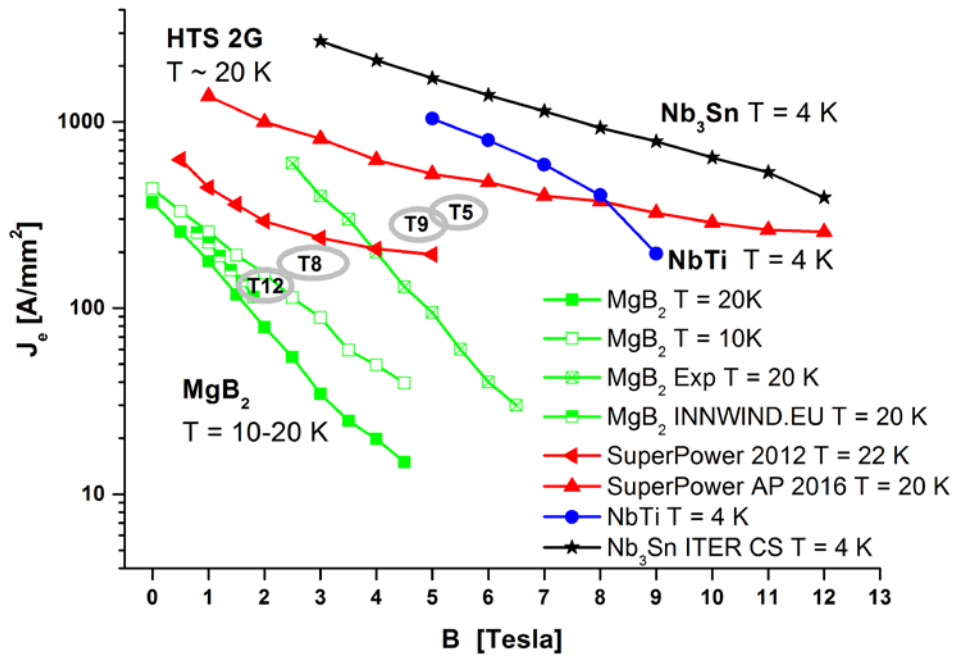
Figure 10-6 Mapping of 10 MW superconducting direct drive generators onto the engineering critical current density as function of magnetic flux density for the main commercial superconducting wires. Reproduced from A7.10 (Liu D. , 2017).

(INNWIND.EU, Deliverable 3.11, Superconducting generators)

10.3 Disruptions?

It is indicated in the present report that the choice of generator topology and cooling system for superconducting wind turbine generators is not clear in order to beat the permanent magnet direct drive generator. Thus one could ask what will happened if a much more powerful superconductor is discovered tomorrow?

Well first of all one might ask what the chance of finding a new superconductor is and what kind of properties could be imagined?

Figure 10-7 is showing the irreversibility field B_{Irr} of most of the commercial superconductors used for the INNWIND.EU generators as function of operation temperature. B_{Irr} is indicating the transition where the critical current of the superconductor decreases to zero and above this field the superconductor can no longer support a loss free current. They are however still superconducting, but some tube shaped regions of rotational supercurrent called vortex lines created by the magnetic field will start to move due to the transport current and dissipate heat. A superconductor used for a generator having magnetic flux density up to several Tesla must therefore have a B_{Irr} substantially higher in order to provide sufficient critical current density. This is basically why both MgB$_2$ and RBCO must be cooled down to half of the T_C in order to be use in wind turbine generators.
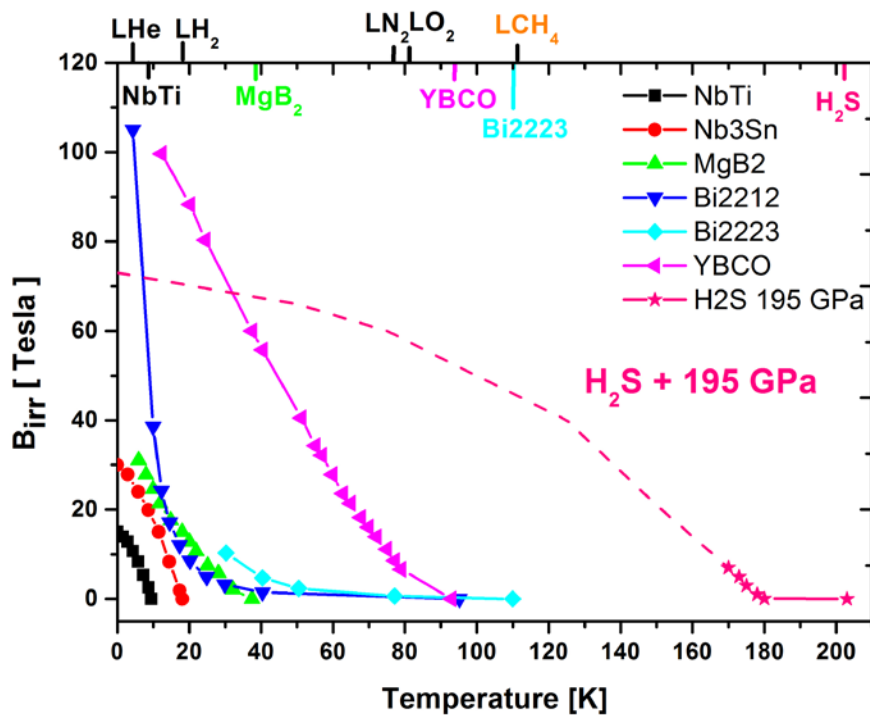
Figure 10-7 Plot of the irreversibility field B_{Irr} above which the critical current of most commercial superconductors is vanishing as function of the operation temperature. The critical temperature T_C, where the superconducting phase is first established, is indicated below the top axis and boiling points of the liquid form of most common gasses are indicated above the top axis. On top of that is a plot of the upper critical field B$_{C2}$ of the gas H2S frozen to the solid state and exposed to a very high pressure of 195 GPa as reported by Drozdov *et. al.* in Nature in 2015 (Drozdov, Eremets, Troyan, Ksenofontov, & Shylin, 2015). The critical temperature of T_C = 203 K is observed as well as a substantial $B_{Irr} \sim$ 10 T at T = 170 K. Based on previous plot from (Jensen, Mijatovic, & Abrahamsen, Development of superconducting wind turbine generators, 2013).

(INNWIND.EU, Deliverable 3.11, Superconducting generators)

It seems that the main challenge remaining for the superconducting direct drive generator is to decrease the cost of the cryogenic system, while demonstration a sufficient reliability of the cooling system. In that context it would be very beneficial to increase the operation temperature and the plot of Upper critical field B_{C2} of the new superconductor H_2S in Figure 10-7 is therefore interesting, since the critical temperature is T_C = 203 K (Drozdov, Eremets, Troyan, Ksenofontov, & Shylin, 2015). It should be said that H_2S is a gas and that it must be cooled down and exposed to a large pressure, before it becomes superconducting. Thus it will not be possible to make a wire out of this material, but it proves that materials with a critical temperature of T_C = 203 K (-70 ^{o}C) do exist. If we apply the rule of thumb that one would have to cool down to ½ of T_C to use it for a generator then a T = 100 K operation might be possible. The cryostat and cooling system for T = 100 K is much easier to make than designing a T = 20-30 K cryostat, which is the target temperature of INNWIND.EU generators.

The discovery of H_2S is maybe not of large practical importance, since it is not possible to make a wire out of it, but it is important input to the discussion of how high a critical temperature T_C that is predicted from theoretical solid state physics. For 75 years after the discovery of superconductivity in 1911 it was stated that T_C would never exceed about 25 K, but with the discovery of the HTC ceramic superconductor like the $RBa_2Cu_3O_{6+x}$ (RBCO) used in the coated conductors the limit was challenges by a T_C = 93 K. It was clear that a new theory was needed to explain the superconducting state of the RBCO compound and this theoretical explanation is still not present today. It did however also start a discussion if a room temperature superconductor would be possible based on the old theory and it was argued that light elements like hydrogen, might become a room temperature superconductor if frozen and pressed. The H_2S is now giving experimental evidence to this idea and it is believed that a room temperature superconductor is possible (Kresin, 2017).

One could ask if any cryostat design effort on superconducting wind turbine generators is wasted if a new superconductor is found and the answer is no, since the $T_{operation}$ = ½ T_C will most likely still apply. Thus a room temperature superconductor will most likely need a cryostat for $T \sim 140$ K, which is very similar to a T = 100 K cryostat since a thermal isolation preventing condensation of water or the collection of ice will still be needed as long the operations temperature is substantially below the freezing point of water. Increasing the operation temperature of a 20-30 K cryostat and cooling system of a superconducting wind turbine generator to about 100 K will only make the design easier and less costly, whereby the performance of the generator is expected to improve. In order to get rid of the cryostat and cooling system one would need to find a superconductor with a T_C in the order of 600 K and that might require a lot of patience.

(INNWIND.EU, Deliverable 3.11, Superconducting generators)

11 CONCLUSION ON SUPERCONDUCTING WIND TURBINE GENERATORS

The INNWIND.EU task on superconducting direct drive wind turbine generator has investigated the following series of technical challenges of superconducting wind turbine generators

1) **Which superconducting direct drive generator topology is providing the lowest Levelized Cost of Energy?**

   A substantial effort has be done to establish a method for optimizing superconducting direct drive wind turbine generators for offshore installation in 50 m of water with the lowest Levelized Cost of Energy (LCoE) based on a series of material cost specifications. It has been found that the Iron-cored topologies are providing the lowest LCoE with the current properties of MgB_2 and RBCO coated conductors (section 5).

2) **Can superconducting wires be wound into operational field coils for a superconducting wind turbine generator?**

   Two coil demonstrations have shown that it is possible to make field winding coils, but it was also found that industrialization is needed to increase the Manufacturing Readiness Level (MRL) of the technologies (section 5.3).

3) **Will the AC losses in superconductor associated with operation in a direct drive wind turbine generator cause unacceptable low efficiencies?**

   It has been shown that the AC losses of MgB_2 in direct drive generator are small in comparison to the other losses of the generator (Appendix A section 4) and that will not excluded the usage of superconductor for direct drive wind turbines.

4) **Is it possible to limit the short circuit torque of superconducting direct drive wind turbine generators?**

   It has been shown that segmentation of the generator into 4 segments can solve this problem and little extra cost associated with the power converter is foreseen (section 6.2).

5) **Will the low frequency of superconducting generator demand more expensive power converters due to higher losses?**

   It has been found that this will not be the case and a cost of ~ 80 k€/MW is expected for the power converters for the superconducting generator both for the segmented and non-segmented case (section 6.2).

6) **Can a superconducting generator be integrated with the kingpin nacelle in a front mounted position?**

   This has been examined for the iron cored MgB_2 superconducting direct drive generator and aero elastic load simulations have indicated that the 10 MW turbine can be realized with further engineering work in the kingpin bearing design. Secondly it has been found that the difference of cost of the structural mass supporting a front or back mounted superconducting generator is small (section 8).

(INNWIND.EU, Deliverable 3.11, Superconducting generators)

The following feasibility challenges have also been investigated:

7) **Will "a light weight" generator result in large cost savings of the remaining turbine structure?**

   In the case of the INNWIND.EU 10 MW offshore turbine and jacket foundation it was found that the turbine excitations were coinciding with a resonance of the foundation. Thus reducing the weight would move the resonance closer to the excitation and thereby reduce the lifetime of the foundation considerably. Thus it was concluded that reducing the generator weight would not be beneficial. This frequency overlap was later removed by redesign, but is has been shown that improving generator efficiency and operation and maintenance cost of the superconducting generator is expected to have the largest impact on the Levelized Cost of Energy (LCoE) (section 4).

8) **Will the active generator mass of the SCDD with the lowest LCoE be lower than the active mass of Permanent Magnet Direct Drive (PMDD) generators?**

   The current path to the lowest LCoE for the superconducting machines is to introduce as much magnetic iron in the generator and thereby reduce the usage of superconductor. This result in active masses being higher that what is expected from the PMDD generator (section 5).

9) **Will the iron cored superconducting direct drive generator resulting in the lowest LCoE be lower than the LCoE of the Permanent Magnet Direct Drive generators?**

   No, not yet. The cost of the cryogenic cooling system and the cryostats of the superconducting direct drive generators are larger than the cost of the superconductors in the case of MgB_2 and will most like also be in the future for RBCO. Thus it is proposed to compare the cost of the permanent magnets of the PMDD with the combined cost of superconductors, cryostat and cooling system in order to determine if the SCDD is competitive. It has been shown that a $R_2Fe_{14}B$ permanent magnet cost of $C_{PM} > 114$ €/kg is needed before the current 10 MW MgB_2 INNWIND.EU generator becomes competitive (see section 9). The current world market cost of the $R_2Fe_{14}B$ magnets is estimate to be about a factor of 4 lower that the criteria above.

11.1 MgB_2

Detailed optimization studies of the MgB_2 direct drive generators have been performed and designs for 10 MW and 20 MW have been obtained using an iron-cored topology to reduce the Levelized Cost of Energy (LCoE). The generators have been integrated into the kingpin nacelle in a front mounted version and the Rotor Nacelle Assembly (RNA) mass has been determined. It is found that the RNA is scaling slightly better than the INNWIND.EU reference turbines.

The cost of the iron cored MgB_2 generators is however not expected to be competitive to the Permanent Magnet Direct Drive (PMDD) generator, because the cost of the cryogenic cooling system and the cryostats must be added to the superconductor and then compared to the cost of the $R_2Fe_{14}B$ permanent magnet material. With the current MgB_2 wire cost of 4 €/m then the cost of the $R_2Fe_{14}B$ permanent magnet material will have to go beyond 114 €/kg compared to the level about 4 times lower today. Reducing the cost of the superconductor will not change this much, since the cryostat and cooling system are more expensive than the superconductor is. Thus further work is needed to reduce the cost of the cryostat and cooling system of the superconducting direct drive generators.

The weight of the active material of the iron cored MgB_2 direct drive generator is higher than for the PMDD, since heavy iron is added to decrease the amount of expensive superconductors. It has

(INNWIND.EU, Deliverable 3.11, Superconducting generators)

been investigated if more light weight designs can attain a lower Levelized Cost of Energy (LCOE) and this seem to become the case if either the cost of MgB_2 is reduced by a factor of 4 to 1 €/m, if the critical current density as function of magnetic field is increased by a factor of 4 up to a few Tesla of applied field or if both the scenarios will take place. These more light weight generator topologies will open up the design space for the cryostats, but the cryostats will have to be equipped with stronger force transmitting parts. Thus it has not been possible to select a clear winning superconducting direct drive generator topology in terms of the low LCOE and a light weight.

An MgB_2 high field race track field coil with an opening of 0.3 m and a straight section of 0.5 m have been designed, constructed and tested at $T \sim 20$ K. It was found that the coil reached the predicted operation current, but it was also found that 3 out of the 10 double pan-cake coils showed a section with a resistive signature and 8 out of 10 coils contained segment of weak superconducting properties. Further tests are undertaken to clarify if these weak segments can be related to the INNWIND.EU winding procedure. The race track coil was quenched as part of the testing and this resulted in a burnout of the connections between two of the coils. The remaining coils were subsequently tested again, whereby the initial properties were re-observed. This is indicating that the coil design is conceptually correct, but the manufacturing problems resulting in the weak superconducting segments must be solved in future work. It is believed that the high field MgB_2 coils demonstrated in the INNWIND.EU project is one of the largest high field MgB_2 coils ever build and based on that the Technology Readiness Level of the technology is estimated to be TRL = 4 (Component validation in laboratory environment).

11.2 High Temperature superconducting coated conductors

The high temperature superconducting direct drive generators have been investigate by Siemens Wind Power and it is found that the cost of the RBCO coated conductor will have to be reduced by a factor of 10 to a level of 10 €/m, before the technology is competitive with the Permanent Magnet Direct Drive (PMDD) generator technology of Siemens Wind Power.

Secondly it is concluded that the weight of the active materials of the iron-cored high temperature superconducting generator topology will be higher than of the PMDD even if the superconductor cost is reduced towards zero. It has been shown that much lower weight topologies can be obtained using the high temperature superconductors, but the cost is too high.

A RBCO coated conductor race track coil consisting of 3 single layer coils with an opening of 0.12 m and an straight section of 0.3 m has been demonstrated at $T = 30$ K and 77 K. The coils passed the $T = 77$ K test, but one of the single layer coils shown degradation when cooled to $T = 30$ K. The critical current was ramped to 69 % of the design current after which AC loss measurements were done. Based on the manufacturing difficulties then the Technology Readiness Level (TRL) of the RBCO coil technology is estimated to be TRL = 4 (Component validation in laboratory environment). Further work on industrialization of the coil manufacturing is needed before the TRL can be raised.

(INNWIND.EU, Deliverable 3.11, Superconducting generators)

12 OUTLOOK

Based on the findings of the work on superconducting direct drive wind turbine generators the following recommendations are given for further work:

1) Superconducting direct drive generators can still not compete with the Permanent Magnet Direct Drive (PMDD) generator due to the high cost of the cryostat and cooling system. The superconducting wires in terms of NbTi, Nb_3Sn and MgB_2 seem to be cheap enough (some reduction of MgB_2 will be beneficial), but the high temperature superconducting tapes will need cost reductions, which up-scaling to mass production should allow. Thus effort on how to design, construct and test the cryostat and cooling system for superconducting generators is the main barrier and further work is needed where the wind turbine environment is projected onto the superconducting coils, cryostat and cooling system to test their reliability. It has not been possible to down select a single generator topology providing the lowest Levelized Cost of Energy (LCoE) in the present work if more powerful superconductors than MgB_2 are taken into account. The choice of generator topology, cryostat and cooling system most likely have to be selected using a multi physics optimization approach searching for the lowest Levelized Cost of Energy. The competition from the PMDD with current magnet costs around 30 €/kg is however very tough. The reader is referred to the final comparison in deliverable report D3.44 of the drive trains of the electromechanical work package to obtain the quantitative differences in the LCOE of the MgB_2 superconducting generators presented in this report and several reference drive trains (Abrahamsen, Liu, & Polinder, 2017).

2) Winding superconductors into operational generator field coils has been shown to be difficult and with high failure rates in the INNWIND.EU demonstrations. In order to provide about 40000 superconducting field coils in a 10 year period to provide 10 GW of offshore wind turbines then industrialization of the superconductor coil manufacturing is needed. The same is true for the cryostat and to some extend the cooling system. Here a major questions is if the industrialization should be done by some wind turbine manufacture including coil manufacturing, cryostat construction and cooling system installation into their generator activities or if it can be done by the industrial sectors with in the superconducting and cryogenic industry supplying sub-components to the wind industry. Thus the discussion if to use modular cryostats versus one (few) large cryostat(s) with the same size as the generator have to be settled. The first investigation of this question will be answered by comparing the outcome of the EU projects SUPRApower (MgB_2) (Suprapower, 2017) and ECOswing (RBCO coated conductors) (ECOswing, 2017).

3) It has become clear that the possible "light weight" properties of superconducting direct drive generators is not giving a considerable impact on the LCoE. Thus light weight is just "nice to have" if the generator is as cheap as the alternatives. The main focus of the superconducting machines should therefore be the efficiency (including availability) and on the cost. It has been shown that the minimum loss of a partial superconducting direct drive generator, which also have a high shear force density of twice the level of a PMDD, is around 2 % before adding the cryogenic losses. If this should be decreased even further then the fully superconducting direct drive generators with also the armature being wound from superconducting wire could be considered. Such machines will however have a more complicated cryostat and cooling system, which should not make the cost increase much. An advantage of such a fully superconducting machine will be a low heat dissipation in the generator structures and thereby a possible much lower operation temperature compared the traditional direct drive generators.

4) The advantages of light weight and no magnetic field during installation have not been examined in the INNWIND.EU project, because the INNWIND.EU turbine will anyhow need very large cranes to install the remaining turbine parts and these cranes do currently not exist. The advantage of having no field in the generator during installation might however

(INNWIND.EU, Deliverable 3.11, Superconducting generators)

be beneficial, because there will be no attractive forces between the generator rings as in the PMDD. A full design of both a SCDD and PMDD as well as knowledge of installation procedures is however needed in order to evaluate this benefit.

(INNWIND.EU, Deliverable 3.11, Superconducting generators)

13 REFERENCES

Kooroshy, J., Tiess, G., Tukker, A., & Walton , A. (2015). *Strengthening the European rare earths supply chain: Challenges and policy options.* ERECON.

(AMSC), A. S. (2016, March 8). *AMSC and BASF Form Strategic Relationship to Develop Lower Cost Superconductor Wire.* Retrieved from http://ir.amsc.com/releases.cfm?Year=&ReleasesType=&PageNum=2.

Abrahamsen, A. B., Magnusson, N., Liu, D., Stehouwer, E., Hendriks, B., & Polinder, H. (2014). Design study of a 10 MW MgB2 superconductor direct drive wind turbine generator. *Proceedings of EWEA 2014 European Wind Energy Association (EWEA).*

Abrahamsen, A. B., Magnusson, N., Jensen, B. B., Liu, D., & Polinder, H. (2014). Design of an MgB2 race track coil for a wind generator pole. *Journal of Physics: Conference Series, 507,* 032001. doi:10.1088/1742-6596/507/3/032001

Abrahamsen, A., & Natarajan, A. (2016). Variation of Extreme and Fatigue Design Loads on the Main Bearing of a Front Mounted Direct Drive System. *Journal of Physics: Conference Series, 753,* 112006.

Abrahamsen, A., Liu, D., & Polinder, H. (2017). *Final assessment of superconducting (SC) and Pseudo Direct Drive (PDD) generator performance indicators (PI's).* INNWIND.EU deliverable report D3.44. Retrieved from http://www.innwind.eu/publications/deliverable-reports

Abrahamsen, A., Liu, D., Magnusson, N., & Polinder, H. (2015). Potential of MgB2 superconductors on direct drive generators for wind turbines. *Scientific Proceedings. EWEA Annual Conference and Exhibition 2015* (pp. 55-58). European Wind Energy Association (EWEA).

Abrahamsen, A., Mijatovic, N., Seiler, E., Zirngibl, T., Træholt, C., Nørgård, P., . . . Østergård, J. (2010). Superconducting wind turbine generators. *SUPERCONDUCTOR SCIENCE AND TECHNOLOGY, 23,* 034019.

Advanced Magnet Lab. (2017, July). *http://amlsuperconductivity.com/applications/energy/doe-approved-wind-turbine-solution/.*

Azar, Z., & Thomas, A. (2016). *Summary Report for Work Package 3.1.2 – Investigation of HTS Superconducting Direct Drive Generators.* INNWIND.EU deliverable report.

Bak, C., Zahle, F., Bitsche, R., Kim, T., Yde, A., Henriksen, L. C., . . . Hansen, M. (2013). *Description of the DTU 10 MW Reference Wind turbine.* Roskilde: INNWIND.EU Deliverable 1.21 Reference Wind Turbine Report.

Berger, F., Sørensen, J., Gintautas, T., Kühn, M., & Kraft, M. (2015). *System design assessment for innovative support structures.* INNWIND.EU deliverable report D1.35.

CCA2016. (2016, September 11-14). Coated Conductors for Applications 2016: Workshop Presentations. Aspen. Retrieved from https://nationalmaglab.org/magnet-development/applied-superconductivity-center/asc-resources/coated-conductors-for-applications-2016

Chaviaropoulos, P., Sieros, G., Lekou, D., Bacharoudis, K., Tibaldi, C., Barlas, T., . . . Armendariz, J. A. (2015). *PI-based Assessment on the Results of WP2-WP4. Ongoing Integration Action.* INNWIND.EU deliverable D1.24.

Chen, Z. (2014). *D3.31 Power electronics tailored to SC and PDD generators.* INNWIND.EU deliverable report.

Columbus Superconductors SpA. (2017). *www.columbussuperconductors.com.*

D. Liu, H. P. (2017). Topology Comparison of Superconducting Generators for 10-MW Direct-Drive Wind Turbines: Cost of Energy Based. *IEEE TRANSACTIONS ON APPLIED SUPERCONDUCTIVITY, 27*(4), 5202007.

DanskVindmølleIndustri. (2016, November 9). *http://www.windpower.org/da/aktuelt/aktuelt_i_vindmoelleindustrien/news_q4_2016/kystnaere_havvindmoeller_fortsat_billigst.html.*

de Vries, E. (2013, September 9). Close up - Vestas V164-8.0 nacelle and hub. *Wind Power Mountly.*

Dong Energy A/S. (2017, April 13). *http://www.dongenergy.com/en/media/newsroom/company-announcements-details?omxid=1557851.*

(INNWIND.EU, Deliverable 3.11, Superconducting generators)

Drozdov, A., Eremets, M., Troyan, I., Ksenofontov, V., & Shylin, S. (2015). Conventional superconductivity at 203 kelvin at high pressures in the sulfur hydride system. *Nature, 525*, 73.

ECOswing. (2017, July). *ECOswing*. Retrieved from https://ecoswing.eu/project.

Fair, R. (2012). *Superconductivity for Large Scale Wind Turbines.* GE, General Electric – Global Research, Niskayuna, US. Niskayuna: Department of Energy (DOE), US.

Guan, Y., Zhu, Q., Azar, Z., Thomas, A., Vedrenõ-Santos, F., Li, G., & Odavic, M. (2017). Comparison of Electromagnetic Performance of 10MW Superconducting Generators with Different Topologies for Offshore Direct-Drive Wind Turbines. *IEEE transaction on Superconductivity*, Accepted.

Hassan, G. G. (2013). *A Guide to UK Offshore Wind.* Scottish Enterprise and The Crown Estate.

INNWIND.EU. (2017, April). Retrieved from http://www.innwind.eu/

ITER. (2017, June). *https://www.iter.org/mach/magnets*.

Jensen , B., Mijatovic, N., & Abrahamsen, A. (2013). Development of superconducting wind turbine generators. *JOURNAL OF RENEWABLE AND SUSTAINABLE ENERGY 5, 023137 (2013)*, 023137.

Jensen, B., Mijatovic, N., & Abrahamsen, A. (2013). Development of superconducting wind turbine generators. *JOURNAL OF RENEWABLE AND SUSTAINABLE ENERGY, 5*, 023137.

Kalsi, S. S. (2014). Superconducting Wind Turbine Generator Employing MgB2 Windings Both on Rotor and Stator. *IEEE TRANSACTIONS ON APPLIED SUPERCONDUCTIVITY 24*, 5201907.

Kresin, V. (2017, July). Road to Room Temperature Superconductivity: Hydrides and Other Systems. *IEEE/CSC & ESAS SUPERCONDUCTIVITY NEWS FORUM (global edition)*.

Liu, D. (2017). *INCREASING THE FEASIBILITY OF SUPERCONDUCTING GENERATORS FOR 10 MW DIRECT-DRIVE WIND TURBINES* (ISBN 978-94-6299-627-4 ed.). Delft: Delft University of Technology. Retrieved from http://repository.tudelft.nl/.

Liu, D., polinder, H., Abrahamsen, A., & Ferreira, J. (2017). Potential of Partially Superconducting Generators for Large Direct-Drive Wind Turbines. *IEEE TRANSACTIONS ON APPLIED SUPERCONDUCTIVITY, 27*(5), 5203711.

Magnusson, N., Hellesø, S., Paulsen, M., Eliassen, J., & Abrahamsen, A. (2016). *Fabrication of MgB2 Coils – A superconducting generator pole demonstrator.* Roskilde, Denmark: INNWIND.EU deliverable report.

Marino, I., Pujana, A., Sarmiento, G., Sanz, S., Merino, J. M., Tropeano, M., . . . Canosa, T. (2016). Lightweight MgB2 superconducting 10MW wind generator. *Supercond. Sci. Technol. 29*, 024005.

MEGAvind. (2015). *Megavind LCOE Model - Guidelines and documentation.* Danish Wind Industry Association www.windpower.org. Retrieved from https://megavind.windpower.org/download/2452/1500318_documentation_and_guidel inespdf

Muñoz, A., Rodriguez, J., Salvatierra, C., Yagüe, J., Granados, X., López-López, J., . . . Cabista, I. (2017). Design of a new generation of Generators and ancillary systems for Wind Energy based on Superconducting materials. *SUPRApower final workshop.*

Natarajan, P. C. (2014). *D1.22 Definition of Performance Indicators (PIs) and Target Values.* INNWIND.EU deliverable.

Noe, M. (2016). Electric Power Applications of Coated Conductors – an update on recent activities and future directions. *Coated Conductors for Applications 2016 (CCA2016), 11-14 September 2016*, (pp. I0-11). Aspen.

Oerlikon. (2017, August). *https://www.oerlikon.com/ecomaXL/files/oerlikon_Cryo.pdf*. Retrieved from www.oerlikon.com.

P.K. Chaviaropoulos, I. K. (2014). *D1.23 PI-based assessment of innovative concepts (methodology).* INNWIND.EU deliverable.

Pallecchi, I., Eisterer, M., Malagoli, A., & Putti, M. (2015). Application potential of Fe-based superconductors. *Supercond. Sci. Technol. 28*, 114005.

Polinder, H., Bang, D., van Rooij, R., McDonald, A., & Mueller, M. (2007). 10 MW Wind Turbine Direct-Drive Generator Design with Pitch or Active Speed Stall Control. *Proceedings of the International Electric Machines and Drives Conference. 2*, p. 1390. IEEE.

(INNWIND.EU, Deliverable 3.11, Superconducting generators)

Radebaugh, R. (2009). Cryocoolers: the state of the art and recent developments. *J. Phys. Condens. Matter , 21*, 164219.

REACT, A.-E. (2016, June 30). *https://arpa-e.energy.gov/sites/default/files/documents/files/Brookhaven_AMSC_University%20of%20Houson_SuperPower_ImpactSheet_FINAL.pdf.* Retrieved July 2017

Siemens. (2016). The standard for offshore wind - The Siemens Offshore Direct Drive platform - incorporating three decades of engineering. Hamburg, Germany.

Snitchler, G. (2010). Progress on high temperature superconductor propulsion motors and direct drive wind generators. *The 2010 International Power Electronics Conference* (pp. 1-6). Sapporo: IEEE.

Song, X., Mijatovic, N., Kellers, J., Bührer, C., Rebsdorf, A., Hansen, J., . . . Holbøll, J. (2017). A Full-Size High-Temperature Superconducting Coil Employed in a Wind Turbine Generator Setup. *IEEE TRANSACTIONS ON APPLIED SUPERCONDUCTIVITY, VOL. 27*, 5201105.

Stautner, W., Fair, R., & et, a. (2013). Large Scale Superconducting Wind Turbine Cooling. *IEEE TRANSACTIONS ON APPLIED SUPERCONDUCTIVITY, VOL. 23,, 23*(3), 5200804.

Stehouwer, E., van Zinderen, G., & Hossain, S. (2017). *Conceptual nacelle designs of 10-20 MW wind turbines.* INNWIND.EU deliverable report D3.41.

Stirling Cryogenics. (2018). *https://www.stirlingcryogenics.com/en/markets/applications/hts-rotating-machine*. Retrieved August 2017, from www.stirlingcryogenics.com.

Sun, J., Sanz, S., & Neumann, H. (2015). Conceptual design and thermal analysis of a modular cryostat for one single coil of a 10 MW offshore superconducting wind turbine. *IOP Conf. Series: Materials Science and Engineering, 101*, 012088.

Suprapower. (2017, July). *http://www.suprapower-fp7.eu/*.

Y. Liu, R. Q. (2015). Influences of generator parameters on fault current and torque in a large-scale supersuperconducting wind generator. *IEEE Transactions on Applied Superconductivity, 25*(6), 5204309.

(INNWIND.EU, Deliverable 3.11, Superconducting generators)

14 ACKNOWLEDGEMENT

Sincerely

Asger B. Abrahamsen, Task-leader of Task 3.3 Superconducting Generators

DTU Wind Energy, Technical University of Denmark
DTU Risø Campus
Frederiksborgvej 399
DK-4000 Roskilde
Denmark
asab@dtu.dk
Mob.: +4524921613

(INNWIND.EU, Deliverable 3.11, Superconducting generators)

15 APPENDIX A: PHD THESIS OF DONG LIU

Appendix A of Direct drive superconducting generators for INNWIND.EU wind turbines:

INCREASING THE FEASIBILITY OF SUPER-CONDUCTING GENERATORS FOR 10 MW DIRECT-DRIVE WIND TURBINES

PhD thesis of Dong Liu (June 2017)

Document information

Document Name:	**Appendix A of Direct drive superconducting generators for INNWIND.EU wind turbines:**
	INCREASING THE FEASIBILITY OF SUPERCONDUCTING GENERATORS FOR 10 MW DIRECT-DRIVE WIND TURBINES – PhD thesis of Dong Liu (June 2017)
Document Number:	**Deliverable D3.11**
Author:	**Dong Liu**
Document Type	Report
Dissemination level	PU
Review:	**Asger Bech Abrahamsen and Henk Polinder**
Date:	**27 July 2017**
WP:	**Electromechanical conversion WP3**
Task:	**Task 3.11 Superconducting generator design at 10 and 20 MW**
Approval:	Approved by Task Leader

1   INTRODUCTION

This appendix holds the PhD thesis of Dong Liu on the topic "INCREASING THE FEASIBILITY OF SUPERCONDUCTING GENERATORS FOR 10 MW DIRECT-DRIVE WIND TURBINES". The work have been done as part of the task 3.11 superconducting generators in the INNWIND.EU project and will be seen as providing the details of the method on optimizing superconducting direct drive generators for the lowest Levelized Cost of Energy (LCoE) when based on the MgB_2 superconductor. The method can however be applied to other superconductors by replacing the characteristic properties of MgB_2.

Secondly a series of technical challenges such as AC losses, short circuit torque and the future potential of superconducting generators for wind turbines have been evaluated.

References to this work will be provide in the main report "Direct drive superconducting generators for INNWIND.EU wind turbines".

Increasing the Feasibility of Superconducting Generators for 10 MW Direct-Drive Wind Turbines

Increasing the Feasibility of Superconducting Generators for 10 MW Direct-Drive Wind Turbines

Proefschrift

ter verkrijging van de graad van doctor
aan de Technische Universiteit Delft,
op gezag van de Rector Magnificus prof. ir. K.C.A.M. Luyben,
voorzitter van het College voor Promoties,
in het openbaar te verdedigen op 20 juni 2017 om 10:00 uur

door

Dong Liu

Master of Science in Electrical Engineering,
Technische Universiteit Delft,
geboren te Lanzhou, Gansu, China.

Dit proefschrift is goedgekeurd door de

promotor: prof. dr. J. A. Ferreira
copromotor: dr. ir. H. Polinder
copromotor: dr. A. B. Abrahamsen

Samenstelling promotiecommissie:

Rector Magnificus,	voorzitter
Prof. dr. J. A. Ferreira,	Technische Universiteit Delft, promotor
Dr. ir. H. Polinder,	Technische Universiteit Delft, copromotor
Dr. A. B. Abrahamsen,	Technical University of Denmark, copromotor

Onafhankelijke leden:

Prof. dr. Z. Q. Zhu	The University of Sheffield
Prof. dr. G. J. W. van Bussel	Technische Universiteit Delft
Prof. dr. R. Ross	Technische Universiteit Delft
Dr. M. Dhallé,	Universiteit Twente

An electronic version of this dissertation is available at
`http://repository.tudelft.nl/`.

CONTENTS

SUMMARY

In recent years, superconducting synchronous generators (SCSGs) have been proposed as an alternative to permanent magnet synchronous generators (PMSGs). They are expected to reduce the top head mass and the nacelle size for such large wind turbines. In 2012, the INNWIND.EU project initiated this research to investigate SCSGs for 10-20 MW direct-drive offshore wind turbines. However, the feasibility of SCSGs was limited by a few critical issues, such as high costs, AC losses in the superconducting winding and excessive short circuit torque. Furthermore, SCSG designs proposed in the literature were various but all less competitive than PMSGs. There had been no agreement on the most feasible SCSG designs.

This thesis aims at increasing the feasibility of SCSGs for large wind turbines and identify the most feasible SCSG designs by investigating the following four questions:

• How to reduce the capital cost of energy of an SCSG by selecting appropriate generator topologies?

• Is the AC losses of the selected generator topologies acceptable?

• Can the short circuit torque be reduced to an acceptable level?

• What is the potential of SCSGs to have significant advantages over PMSGs?

This thesis focuses only on partially superconducting generators in which the field winding is superconducting while the armature winding is with copper conductors. This type of SCSGs is considered more feasible than fully superconducting generators for the moment. A 10 MW reference wind turbine provided by the INNWIND.EU project is used throughout this thesis.

TOPOLOGY COMPARISON BASED ON CURRENTLY AVAILABLE MGB_2 SUPERCONDUCTORS
The levelized cost of energy (LCoE) of a wind turbine using an SCSG could be much higher than that of conventional wind turbines due to the employment of costly superconducting wires and cryogenic cooling systems. The high LCoE hinders the commercialization of SCSGs for wind power industry and limits the feasibility of SCSGs. Electromagnetic designs for reducing the capital cost of energy of SCSGs are assessed by comparing twelve different generator topologies. These topologies combine iron and non-magnetic material in the rotor back core, rotor pole core, stator tooth and stator yoke. Each topology is optimized for the lowest levelized capital

cost of energy (LCCoE). The optimization applies the genetic algorithm. The optimization method combines 2D stationary finite element (FE) models and analytical models to calculate the active material costs and energy production. A commercial MgB_2 superconducting wire supplied by Columbus Superconductors is used in the field winding operating at 20 K.

Based on the current unit cost and current density capability of the employed MgB_2 wire, the topologies with more iron have a lower LCCoE than the other topologies with more non-magnetic cores. The fully iron-cored topology with salient iron poles is most advantageous regarding the LCCoE as well as the resulting annual energy production, active material cost and superconductor length.

Since the superconductor technology is developing fast, only using the current properties of the MgB_2 wires may limit the perspective of comparing the topologies. The topologies that are less advantageous at present may become promising in the long run. Three scenarios on the employed MgB_2 wire are therefore investigated, assuming

    1) reducing the wire cost per unit length to 1/4,

    2) four times engineering critical current density, and

    3) the combination of both.

These scenarios can effectively lower the capital LCCoE for all the topologies, especially those with more non-magnetic cores. The third scenario, considered as a long-term goal, results in very small differences of LCCoE among the twelve topologies. Then the topologies with more non-magnetic cores will catch up those with more iron. Aiming at a lower LCCoE, however, those topologies having the most iron in the core are still the most promising candidates for both now and the long term, although they could result in large generator masses.

RIPPLE FIELD AC LOSSES IN MgB_2 SUPERCONDUCTING FIELD WINDINGS

The most promising fully iron-cored topology with salient poles has iron teeth in the stator. These iron teeth produce high-order magnetic field harmonics. These harmonics produce AC losses in the superconducting field winding. The AC loss level is evaluated by combining 2D transient FE models for calculating the magnetic field and analytical models for calculating the AC losses. The result shows that the amount of AC losses produced by iron teeth can be very small and this topology is feasible from the perspective of AC loss production.

REDUCING THE SHORT CIRCUIT TORQUE

SCSGs usually have larger magnetic air gaps than conventional generators because of space for a cryostat or use of non-magnetic cores. As a result, the inductance becomes lower and then the short circuit torque can become as high as more than 10 times the rated torque which is too high for wind turbine constructions. Three

approaches of suppressing the short circuit torque are assessed. The first is to use an electromagnetic shield between the field winding and the armature. The second is to use iron teeth instead of non-magnetic teeth in the stator. The third is to use armature winding segmentation with multiple power electronic converters. 2D transient FE models are used to simulate the torque during a no-load three-phase short circuit. The first and second approaches are not effective. The third approach of armature winding segmentation can effectively suppress the short circuit torque for all the four selected generator designs when only one segment is shorted, assuming the segments are independent of each other in the FE model. Increasing the number of segments improves the torque reduction and four segments can limit the peak torque below 3 times the rated torque.

POTENTIAL OF PARTIALLY SUPERCONDUCTING GENERATORS

By conducting a comparison between 10 MW SCSGs and PMSGs, the SCSGs are not competitive yet if the cost or cost of energy is chosen as the primary design objective. It is needed to look for significant advantages which will make SCSGs sufficiently attractive in the wind energy industry. The potential of partially SCSGs for 10 MW direct-drive wind turbines is assessed by investigating their performance for a very wide range of excitation currents. Performance indicators such as shear stress and efficiency and other generator characteristics are compared for the twelve generator topologies. To be sufficiently attractive, superconducting generators must have significant advantages over permanent magnet direct drive generators which typically have shear stresses in the order of 53 kPa and efficiencies of 96%. Therefore, as an example, it is investigated what excitation is required to obtain a doubled shear stress and an efficiency of 98% for four selected topologies. To achieve this generator performance, the four topologies require a range of excitation from 200 to 550 kAt (Ampere-turns) with a low armature current density of 2 A/mm^2. The more iron is used in the core of these topologies, the easier they achieve this performance. By examining the maximum magnetic flux density at the location of the superconducting field winding, feasible superconductors can be chosen according to their engineering current density capabilities. It is found that high- and low temperature superconductors can meet the performance criteria for many of the four topologies. MgB$_2$ superconductors are feasible for the fully iron-cored topology with salient poles but needs cooling down to 10 K.

▽ ▽ ▽

From the perspective of electromagnetic design, this thesis points out a direction to increase the feasibility of SCSGs for large direct-drive wind turbines:

   • Aiming at a lower LCCoE, iron-core based generator topologies are more feasible than the other topologies and the used lengths of superconducting wires are

shorter. The fully iron-cored topologies are most feasible and their AC loss level is acceptably low. If low generator weight is also desired, however, the topologies with more non-magnetic cores can be considered once the superconducting wire becomes much cheaper and capable of much higher current densities.

• Currently, the SCSG do not show advantages of LCCoE over PMSGs. To make superconducting generators attractive to wind energy industry, the shear stress and efficiency of the generator should be much higher than those of permanent magnet generators. Such advantages may offset the disadvantages of high generator costs and complicated cryogenic cooling.

• To achieve competitive shear stresses and efficiencies, the excitation of the superconducting field winding should be increased to a high level. To realize such high excitation, LTS and HTS are more feasible than MgB_2 wires at present. In addition, iron-core based generator topologies are again more feasible than the other topologies to reach high shear stresses and efficiencies, especially the fully iron-cored topologies.

• Aiming at an acceptable short circuit torque, armature winding segmentation with multiple power electronic converters can be considered.

This direction may not be the only one. However, it takes into account the key feasibility issues at the moment from the electromagnetic design perspective. Prototypes can be built following this direction to demonstrate and prove this technology. This thesis makes a step of contribution to increase the technology readiness level of SCSGs for large direct-drive wind turbines. Efforts are still going on to achieve a mature SCSG design that should be proven to be compact, lightweight, efficient, reliable and cheap.

Samenvatting

De afgelopen jaren is er steeds meer interesse in supergeleidende synchrone generatoren (SCSG). Supergeleidende synchrone generatoren (SCSG) worden steeds meer als een alternatief voor permanent magneet synchrone generatoren (PMSG) gezien. Het is de verwachting dat de topmassa en de gondel afmetingen gereduceerd kunnen worden bij grote windturbines. In 2012 is het INNWIND.EU proje-ct gestart met als doel om het gebruik van SCSG in 10-20 MW direct aangedreven offshore windturbines te onderzoeken. Echter, de haalbaarheid van SCSG is gelimiteerd door een paar kritische zaken, waaronder: hoge kosten, wisselstroomverliezen in supergeleidende spoelen en een zeer hoog kortsluitkoppel. Verder waren zeer verschillende SCSG ontwerpen in de literatuur niet competitief met PMSG's. Er is geen convergentie in de ontwerp methodologie van een SCSG, er is niet één ontwerp dat eruit springt.

Dit proefschrift heeft als doel om de toepasbaarheid te vergroten van SCSG voor grote windturbines en om de meest waarschijnlijke ontwerpen te identificeren. Dit wordt gedaan op basis van de volgende 4 vragen:

- Hoe kan de kostprijs van energie beperkt worden door de generator topologie?
- Is het mogelijk om de wisselstroomverliezen terug te brengen tot een acceptabel niveau?
- Kan de kortsluitstroom beperkt worden tot een acceptabel niveau?
- Wat is het significante potentiële voordeel van een SCSG boven een PMSG ontwerp?

In dit proefschrift wordt de focus gelegd op generatoren welke gedeeltelijk supergeleiding gebruiken. De veldwikkeling is gebaseerd op supergeleidende technologie. De stator is gebaseerd op koper technologie. Dit type SCSG wordt op dit moment beschouwd als een meer haalbare oplossing dan een volledige generator gebaseerd op volledige supergeleidende techniek. Een 10 MW referentie windturbine ontwerp is aangeleverd door het INNWIND.EU project en wordt in dit proefschrift veelvuldig gebruikt.

Vergelijking van topologien op basis van beschikbare MgB_2 supergeleiders
De genormaliseerd kosten van energie (zgn. Levelized Cost of Energy, LCoE) van een windturbine gebaseerd op een SCSG ontwerp kan veel hoger zijn dan van conventionele windturbines. Dit komt doordat er gebruik wordt gemaakt van dure super

geleidende geleiders en cryogene koeling. De hoge LCoE verhindert de vermarkting van SCSG binnen de wind turbine industrie en beperkt de haalbaarheid van SCSG. Elektromagnetische ontwerpen om de kapitaalkosten van SCSG te reduceren zijn onderzocht door twaalf verschillende generator ontwerp topologien met elkaar te vergelijken. In deze topologien worden verschillende combinaties van ijzer en niet-magnetische materialen voor het: rotor juk, rotor pool kern, stator tand en stator juk met elkaar vergeleken. Iedere topologie is geoptimaliseerd voor de laagste genormaliseerd gekapitaliseerde kosten van energie (zgn. Levelized Capital Cost of Energy, LCCoE). Een genetisch algoritme is gebruikt voor de LCCoE optimalisatie. De optimilisatie methode combineert 2D stationaire eindige elementen (FE) modellen en analytische modellen om de materiaalkosten en energie productie te berekenen. Een commerciele MgB_2 supergeleidende draad welke geleverd werd door Columbus Superconductors is gebruikt in de veld spoel welke operationeel is op 20 K.

Gebaseerd op de huidige kosten en mogelijken in de stroomdichtheid van het toegep-aste MgB_2 draad hebben de topologien met meer ijzer een lagere LCCoE dan de andere topologien met meer niet-magnetische kern materialen. De versie met een volledige ijzer kern topologie en uitspringende ijzeren polen is de meest interessante optie met betrekking tot de LCCoE en de totale opgewekte energie, materiaal kosten en gebruikte lengte van supergeleidend materiaal. De supergeleidende technologie ontwikkelt zich snel, alleen is de nu beschikbare MgB_2 draad een beperkend element in de vergelijking tussen de verschillende topologien. De topologien die nu minder interessant zijn kunnen een winnaar zijn in de toekomst. Drie verschillende scenario's in de ontwikkeling van het MgB_2 draad zijn onderzocht:

1) De kostprijs van de draad per lengte eenheid word ¼ van de huidige prijs,

2) De nuttige stroomdichtheid in de applicatie stijgt met een factor 4, en

3) Optie 1 en 2 samen.

Deze scenario's kunnen effectief de LCCoE verlagen voor alle topologien, in het bijzonder die met niet-magnetische kern materiaal. De derde optie is een langer termijn doel, en zal resulteren in hele kleine verschillen in de LCCoE tussen de 12 topologien.

In dat geval zullen de topologieen met niet-magnetisch materiaal in de buurt komen van topologieen die meer ijzer gebruiken. Teneinde een zo laag mogelijke LCCoE te krijgen zijn die topologieen die het meeste ijzer in de kern hebben desalniettemin de meest geschikte kandidaten voor nu en in de toekomst, hoewel zij leiden tot in een hoger gewicht van de generator.

WISSELSTROOMVERLIEZEN IN SUPERGELEIDENDE MgB_2 VELDWIKKELINGEN

De meest veelbelovende topologie is gebaseerd op een volledig ijzeren kern met uit-springende polen en maakt gebruik van een stator met ijzeren tanden. Deze ijzeren tanden produceren een magnetisch veld met harmonischen van hogere orde. Deze

harmonischen produceren wisselstroomverliezen in de supergeleidende veldwikke-ling. Het nive-au van deze AC verliezen wordt bepaald door combinatie van 2D tran-siente FEM modellen die het magnetische veld bepalen in combinatie met analyti-sche modellen die de wisselstroomverliezen bepalen. De resultaten laten zien dat de wisselstroomverliezen die geproduceerd worden door de ijzeren tanden erg laag kunnen zijn en daarmee is deze topologie geschikt uit oogpunt van beperking van wisselstroomverliezen.

REDUCTIE VAN KORTSLUITKOPPEL

SCSG's hebben een grotere magnetische luchtspleet dan conventionele generatoren door de ruimte benodigd voor een cryostaat of het gebruik van niet-magneti-sche kern materialen. Het gevolg hiervan is dat de inductantie lager wordt en dat hi-erdoor het koppel als gevolg van een kortsluiting meer dan 10 keer zo groot kan worden als het nominale koppel. Een dergelijk koppel is te groot voor een wind tur-bine constructie. Drie methoden om het kortsluitkoppel te beperken worden on-derzocht. De eerste is het gebruik van een elektromagnetische afscherming tussen de veldwikkelingen en het anker. De tweede methode is het gebruik van ijzeren in plaats van niet-magnetische tanden in de stator. De derde methode is segmentatie van de ankerwikkeling met behulp van meerdere vermogensomvormers. 2D tran-sient FEM modellen worden gebruikt om het koppel gedurende een kortsluiting in onbelaste toestand te bepalen. De eerste en de tweede methode zijn niet effectief. De derde methode die gebruik maakt van segmentatie van de ankerwikkeling is in staat om effectief het kortsluitkoppel te verlagen voor alle vier ontwerpen van de generator, wanneer een segment wordt kortgesloten, ervan uitgaande dat de seg-menten onafhankelijk van elkaar zijn in het FE model. Verhoging van het aantal segmenten verlaagt het kortsluitkoppel; vier segmenten beperken het kortsluitkop-pel tot minder dan drie keer nominaal koppel.

HET POTENTIEEL VAN GEDEELTELIJK SUPERGELEIDENDE GENERATOREN

Door het uitvoeren van een vergelijking tussen 10 MW SCSG en PMSG blijkt dat SCSG's nog niet competitief zijn als er op basis van de energie kostprijs ontworpen word. Er moet worden gekeken naar specifieke voordelen van SCSG welke ze in-teressant kunnen maken voor de windturbine industrie. Het potentieel van gedeel-telijke SCSG voor 10 MW direct aangedreven windturbines is uitgevoerd door hun prestaties voor verschillende bekrachtigings-stromen te onderzoeken. De 12 topolo-gien zijn vergeleken met elkaar op basis van onder andere genomen: kracht-dichth-eid en rendement. Om aantrekkelijk genoeg te zijn moeten SCSG's een significant hogere krachtdichtheid en rendement hebben dan PMSG, een PMSG heeft typisch een krachtdichtheid van 53 kPa en een rendement van 96%. Als voorbeeld is on-derzocht voor 4 topologien wat de impact is op de bekrachtiging is om de kracht-

dichtheid te verdubbelen en een rendement van 98% te bereiken. Om dit te bereiken hebben de 4 topologien een bekrachtiging van 200 to 500 kAt (Ampere-turns) nodig met een bekrachtigings-stroomdichtheid van 2 A/mm2. Des te meer ijzer er gebruikt wordt in het ontwerp des te makkelijker het doel bereikt kan worden. Door de maximale magnetische fluxdichtheid in de supergeleidende veldwikkeling te onderzoeken, kan er een geschikte supergeleider gekozen worden op basis van hun stroomdichtheid ontwerpspecificatie. Uitkomst is dat hoge en lage temperatuurgeleiders aan de eisen kunnen voldoen voor de meeste van de vier topologien. MgB_2 supergeleiders zijn haalbaar in een volledig ijzer kern topologie met uitspringende polen, echter is een temperatuur van 10 K noodzakelijk.

$\triangledown \, \triangledown \, \triangledown$

In dit proefschrift wordt er vanuit perspectief van het het elektromagnetische ontwerp gewezen op een richting om de haalbaarheid van SCSG in grote direct aangedreven windturbines te vergroten.

Als het doel een zo laag mogelijke LCCoE is, dan is een generatorontwerp gebaseerd op een ijzer-kern meer haalbaar dan andere topologien en is de noodzakelijke lengte van supergeleidend materiaal korter. De ontwerpen op basis van ijzerkernen zijn het best haalbaar en de wisselstroomverliezen zijn op een acceptabel niveau. Als een laag generator gewicht ook een eis is dan moeten de concepten met meer niet-magnetisch materiaal in overweging genomen worden als de supergeleidende draden een stuk goedkoper worden en veel hogere stroomdichtheden kunnen halen.

Op dit moment heeft een SCSG in de LCCoE analyse geen voordeel boven een PMSG. Om supergeleiding aantrekkelijk te maken voor de windturbine industrie moet de krachtdichtheid en het rendement veel beter zijn dan een permanent magneet generator. De voordelen van een hoger rendement en hogere krachtdichtheid kunnen de nadelen van hogere kosten en de cryogene koelingcompense-ren.

Om competitieve krachtdichtheden en rendementen te halen moet de sterkte van de bekrachtiging van de veldwikkeling naar een hoger niveau gebracht worden. Om dit mogelijk te maken zijn LTS en HTS beter kandidaten dan MgB_2 draden op dit moment. Daarbij zijn ontwerpen gebaseerd op ijzerkernen beter haalbaar dan andere topologien om de hoge krachtdichtheden en rendementen te halen. In het bijzonder de ontwerpen met een volledig ijzeren kern. De kortsluitkoppels kunnen gereduceerd worden door de generator op te delen in meerdere segmenten en door ieder segment zijn eigen vermogensomzetter te geven.

Dit is niet de enige ontwerprichting. Echter houdt deze ontwerprichting rekening met de hoofdfactoren van de huidige elektromagnetische ontwerpmethodologie. Prototypes kunnen gebouwd worden volgens deze richtlijn om deze technologie te valideren en te demonstreren. Dit proefschrift helpt mee in de ontwikkeling

en opbouw van kennis voor grote direct aangedreven SCSG windturbine genera-
toren. De huidige stand van de techniek in het vakgebied wordt in dit proefschrift
samengevat. De ontwikkeling gaat verder, de techniek zal steeds meer volwassen
worden om een bewezen compacte, lichtgewicht, hoog rendement en goedkope
SCSG generatoren te ontwikkelen.

1

INTRODUCTION

1

1.1. BACKGROUND

T HE conservation of fossil fuels and the need for reducing green house gas emission accelerates the development of renewable energy. Wind energy, as a promising renewable energy source, is developing rapidly nowadays. Onshore wind energy has been extensively developed in the last two decades. A few countries with a vast land area, such as China, have established large-scale wind farms inland [1]. A large number of wind turbines of 1-3 MW form such wind farms. In those with small land areas, such as European countries, the capacity for onshore wind farms is limited, which are greatly constraining the development of onshore wind energy utilization in such countries [2].

For this reason, offshore wind has been drawing increasing attention in European countries [3], [4]. In offshore regions, particularly the North Sea, wind resources are superior to those of onshore regions, as illustrated in Fig. 1.1. The naturally vast area of ocean makes offshore wind energy quite promising to European countries around the North Sea. Denmark, Norway, UK, Netherlands and Germany are building and testing offshore wind farms in the North Sea. An advanced high voltage direct current (HVDC) network is also under development to connect those offshore wind farms to inland power grids [5].

However, utilization of offshore wind energy brings about much higher costs in installation, maintenance and repair due to long distances between a wind farm and its neighboring land. Harsh offshore environment elevates the difficulties and complexities. As a result, the costs of building and maintaining an offshore wind farm can be several times higher than those of an onshore wind farm.

An effective way to lower such costs is to decrease the number of individual wind turbines in a wind farm. Then the major costs of a wind farm, expensive foundations and grid connections, can effectively be limited. To maintain the same capacity of the wind farm, an individual wind turbine must have a very large power rating. Most onshore wind turbines are in the range of 1-3 MW. An offshore wind turbine needs to be much larger to be competitive. A large wind turbine is more expensive than a smaller one regarding the capital expenditure (CAPEX) of the turbine itself. However, the costs of installation, maintenance and repair of a wind farm of large wind turbines are thought to be reduced when the number of wind turbines effectively decreases. As a whole, the cost per unit energy production can be reduced, which is highly desired in wind energy industry.

The trend of the power rating of a single offshore wind turbine, as illustrated in Fig. 1.2, proves that offshore wind turbines are becoming increasingly larger in recent years. The deployment of 4-6 MW turbines seen in 2015 will be followed by the gradual introduction of 6-8 MW turbines closer towards 2018 [7]. In industrial
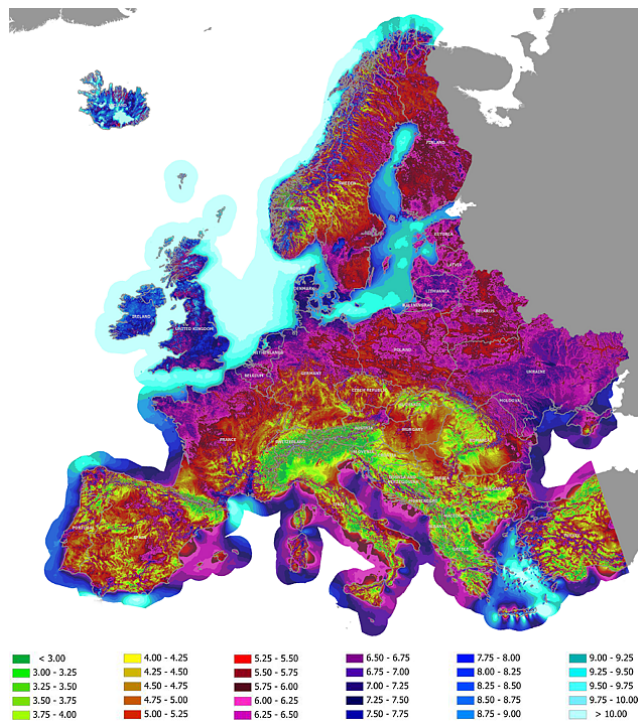
Figure 1.1: Annual mean wind speed in Europe at 80 m high. Reproduced from [6].

practices, Siemens is commercially supplying 8 MW offshore wind turbines [8] and Vestas has also increased the power level of a single wind turbine to 8 MW [9].

Large wind turbines (e.g. over 6 MW) put forward new issues with drive trains. A drive train in a wind turbine converts the kinetic energy from wind into electrical energy. Conventional drive trains for wind turbines below 6 MW are categorized into two main types. One is a high-speed or medium-speed generator integrated with a gearbox. This gearbox is located between the faster generator rotor and the slower aerodynamic rotor (i.e. the wind turbine rotor with three blades). This geared drive train mainly contains the following concepts:

• A high speed doubly-fed induction generator with a partially rated power converter. A three-stage gearbox is used.

• A high speed synchronous generator with a fully rated power converter and a three-stage gearbox is used. A modification is the medium speed synchronous generator with a fully rated power converter and a single or double stage gearbox is

1
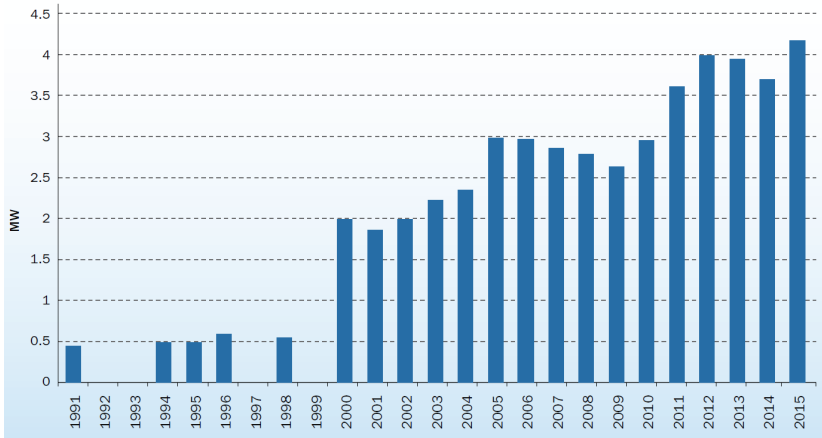
Figure 1.2: Average power rating of offshore wind turbines newly installed per year in Europe. [7]

then used.

The other drive train type is simply a low-speed synchronous generator directly connected to the low-speed aerodynamic rotor without a gearbox. Both the rotors rotate at the same speed. A fully rated power converter is used. This type is called direct drive and two generator types are primarily employed to it. One is electrically excited synchronous generator (EESG) and the other is permanent magnet synchronous generator (PMSG). Using fully rated converters decouples the generator and the power grid, and enables the electrical output to comply with the latest grid codes.

For small and medium wind turbines in onshore applications, these two drive trains are both extensively employed. Geared generators are compact and lightweight due to high speed operation. Direct-drive trains are, however, expected to be more reliable because of the removal of the less-reliable gearbox [10]. The resulting size and weight of an onshore direct-drive generator are not problematic for the wind turbine support, installation and transportation.

In offshore wind energy conversion, when larger wind turbines (above 6 MW) are desired for a low cost of energy, geared drive trains encounter a challenge with the large and expensive gearbox. Such big gearboxes are not easy to be manufactured and their reliability is of a question. Direct-drive generators, such as EESGs and PMSGs, would become very large in size due to low rotational speeds (e.g. 10 rpm for a 10 MW wind turbine). Larger sizes usually mean higher costs. Since EESGs are usually less efficient than PMSGs due to resistance in the excitation circuit, the

PMSGs are of more interest in the design of direct-drive wind turbines. However, PMSGs need a large amount of rare-earth materials, i.e. permanent magnets. Since the natural resources of rare-earth materials are limited, the fact of markets shows that permanent magnets (PMs) are not cheap and their price is hardly predictable. Due to such uncertainty of PM costs, European countries are looking for alternatives which can replace permanent magnets or reduce the use of permanent magnets for wind energy conversion with large wind turbines.
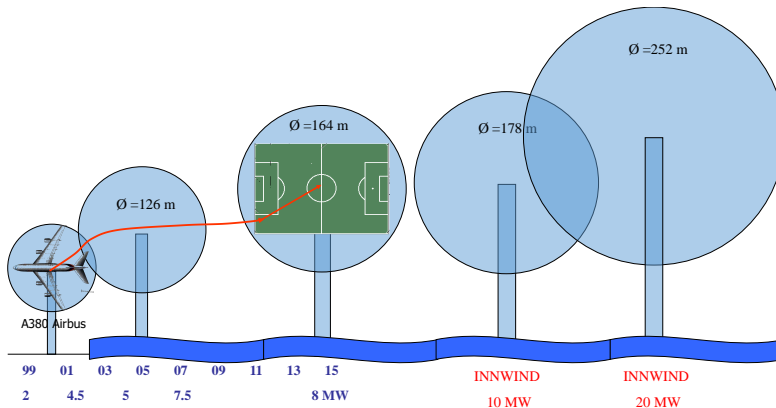
Figure 1.3: Trend of wind turbine sizes, including the expectation by the INNWIND.EU project. The most left turbine is the largest inland, which has a power below 4 MW and was established in around 2000. Then the record of sizes is being broken by offshore wind turbines.

The INNWIND.EU project funded by the European seventh framework (FP7) started in 2012 and has been studying two promising candidate generator systems which could become such alternatives [11]. One of the generator systems is pseudo direct drive (PDD) generator system and the other is superconducting generator system. Both are intended for 10-20 MW direct-drive wind turbines whose sizes are sketched in Fig. 1.3.

A PDD generator applies a magnetic gearbox for contactless torque transmission [12] so that the generator can be made small, lightweight and reliable, [13, 14]. This generator system is being studied, designed and demonstrated by Magnomatics Ltd. and the University of Sheffield. A superconducting generator makes use of the large current capability of superconducting materials to produce high magnetic fields so that the generator can be made small, lightweight and efficient [14–16]. Within the INNWIND.EU project, the superconducting generator system is being studied, designed and demonstrated by DTU Wind Energy, Delft University of Tech-

nology, SINTEF and Siemens Wind Power. The INNWIND.EU project aims at finding a promising alternative for large offshore wind turbines and considers these two generator systems.

1.2. Motivation

Superconducting machines have been studied for several decades. Besides theoretical studies, a few laboratory or industrial practical demonstrations were also designed and operated, especially for military ship propulsion [17, 18]. These studies focused on proving the technical feasibility of superconducting machines. However, successful industrial applications for power engineering are still far away. The challenges for industrial application involve many aspects, such as cryogenic cooling, performance of large-scale superconducting wires, mechanical construction and costs. Applying superconducting generators in wind energy conversion systems has drawn attention. This is because this generator has potential in large offshore wind turbines to reduce the size and weight of the tower head.

Theoretical studies and ship propulsion experiences on superconducting machines may not be directly transplanted to wind energy conversion, since they may have quite different requirements. First of all, wind energy industry requires a low cost of energy. Secondly, a wind turbine itself puts mechanical and spatial constraints onto the drive train. Thirdly, offshore wind energy conversion requires a high reliability and availability. These special issues challenge the drive train and particularly the performance of the superconducting generator.

The performance of an electrical machine significantly depends on the electromagnetic design. However, academia and industry have not yet found or agreed on a dominant design concept. There are many trade-offs in the design process depending on a specific application and its requirements. For example, military or aerospace engineering may not very much care about costs but size, weight and efficiency are essential. As a result, such applications tend to use lightweight but costly materials and designs.

Unlike in military applications, wind energy conversion rigorously requires low costs and high energy production which can facilitate commercialization. Small size and weight of a generator are advantages as expected by both the academia and commercial companies [15, 16, 19–22]. However, size and weight may become less important (but still important) in large offshore wind turbines. Those electromagnetic designs of generator which result in low costs per unit energy production are preferred. Therefore, they should be found out in the first place.

Despite the intention of low costs of energy, there are still many different electromagnetic design concepts being proposed and developed. AMSC [21], General Electric (GE) [20] and the Suprapower project [23] proposed designs using HTS (BSCCO

or YBCO), LTS (NbTi) and MgB$_2$, respectively. Moreover, GE employed a retrofit stator core with steel laminates but a novel non-magnetic rotor core for the superconducting field winding. Suprapower proposed conventional salient iron rotor poles but introduced non-magnetic teeth to the stator core. Keysan designed transverse-flux superconducting generators which are quite different from conventional radial-flux ones [24]. In addition to all the above mentioned partially superconducting concepts, AML Superconductivity and Magnetics is developing a fully superconducting design [22] in which both the field and armature windings are superconducting [25, 26]. These concepts have formed a vast range of electromagnetic design possibilities.

Permanent
magnet
320 tons

Partially
superconducting
150 tons

Fully
superconducting
80 tons
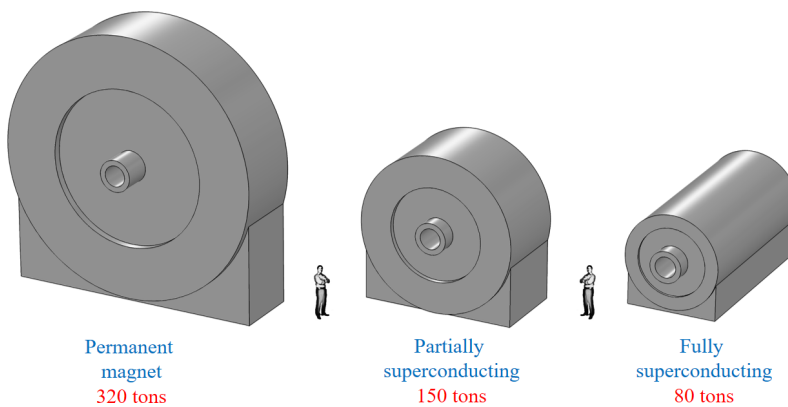
Figure 1.4: Size and weight reduction by using superconducting generators for 10 MW direct-drive wind turbines. The permanent magnet generator is estimated based on [27]. The partially superconducting generator is estimated based on [20]. The fully superconducting is estimated by [28].

An electromagnetic design of a superconducting machine usually starts from topology selection, which defines the combination of ferromagnetic and non-magnetic in the machine cores. Using ferromagnetic cores or not can make the cost, efficiency, size and weight of a generator quite different [29, 30]. Generally speaking, the design of a superconducting machine is made by integrating a particular topology with currently available superconductors. Such a design is capable of certain performance for evaluation. For offshore wind energy conversion, we evaluate different designs by the cost of energy.

Unlike such forward thinking from design to performance, a design can also be made and evaluated through reverse thinking from required performance to design.

This way of thinking is enabled due to the fact that the superconductor technology is still developing fast. A design based on the present superconductor technology will probably be out of date soon in near future. Hence, we may not limit ourselves to the currently available superconductors. Instead, we can set the values of desired performance indicators, such as a specific size, weight, efficiency or cost, for the application. Then, we find out the required design parameters and suitable or potentially suitable superconductors to achieve such high performance. This approach is expected to reveal the potential performance of a superconducting generator for future.

Accompanying the general electromagnetic design, i.e. topology selection, AC losses are always an issue uniquely with superconductors. Some generator designs may produce excessive AC losses in the superconducting winding due to ripple magnetic fields from winding distribution or slotting effects [31, 32]. Such losses either reduce the efficiency or challenge the cooling system. Hence, an electromagnetic design should also be evaluated from the perspective of AC losses.

Another unique challenge for designing a superconducting machine is the high short circuit torque due to a large magnetic air gap. The peak torque during a short circuit (at the generator terminal) could reach as high as more than ten times the rated torque [33], which is way beyond the mechanical limit usually designed for a wind turbine. This problem must be addressed. Otherwise, application of superconducting generators in wind turbines will stay infeasible.

1.3. Research Objective

I N line with the background and motivation, the objective of this thesis is to
"Provide insights and solutions from the perspective of electromagnetic design to increase the feasibility of superconducting generators for large wind turbines."

To achieve this objective, this thesis will investigate the following four aspects of feasibility:

- Costs,
- AC losses,
- Short circuit torque, and
- Performance, i.e. shear stress and efficiency,

These four aspects greatly determine the feasibility level of superconducting generators applied in large wind turbines. Apparently, electromagnetic design is the backbone of this research. However, we cannot overlook the role that mechanical and cryogenic cooling designs play in such a complicated multi-physical system. Appropriate considerations will be taken to form realistic electromagnetic designs.

1.4. RESEARCH QUESTIONS

$\mathbf{A}$ccording to the research objective, four research questions must be answered in this thesis:

• Q1: *Which topologies result in the lowest cost of energy, based on currently available superconductors?* The purpose of answering Q1 is to *"find out superconducting generator topologies suitable for wind turbine application and provides insights to selection of topologies for superconducting generator design"*.

• Q2: *What are the levels of AC losses in the superconducting winding of different electromagnetic designs due to ripple magnetic fields? Are the AC losses acceptably small or not?* The purpose of answering Q2 is *"evaluate the technical feasibility of AC loss levels in superconductors of different electromagnetic designs"*.

• Q3: *How can the short circuit torque be effectively suppressed by electromagnetic design?* The purpose of answering Q3 is to *"assess that the short circuit torque of a superconducting generator can be sufficiently small for mechanical construction of a wind turbine"*.

• Q4: *How competitive is a superconducting generator compared with a permanent magnet generator?* The purpose of answering Q4 is to *"evaluate the feasibility of performance indicators of a superconducting generator when comparing it to a technically mature competitor"*.

• Q5: *What is the potential of a superconducting generator for large wind turbines? What are the design parameters and suitable superconductors required to achieve high generator performance?* The purpose of answering Q5 is to *"reveal the prospect of superconducting generators for wind energy conversion"*.

1.5. THESIS LAYOUT

$\mathbf{B}$ased on the research questions, this thesis has a structure shown in Fig. 1.5 and is divided into seven chapters. Chapters 3-7 answer the four research questions in the order which constitute the scientific contributions of this thesis.

• Chapter 2 introduces superconductivity and describes how a superconducting generator is integrated into a large offshore wind turbine.

• Chapter 3 overviews possible topologies for a 10 MW superconducting machine and compares them by the criterion of cost of energy. Chapter 3 answers Q1.

• Chapter 4 models the AC losses in the superconducting winding due to ripple magnetic fields and evaluates the loss level for different 10 MW superconducting generator designs. Chapter 4 answers Q2.

• Chapter 5 models the short circuit torque of 10 MW superconducting generators and then presents and evaluates the methods to suppress the excessive short circuit torque. Chapter 5 answers Q3.

• Chapter 6 compares 10 MW superconducting generators and permanent magnet generator under the same design and optimization methods and the same operating conditions. Chapter 6 answers Q4.

• Chapter 7 reveals the potential performance of 10 MW superconducting generators and the requirements to design parameters and superconductors to achieve high performance. Chapter 7 answers Q5.

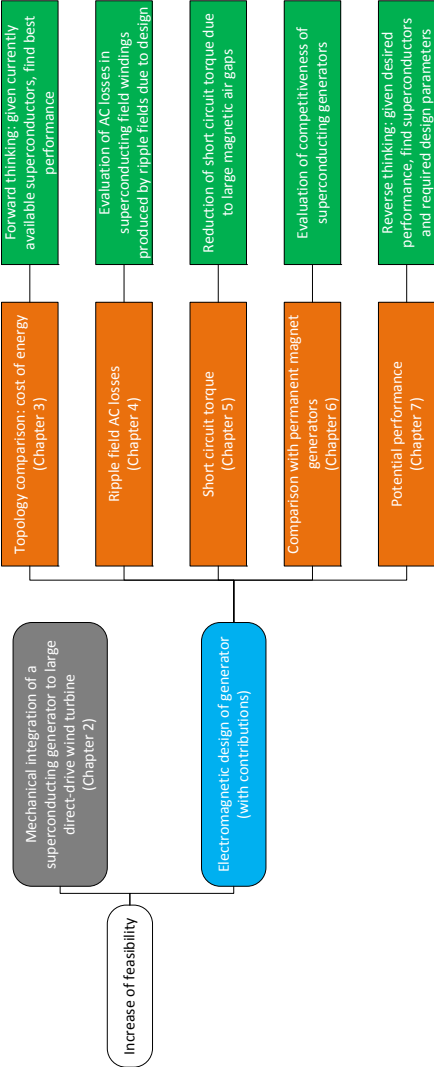• Chapter 8 concludes this thesis and gives recommendations for future work.

1

Figure 1.5: Thesis structure.

2

SUPERCONDUCTING DRIVE TRAIN FOR LARGE WIND TURBINES

2

2.1. INTRODUCTION

Superconducting machines take advantage of the large current density capability of superconductors for exciting high magnetic fields. This chapter starts with introducing basic physical properties of superconductor. Then the basic structure of a superconducting machine is described and its fundamental properties, such as machine type, partially or fully superconducting, radial or axial flux and cryogenic cooling method, are reviewed for wind turbine applications. In the end, integration of a superconducting generator to a 10-20 MW direct-drive wind turbine nacelle concept is introduced, followed by an brief overview of the other 10 MW up-to-date superconducting nacelle concepts. The objective of this chapter is to depict a superconducting drive train and its integration into a large wind turbine.

2.2. INTRODUCTION TO SUPERCONDUCTIVITY

Superconductivity is a phenomenon where some materials exhibit no electrical resistance below certain cryogenic temperatures. It was discovered on 8 April, 1911 by Heike Kamerlingh Onnes, who was studying the resistance of solid mercury at cryogenic temperatures using the recently produced liquid helium as a refrigerant. At the temperature of 4.2 K, he observed that the resistance abruptly disappeared [34, 35].

Superconductors have two distinct properties: zero resistance and Meissner effect. Basically, all superconductors can be divided into two basic types: Type-I and Type-II superconductors. Alternating currents or magnetic fields produce losses in superconductors. Striped superconductors are anisotropic, and their $B - J$ critical characteristics and AC losses depend on the direction of the applied magnetic field.

2.2.1. ZERO RESISTANCE

The first property of superconductors is zero resistance. The temperature for achieving zero resistance for a superconductor has become increasingly higher over the last 100 years, from 4.2 K to above 100 K and even 203 K (H_2S at 150 GPa pressure). The material which can be superconducting has also become more various, from mercury to, for instance, NbTi, YBaCuO, MgB_2 and H_2S. The coolant for cooling superconductors originates from liquid helium and now goes to liquid nitrogen and even liquid tetrafluoromethane (CF_4). The time line of the development of superconductors is shown in Fig. 2.1.

Zero resistance of a superconductor is true under the condition of unchanged currents and magnetic fields. However, losses will occur if a superconductor is with changing currents or magnetic fields. Thus, strictly speaking, we should say that superconductors have zero DC resistance for the sake of considering their AC resis-
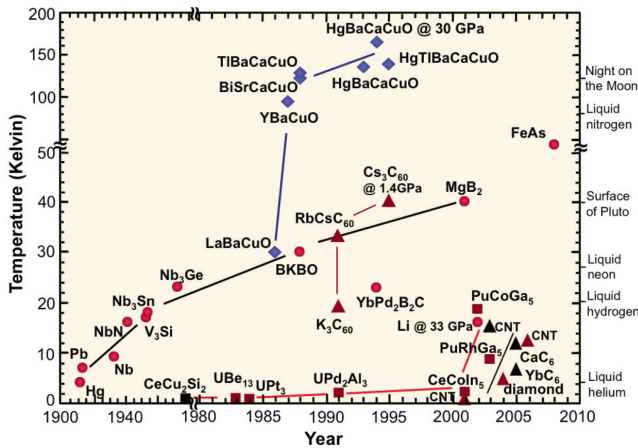
Figure 2.1: Timeline of the development of superconductors from 1911 to 2010 [36]. The boiling point of different coolants is also indicated. In 2015, it was discovered that sulfur hydride (H_2S) becomes superconducting at 203 K at a high pressure of 155 GPa [37].

tance.

2.2.2. MEISSNER EFFECT AND TYPE-I SUPERCONDUCTORS

In 1933, Walther Meissner and Robert Ochsenfeld discovered the Meissner effect, which is the second property of superconductors [38]. This effect shows that the magnetic field is not fixed inside a superconductor when it is cooled down through the critical temperature. Instead, the magnetic field is forced out of the material. The magnetic field is suddenly expelled from the center of the material, forcing the field lines to run around the superconductors, as illustrated in Fig. 2.2. When the material becomes superconducting, screen currents occur near the surface of the material, screening the inside from the outside magnetic field [39].

This effect occurs in Type-I superconductors which suddenly lose their superconducting properties once the field strength reaches above a certain magnetic field strength H_{c1} [40]. This type of superconductivity is normally exhibited by pure metals, e.g. aluminum, lead, and mercury.

2.2.3. TYPE-II SUPERCONDUCTORS

The superconductors currently applied in electrical apparatus, e.g. NbTi, Nb_3Sn, MgB_2, BSCCO and ReBCO, are all Type-II superconductors, which are capable of higher magnetic fields compared to Type-I superconductors [40, 42].

2
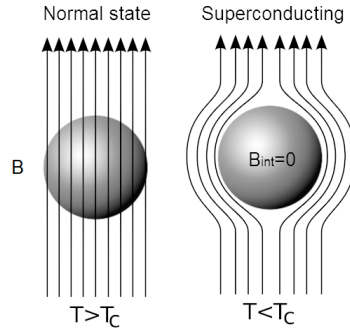
Figure 2.2: Meissner effect in a superconductor. The conductor on the left is in the normal state (not superconducting) when it is above its critical temperature. The conductor on the right is in the superconducting state when it is below its critical temperature and the magnetic field inside the conductor is zero. The external magnetic field is below H_{c1} in the both cases. Reproduced from [41].

Type-II superconductors behave the same as Type-I superconductors below H_{c1}. But at a higher magnetic field strength, the flux lines gradually penetrate the superconductor whose superconducting properties remain. When the magnetic field strength increasingly reaches above a value H_{c2}, the superconducting properties are lost. The region between H_{c1} and H_{c2} can be considered as a transition from no magnetic field penetration to full penetration. Although the flux lines seem to enter the superconductor, they are still shielded from the superconducting parts by current vortices. This transition region is called a mixed state. The mixed state makes Type-II superconductors usable since such superconductors can withstand higher magnetic fields. All the states of Type-I and Type-II superconductors are depicted in Fig. 2.3b.

2.2.4. CHARACTERISTICS OF A SUPERCONDUCTOR

$E - J$ CHARACTERISTIC

A superconductor can be characterized by its $E - J$ characteristic, where E is the electric field and J is the current density. This characteristic measures the resistance in a superconductor when a certain current density is applied. In a limited range (below the current density for a flux flow state [44]), an $E - J$ characteristic can be modeled by the power law:

$$E = E_c(\frac{J}{J_c})^n, \tag{2.1}$$

(a) Type-I   (b) Type-II
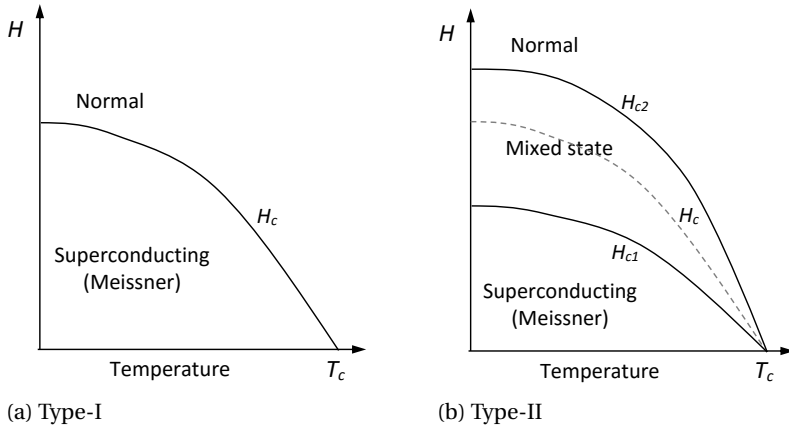
Figure 2.3: Phase diagrams for Type-I and Type-II superconductors with the superconducting, mixed and normal states indicated. Reproduced from [43].

where $E_c = 1$ μV/cm, J_c is the critical current density when E reaches E_c, and n is the power value which indicates how fast a superconductor transits from the super-conducting state to the normal state. To illustrate the power law, a few measured $E - J$ characteristics of a superconductor are plotted in Fig. 2.4.
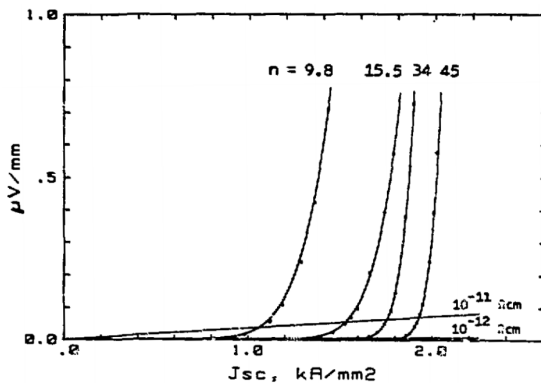
Figure 2.4: $E - J$ characteristic of multi-filamentary NbTi superconductor at $T = 4.23$ K and $B = 5$ T. High (low) values of n are the results of large (small) diameter filaments [45].

Critical surface

A superconductor is only superconducting within its critical surface, which is constrained by current density J, temperature T and magnetic flux density B, as illustrated in Fig. 2.5. Superconductivity exists within the volume bounded by the surfaces bordered by the functions: $f_1(T = 0, J, H)$, $f_2(H = 0, J, T)$ and $f_3(J = 0, H, T)$. Each superconductor has its unique critical surface. A superconductor operating outside its critical surface leaves its superconducting state. Thus, most designs with superconductors (except for applications like a fault current limiter (FCL)) must ensure that all the superconductors are operating within this limit enclosed by critical current density J_c, critical temperature T_c and magnetic flux density B_c.
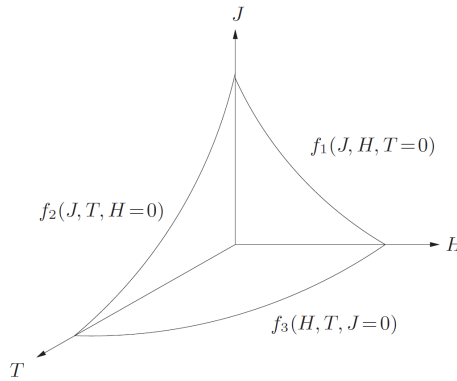
Figure 2.5: Critical surface of a typical Type-II superconductor [41].

When temperature is fixed, we can obtain a $B - J$ characteristic at this temperature. The $B - J$ characteristic of different superconductors at 4.2 K is plotted in Fig. 2.6. A series of $B - J$ characteristics of a certain superconductor at different temperatures is practically useful especially when the operating point of the superconductor is determined.

2.2.5. Origin of losses in a superconductor

As the first property, a superconductor has zero DC resistance. Thus, DC losses do not exist in a superconductor. However, AC losses can be produced in a Type-II superconductor due to the penetration of magnetic fields. In the penetration depth, an electric field is excited by a changing magnetic field by

$$\nabla \times E = \frac{\partial B}{\partial t}, \tag{2.2}$$
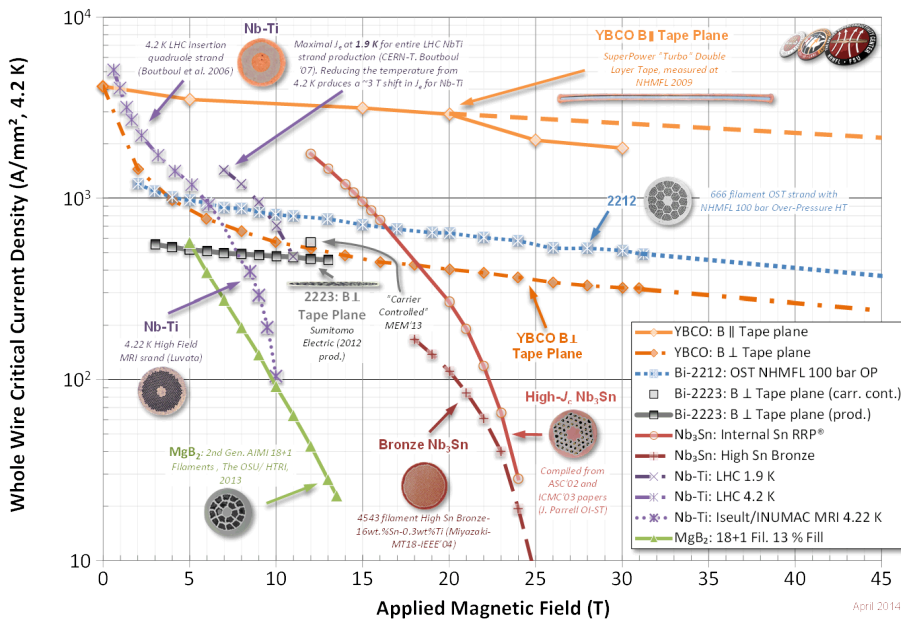
Figure 2.6: Critical characteristics of different superconductors at 4.2 K. Bi-2212 and Bi-2223 are both 1G HTS (BSCCO) with different wire architectures. YBCO is 2G HTS (ReBCO). $B \perp$ and $B \parallel$ are the magnetic fields perpendicular and parallel to the longer side of a superconductor (tape plane), respectively. LHC stands for large hadron collider. MRI stands for magnetic resonance imaging. Reproduced from [46].

and the resistive loss (Joule loss) per unit volume p is then produced by

$$p = J \cdot E. \tag{2.3}$$

where J is the current density flowing in the penetration depth of the superconductor, as illustrated in Fig. 2.7. This current density reaches as high as the critical value J_c according to Eq. (2.1). The AC loss due to this mechanism is called hysteresis loss. The hysteresis loss can be reduced by decreasing the dimensions of the superconductor [47].

Furthermore, a superconducting wire consisting of multiple superconducting filament is subject to coupling losses. These filaments are embedded in a normal-metal matrix. Eddy current losses are produced in the matrix by alternating magnetic fields. Besides, alternating magnetic fields produce electric fields which drive currents to flow in both the filaments and the matrix, as illustrated in Fig. 2.8. These
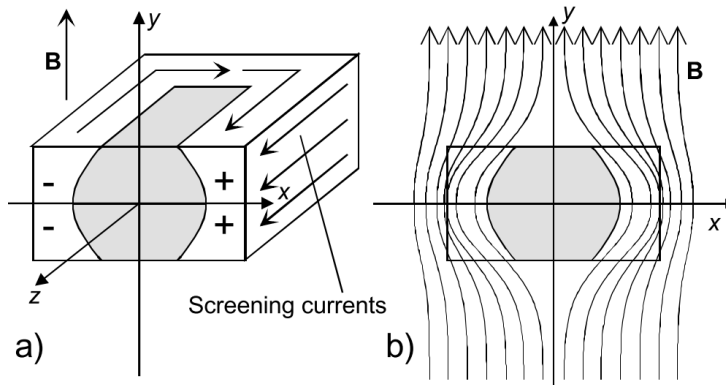
Figure 2.7: Cross-section of a superconductor in a changing external magnetic field. The screening currents in the white region shield the interior (gray) from the magnetic field. [47]

currents couple different filaments through the matrix at the end of the filaments. In the filaments, the current flows without resistance and is therefore large. In the matrix, the same large current encounters the resistance of the matrix and produces high losses. The coupling currents can be decreased by applying a twist to the filaments, by reducing the dimension of the wire or by increasing the resistivity of the matrix material [47].
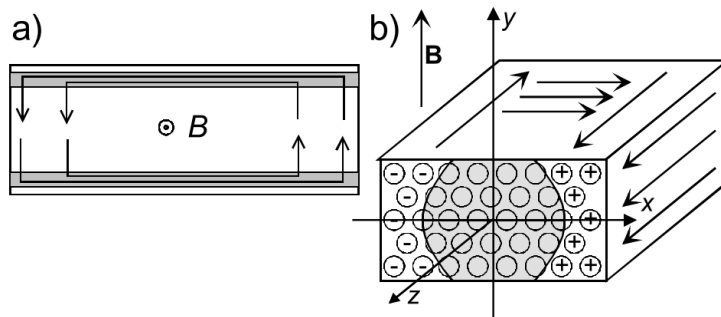
Figure 2.8: Coupling currents between non-twisted filaments in a composite conductor [47]. In (a), the filaments are shown in the gray and the arrows are coupling currents.

2.2.6. ANISOTROPY

A round superconductor has isotropic properties which are independent of the direction of applied magnetic fields. A striped superconductor is, however, anisotropic. The anisotropy of a striped superconductor especially affects the $B - J$ critical characteristic. A perpendicular magnetic field lowers the critical current density compared to a parallel one of the same value [48, 49] as shown in Fig. 2.9. This effect can also be observed in striped wires as shown in Fig. 2.6 (Bi-2223 and YBCO). In this figure and by convention, $B \perp$ and $B \parallel$ are the magnetic fields perpendicular and parallel to the longer side of a superconductor, respectively. In addition, AC losses of a single striped superconductor or a striped wire of multiple superconductor filaments are also dependent on the direction of the magnetic field [50]. The significant effect of anisotropy on the performance of a striped superconductor must be taken into account in the design process of a superconducting apparatus.
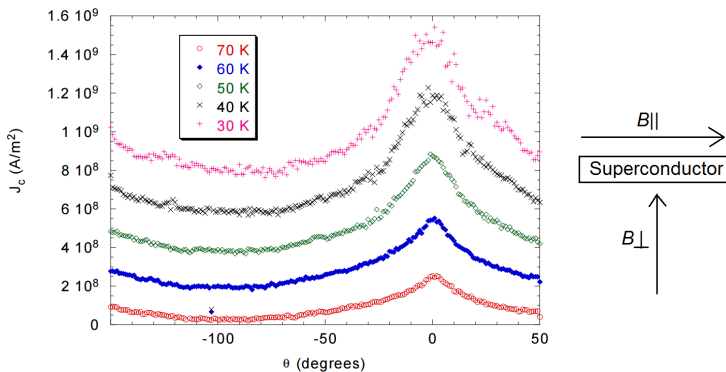
Figure 2.9: Critical current density measurements performed on a sample YBCO film at temperatures of 30-70 K. The data was obtained in a magnetic field of $B = 1$ T. At $\theta = 0$ ($\theta = -90°$), and the magnetic field is parallel (perpendicular) to the striped superconductor. Reproduced from [49].

2.2.7. OVERVIEW OF SUPERCONDUCTOR TYPES

Superconductors can be divided into three categories according to the operating temperature: low temperature superconductor (LTS), magnesium diboride (MgB_2) and high temperature superconductor (HTS).

LTS operates at liquid helium temperatures (4 K) or even lower temperatures. Typical LTS's are niobium-titanium (NbTi) and niobium-tin (Nb_3Sn). NbTi is an alloy and Nb_3Sn is a compound. Wires of either NbTi or Nb_3Sn are multi-filamentary.

MgB_2 is superconducting below $T_c = 39$ K and is expected to operate at 10-20 K, a temperature range between 4 K (liquid helium) and 65 K (liquid nitrogen). MgB_2

wires are multi-filamentary.

The term of high temperature means that all HTS has critical temperatures over the boiling point of nitrogen (77 K). HTS is further divided into the 1st generation (1G) HTS (i.e. BSCCO) and the 2nd generation (2G) HTS (i.e. ReBCO). The composition of BSCCO is $Bi_2Sr_2Ca_{n-1}Cu_nO_{2n+4}$. Typical BSCCOs are Bi-2212 ($n = 2$) and Bi-2223 ($n = 3$). Regarding the 2G HTS, the industry currently uses Rare Earth compounds (Yttrium, Samarium, Neodymium, Gadolinium) with Barium-Copper-Oxide (BCO) to surpass the 1G HTS in electrical performance but at higher cost. BSCCO wires are multi-filamentary while ReBCO wires are generally coated.

Table 2.1 summarizes the most popular commercial superconductors and their properties and typical applications. The cross-section of wires consisting of these superconductors is sketched in Fig. 2.10.

Table 2.1: Properties of most popular commercial superconductors.

Category	LTS		MgB_2	HTS	
Composition	NbTi	Nb_3Sn	MgB_2	BSCCO (1G)	ReBCO (2G)
Critical temp.	9.2 K	18 K	39 K	85-110 K[†]	92 K
Wire architecture	MF[††]	MF[††]	MF[††]	MF[††]	coated
Magnetic field level	high		low, medium	medium, high	
Applicable temp.	≤4.2 K		10-20 K	20-77 K	
AC loss level	medium	medium	medium	medium	high
Wire cost	low	low	medium	high	high
Application	MRI, accelerator		machine	power cable, machine, maglev, FCL	

[†]85 K: Bi-2212, 110 K: Bi-2223.

[††] Multi-filamentary.

2.2.8. SUPERCONDUCTORS UNDER CONSIDERATION

At present, LTS is mainly used in high-field application such as magnetic resonance imaging (MRI) [52] and accelerator magnets [53, 54] cooled by liquid helium. GE has proposed a 10 MW generator design using NbTi at 4.2 K, which has established a concept for LTS generators [20]. HTS cooled by liquid nitrogen at 77 K is mainly used in power cables [55] and fault current limiters (FCLs) [56]. When it comes to generators, HTS usually has to be cooled down to below 40 K to achieve good performance. Furthermore, HTS materials are currently rather expensive (one order more expensive than LTS and MgB_2). MgB_2 seems to lie in a moderate position. It requires a temperature of 10-20 K to make a generator with decent performance but it is much cheaper than HTS. Although MgB_2 has shortcomings such as low magnetic
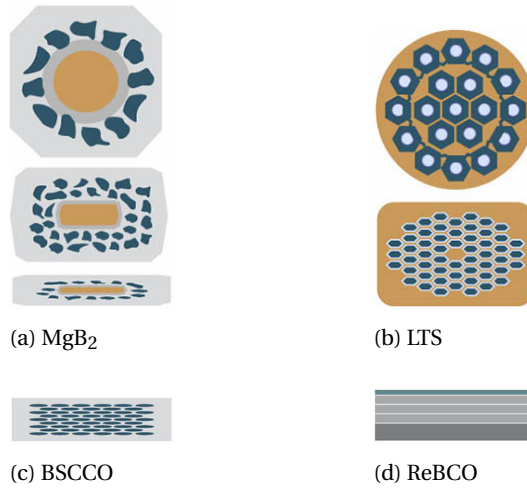
(a) MgB$_2$

(b) LTS

(c) BSCCO

(d) ReBCO

Figure 2.10: Cross-section sketch of LTS (NbTi or Nb$_3$Sn), MgB$_2$ and HTS (1G: BSCCO and 2G: ReBCO). Except that ReBCO is coated superconductors, BSCCO, MgB$_2$ and LTS are all multi-filamentary superconductors. Coated superconductors are in strip shape while multi-filamentary ones can be round or striped. [51]

field capability and hardness of the material, it is considered as a good starting point to design a superconducting generator for wind turbines. In this thesis, we mainly use MgB$_2$ for the electromagnetic study for designing a superconducting generator. LTS and HTS will be discussed in Chapter 7 when we look for the potential performance of a partially superconducting generator.

The MgB$_2$ wire used in this thesis is fabricated by Columbus Superconductors [57]. The cross-section of the wire is depicted in Fig. 2.11. A single wire has 19 MgB$_2$ filaments embedded, and arranged approximately elliptically, in a nickel matrix. The fill factor is 21.5% and the twist pitch is 0.3 m. The dimension is 0.5 mm x 3 mm with an additional 0.2 mm thick copper strip soldered to one longer side of the wire. The critical characteristics of the employed MgB$_2$ wire in the $J - T$ plane are shown in Fig. 2.12. At 10 K and 20 K, a current density above 100 A/mm^2 can be achieved in the magnetic field below 5 T and 3 T, respectively. The operating temperature remarkably limits the current density in high magnetic fields. However, to avoid cooling difficulties similar to LTS, we primarily study the performance of the MgB$_2$ at 20 K in this thesis as a starting point. Other temperatures will be involved in Chapter 7 when we look for the potential performance of a partially superconducting generator.

Note that engineering (critical) current density is different from (critical) cur-
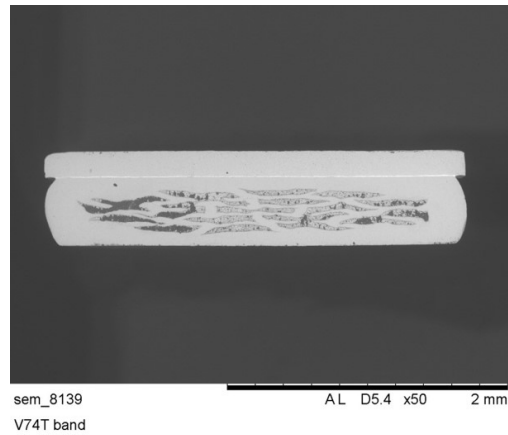
2

Figure 2.11: Cross-section of a single MgB$_2$ wire used in this thesis.
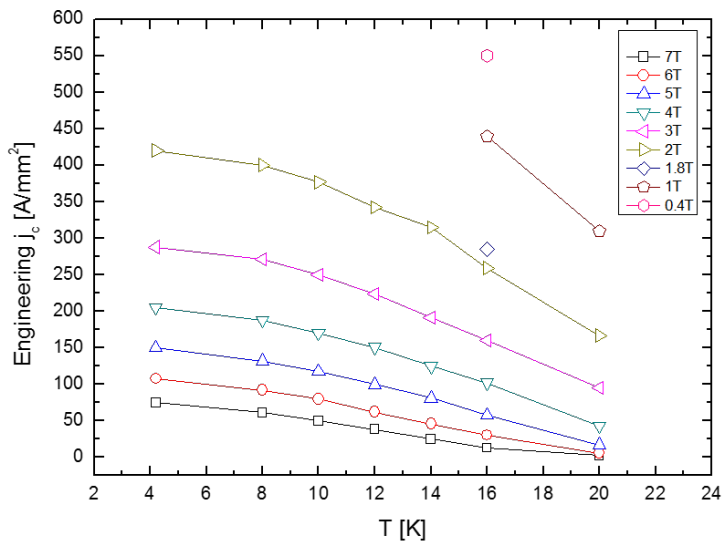

Figure 2.12: Critical characteristics of the employed MgB$_2$ in the $J - T$ plane.

rent density for characterizing a superconducting material. Engineering (critical) current density is defined as the (critical) current density of a superconducting wire. Critical current density is defined as the critical current density of the superconduct-

ing region of a superconducting wire. In large-scale applications, such as electrical machines, engineering critical current density is extensively used instead of critical current density. In this thesis, we use the term "critical current density" for engineering critical current density for the purpose of simplicity unless particularly pointed out.

2.3. SUPERCONDUCTING MACHINES

Superconducting machines are electrical machines which have superconducting windings to excite the magnetic field and produce the electromagnetic torque. Superconducting generators are superconducting machines which operate in generator mode. The used superconducting materials are multi-filamentary or coated wires consisting of multiple superconductors and other functional materials.

With zero DC resistance, superconducting wires are capable of carrying very large current densities. Superconducting machines take this advantage to excite magnetic fields which can be much greater than conventional machines using copper wires or permanent magnets.

2.3.1. SIZING OF AN ELECTRICAL MACHINE

Interests of applying superconductors in electrical machines originate from sizing electrical machines. The electromagnetic power of an electrical machine is defined by

$$P = \omega_m T_e \tag{2.4}$$

where ω_m is the mechanical rotational speed of the rotor of a machine and T_e is the electromagnetic torque of a machine. In large direct-drive wind turbines, the rotational speed ω_m is very low due to the limitation of keeping a safe tip speed of the wind turbine blades. Hence, the electromagnetic torque T_e must be sufficiently high to achieve the electromagnetic power and then the nominal output power.

The average electromagnetic torque T_e is a function of the average shear stress σ, the air gap diameter D and the active length L of a machine [58]:

$$T_e = \frac{\pi}{2} D^2 L \sigma \tag{2.5}$$

where the average shear stress σ of an electrical machine can be calculated by

$$\sigma = BA \tag{2.6}$$

where B and A are called the magnetic loading (average air gap magnetic flux density) and electrical loading (linear current density) of a machine, respectively. The

electrical loading A is proportional to the current density of the armature winding $A \propto J_s$. The magnetic loading B is determined by the field current density J_f [59].

The electromagnetic torque T_e must be very high in a direct-drive generator. To limit the size of the generator (D or L), we need to increase the shear stress σ by either increasing the magnetic loading B or the electrical loading A. The need for such increases means that we need to increase the current density either in the field winding J_f or in the armature winding J_s or both.

Large wind turbines require electromagnetic torques in the order of about 10 MNm for 10 MW and about 30 MNm for 20 MW. The generator size can roughly be estimated for a 10 MW direct-drive wind turbine. If we use copper conductors for the field and armature windings, the current density of about $J_f = J_s = 3$ A/mm^2 will result in a generator diameter of about $D = 10$ m if the generator length is set to $L = 1$ m. Instead, if we apply superconducting field winding with $J_f = 260$ A/mm^2, it is possible to reduce the generator diameter to $D = 4.3$ m with the generator length of $L = 1.88$ m [20]. Further, if we apply both superconducting field and armature windings with $J_f = 160$ A/mm^2 and $J_s = 100$ A/mm^2, it is claimed to reduce the generator diameter to $D = 3.8$ m with the generator length of only $L = 0.8$ m [26].

Hence, the reduction of generator size will be remarkable by applying superconductors, like what is expected in Fig. 1.4. It can be expected that the weight of electrical machines can also be effectively reduced with a smaller size, both of which are radically the motivation to study and develop superconducting machines.

Table 2.2: Overview of three fundamental machine types.

	DC	Induction	Synchronous
Rotor winding	AC	AC (variable frequency)	DC
Stator winding	DC	AC (fixed frequency)	AC (variable frequency)
Power capacity	low	high	high
Primary application	motor, diesel gen.	motor, DFIG	power generator
Application in MW wind turbines	none	geared DFIG	direct-drive or geared
Suitability for MW SC generators	low	low	high[†]

[†] Only when the field winding is superconducting while the armature is not.

2.3.2. MACHINE TYPE

Electrical machines can generally be divided into three basic types: DC (direct current) machine, induction machine and synchronous machine [60]. Each type can operate in both generator and motor modes, but only one of the modes can be de-

signed for satisfactory performance. Above all, not all the three machine types are suitable for applying superconductors. When talking about the suitability of a machine type, we have two criteria:

- adoption of superconductors, and
- feasibility for mega-watt wind turbines.

By overviewing the properties of the three generator types in Table 2.2, the choice space is narrowed down to only synchronous generators which meet both of the criteria.

2.3.3. BASIC STRUCTURE OF A SUPERCONDUCTING SYNCHRONOUS GENERATOR

A superconducting synchronous generator has a DC field winding and an AC armature winding. The field winding is superconducting with superconductors at a low temperature. The armature winding can be either superconducting at a low temperature or non-superconducting with copper conductors at an ambient temperature. Appropriate cooling must be provided to the superconducting winding(s) to maintain the low operating temperature. Structural support must withstand the high torque produced by high magnetic fields. A torque tube or more precisely, a torque transfer element must transfer the torque through the cold winding to warm supports of the generator [61, 62].

One of the basic structures of a superconducting synchronous generator is sketched in Fig. 2.13, which has been widely proposed in the literature. The rotor is accommodated in a cryostat which maintains the operating temperature for the superconductors. Effective cooling is achieved by several means and cryocooler cooling shown in this figure is a popular concept. The electromagnetic part of a superconducting machine consists of field winding, armature winding and the cores to support the windings and increase the magnetic field.

Superconducting coils are usually designed in racetrack shape as illustrated in Fig. 2.14. This shape facilitates manipulating the bending of wires according to the minimum bending radius of superconductors [64, 65]. Each superconducting field coil forms a pole of the synchronous generator. Each pole excites a magnetomotive force (MMF) which is almost squarely distributed along the air gap circumference. Individual field coils are connected in series to form the field winding.

2.3.4. PARTIALLY OR FULLY SUPERCONDUCTING

If a generator has a superconducting field winding with a non-superconducting armature winding, we call it a partially superconducting generator (Fig. 2.13). If both windings are superconducting, as illustrated in Fig. 2.15, we call it a fully superconducting generator. In wind turbine application, most of attention is being paid to

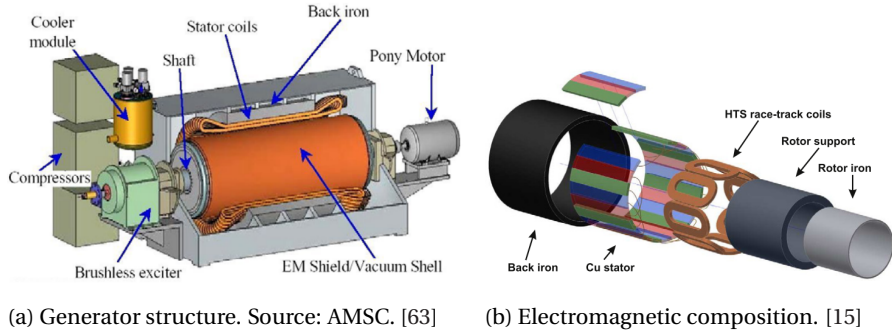(a) Generator structure. Source: AMSC. [63]   (b) Electromagnetic composition. [15]

Figure 2.13: Sketch of a superconducting synchronous generator structure. There are many possibilities of a superconducting machine design. This is only one of them, which is HTS partially superconducting machine, and its magnetic flux is in the radial direction.
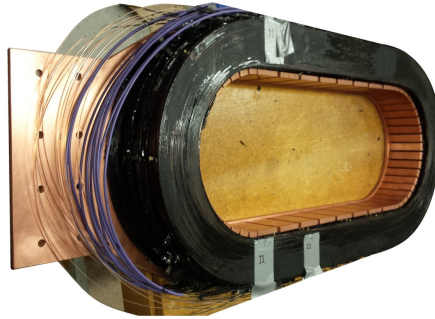

Figure 2.14: Racetrack superconducting coil (MgB$_2$) for test in the INNWIND.EU project. [66]

partially superconducting generators mainly due to three reasons:

• The level of AC losses in a superconducting armature winding is unacceptable for currently available cryogenic cooling technology [26, 29, 67]. The unacceptability is high for HTS but low for multi-filamentary LTS and MgB$_2$ with ultra-fine filaments.

• Conventional armature winding design can easily be retrofitted to use and only the rotor needs new design [20, 21]. Design of a superconducting armature winding and its cooling takes much more innovative efforts [25, 68–70].

• The cold mass of a partially superconducting generator is smaller compared to that of a fully superconducting generator. The cold mass can further be reduced when special cryostat design applies to the field winding, e.g. modular cryostat pro-

posed by Technalia [23]. Cooling for smaller cold mass can be easier to manipulate, although the thermal capacity will become smaller.
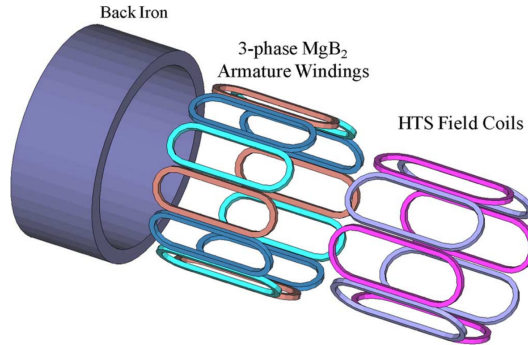
Figure 2.15: Sketch of a fully superconducting machine concept. This is one possibility with an HTS field winding and an MgB$_2$ armature winding. [70]

However, fully superconducting generators have their own advantages. As mentioned in Section 2.2.1, the ultimate and most exciting advantage is significant reduction of the generator size (to boost the power density, in other words), because the superconducting armature winding produces a high electrical loading. As listed in Table 2.3, we can also break down the advantages and disadvantages of these two superconducting types from the generator design point of view.

Some meaningful attempts have been made to utilize superconductors in the armature winding. Conceptual designs are being developed to reduce the AC losses in the armature winding [71–75]. Fully superconducting generators are considered as a long-term goal for being applied to wind turbines. On one hand, the AC losses will become increasingly smaller and finally acceptable as the superconducting materials are advancing. On the other hand, the cryogenic cooling technology will one day become capable of the high level of AC losses that a superconducting armature winding produces today.

At present or in near future, the most feasible option is thought to be partially superconducting generators, although their effects on increasing power density is not as remarkable as fully superconducting generators.

2.3.5. RADIAL OR AXIAL FLUX

Electrical machines can also be divided into radial, axial [76, 77] and transverse flux machines [78, 79], regarding the direction of magnetic flux as their names suggest. Radial flux generators have dominated the power generation industry as well as the

Table 2.3: Comparison between partially and fully superconducting generators.

	Partially superconducting	Fully superconducting
Field winding	superconducting	superconducting
Armature winding	non-superconducting	superconducting
Magnetic loading	high	high
Electrical loading	low	high
Power density[†]	moderately high	very high
AC loss	low	high[††]
Magnetic air gap	large	small[†††]
Size and weight[†]	moderately small	very small
Cost[†]	high	very high
Proposed application	wind energy, ship propulsion	aerospace

[†]Compared to conventional synchronous generators.

[††]Ultra-fine filaments can limit the AC loss of a superconductor at a moderate level.

[†††]Assuming the field and armature windings are located within the same cryostat.

wind turbine market. Because not only people can use the well established design and operation experiences of such machines, but also they are superior to axial flux and transverse flux ones in most aspects. Transverse flux concepts are not mature yet in any power generator. They have low power factors due to large armature leakage fields so the output active power is small. Although power factors can be corrected by a few means, such as active current control by power converters or magnetic circuit optimization, transverse flux machines have rather complicated structures with complex core designs for manufacturing [80]. Thus, we only compare here the radial and axial flux machines (Fig. 2.16) as given in Table 2.4. Nevertheless, transverse flux superconducting generators are being investigated for wind turbine applications (Fig. 2.17). The latest concept can be found in [24] with a few merits highlighted.

Radial flux machines have been concluded to be better than axial flux machines regarding costs when the output is more than 100 kW [29]. Thus, the radial topology is more suitable for generators for mega-watt wind turbines. Axial flux machines are pointed out to become attractive when the number of poles is high and axial length is short [83]. However, superconducting machines usually have a small number of poles which could be a result of the minimum bending radius of superconductors as well as space limitation from mechanical supports [29]. In large offshore wind wind turbines (10-20 MW), radial flux generators are therefore preferred when cost and reliability are of highest design priority.
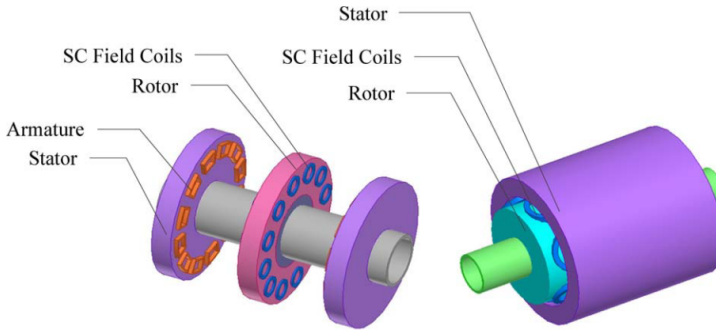
Figure 2.16: Sketch of axial flux and radial flux machine structures. Left: axial flux. Right: radial flux. [29]
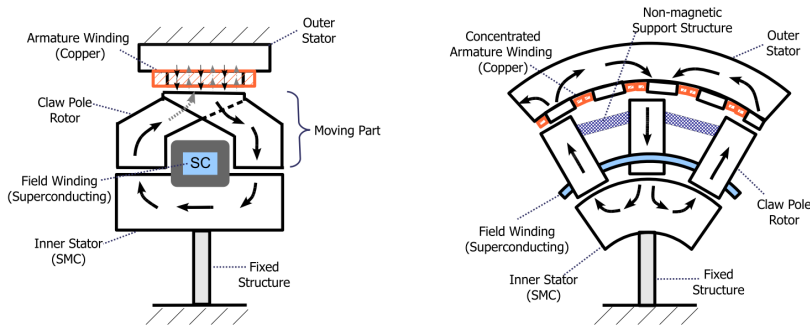

Figure 2.17: Concept of transverse flux superconducting machine. Left: axial cross-section view. Right: vertical cross-section view. [81]

2.3.6. CRYOGENIC COOLING

Superconductors must operate below their critical temperatures. In most cases, they need to be cooled down further to a lower temperature to attain satisfactory performance. For example, LTS prefer 4.2 K or even lower, MgB_2 are proposed for 10-20 K, and HTS are usually proposed for 20-50 K for electrical machines and 77 K for cables and FCLs. In such a vast range of cryogenic temperatures, the cooling efficiency is quite different. Cooling methods and applied coolants are not the same either. Moreover, couplings must be designed to incorporate the cooling system to the rotating electrical machine.

COOLING EFFICIENCY

In general, the cooling efficiency at the required cryogenic temperatures is low. Two factors limit the cooling efficiency. One is the Carnot efficiency which depends on

Table 2.4: Comparison between radial and axial flux superconducting generators [82].

	Radial flux	Axial flux
Torque to volume ratio	larger	smaller
Torque to mass ratio	smaller	larger
Generator diameter[†]	larger	smaller
Generator length	larger	smaller
Air gap maintaining	easy	difficult for large diameter
Cogging and noise	design dependent	low[††]
Field coil shape	racetrack (locally concentrated field)	can be circular (more uniform field)

[†]Due to structural stability.

[††]Slotless machines.

temperature gradients [84] and the other is the efficiency of refrigerators.

The Carnot efficiency η_c is defined as

$$\eta_c = \frac{T_L}{T_H - T_L} \tag{2.7}$$

where T_L is the cryogenic temperature and T_H is the ambient temperature. It can be seen that the lower the cryogenic temperature, the lower the Carnot efficiency. For example, $\eta_c = 1.4\%$ for $T_L = 4.2$ K and $\eta_c = 34.5\%$ for $T_L = 77$ K, both with $T_H = 300$ K.

At present, the typical efficiency of a refrigerator is 20% which has to be multiplied to the Carnot efficiency. Consequently, the overall cooling efficiency η is even much lower. For example, $\eta = 0.28\%$ for $T_L = 4.2$ K and $\eta = 6.9\%$ for $T_L = 77$ K ($T_H = 300$ K).

Another way to express the overall cooling efficiency is the specific power or so-called cryogenic penalty ($= 1/\eta$). This expression means the number of watts of input power required to remove 1 W of heat at the cryogenic temperature. For example, it requires 14.5 W of input power to remove 1 W of heat from the 77 K region. The cryogenic penalty is 357 W input for 1 W at 4.2 K. The cryogenic penalty at cryogenic temperatures is shown in Fig. 2.18. In this figure, the boiling point of widely used coolants and the critical temperature of different superconductors are also provided for giving a clearer picture of how the cryogenic penalties affect the selection of superconductor types.

CONDUCTION (INDIRECT) OR DIRECT COOLING

The cooling methods for superconductors can be divided into direct and indirect cooling [41, 86, 87]. LTS magnets employing NbTi or Nb_3Sn are in general cooled by submerging them into liquid helium (LHe). This cooling is called pool-boiling
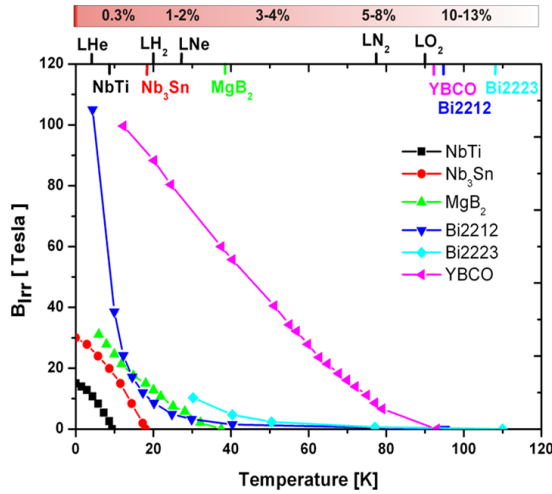
Figure 2.18: $B - T$ critical characteristic of different superconductors, on top of which is the cryogenic penalties at different cryogenic temperature. Different superconductors lie in different ranges of critical temperatures and cryogenic penalties. [85]

method which can also apply to other liquid coolants such as liquid hydrogen (LH$_2$), neon (LNe), nitrogen (LN$_2$) and oxygen (LN$_2$). When demanding more effective and controllable cooling, superconducting magnets are cooled by a forced flow of liquid coolants through conduits between superconductor strands. Very large magnets may use both the approaches.

(a) Coil in close contact with coolant tubes.

(b) Coil in contact with a cryocooler.
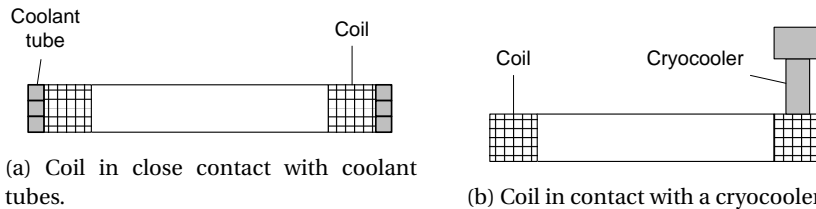
Figure 2.19: Sketch of conduction cooling concepts. Reproduced from [88].

Indirect cooling is also referred to as conduction cooling. This cooling method is simple and convenient with cryocooler refrigerators [89]. The heat generated in part of superconducting coils is transfered to the cold head of a cryocooler by thermal conduction. The thermal resistance between the coil and the cryocooler must

be designed sufficiently low. The heat transfer can also be realized through tubes in close contact with the surface of a superconducting coil. A coolant which can operate in a closed cycle or with a storage container flows inside the tubes to transfer heat. These two conduction cooling concepts are sketched in Fig. 2.19.

The popular cryocoolers are cryogen free: Gifford-McMahon (G-M) [90, 91], Stirling [92] and Pulse-Tube coolers [93]. All of them apply regenerative heat exchange with oscillating gas flow. The G-M concept is most popular, primarily because it isolates the compressor from the regenerator and displacer and then allows a modified commercial air-conditioning compressor to be used [88]. For low temperature applications, the coolers usually have two stages of temperature, e.g. 300 K-30 K-4 K or 300 K-80 K-20 K, for the purpose of increasing the Carnot efficiency. Single-stage coolers are also used but usually for high temperatures. Stirling cryocoolers are more efficient but more costly than G-M cryocoolers. At present, pulse-tube cryocoolers to date only have small cooling capacities and they need further development.

(a) Gifford-McMahon (Sumitomo RDK-415D).

(b) Stirling (CryoTel GT).

(c) Pulse-tube (Sumitomo RP-062B).
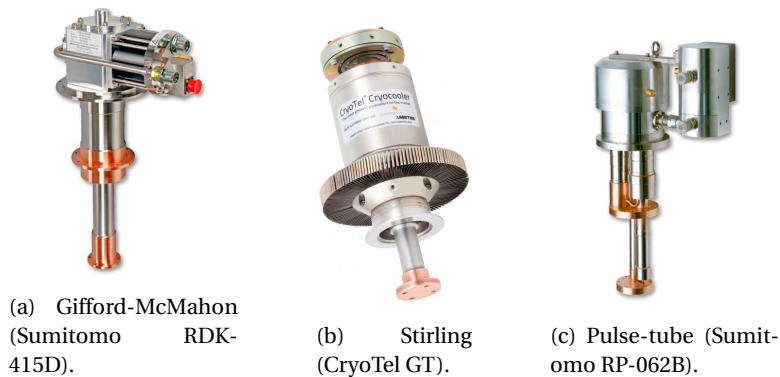
Figure 2.20: Commercial products of three typical cryogen-free cryocooler concepts with regenerative heat exchange.

In wind turbine applications, either direct or indirect cooling can be adopted to a superconducting generator. Regarding cost and construction complexity, conduction cooling with cryocoolers is preferred. The cryocoolers and compressors can be placed outside the generator. Only the cold heads are plugged into the cryostat of the generator and contact the thermal conductor. However, conduction cooling may lead to non-uniform temperature distribution over a superconducting coil and must be carefully examined.

CRYOSTAT

A cryostat is used to house and maintain the superconducting winding in cryogenic environment suitable for the operation of superconductors [94]. Usually, a cryostat means a cryostat assembly which contains a shell, a vacuum chamber, multi-layer thermal insulation and torque transfer elements. With conduction cooling, thermal conductors or cooling tubes are also integrated into the cryostat. Thermally, a cryostat prevents ambient and radiation heat from getting into the cryogenic environment. Mechanically, it transfers the force or torque from the cold parts to the warm parts of the generator. Magnetically, its electrically conductive shell may act as a damping winding or an electromagnetic shield.

Conventionally, a cryostat is shaped cylindrically as large as capable of accommodating the whole rotor or only the field winding assembly, as shown in Fig. 2.21 and Fig. 2.22. This configuration originates from the design and practice of superconducting magnets for MRI and accelerators but results in a relatively large cold mass to be cooled. To minimize the cold mass inside the cryostat as well as modularize the superconducting winding, a modular cryostat concept has been proposed by [23] and [30]. As illustrated in Fig. 2.23, each superconducting field coil has its own cryostat in the same racetrack form. Shells, vacuum chambers and multi-layer thermal insulation are still necessary. Forces are transfered from the cold coil to the warm rotor pole core in the coil center through the cryostat wall. Besides the advantages of cold mass and modularity, this concept enables to employ salient poles which have been extensively applied in conventional synchronous generators. More advantages and applications of such combination of salient poles and modular cryostat will be involved or discussed in every later chapter.

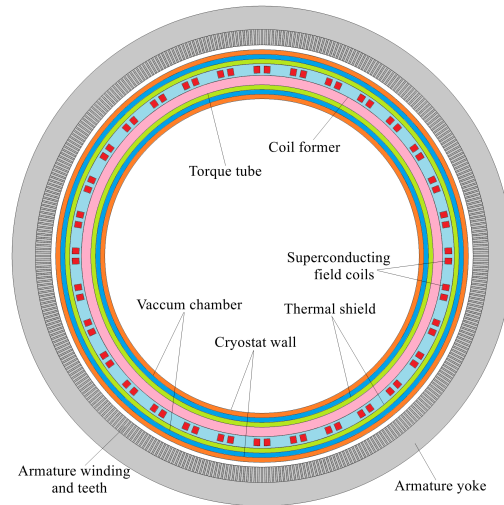Figure 2.21: Cylindrical cryostat of a commercial product (Babcock Noell GmbH). [95]

Figure 2.22: Sketch of the cross-section of a cylindrical cryostat in a partially superconducting machine. The superconducting field winding assembly is located within the cryostat. Reproduced from [96].

(a) Assembly.   (b) Coil and cooling.
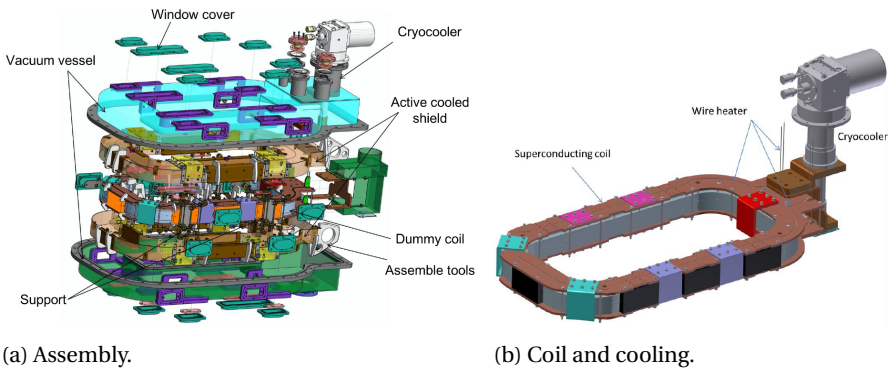
Figure 2.23: Modular cryostat assembly with its components, proposed by the Suprapower project [97, 98].

ROTATING OR STATIONARY SUPERCONDUCTING FIELD WINDING

When cooling the rotating superconducting field winding of a synchronous generator, coupling or sealing is required between the stationary part of the cryogenic

cooling system and the rotating cryostat and field winding. However, the rotating coupling can be avoid by letting the field winding stand still but the armature winding rotate. This reversal of the rotating role requires brushes and slip rings to couple the rotating armature winding to the power converter. The full power will impose onto the brushes which require sophisticated contact. The superconducting field winding remains stationary for simpler cooling system coupling. GE proposed in [20] this concept of rotating armature for their LTS generator design for 10 MW wind turbines.

However, a rotating coupling is not so difficult to realize that most of the superconducting machine designs have still proposed rotating field windings. Although the cooling efficiency may drop due to slight leakage, it is not necessary to introduce less-reliable fully rated brushes to a rotating armature winding. The advantage of rotating field windings may not be recognized by LTS generators but can apply well to HTS generators.

So far, most of the superconducting machine prototypes have employed the G-M cryocoolers. The cold heads are placed inside the generator and pinned to the rotating cryostat. As sketched in Fig. 2.24 for instance, the cold heads connect to stationary compressors outside the generator housing through a rotating coupling.
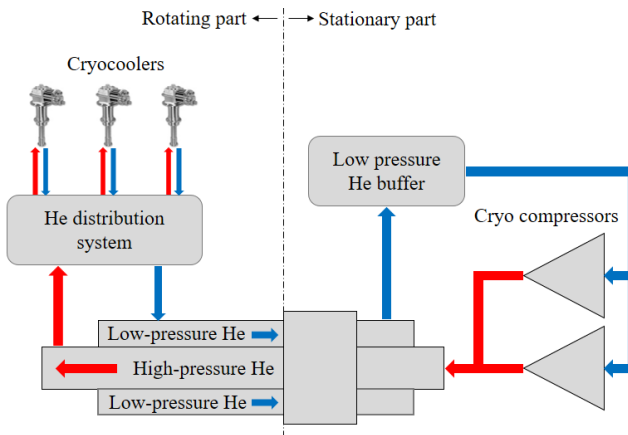

Figure 2.24: Rotating coupling concept: the cryogenic system connected to the rotating and stationary parts of a superconducting generator through rotating coupling (based on G-M cryocoolers). Reproduced from [23].

The rotating coupling concept can also be visualized in Fig. 2.25 proposed by Stirling Cryogenics. Two Stirling cryocoolers are placed outside the generator housing and exchange the warm and cold helium gas out of and into the cold heads in

the generator. The superconducting coils are cooled by the oscillating helium gas flow via cold heads.
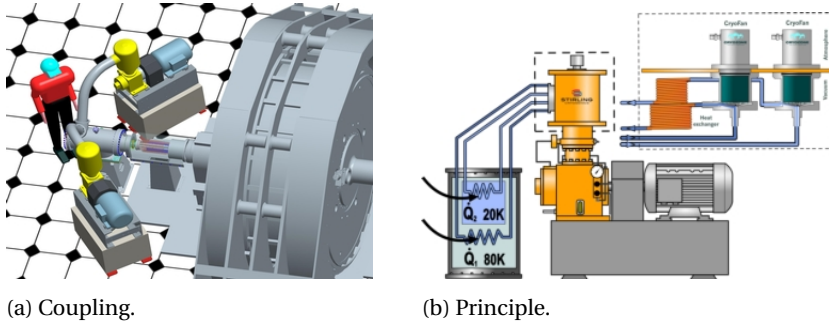

(a) Coupling.

(b) Principle.

Figure 2.25: Sketch of the coupling and principle of Stirling cryocoolers for rotating generators, as proposed by [99].

When it comes to a modular cryostat shown in Fig. 2.23, the cooling is more straightforward. the cryocooler's cold head closely contacts the thermal conduction plates (copper). The heat generated by each coil is transferred to the cold head through the copper plates attaching the coil.

2.3.7. DEMONSTRATING PROTOTYPES OF SUPERCONDUCTING MACHINES
Over the last decades, a few pilot projects experimentally demonstrated the feasibility and operation of superconducting machines. At the beginning, the superconducting machine prototypes were designed, built and tested for ship propulsion as motors. Then, more power generators were built and tested. In recent years, a few projects are trying to demonstrate superconducting generators in wind turbine applications. These projects and the corresponding superconducting machines are summarized in Table 2.5.

2.4. INTEGRATION OF SUPERCONDUCTING GENERATORS IN WIND TURBINES

Based on the previous overviews and discussions, we can make a few fundamental choices for a superconducting generator design for wind turbines. The following properties are now preferred for designing the generator:

• Synchronous machine.

• Partially superconducting- only the field winding is superconducting while the armature winding is not.

2

Table 2.5: Demonstrating projects and superconducting machine prototypes built or being built.

Designer	Report year	Power	Speed	SC material	Cryogenic Temperature	Application
AMSC [100]	2002	3.5 MW	1800 rpm	BSCCO-2223	35 K	Ship propulsion
AMSC [17]	2006	5 MW	230 rpm	BSCCO-2223	32 K	Ship propulsion
AMSC [101]	2011	36.5 MW	120 rpm	BSCCO-2223	30 K	Ship propulsion
AMSC [63]	2006	8 MVar	-	BSCCO	-	Synchronous condenser
Converteam [102]	2009	1.7 MW	214 rpm	BSCCO-2223	30 K	Power generator
GE [103]	1985	20 MVA	3600 rpm	NbTi	4 K	Power generator
GE [104]	2008	1.3 MW	10500 rpm	BSCCO	30 K	Airborne generator
Siemens [105]	2006	400 kW	1500 rpm	BSCCO-2223	25-30 K	Power generator
Siemens [105]	2006	4 MVA	3600 rpm	BSCCO-2223	25-30 K	Power generator
AMSC Sea-Titan* [106]	Ongoing	10 MW	10 rpm	2G HTS	-	Wind power generator
AML* [28]	Ongoing	10 MW	-	MgB$_2$	-	Wind power generator
EcoSwing* [107]	Ongoing	3.6 MW	15 rpm	YBCO	-	Wind power generator
ICMAB-CSIC* [108]	Ongoing	2 MW	-	-	-	Wind power generator

*The details of the ongoing wind power projects are very limited.

- Radial magnetic flux.
- Conduction cooling with cryocoolers.
- Rotating superconducting field winding.

Given these five choices, a superconducting generator can be integrated into a direct-drive wind turbine nacelle and connected to the power grid through a fully rated power electronic converter, as sketched in Fig. 2.26. Various converter concepts and control strategies have been concretely reviewed in [80, 109, 110] for direct drive systems.
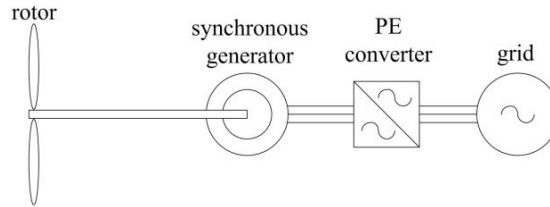

Figure 2.26: Sketch of direct-drive concept. The direct-drive (superconducting) synchronous generator is connected to the power grid through a fully rated power electronic converter. [14]

Different nacelle structures may result in different integration concepts [111, 112]. Here, we introduce three up-to-date wind turbine integration concepts for 10 MW wind turbines available in detail and then the conceptual nacelle from the INNWIND.EU project for 10-20 MW wind turbines. All these concepts are aimed at improving the feasibility of integrating a superconducting generator to a large direct-drive wind turbine.

2.4.1. THREE CONCEPTS IN THE LITERATURE

A few integration concepts have also been proposed by other research projects prior to or in parallel with the INNWIND.EU project. Some are completely new while the others evolve from conventional concepts. Many interesting concepts are proposed for 10 MW direct-drive wind turbines which employ partially or even fully superconducting synchronous generators. Three of them have been published and the details can be found in the literature. The others, e.g. AMSC's and AML's concepts, are not available in detail due to confidentiality issues. Here, the three published concepts are briefly introduced.

GE CONCEPT

GE proposed their integration concept in [20] for a 10 MW direct-drive LTS generator. There are two shafts together supporting the generator as shown in Fig. 2.27. One is stationary in the center for supporting the inner field assembly. The other

for supporting the outer armature assembly is rotating on the stationary shaft via a bearing. The field assembly is inside a cryostat in which liquid helium is cooling the field winding through conduction cooling tubes. The liquid helium is liquefied by cryocoolers located at the two ends of the field assembly.

This concept is novel and suitable for the designed small generator diameter. The nacelle is located behind the hub, but the two-shaft concept can also be used for a front nacelle when an inner stationary field winding is preferred.
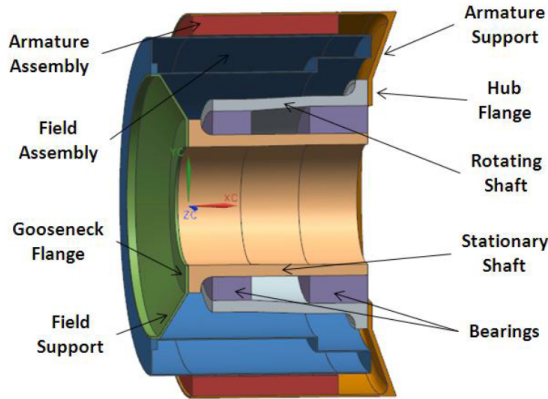
Figure 2.27: Integration concept by General Electric for a 10 MW direct-drive LTS generator. [20]

SUPRAPOWER CONCEPT

The European FP7 project Suprapower [98] has proposed a conceptual nacelle integration. They designed such a large-diameter generator to reduce the generator weight that the generator is axially very short. The small aspect ratio results in the current nacelle concept as depicted in Fig. 2.28. The rotor with field winding is spinning on a stationary hollow shaft via long supporting beams and a bearing. The stator with armature winding is fixed to a large frame which houses both the rotor and stator.

As introduced in 2.3.6, the field coils are housed in individual modular cryostats. Distributed cryocoolers exchange the warm and cold helium gas with the compressors which are concentratedly placed in the hollow shaft. The nacelle is placed behind the hub and may not be capable of being in front due to the large diameter.

SIEMENS CONCEPT

Siemens Wind Power [113] designed a nacelle concept by changing the current direct-drive PM generators into a superconducting version. As shown in Fig. 2.29, in the
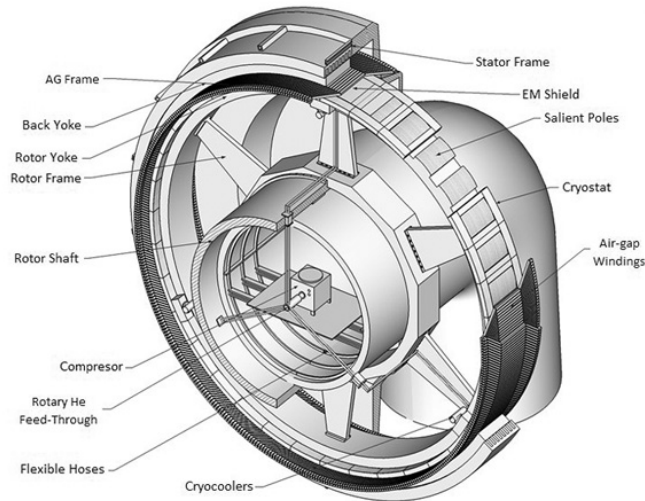
2

Figure 2.28: Integration concept from the Suprapower project for a 10 MW direct-drive MgB$_2$ generator. Patented by Tecnalia. [98]

center of the nacelle is also a stationary hollow shaft supporting the inner armature winding. The outer field winding is driven by the spinning hub. This layout and the placement of the cooling system are both similar to those of the "Kingpin" nacelle, but the location of the nacelle is behind the hub and the generator can be designed with an either large or small diameter.

2.4.2. INNWIND.EU CONCEPT

For the INNWIND.EU project, a conceptual nacelle using a kingpin [114] is designed for direct-drive generator systems. As shown in Fig. 2.30, the nacelle is located in front of the turbine hub. The designers claim that this concept not only can be used for 10-20 MW wind turbines but will be the only feasible option for 20 MW [85]. In this concept, the stationary axle (called kingpin) holds both the blades and the generator through one or two bearings. The shorter distance between the large blades for capturing 10-20 MW power and the tower will effectively reduce the bending moment. The front generator will not add significant mechanical loads to the tower because the nacelle weight is negligible compared to the whole mechanical loads.

To adapt to the stationary kingpin, the generator would better have an inner stationary armature winding and an outer rotating field winding. As illustrated in Fig. 2.31, the hollow axle provides a tunnel for placing cryogenic cooling pipes connect-
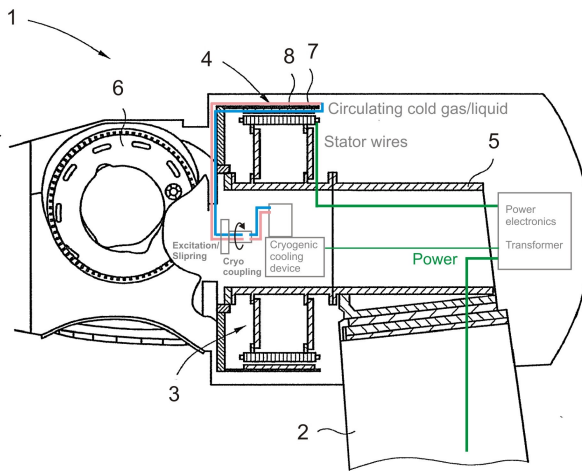
Figure 2.29: Integration concept by Siemens Wind Power for a 10 MW direct-drive HTS generator. (1-Nacelle. 2-Tower. 3-Stator support. 4-Rotating superconducting field winding. 5-Stationary hollow shaft. 6-Hub. 7-Cryostat. 8-Fixed armature winding.) [85]

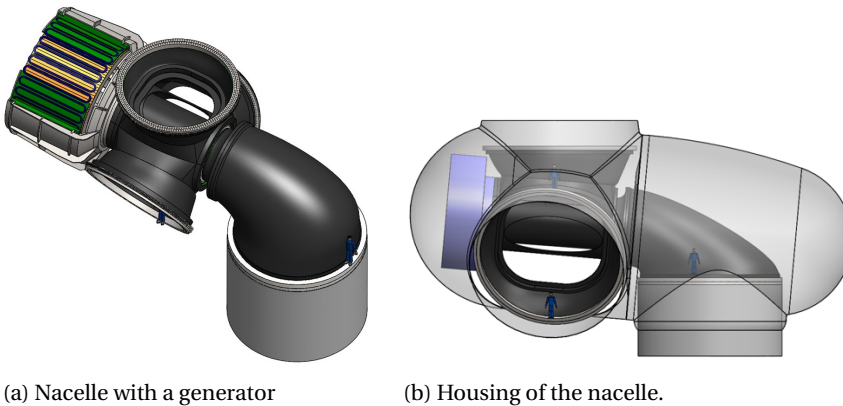ing cryocoolers at the generator side to compressors at the tower side.

(a) Nacelle with a generator   (b) Housing of the nacelle.

Figure 2.30: INNWIND.EU nacelle concept using a kingpin for 10-20 MW direct-drive wind turbines. The generator is located in front of the hub. [11]

Mechanically, the generator can be supported by the main bearing of the hub or a separate bearing, depending on the mechanical load from the generator. A possi-
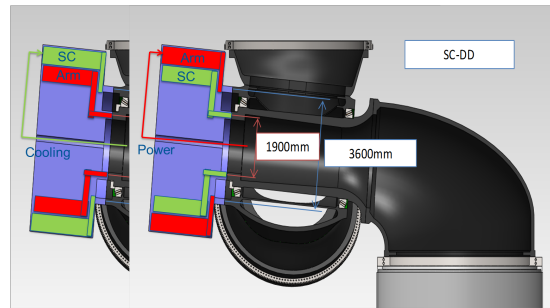
2

Figure 2.31: Two possibilities of arranging the superconducting field winding and the copper armature winding in the INNWIND.EU nacelle concept. The superconducting field winding will rotate if placed outside. The axle hollow can be used as a channel for placing pipes connecting rotating cryocoolers' cold heads to stationary compressors. [85]
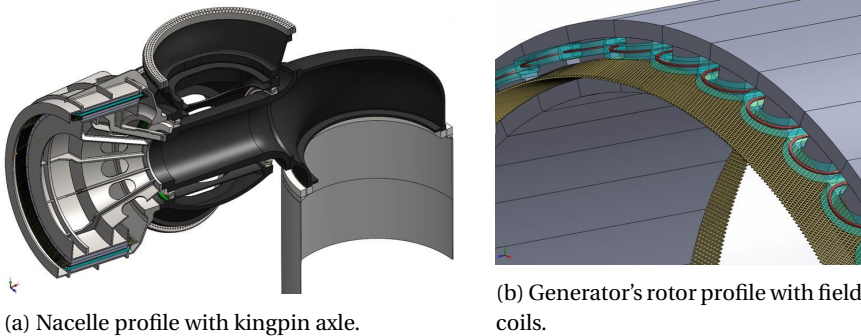

(a) Nacelle profile with kingpin axle.

(b) Generator's rotor profile with field coils.

Figure 2.32: A single-bearing scenario of mechanical integration of the superconducting generator to the conceptual INNWIN.EU nacelle. The stationary kingpin holds both the hub and the generator. It is also possible for the generator to have a separate bearing with a lengthened kingpin. Courtesy of DNV GL.

ble scenario of mechanical integration with a single-bearing is depicted in Fig. 2.32. Note that the generator for this scenario employs modular cryostats with salient poles, which is just a particular design possibility to be examined in later chapters. This nacelle may not like large generator diameters due to the limitation of the conic angle of blades, suggesting that the generator diameter would better remain sufficiently small.

The INNWIND.EU nacelle concept will exclusively be adopted throughout the following chapters.

2.5. CONCLUSION

T HIS chapter has introduced and pictured a superconducting drive train for 10-20 MW direct-drive wind turbines, from superconductors to superconducting generators then to superconducting drive trains. Relevant concepts around superconducting machines, e.g. superconductivity, cooling efficiency, have been described. The integration shows that it is realistic to mount a superconducting generator in a direct-drive wind turbine.

Whatever the nacelle structure, a superconducting generator for this application has four fundamental properties:

• Synchronous machine. This choice is believed to dominate the design of superconducting machines.

• Partially superconducting. This choice may change to fully superconducting as long as either AC losses can effectively be reduced to acceptable levels or cooling technologies become sufficiently advanced to handle the AC losses in a superconducting armature winding.

• Radial magnetic flux. This choice is believed to dominate the design of superconducting machines.

• Rotating superconducting field winding. Rotating field is considered easier than rotating armature. The choice of this property may not be critical and in some cases dependent more on mechanical construction of a wind turbine nacelle.

To simplify the construction of the conceptual INNWIND.EU nacelle, the generator structure of inner armature and outer field is selected. However, this choice does not change the electromagnetic performance of the generator. In next chapters, we will therefore not be limited by this generator structure. Both inner and outer field winding can be considered.

The choice of cooling method, i.e. conduction or direct cooling, does not change the electromagnetic performance of the generator either. We assume conduction cooling with cryocoolers in the next chapters just for providing a context of cooling, as shown in Fig. 2.31, for electromagnetic studies.

3

TOPOLOGY COMPARISON BASED ON CURRENTLY AVAILABLE MGB$_2$ SUPERCONDUCTORS

3.1. INTRODUCTION

S UPERCONDUCTING synchronous generators are drawing more attention for 10-20 MW direct-drive wind power conversion [11], because they can be lightweight and compact and reduce the levelized cost of energy (LCoE) of the wind turbine [14–16]. Due to the high magnetic field production by superconducting coils, many possibilities exist for designing a superconducting generator. The superconducting coils can be applied only in the DC field winding or also in the AC armature winding. A commonly applied approach is to use an superconducting field winding at a low temperature with a copper AC armature winding at an ambient temperature [29, 115–117]. In such partially superconducting generators, excessive AC losses in the armature winding can be avoided and the feasibility of superconducting generators increases. Among typical superconductor types, MgB$_2$ could be a starting point as a low-LCoE possibility. This superconductor material is usually for operating temperatures of 10-20 K. It is not as expensive as high temperature superconductors but requires less rigorous cryogenic cooling than low temperature superconductors.

For a partially superconducting generator design, many topologies can be considered from the perspective of electromagnetics. A topology differently combine iron and non-magnetic cores in the rotor back core, rotor pole core, stator tooth and stator yoke. They differ in the magnetic reluctance of an electrical machine. Choice of topology could significantly change the cost and efficiency of a superconducting generator and consequently affect the levelized capital cost of energy (LCCoE) of a wind turbine employing this superconducting generator.

This chapter considers twelve topologies employing MgB$_2$ in the field winding, which cover most of the applicable radial-flux possibilities. Some of them have already been proposed in the literature or industry. This chapter compares these topologies regarding the LCCoE of a 10 MW direct-drive wind turbine. This chapter only focuses on the LCCoE as the key performance indicator. The other costs, e.g. installation, operation and maintenance costs, are not taken into account since the LCCoE should be evaluated in first place to identify promising candidates which then move onto further evaluations.

Since the superconductor technology is developing fast, only using the current unit cost and critical characteristic of the MgB$_2$ wires may limit the perspective of comparing the topologies. The topologies that are less advantageous at present may become promising in the long run. Three scenarios are therefore investigated, assuming 1) reducing the wire cost per unit length to 1/4, 2) four times engineering critical current density and 3) the combination of both. The purpose is to check if the topologies providing the lowest LCCoE at present will be overtaken by other topologies if the properties of the MgB$_2$ wire significantly improve.

3.2. Topology-Related Design Issues

3.2.1. Definition of topology

The term of topology can be defined differently. In electrical machinery, the generalized definition of topology covers the following design options:

- Radial/axial/transverse flux.
- Inner/outer rotor/stator.
- Rotating/stationary field winding/armature winding.
- Ferromagnetic/non-magnetic core.
- Fully/partially superconducting.

Regarding superconducting machines, the choice of fully or partially superconducting is another topology issue, but we only consider partially superconducting according to the conclusions in Chapter 2.

As discussed in Chapter 2, only the radial flux is considered for superconducting generators for large wind turbines. The choice of inner or outer rotor and the choice of rotating field or armature winding do not matter unless the nacelle or cryogenic design puts limits onto the structure of the generator. Here we suppose that these two choices are not fixed but open in the rest of this thesis, because this thesis will not address the nacelle design or the cryogenic design.

Hence, only the choice of ferromagnetic or non-magnetic core remains, which can also be defined as topology in a narrow sense. In the rest of this thesis, particularly, a topology is defined as the combination of ferromagnetic and non-magnetic materials in four core components:

- Field core back,
- Field pole core,
- Armature tooth, and
- Armature yoke.

The other three design options covered in the generalized definition of topology will not be considered as topology issues anymore in the rest of this thesis.

3.2.2. Design issues related to topology

In a conventional synchronous machine with a copper field winding or permanent magnets, the core material is usually ferromagnetic, e.g. laminate steel for stator cores and solid steel for the rotor cores. The ferromagnetic material will be saturated when the magnetic flux density goes to a high level, e.g. 1.8 T. A synchronous machine is usually designed for operating with light saturation in its ferromagnetic cores. The purpose of such a design is to produce a sufficiently high magnetic flux density but to avoid negative effects caused by heavy saturation.

This design philosophy would probably change when a superconducting field winding comes into a synchronous machine for field excitation. In the supercon-

ducting field winding flows a rather high current density. e.g. 100 to 200 A/mm^2, which can excite a high magnetic flux density to, e.g., 3 T or even higher in the armature winding. With such a high magnetic flux density, the ferromagnetic core will be heavily saturated. In this case, the use of ferromagnetic cores has four main drawbacks:

• High magnetic flux density in the ferromagnetic material will induce more iron losses, especially when the electrical frequency is high.

• The magnetic flux leakage between adjacent ferromagnetic armature teeth will cause eddy currents in the copper conductors in the armature slots, if the copper conductors are not specially designed for reducing eddy currents.

• Ferromagnetic armature teeth will cause slotting effects which can induce AC losses in the superconducting field winding. Too much AC losses are not acceptable due to both cryogenic cooling capability and efficiency reduction. The slotting effects will reduce if iron teeth are saturated.

• Ferromagnetic materials are heavy so they may reduce the power density. This conflicts with the initial motivation of employing superconducting windings in a wind turbine generator to increase the power density.

It is thus needed to find an alternative material to overcome such downsides of ferromagnetic materials. Generally, this alternative material should have five properties:

• Low iron losses with a high magnetic flux density,

• Less or even no slotting effects,

• Lightweight,

• Not too expensive, and

• Mechanically strong.

From electromagnetics point of view, the suitable material can be characterized as non-magnetic materials. Here a non-magnetic material should also be non-conductive, because we do not want eddy currents in such a material either. Many composite materials are both non-magnetic and non-conductive while stainless steel, for example, is not magnetic but conductive.

Considering mass density, mechanical strength and unit cost, glass fiber G10 has been extensively applied to electrical apparatus [118]. G10 is a composite which is both non-magnetic and non-conductive. Its mass density is about 1850 kg/m^3, which is only about a quarter of the mass density of ferromagnetic steel. Mechanically, G10 is comparable to ferromagnetic steel. A comparison is summarized in Table 3.1 to show the key property differences between glass fiber G10 and ferromagnetic steel.

Using non-magnetic material, e.g. G10, in the machine cores does not definitely mean a better machine design. Despite its advantages over ferromagnetic steel, it has four main disadvantages:

Table 3.1: Property comparison between glass fiber G10 and a typical ferromagnetic steel.

	Glass fiber G10 (FR-4)	Ferromagnetic steel
Relative permeability	1	8000
Electrical conductivity	0	$2 \cdot 10^6$ S/m
Thermal conductivity	0.81 W/(m·K)	50 W/(m·K)
Tensile strength	>310 MPa	490 MPa
Mass density	1850 kg/m^3	7650 kg/m^3

3

• It is not magnetic. The magnetic reluctance of a machine becomes much larger if non-magnetic material replaces ferromagnetic steel. The machine thus demands more superconducting materials to excite a sufficiently high magnetic field, which can be quite costly.

• It has a poor thermal conductivity. If a non-magnetic material is applied to armature teeth, the cooling of the armature winding will need special attention. For example, indirect forced-air cooling may not be capable anymore but direct cooling would be required.

• It introduces manufacturing difficulties. Large machines have hardly employed non-magnetic cores and their manufacturing is nearly all based on the experience of ferromagnetic steel. Therefore, a design of large machines with non-magnetic cores leads to extra costs in money and time due to difficulties in manufacturing the non-magnetic core structures.

• It is generally more expensive than ferromagnetic steel. For example, the current market price of glass fiber G10 is approximately in the order of 15 €/kg while that of ferromagnetic steel laminates is only about 3 €/kg.

As a result of the above-mentioned facts, comparisons between ferromagnetic and non-magnetic cores are necessary for designing a superconducting machine. Based on such comparisons, the design process may require a few critical trade-offs between adopting ferromagnetic and non-magnetic core materials [29]. Generally, the comparison criteria can be the following characteristics for a superconducting machine:

• Cost,

• Size,

• Weight,

• Efficiency,

• Electromagnetic performance, and

• Thermal performance.

3.2.3. ISSUES ON USING FERROMAGNETIC CORES

Using ferromagnetic cores in a superconducting machine needs special attention due to the high magnetic field. Magnetic saturation, losses, forces and slotting effects are worthy of a discussion.

MAGNETIC SATURATION

A ferromagnetic core saturates in a high magnetic field while a non-magnetic core does not. It is then a question of whether to use ferromagnetic cores or not in a superconducting machine, because a superconducting field winding can produce a high magnetic field which can potentially severely saturate the ferromagnetic cores.

Ferromagnetic materials will have lower magnetic permeabilities when heavily saturated. The relative permeability of a heavily saturated ferromagnetic core will approach $\mu_r = 1$ which is the same as that of a non-magnetic material, e.g. air. However, saturation at this time instant depends on its previous state. With the same magnetic field intensity H, the magnetic flux density B has already become much higher in a ferromagnetic core than that in a non-magnetic core, as illustrated in Fig. 3.1. This shows that saturation of a ferromagnetic core does not deteriorate the excitation of high magnetic fields although the excitation is significantly limited. However, the negative effects of iron cores in high magnetic fields must not be ignored.
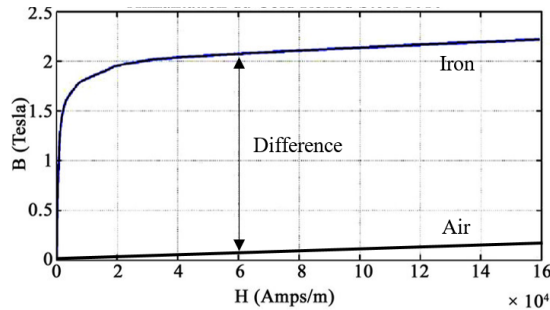

Figure 3.1: Sketch of higher magnetic flux density of iron with full saturation compared to that of air without saturation.

LOSSES AND FORCES

Negative effects could occur in ferromagnetic cores when the magnetic flux density is quite high. One effect is iron losses as a function of magnetic flux density and frequency. However, the fundamental frequency of a 10 MW direct-drive generator could be as low as 3 Hz, for example. In this case, iron losses may be very small.

Another effect is that part of the magnetic flux lines will go through the conductors, i.e. superconducting wires in the field winding and copper conductors in the armature winding. Eddy currents will be induced in these conductive parts and resulting losses could cause problems. Moreover, magnetic forces will directly be imposed on the current-carrying conductors. Hence, special designs will be necessary to suppress the induction of eddy currents and to well support these conductors. In addition, superconducting wires must be sufficiently strong to withstand large mechanical stresses.

SLOTTING EFFECTS

Besides armature winding distribution, slotting effects due to ferromagnetic armature teeth change the air gap flux density at a high frequency [119]. This air gap flux density contains space harmonics which are not synchronous with the rotor rotation. In Fig. 3.2, an example shows the space harmonics of flux density in an air gap. The left figure (Fig. 3.2a) is from a machine with non-magnetic armature teeth and the right one (Fig. 3.2b) is from the same machine with iron armature teeth instead. The spectrum shows that space harmonics contents significantly rise from using non-magnetic to using ferromagnetic armature teeth.

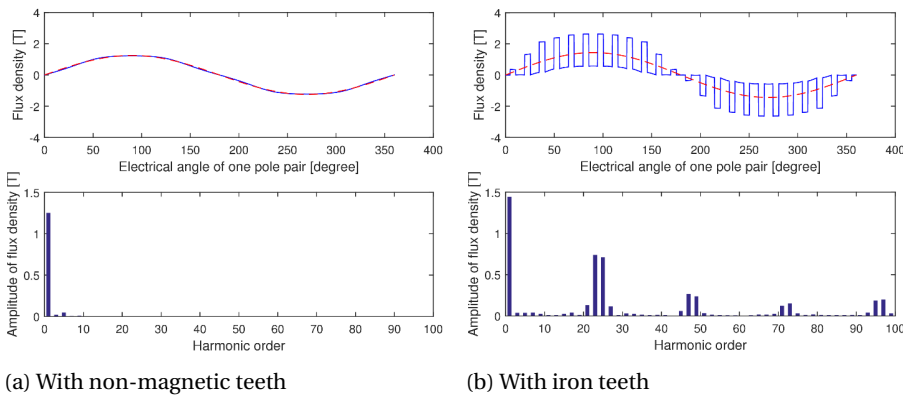(a) With non-magnetic teeth   (b) With iron teeth

Figure 3.2: Slotting effects with iron teeth compared to effects of non-magnetic teeth.

Such space harmonics can go to the region of superconducting field winding and produce AC losses in the superconducting wires and iron losses in the ferromagnetic core parts. If an electromagnetic shield is placed between the field winding and the armature winding for screening the space harmonics and protecting the superconducting wires, eddy current losses will still be produced in this shield itself. All these losses due to slotting effects could lead to reduction of the efficiency and increase of

cooling budgets.

3.2.4. INFLUENCE OF CRYOSTAT DESIGN ON TOPOLOGY

As introduced in Chapter 2, different cryostat designs are accompanied with cold or warm core concepts. The cold core concept makes the topology easy to understand: both the superconducting field winding and the field cores are located inside the cryostat, as sketched in Fig. 3.3a. The cryostat walls are located at both the inner and outer sides of the field winding and the field cores.

The warm core concept consists of two options: cylindrical cryostats or modular cryostats. The former option still uses a tube-shaped cryostat, but the inner cryostat wall separate the field pole core and the field back core. As a result, the field pole core is cold while the field back core is warm, as illustrated in Fig. 3.3b. For topology studies, it is not necessary to separate the field pole core and the field back core so they contact each other with an assumed infinitely thin cryostat wall. However, space for vacuum and thermal insulation must be left between the field winding and this infinitely thin inner cryostat wall.

The modular cryostat concept [23] can be considered as an extension of the cylindrical cryostat concept, but space for vacuum and thermal insulation must be left between one side of the field coil and its surrounding warm cores, as illustrated in Fig. 3.3c. The field pole core can therefore be warm in the center of a field coil and be made as close to the armature as allowed.

For simplification in topology studies, the warm core cylindrical concept is usually considered the same as the cold core concept. Thus, in both these cases, there is not an air gap between the field pole core and the field back core and they contact each other as a whole piece.

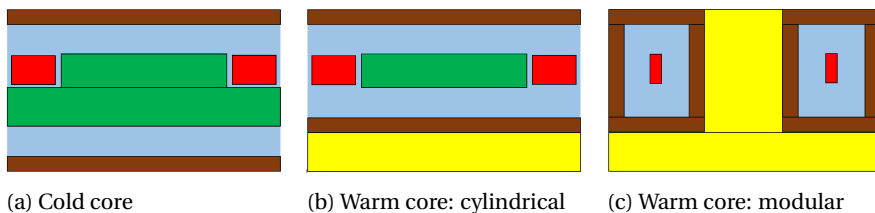(a) Cold core   (b) Warm core: cylindrical   (c) Warm core: modular

Figure 3.3: Sketch of one pole for illustrating cryostat concepts. Brown: cryostat wall. Red: superconducting field winding. Green: cold core. Yellow: warm core.

3.3. OVERVIEW OF TOPOLOGIES

COMBINING ferromagnetic and non-magnetic cores in the field back core, field pole core, armature tooth and armature yoke results in 12 applicable topologies (T1-T12) in total as listed and sketched in Fig. 3.4. In this list, nine topologies T1-T3, T5-T7, and T9-T11 have a large effective air gap length due to space allocated to the wall, vacuum and thermal insulation of the used cylindrical cryostat. The other three topologies T4, T8 and T12 with salient iron poles have significantly reduced effective air gap length. Because in these three topologies, the cryostat is made modular in the shape of a racetrack and the iron pole can go as close to the stator as allowed [30, 120, 121]. Topologies T4, T8 and T12 can be regarded as the extensions of topologies T3, T7 and T11, respectively.

(a) T1　　　　　(b) T2　　　　　(c) T3　　　　　(d) T4

(e) T5　　　　　(f) T6　　　　　(g) T7　　　　　(h) T8

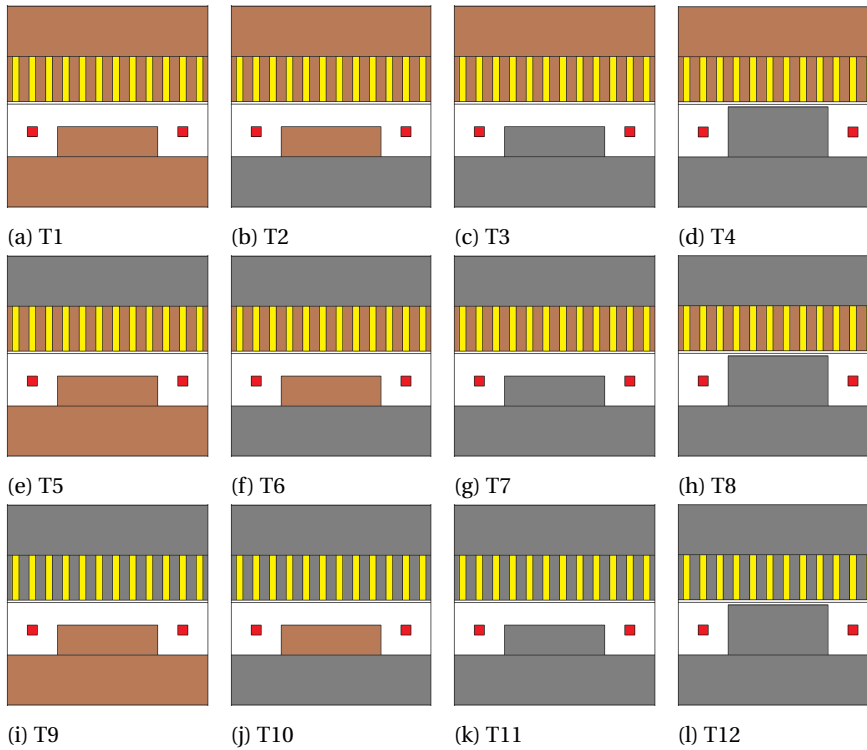(i) T9　　　　　(j) T10　　　　　(k) T11　　　　　(l) T12

Figure 3.4: Topologies to be compared. Red: superconducting field winding. Yellow: copper armature winding. Brown: non-magnetic core. Grey: iron core.

3.3.1. NON-MAGNETIC ARMATURE CORE (T1-T4)

The first four topologies T1-T4 are with a non-magnetic armature core, as sketched in Figs. 3.4a-3.4d. Both the armature teeth and the armature yoke are non-magnetic. The magnetic field has to be confined somewhere outer the non-magnetic armature yoke or these topologies are used for an inner-armature-outer-field layout. The cooling for the armature winding could be difficult, since classic forced-air cooling used in conventional machines would probably not be sufficiently effective. Direct cooling methods would have to be applied with an increased complexity. Magnetic fluxes go through the copper conductors in the armature slots. Eddy currents and losses are therefore produced in the copper conductors. The copper conductors must be specially twisted by, e.g. Litz wires, or transposed to reduce eddy current losses. However, the non-magnetic armature teeth avoid slotting effects and therefore significantly reduce space harmonics in the air gap flux density. The most decisive fact is that these four topologies may demand a large amount of superconducting wires in the field winding to excite a sufficient flux linkage in the armature winding.

The topology T1 has fully non-magnetic cores since its field pole core and field back core are also non-magnetic. This topology is an extreme case since the magnetic circuit has no ferromagnetic part to reduce the magnetic reluctance. Thus, T1 may demand the largest length of superconducting wires among all the twelve topologies. The advantage is that the manufacturing of such non-magnetic cores can be easy, because all the core materials are the same and there are no joints between different materials. Another advantage is that this topology may result in a lightweight machine because of the lightweight non-magnetic cores.

The topologies T2 and T3 use ferromagnetic field cores instead of non-magnetic ones. The reluctance of the magnetic circuit is reduced. However, due to the fact that the armature core is purely non-magnetic, the reduction of reluctance is very limited. The manufacturing of the field core pieces could be complicated for T2, since the core has two different materials. The topology T3 is different from T2 because T3 is able to employ a whole piece of solid iron for the field core.

By using modular cryostats, the topology T4 with salient ferromagnetic poles has become possible. This topology can be regarded as an extension of T3 but can remarkably reduce the magnetic air gap length. As a result, the reluctance decreases and the demanded amount of superconducting wires will become smaller, but the effect may be very limited due to the absence of ferromagnetic cores in the armature.

These four topologies have hardly be applied in superconducting machine designs, since the ferromagnetic armature yoke which confines the magnetic flux and reduces the reluctance is absent.

3.3.2. NON-MAGNETIC ARMATURE TEETH WITH IRON ARMATURE YOKE (T5-T8)

The topologies T5-T8 have a ferromagnetic armature yoke to confine the magnetic flux within the machine, as sketched in Figs. 3.4e-3.4h. The armature yoke is usually made from silicon-steel laminates. The addition of a ferromagnetic yoke reduces the reluctance of the magnetic circuit and a smaller amount of superconducting wires is demanded for the field winding. These four topologies still have non-magnetic armature teeth so the advantages and disadvantages of such teeth still hold. In addition, the manufacturing for contacting the non-magnetic teeth and the ferromagnetic yoke remains challenging.

The topology T5 looks much more realistic than T1. In many publications, T5 is called "air core" topology. The topologies T6-T8 use ferromagnetic field cores and can significantly reduce the reluctance of the magnetic circuit. Such topologies are often applied to the designs called "air winding" machines, because the armature teeth are non-magnetic and slotting effects disappear. Again, cooling of the armature winding could be challenging and would require extra design efforts. The topology T8 can be regarded as an extension of T7 and remarkably reduces the reluctance of the magnetic circuit.

These four topologies have been more or less applied in superconducting machine designs. Taking wind energy for example, Abrahamsen [122] and Suprapower [23] employed T5 and T8, respectively, to achieve a lightweight design with MgB_2 superconductors for a 10 MW generator.

3.3.3. IRON ARMATURE CORE (T9-T12)

The topologies T9-T12 have a fully ferromagnetic armature core as sketched in Figs. 3.4i-3.4l. These topologies therefore enable the direct use of silicon-steel laminates from the stator core of conventional synchronous or induction machines. Classic forced-air cooling can directly be adopted for the armature winding, which simplifies the armature cooling system. The downsides due to ferromagnetic teeth are mainly slotting effects and resulting losses in the superconducting field winding and the ferromagnetic cores. The losses in the superconducting wires must be carefully examined, since this is about the survival of superconducting wires as well as the budget for cryogenic cooling.

The four topologies keep the armature winding design similar to the stator in conventional synchronous or induction machines. The design of the field cores are therefore made flexible. A fully non-magnetic field core is used in T9 which can provide a lightweight machine. If light weight is less important than the amount of superconducting wires, T11 and T12 could be quite desirable. T10 could be an option to be considered if a balance between weight and superconducting wire usage

is required.

The topology T12 with salient ferromagnetic poles minimizes the reluctance of the magnetic circuit and may remarkably reduce the use of superconducting wires. It looks the same as the topology of a conventional salient-pole synchronous machine. An added value of using salient poles is that the field coils can be moved farther off the armature winding in the radial direction. This feature enables reduction of the influence of magnetic field harmonics from the armature winding and teeth to the field winding. However, the losses in the superconducting wires still need to be examined for the purpose of locating the field coils at an appropriate position.

In terms of application of these four topologies, GE [20] reported a 10 MW superconducting generator design with LTS based on the topology T9, which was aiming at light weight. Xu [120] investigated the topology T12 with 2G HTS at different cryogenic temperatures for 10 MW wind turbines.

3.4. BASIC GENERATOR DESIGN PARAMETERS

THE superconducting generator for topology comparison is designed for 10 MW direct-drive wind turbine with a rated speed of 9.6 rpm. The employed superconductor is magnesium diboride (MgB$_2$). This type of superconductor can operate superconductingly at higher cryogenic temperatures than LTS, e.g. NbTi, Nb$_3$Sn. It is also less expensive than HTS. e.g. YBCO, BSSCO.

Only the field winding is superconducting with MgB$_2$ while the armature winding is still with copper conductors at an ambient temperature. This use of superconductivity has already been defined as partially superconducting. The basic generator design parameters are summarized in Table 3.2. These basic parameters are fixed for the upcoming topology comparison, which means their effects on the comparison results are considered insignificant.

The required torque T_n is 6% higher than the nominal torque calculated from the nominal power of 10 MW. The root-mean-squared (RMS) armature current density of 3 A/mm^2 follows the current density range recommended for large synchronous machines [123]. The armature winding fill factor is 0.6 since this is a typical number for rectangular copper conductors with consideration for appropriate twisting or transposing.

For only comparison purposes, the air gap diameter of the generator is of no importance but it should be selected in such a way that the generator can be well placed in the nacelle of a 10 MW wind turbine. For the conceptual INNWIND.EU nacelle introduced in Chapter 2, the generator diameter is considered not too large so that the hub and generator sizes fit. Here the air gap diameter of 6 m is used and assumed to accomplish such compactness. The mechanical air gap is then set to 6 mm (0.1% of the air gap diameter as a role of thumb). The distance from the

Table 3.2: Basic generator design parameters.

Basic parameter	Value
Required torque	$T_n = 10.6$ MNm
Air gap diameter	$d_s = 2 \cdot r_s = 6$ m
Number of phases	$m = 3$
Number of slots per pole per phase	$q = 4$
Armature current density	$J_s = 3$ A/mm^2
Distance from outer field winding to air gap	$h_{fg} = 40$ mm
Mechanical air gap length	$g = 6$ mm
Armature winding fill factor	$k_{fil} = 0.6$
Cryogenic temperature	20 K

3

outer field winding to the air gap contains a cryostat wall, vacuum and multi-layer thermal insulation.

The cryogenic temperature for operating the MgB$_2$ superconductor is 20 K which is sufficient far from the critical temperature of 39 K for MgB$_2$. This temperature allows for easier cryogenic cooling, compared to the operating temperature of 4 K for low temperature superconductors.

The number of slots per pole per phase q is selected based on the concerns of slot pitches and slotting effects, although its effects will not change the topology comparison results. Due to the minimum bending radius of a superconducting wire, the pole pitch should be sufficiently large. A large pole permits a relatively large number of q. However, a large number of q may result in a too small slot pitch within the fixed air gap diameter of 6 m. A small number of q can lead to more slotting effects which are not wanted by the superconducting field winding due to AC losses. The number of $q = 4$ is expected to satisfy both of the concerns. However, determining the number of q needs other studies, which is out of the scope of this chapter.

The generator has an outer armature winding and an inner field winding. This structure can be reversed and the topology comparison results will still hold. Either the armature winding or the field winding can be rotating. The superconducting field winding is operated with a 25% safety margin to its in-field critical current density. The generator axial length is obtained in such a way that the required torque is fulfilled when the air gap diameter is fixed to 6 m. The chosen material for the non-magnetic cores is glass fiber G10 whose main properties have been summarized in Table 3.1.

3.5. COMPARISON CRITERION: CAPITAL COST OF ENERGY

3.5.1. WHY COST OF ENERGY?

COST of energy is the key performance indicator for wind energy conversion. For a new technology, like superconducting generator, cost of energy is used to evaluate its feasibility of commercialization. If the cost of energy is too high, industry will not be interested.

For the purpose of topology comparison, cost of energy is also used to eliminate those too expensive or too inefficient topologies. The rest topologies can then be chosen for further investigation. Therefore, we use cost of energy as the criterion for topology comparison.

3.5.2. DEFINITION OF COST OF ENERGY

A levelized cost of energy of a wind turbine is defined by [124, 125]

$$LCoE = \frac{C_{CAPEX}}{a \cdot E_{AEP} \cdot T_{LT}} + \frac{C_{O\&M}}{E_{AEP}} + \frac{C_{Decom}(1+r)^{-T_{LT}}}{a \cdot E_{AEP} \cdot T_{LT}} \tag{3.1}$$

Where C_{CAPEX} is the total capital expenditure of a wind turbine, $C_{O\&M}$ is the annual operation and maintenance expenditures of a wind turbine, C_{Decom} is the decommissioning expenditure in the year of shutting down the wind turbine, E_{AEP} is the annual energy production, a is the annuity factor assuming an interest rate of r, and T_{LT} is the design life time of the wind turbine. In this thesis, we assume $a = 0.564$, $r = 5\%$ and $T_{LT} = 25$ years.

Although the operation and maintenance expenditures are important, C_{CAPEX} is much more sensitive for designing a superconducting drive train. There have been no experience of operating and maintaining a superconducting generator system in a wind turbine. Feasibility assessment of applying superconducting machines to wind turbines highly depends on the level of C_{CAPEX}. We can only consider C_{CAPEX} at this moment for feasibility studies, after which the operation and maintenance expenditures can be estimated and added to the calculation of cost of energy.

3.5.3. CAPITAL EXPENDITURE

A capital expenditure of a wind turbine consists of the cost of the generator system and the total cost of the other parts of the wind turbine. The generator system cost consists of the cost of the generator's active material C_{act}, the cost of the generator's supporting structure C_{str}, the cost of the generator's cryogenic system C_{cryo} and the cost of the power electronic converter C_{PE}. Now the LCCoE can be written as

$$LCCoE = \frac{C_{CAPEX}}{a \cdot E_{AEP} \cdot T_{LT}} = \frac{C_{act} + C_{str} + C_{cryo} + C_{PE} + C_{other}}{a \cdot E_{AEP} \cdot T_{LT}} \tag{3.2}$$

Choice of topologies changes C_{act}. The other costs of the wind turbine in Eq. (3.2) is assumed to be constant since they can hardly be changed by topology choice. Thus, the LCCoE can now be written as

$$LCCoE = \frac{C_{act} + C'_{other}}{a \cdot E_{AEP} \cdot T_{LT}} \tag{3.3}$$

Active material cost

Here the active materials under consideration are
- Superconducting wires for the field winding,
- Copper conductors for the armature winding,
- Ferromagnetic material for the core, and
- Non-magnetic material for the cores.

To evaluate the level or feasibility of capital cost of energy, the first step is usually to check if the active material cost of the generator goes too high due to expensive superconducting wires. If the active material cost stays in an acceptable level, the study on other costs as well as the energy production can follow up. If the active material cost turns out to be too high, the value of using superconductivity will become questionable. Thus, we must have a range or level of the active material cost of a superconducting generator before going to evaluate the cost of energy of a wind turbine.

In this chapter, we assume the following unit costs for the active materials:
- MgB_2 superconductor: 4 €/m (based on currently available wires),
- Copper conductor: 15 €/kg,
- Iron core: 3 €/kg, and
- Non-magnetic core (glass fiber G10): 15 €/kg.

The cost of each component of the wind turbine considered in the LCCoE is given in Table 3.3. The cryogenic system cost depends on a particular cryogenic design and can hardly be estimated by electromagnetic analyses, and the cost estimation for supporting structures needs detailed mechanical analyses. Here these two costs are estimated based on a 13.2 MW LTS superconducting generator in [33].

The cost model from the INNWIND.EU project defines a reference 10 MW wind turbine and estimates the cost of each wind turbine component [11]. The balance of plant is the cost of all infrastructural and facilities of a wind farm with an exception of the turbine and all its elements. The balance of plant therefore mainly comprises of foundations, crane pads/hard standing, cabling to substation and grid, transformers and miscellaneous costs. Here this balance of plant is averaged to one turbine. The total cost excluding C_{act} is roughly 27,000 k€ which is given to Eq. (3.3) as C'_{other}. The costs of the turbine tower and the turbine foundation are assumed to be constant in Table 3.3, because the wind loads are the main design drivers. This

Table 3.3: Estimation of the other costs of the 10 MW INNWIND.EU reference wind turbine.

Parameter	Cost	Reference
Wind turbine (excl. gen. system)	7,500 k€	Cost model in [11]
Balance of plant	17,000 k€	Cost model in [11]
Power electronics C_{PE}	800 k€	Cost model in [11]
Cryogenic system C_{cryo}	600 k€	LTS SCSG in [33]
Generator supporting structures C_{str}	880 k€	LTS SCSG in [33]
Total C'_{other}	26,780 k€	-

3

assumption neglects the influence of generator topologies on the costs of the supporting structures of the wind turbine. Therefore, the results of this paper, especially the size and mass of different topologies, need to be exported to structure designers to assess the structural costs for each generator topology. In this paper, the resulting active material masses of the topologies will be compared with a reference mass in Section 3.7 to check if they reach low weight.

The definition of Eq. (3.3) can be applied for optimizing the electromagnetic design of a superconducting generator for the minimum LCCoE of a wind turbine. In such an application, it is not correct to eliminate the constant cost C'_{other} in Eq. (3.3), even if only C_{act} can vary and C_{act} is in fact relatively very small. Because the minimum point will be different between the LCCoEs with and without C_{other}. The constant C'_{other} added to the numerator of Eq. (3.3) changes the minimum point of $LCCoE$.

3.5.4. CALCULATION FOR ACTIVE MATERIAL COST

The procedure of calculating the active material cost follows the flow diagram in Fig. 3.5. When determining the operating current density and the electromagnetic torque per unit length, 2D FE models are used, taking into account the non-linear B-J load curve of the field coil and the non-linear B-H magnetization curve of the magnetic iron.

FINITE ELEMENT MODELING

The 2D FE model of the superconducting generator is illustrated in Fig. 3.6. Only one pole is needed for this model. The boundary condition $\frac{dA_z}{dn} = 0$ is used for both sides of the pole to model the periodicity. The outer boundary is the Dirichlet boundary $A_z = 0$ which means that no magnetic flux can leave this boundary. The domains of air are necessary since the magnetic flux can leave the domains of core. Only half of the phase coils is needed for this model and follows the order described in this
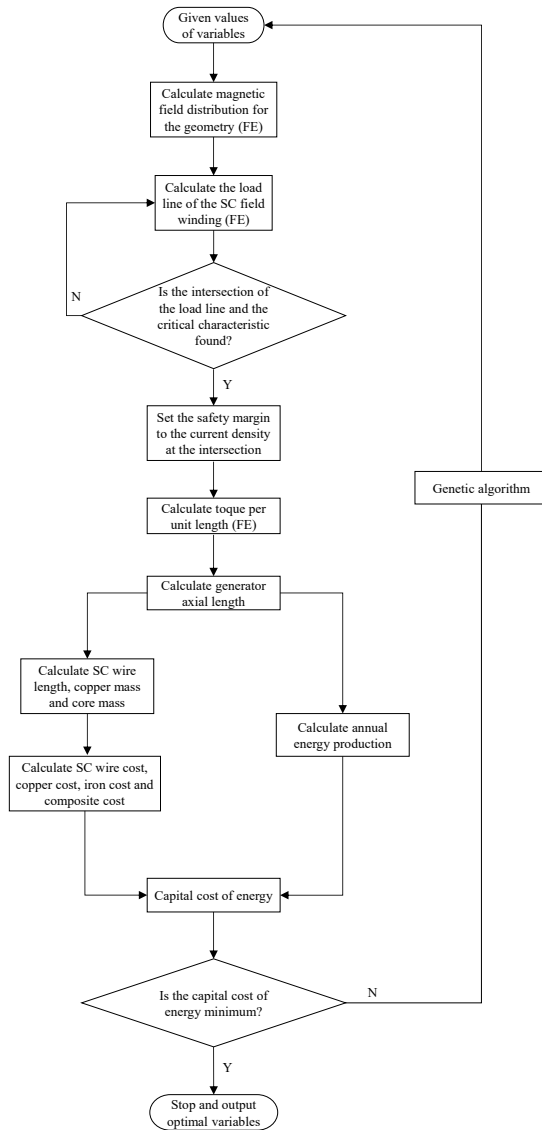
Figure 3.5: Flow diagram for calculating the capital cost of energy and implementing genetic algorithm for optimization.

figure. The material for the iron core is silicon steel NGO M-14 and its B-H curve used in the FE program (COMSOL Multiphysics) is shown in Fig. 3.7.
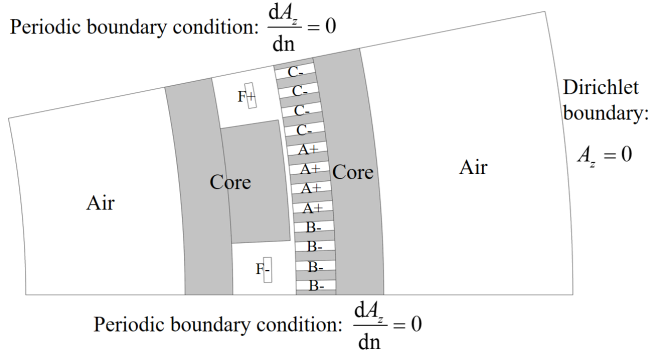

Figure 3.6: Finite element model of the generator. Only one pole needs modeling with boundary conditions.
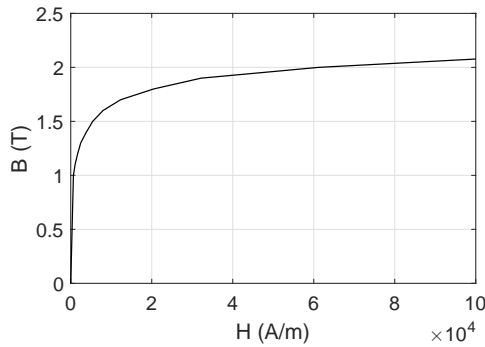

Figure 3.7: B-H curve (silicon steel NGO M-14) used in the FE simulations. Reproduced from COMSOL Multiphysics v4.4.

OPERATING FIELD CURRENT DENSITY

The operating current density of an superconducting field coil must stay below the critical current density of the superconductor wires, otherwise the wires will enter their non-superconducting states. The critical current density J_E as a function of the magnetic flux density B and the temperature T is normally provided by the superconductor wire supplier. The machine topology determines the so-called load line

which is defined here as the maximum flux density of an superconducting coil with respect to the current density flowing in an superconducting wire.

In Fig. 3.8 the critical point is indicated at which the load line (the red line) crosses the critical characteristic (the blue line with dots). The intersection is at the boundary of the superconducting state which does not tolerate small increases of the current density. A margin of 25% is therefore introduced to obtain the operating point for safe operation.
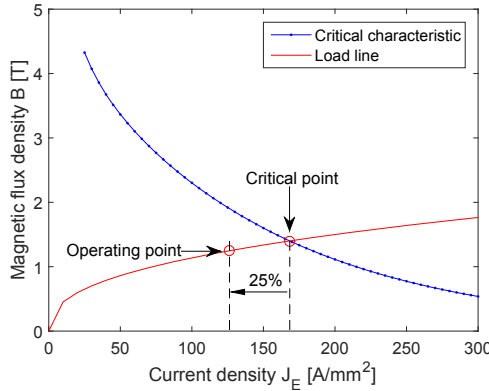

Figure 3.8: Definition of the operating point of the field current density by crossing the load line and the critical characteristic at the temperature of 20 K.
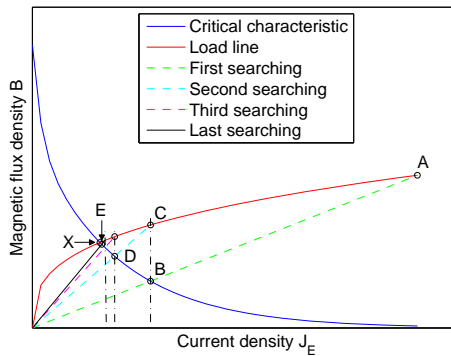

Figure 3.9: Illustration of iteratively finding the critical point of the superconducting field winding by several steps of FE computation, considering a non-linear load line.

The load line may, however, not be linear, depending on the saturation of the

iron core parts of the machine, so we cannot simply find one point on the load line and extrapolate it to the origin linearly. It would also be too time consuming to find all the points on the load line by finite element computations. Here a method is proposed to iteratively find the critical point by a small number of computations with FE models.

First of all, we must distinguish the current density in a wire $J_{E,wire}$ and the current density in a coil $J_{E,coil}$. This is because the critical characteristic given in Fig. 3.8 does not use $J_{E,coil}$ but $J_{E,wire}$ as the current density, whereas we apply $J_{E,coil}$ in the SC field coils in the FE model and compute the magnetic field. We use the corresponding $J_{E,wire}$ to establish its correlation to the maximum magnetic field B in the SC coil. With a filling factor of $k_{fil,sc}$ for the superconducting coil, the relation can be written as

$$J_{E,coil} = k_{fil,sc} \cdot J_{E,wire} \qquad (3.4)$$

As illustrated in Fig. 3.9, the unknown load line in red is not linear. The critical characteristic in blue crosses the load line at point X, which needs to be found right now by a searching process. At the beginning of searching for the intersection point X, we set a uniform coil current density $J_{E,coil,A}$, which is far higher than needed, to the superconducting field coils. The computed maximum flux density in the superconducting coils is at point A which must be located on the load line. We connect point A to the origin linearly and this connecting line crosses the critical characteristic at point B. Here the current density at point B is the wire current density $J_{E,wire,B}$.

Then we give the coil current density $J_{E,coil,B}$ of point B (using the relation in Eq. (3.4)) uniformly to the superconducting coils and compute the maximum flux density of the superconducting coils which must be at point C on the load line. We connect point C to the origin linearly and this connecting line crosses the critical characteristic at point D. We iterate this process a few times, and the computed maximum flux density will finally reach point E which is close enough to point X, judged by a pre-set tolerance ε given by

$$B(k+1) - B(k) \le \varepsilon, \quad k = 1, 2, 3, ... \qquad (3.5)$$

where $B(k+1)$ is the maximum flux density of the superconducting coils for the computation $k+1$ and $B(k)$ is the maximum flux density of the superconducting coils for the previous computation k. Here we use the tolerance of $\varepsilon = 0.02$ T which is roughly 1% of the maximum magnetic field in the field coils.

This final intersection of point E is the critical point of the superconducting field winding (as seen in Fig. 3.8), which is limited by the strongest magnetic field in the superconducting field coil. The current density at point E should then be reduced by the factor of 25% to become the operating field current density, considering a

reasonable margin for safe operation. This searching process for the operating point requires only 4 to 6 iterative FE computations.

ELECTROMAGNETIC TORQUE

The electromagnetic torque obtained in a 2D FE model is the torque per unit length T_z. The generator axial length can then be calculated by

$$l_s = T_n / T_z \tag{3.6}$$

The torque T_z is an average value calculated from two stationary FE simulations. These two simulations differ in the relative position between the rotor and stator, and the phase angle of the armature current. From the first position to the second, as illustrated in Fig. 3.10, the rotor rotates with an angle of $1/(4mq)$ of a mechanical cycle while the phase current shifts by a time of $1/(4m)$ of an electrical cycle. Choosing these two positions is under the assumption that the 6_{th} time harmonic of the magnetic field contributes to the force ripples most. Then, an electrical cycle has 6 cycles of force ripples. Compared with a complete transient simulation of the torque, the error resulted from this averaging method is less than 5% and this accuracy is acceptable for this comparison study.
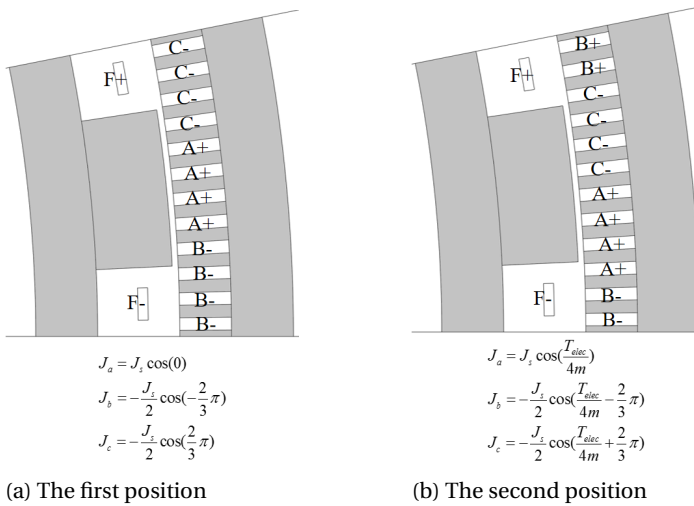

$$J_a = J_s \cos(0)$$
$$J_b = -\frac{J_s}{2}\cos(-\frac{2}{3}\pi)$$
$$J_c = -\frac{J_s}{2}\cos(\frac{2}{3}\pi)$$

(a) The first position

$$J_a = J_s \cos(\frac{T_{elec}}{4m})$$
$$J_b = -\frac{J_s}{2}\cos(\frac{T_{elec}}{4m} - \frac{2}{3}\pi)$$
$$J_c = -\frac{J_s}{2}\cos(\frac{T_{elec}}{4m} + \frac{2}{3}\pi)$$

(b) The second position

Figure 3.10: Two positions in the FE model for calculating the average torque. The phase current density for the corresponding position is provided. T_{elec} is the time period of one electrical cycle.

3.5.5. ENERGY PRODUCTION

The energy production of a wind turbine is determined by energy losses. Here only the electrical energy exported from the generator system is considered as energy production. The losses after the generator system, e.g. cable losses, transformer losses, are not taken into account.

WIND SPEED DISTRIBUTION

The wind condition for designing 10 MW wind turbines is defined by the INNWIND.EU project [11]. The wind speed follows Weibull distribution with the following parameters:

- Average wind speed: $v_{w,avg} = 9.2$ m/s,
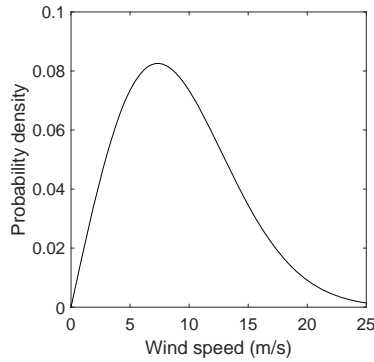- Shape factor $k = 2$, and
- Scale factor $A = 10.39$.

Figure 3.11: Weibull distribution of wind speed.

OPERATION OF THE WIND TURBINE

The operation of the wind turbine is characterized by power and speed.

Power The input power to the generator system P_{in} is the shaft power from the hub of a wind turbine. This power is determined by the aerodynamic power from wind:

$$P_{ad} = 0.5\rho_{air}C_p\pi r_{tr}^2 v_w^3 \tag{3.7}$$

where ρ_{air} is the mass density of air, C_p is the power coefficient of a wind turbine, r_{tr} is the turbine rotor radius, and v_w is the wind speed.

The reference wind turbine has a rotor radius of $r_{tr} = 89$ m. Its cut-in wind speed is $v_{w,cut-in} = 4$ m/s and its cut-out wind speed is $v_{w,cut-out} = 25$ m/s. Note that the
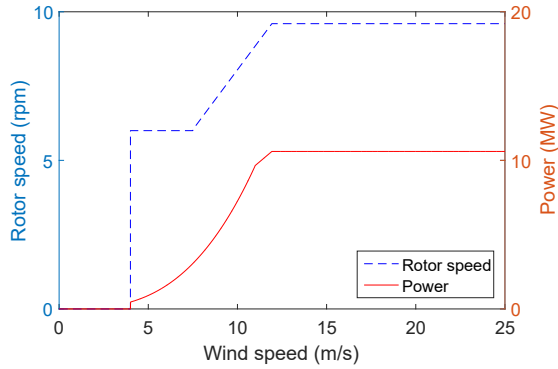
Figure 3.12: Rotor speed and power with wind speed.

rotor rotates at a constant speed of 6 rpm at the wind speed between $v_{w,cut-in} = 4$ m/s and 7.5 m/s.

When the wind speed is smaller than the cut-in speed, the mechanical power to the drive train is zero: $P_{in} = 0$.

When the wind speed is between the cut-in and cut-out speeds and the aerodynamic power is lower than the rated power of the wind turbine $P_{WT,N} = 10.6$ MW, the mechanical power to the drive train follows Eq. (3.7). Now the power coefficient is set to its maximum $C_p = C_{p,max} = 0.476$.

When the wind speed is between the cut-in and cut-out speeds but the aerodynamic power is higher than the nominal power of the wind turbine $P_{WT,N} = 10.6$ MW, the blade pitch control takes action and the power coefficient drops to keep a constant rated power into the drive train:

$$P_{in} = P_{WT,N} \tag{3.8}$$

Speed The generator's rotational speed is given by

$$n = \frac{60\lambda v_w}{2\pi r_{tr}} \tag{3.9}$$

with a tip-speed ratio of $\lambda = 7.9$ and a rated speed of $n_N = 9.6$ rpm. The speed follows the operation as follows:

- If $0 < n < n_N$, then $n = 0$,
- If $n > n_N$ and $v_w < v_{w,cut-out}$, then $n = n_N$,
- If $v_{w,cut-in} < v_w < 7.5$ m/s, then $n = 6$ rpm,
- If $n > n_N$ and $v_w < v_{w,cut-in}$, then $n = n_N$, and
- If $v_w > v_{w,cut-in}$, then $n = 0$.

According to this wind turbine operation, the profiles of wind distribution, aerodynamic power and rotational speed with respect to wind speed are plotted in Fig. 3.12.

OPERATING POINT OF GENERATOR

The generator is operated under the phasor diagram given in Fig. 3.13, which is fully controlled by the power electronic converter. The control strategy is zero d-axis control with which the d-axis current of the generator remains zero and the torque is proportional to the q-axis current. The major advantage of this control strategy is relatively low copper losses in the armature winding.
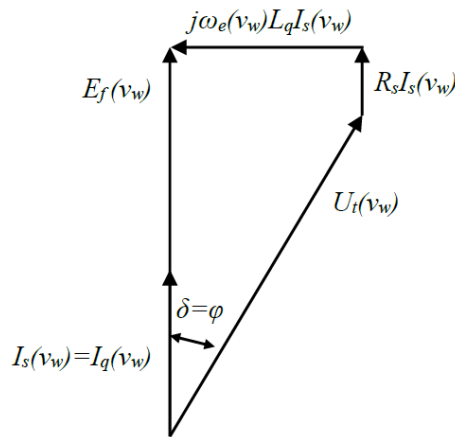

Figure 3.13: Phasor diagram of the generator operating point.

POWER LOSSES

The power flow of a superconducting drive train is sketched in Fig. 3.14. Assuming that mechanical losses, e.g. bearing and windage losses, are neglected, all the aerodynamic power reaches the generator $P_{in} = P_{ad}$. In a superconducting generator, the total power loss consist of

- Joule copper losses in the armature winding $P_{Cu,cond}$,
- Eddy current losses in the armature winding copper $P_{Cu,eddy}$, and
- Iron core losses P_{Fe}.

The losses, both DC and AC losses, in the superconducting winding are negligibly small, according to the study in [121]. Thus, these losses are not considered.

In addition, the refrigeration for cooling the cryogenic environment for super-conducting wires demands a power at an ambient temperature, which can also be considered as a power loss P_{cryo}.

As a part of a generator system, a power electronic converter also produces a loss P_{conv}, which reduces the efficiency of a generator system.

The output power from a generator systems can be calculated by

$$P_{out} = P_{ad} - P_{Loss} \tag{3.10}$$

where P_{Loss} is calculated by

$$P_{Loss} = P_{Cu,cond} + P_{Cu,eddy} + P_{Fe,s} + P_{cryo} + P_{conv} \tag{3.11}$$

Joule copper losses in the armature winding The I^2R copper loss $P_{Cu,cond}$ as a function of wind speed is given by

$$P_{Cu,cond}(v_w) = 3I_s^2(v_w)R_{Cu} \tag{3.12}$$

where $I_s(v_w)$ is the phase current as a function of wind speed, R_{Cu} is the electrical resistivity per phase of the armature winding at the operating temperature of about $120\,°C$.
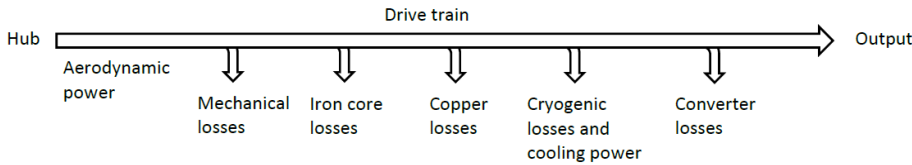

Figure 3.14: Power flow and losses in a superconducting wind turbine drive train.

Eddy current losses in the armature winding The copper loss $P_{Cu,eddy}$ due to in-duced eddy currents can be effectively reduced by stranding the copper conductors. Due to heavy saturation in a superconducting machine, special attention must be paid to the stranding of copper conductors. There are models which can estimate the eddy current loss in copper strands if the dimension of a strand is known. Here we use the model given in [126]:

$$P_{Cu,eddy}(v_w) = \frac{1}{24\rho_{Cu}}\omega_e^2(v_w)(a^2 B_r^2 + b^2 B_t^2)V_{Cu,s} \tag{3.13}$$

where $\omega_e(v_w)$ is the angular electrical frequency as a function of wind speed, B_r and B_t are the radial and tangential components of the flux density (amplitude) in a

copper conductor (or an armature slot), $V_{Cu,s}$ is the copper volume only in the stack length, and a and b are the height and width of a copper strand. In this chapter, we use fine strands for the copper conductors with $a = b = 5$ mm.

Iron core losses Iron core losses exist in iron cores but does not in non-magnetic cores which are also non-conductive. Iron core losses come from hysteresis losses and eddy current losses both of which are functions of flux density and frequency. The total iron loss per unit mass can be modeled by

$$P_{Fe}(v_w) = 2[(\frac{B_r}{1.5})^2 + \frac{B_t}{1.5})^2][k_h(\frac{f(v_w)}{50}) + k_e(\frac{f(v_w)}{50})^2] \qquad (3.14)$$

where $k_h = 2$ W/kg and $k_e = 0.5$ W/kg are respectively the hysteresis loss and the eddy current loss per unit iron mass with the field of 1.5 T and the frequency of 50 Hz. B_r and B_t are respectively the radial and tangential components of the flux density (amplitude) in the iron core, and $f(v_w) = \omega_e(v_w)/2\pi$ is the electrical frequency as a function of wind speed. The factor of 2 is included in Eq. (3.14) because the flux densities do not change sinusoidally and they are not sinusoidally distributed, which increases the iron losses. In addition, manufacturing of steel laminates into a core increases the iron losses [127].

Cryogenic cooling power The cryogenic cooling power is estimated as 0.5% of the rated power of the superconducting generator. This estimation is based on the technical report by GE for a low-temperature superconducting generator design [20], which calculated the cryogenic cooling power at different wind speeds. This report shows that the cryogenic cooling power is constant with wind speed and it value is 22.5 kW. Here we assume a constant cryogenic cooling power of 50 kW at all wind speeds. This power value is more than doubled 22.5 kW to consider a margin.

Converter losses The loss of the power electronic converter is modeled based on the current flowing in the power electronic switches [127] and given by

$$P_{conv}(v_w) = \frac{P_{convm}}{31}(1 + 10\frac{I_s(v_w)}{I_{sm}} + 5\frac{I_s^2(v_w)}{I_{sm}^2} + 10\frac{I_g(v_w)}{I_{gm}} + 5\frac{I_g^2(v_w)}{I_{gm}^2}) \qquad (3.15)$$

where P_{convm} is the loss in the converter at rated power (assuming 2% of the rated power of the converter), I_s is the generator side converter current, I_{sm} is the maximum generator side converter current, I_g is the grid side converter current, and I_{gm} is the maximum grid side converter current.

ASSUMPTIONS FOR CALCULATING ENERGY PRODUCTION

A few assumptions apply to the calculation of losses:

• In an iron tooth and an iron armature yoke, only the fundamental radial and tangential components of the flux density are considered.

• Iron losses in the iron field core back and the iron pole cores are neglected.

• In copper conductors of an armature winding, only the fundamental radial and tangential components of the flux density are considered.

• For reducing eddy current losses in the armature winding, the copper conductors are only stranded with small filaments. Transposing or other means is not used.

• Iron losses and copper eddy current losses are both calculated at no load.

3.5.6. OPTIMIZATION

For the purpose of fair comparison, each of the twelve topologies need to be optimized for its lowest LCCoE. This optimization will find out how low the LCCoE can achieve in each topology. Optimization usually starts with a design which may not be optimum regarding a certain objective. Here we start optimization with a random set of design variables and the initial value of these design variables makes sense. Then the optimization program will search the whole space between the upper and lower limits of the design variables, being constrained by a few geometrical conditions.

OBJECTIVE FUNCTION

The objective function of optimization is the LCCoE which has already been defined by Eq. (3.3)

$$CoE' = \frac{C_{act} + C'_{other}}{a \cdot E_{AEP} \cdot T_{LT}} \tag{3.16}$$

where the active material cost C_{act} is changeable by varying the design variables and defined by

$$C_{act}(\mathbf{V}) = C_{SC} + C_{Cu} + C_{fy} + C_{fpc} + C_{at} + C_{ay} \tag{3.17}$$

where $\mathbf{V}$ is the variables to be optimized, C_{act}, C_{SC}, C_{Cu}, C_{fy}, C_{fpc}, C_{at} and C_{ay} are the costs of active materials, superconductor wires, field back core, field pole cores, armature teeth and armature yoke, respectively. The costs are determined from the unit usage of materials of the 2D FE model and multiplied by the unit cost. The length of the end winding of field and armature coils has been taken into account. The superconducting field coil is in the shape of racetrack and thus its end winding is modeled as semi-circles. The shape of the armature coil follows the conventional copper coil shape for a three-phase distributed winding.

This objective function is minimized by a generic algorithm NSGA-II [128], [129] which has been modified to this single-objective application. The optimization starts from a random set of variables [130] and takes 50 individuals and more than 100 generations to converge.

Table 3.4: Variables for optimization.

	Variable	Boundary
x_1	Number of pole pairs p	[2, 30]
x_2	Start angle of field coil α (elec. deg)	[10, 90]
x_3	End angle of field coil β (elec. deg)	[10, 90]
x_4	Height of field coil h_f (mm)	[10, 400]
x_5	Height of armature slot h_s (mm)	[10, 400]
x_6	Height of armature yoke h_{sy} (mm)	[10, 400]
x_7	Height of field back core h_{ry} (mm)	[10, 400]
x_8	Tooth width/slot pitch b_t/τ_s	[0.3, 0.7]

VARIABLES AND CONSTRAINTS

The variables to be optimized are summarized in Table 3.4 with their upper and lower limits. The definition of these variables can be found in Fig. 3.15. The angles α and β define the dimension and the position of a superconducting field coil. The ratio of the tooth width to the slot pitch b_t/τ_s defines the width of the armature teeth, which cannot be too large or too small.

Besides the upper and lower limits, five linear constraints are imposed to the variables:

$$\alpha - \beta < 0 \tag{3.18}$$

which ensures a positive dimension of the field coils,

$$h_s - h_{sy} < 0 \tag{3.19}$$

which makes the armature yoke sufficiently thick,

$$b_{t,min} - \pi r_s b_t / \tau_s / (mpq) < 0 \tag{3.20}$$

which ensures that the armature tooth width is no less than $b_{t,min} = 2$ cm,

$$k_{fil,arm} J_s h_s (1 - b_t/\tau_s) - K_a < 0 \tag{3.21}$$

which limits the specific electrical loading below $K_a = 75$ kA/m for applying forced-air cooling to the armature winding [123], and

$$r_{bend,min} - \pi \alpha (r_s - g_{eff} - h_f)/(180p) < 0 \tag{3.22}$$

which limits the bending radius of the superconducting wires above the specified minimum bending radius $r_{bend,min} = 100$ mm. The effective air gap length is the sum of the distance from the outer field winding to the air gap and the mechanical air gap length: $g_{eff} = h_{fg} + g$.
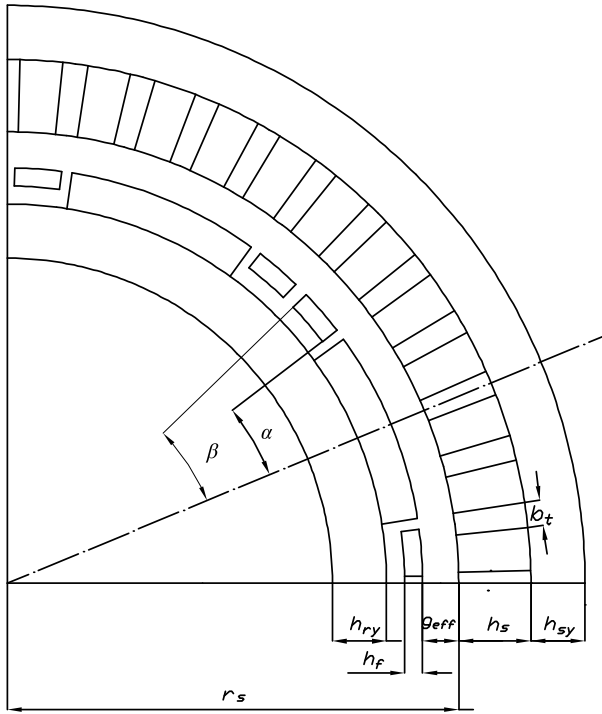
Figure 3.15: Geometrical variables and constants of the generator cross section. The symbols are defined in Table 3.2 and Table 3.4.

For the topologies T4, T8 and T12 which can employ modular cryostat, space around a superconducting field coil must be given and this space brings other linear geometrical constraints, depending on the size of the modular cryostat.

3.6. SCENARIO STUDY

3.6.1. WHY IS SCENARIO STUDY NEEDED?

SINCE superconductor technology is fast developing and superconducting generators for wind energy will take much time to become mature, only using the unit cost and performance of currently available MgB_2 superconductors could be too limited to provide long-term trends of topology comparison. Thus, three scenarios for the unit cost and performance of MgB_2 superconductors are taken into the comparison of PIs.

3.6.2. SCENARIO DESCRIPTION

The three scenarios to be studied are:

• Scenario 1 (S1): The unit cost of MgB$_2$ is reduced from 4 €/m to 1 €/m. This scenario considers the possible reduction of the price of MgB$_2$ in near future. Reduction of the price to a quarter is expected by MgB$_2$ suppliers (Columbus Superconductors) for certain mass production [57].

• Scenario 2 (S2): The critical current density of MgB$_2$ is increased to 4 times the currently available one. This scenario considers the possible enhancement of the critical characteristic of MgB$_2$. The order of 4 times is an assumption since MgB$_2$ suppliers can hardly predict it.

• Scenario 3 (S3): Both of the above. This scenario integrates both the unit cost and the critical current capability of MgB$_2$, which seems difficult to achieve in near future. It is an extreme case which can provide an insight of the topology comparison for future design.

As a reference, the original case (OR) based on currently available commercial MgB$_2$ wires (supplied by Columbus Superconductors) is used to show the present performance of the superconducting generator.

Each topology is optimized for its minimum CoE and has four sets of optimization results. The three scenarios will then be compared with each other and with the original one (OR).

The current density capabilities used in the original case and in Scenario 2 and 3 are plotted in Fig. 3.16.

3.7. RESULTS AND COMPARISON

3.7.1. OPTIMUM VARIABLES

T$_{HE}$ LCCoE and a few resulting generator characteristics, such as the AEP, active material cost, active generator length, superconductor length and active material mass, are obtained from the twelve optimized topologies in the original case and the three scenarios.

The optimum value of the design variables is given in Table 3.5. The geometry and magnetic flux density of the optimized topologies in the original case (OR) is shown in Fig. 3.17. The topologies with more iron (T9-T12) have more pole pairs (18-24 pole pairs) than the other topologies (12-16 pole pairs). Different scenarios do not change much the number of pole pairs. The topologies with salient poles (T4, T8 and T12) have field coil pitches smaller than the pole pitches ($\beta < 90°$) since the modular cryostat occupies fixed space between two adjacent field coils.
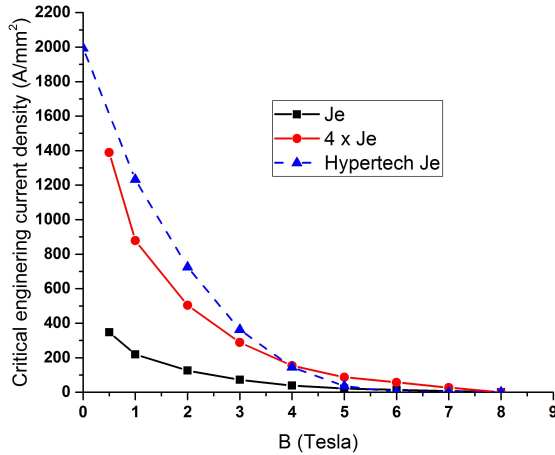
Figure 3.16: Critical current density of MgB$_2$ wires with respect to magnetic flux density used for the scenario study. The curve Je is the critical current density of the MgB$_2$ supplied by Columbus Superconductors, reproduced from [122]. The curve 4 x Je increases the original curve of Je to 4 times. Hypertech Je is reproduced from [25] and this curve was a short-term prediction in [25]. The curve of 4 x Je fits well the predicted curve of Hypertech Je.

3.7.2. COMPARISON

According to the optimization results for each of the twelve topologies for the three scenarios, the LCCoE, AEP, active material costs, active axial length, superconductor length, and active material masses can be obtained. These quantities are compared among the twelve topologies for the three scenarios, respectively, in Figs. 3.18-3.23.

LEVELIZED CAPITAL COST OF ENERGY

The LCCoE is compared among the twelve topologies for the four cases (the original case plus the three scenarios) in Fig. 3.18. In the original case, The general trend of LCCoE from T1 to T12 is decrease. The exception is T9 which has a fully ferromagnetic armature core but a fully non-magnetic field core. The topologies T1-T5 and T9 are relatively expensive in LCCoE, and T1 is the most expensive one. These 6 topologies have generally more non-magnetic cores than the other 6 topologies. The topologies T6-T8 and T10-T12 are relatively cheap in LCCoE, and T12 is the cheapest one. These six topologies have generally more ferromagnetic core than the other six topologies.

In the scenario study, all the three scenarios effectively reduce the LCCoE, especially for the topologies T1-T5 and T9 which have more non-magnetic cores. The reduction of LCCoE for T6-T8 and T10-T11 is limited. The effect is negligible for

Table 3.5: Optimum design variables resulting in lowest LCCoE for the scenarios: original (OR), 1/4 wire cost (S1), 4 times critical current density (S2) and combined S1 + S2 (S3).

	T1				T2				T3			
	OR	S1	S2	S3	OR	S1	S2	S3	OR	S1	S2	S3
p	12	12	12	12	12	12	14	12	14	12	14	12
α (°)	24	24	24	24	24	24	28	24	28	28	30	24
β (°)	90	90	90	90	90	90	90	90	90	90	90	90
h_f (mm)	16	36	10	18	14	28	10	18	16	30	10	18
h_s (mm)	60	60	60	40	74	58	64	42	68	58	64	42
h_{sy} (mm)	60	60	60	40	74	58	64	42	68	58	64	42
h_{ry} (mm)	60	60	60	40	162	182	182	62	158	190	180	58
b_t/τ_s	0.31	0.31	0.31	0.31	0.44	0.31	0.36	0.31	0.39	0.31	0.36	0.31

	T4				T5				T6			
	OR	S1	S2	S3	OR	S1	S2	S3	OR	S1	S2	S3
p	12	12	12	12	14	14	14	14	12	14	16	14
α (°)	38	40	40	26	28	28	28	28	34	28	42	30
β (°)	80	80	80	80	90	90	90	90	90	90	90	90
h_f (mm)	18	38	10	18	14	32	10	18	10	16	10	12
h_s (mm)	60	58	58	44	66	66	64	50	58	56	66	52
h_{sy} (mm)	62	58	58	44	92	114	120	52	240	228	226	206
h_{ry} (mm)	142	174	174	122	92	114	120	52	240	210	180	116
b_t/τ_s	0.31	0.31	0.31	0.31	0.37	0.37	0.36	0.36	0.31	0.36	0.41	0.36

	T7				T8				T9			
	OR	S1	S2	S3	OR	S1	S2	S3	OR	S1	S2	S3
p	14	14	16	14	12	14	14	14	18	20	20	22
α (°)	36	30	46	30	54	50	56	28	36	40	40	44
β (°)	90	90	90	90	80	78	78	78	90	90	90	90
h_f (mm)	10	16	10	12	10	24	10	12	14	34	10	18
h_s (mm)	58	56	64	52	52	54	56	50	78	100	94	100
h_{sy} (mm)	218	226	216	206	228	198	210	204	84	100	102	100
h_{ry} (mm)	222	210	178	116	222	178	196	124	84	100	102	100
b_t/τ_s	0.36	0.36	0.41	0.36	0.31	0.36	0.36	0.36	0.47	0.59	0.56	0.59

	T10				T11				T12			
	OR	S1	S2	S3	OR	S1	S2	S3	OR	S1	S2	S3
p	22	20	24	20	22	24	24	20	20	22	24	18
α (°)	48	40	58	40	56	48	64	42	66	64	66	46
β (°)	90	90	88	90	90	90	88	90	74	72	70	74
h_f (mm)	10	18	10	10	10	14	10	12	10	34	18	14
h_s (mm)	130	82	108	72	118	108	108	74	102	108	116	64
h_{sy} (mm)	134	156	124	172	130	122	122	174	122	128	126	158
h_{ry} (mm)	134	156	118	92	136	128	124	94	118	106	106	110
b_t/τ_s	0.68	0.53	0.62	0.53	0.65	0.62	0.62	0.53	0.65	0.62	0.65	0.47

T12. The scenarios are closing the difference of LCCoE among the topologies. The topologies T1-T5 and T9 become comparable to T6-T9 and T10-T12. However, the topologies with more ferromagnetic core are still cheaper in LCCoE for Scenarios 1
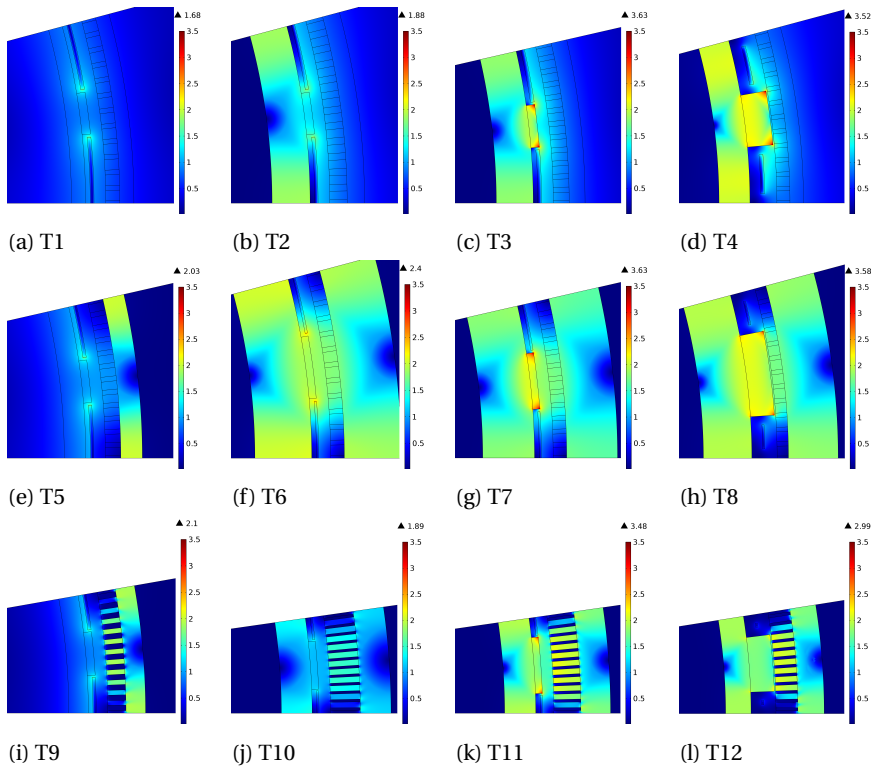
Figure 3.17: One pole of the optimized geometry and the corresponding distribution of magnetic flux density of the twelve optimized topologies in the original case (current unit cost and current density capability of the MgB$_2$ wire).

and 2, which are more suitable for wind energy conversion. Note that, however, the difference of topology is vanishing for Scenario 3. The topologies with more non-magnetic cores (T1-T5 and T9) will become competitive in Scenario 3.

ANNUAL ENERGY PRODUCTION

The AEP is compared among the twelve topologies for the four cases in Fig. 3.19. The information of AEP is extracted from and contained in CoE. In the original case, the general trend of AEP from T1 to T12 is increase. The exception is T9 which has a fully ferromagnetic armature core but a fully non-magnetic field core. The topologies T6-T8 and T10-T12 produce more AEP, and T12 produces the most. These 6 topologies have generally more ferromagnetic core than the other 6 topologies.
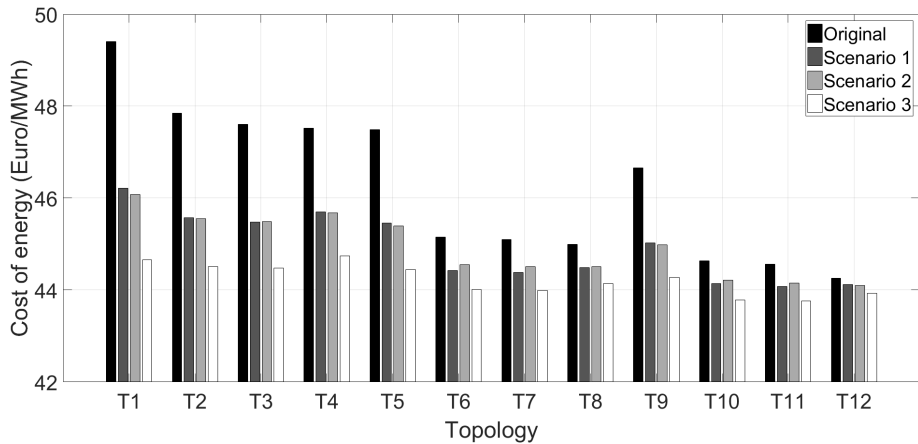
3

Figure 3.18: Comparison of capital cost of energy for twelve topologies.

In the scenario study, all the three scenario increase the AEP, especially for the topologies T1-T5 and T9 which have more non-magnetic cores. The effect is limited for T6-T8 and T10-T11 and negligible for T12. Like the result of CoE, the scenarios are closing the difference of AEP among the topologies. The topologies T1-T5 and T9 become comparable to T6-T9 and T10-T12. However, the topologies with more ferromagnetic core produce more energy for Scenarios 1 and 2, which are more suitable for wind energy conversion. Note that, however, the difference of topology is vanishing for Scenario 3.

ACTIVE MATERIAL COST

It is very interesting to study the active material costs for electromagnetic design of an electrical machine. Therefore, besides CoE we also compare the active material costs among the twelve topologies in Fig. 3.20. In the original case, the general trend of the total active material cost from T1 to T12 is decrease. The exception is T9 which has a fully ferromagnetic armature core but a fully non-magnetic field core. The topologies T1-T5 and T9 are relatively expensive regarding the total active material cost, and T1 is the most expensive one. These 6 topologies have generally more non-magnetic cores than the other 6 topologies. The topologies T6-T8 and T10-T12 are relatively cheap as contrast, and T12 is the cheapest one. These 6 topologies have generally more ferromagnetic core than the other 6 topologies. The fraction of the four active materials contributing to the active material cost is also shown in this figure. In most topologies, the MgB$_2$ superconductor takes up the majority or nearly half of the total active material cost. The cost of MgB$_2$ is minimized in T12 which
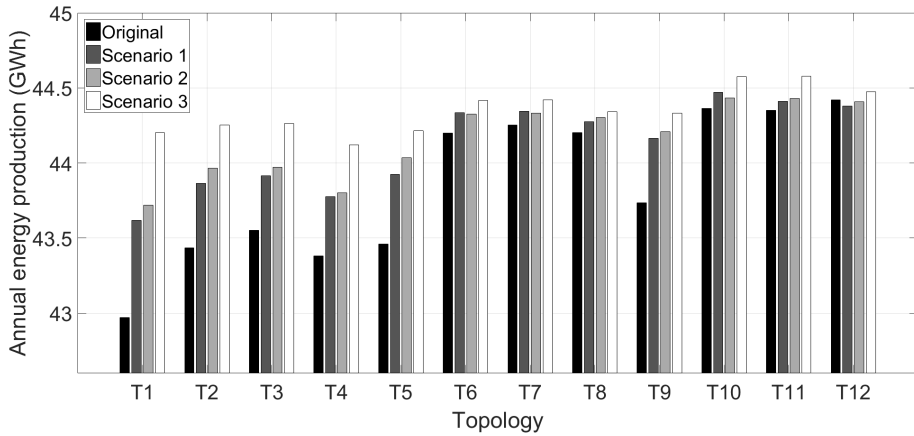
Figure 3.19: Comparison of annual energy production for twelve topologies.

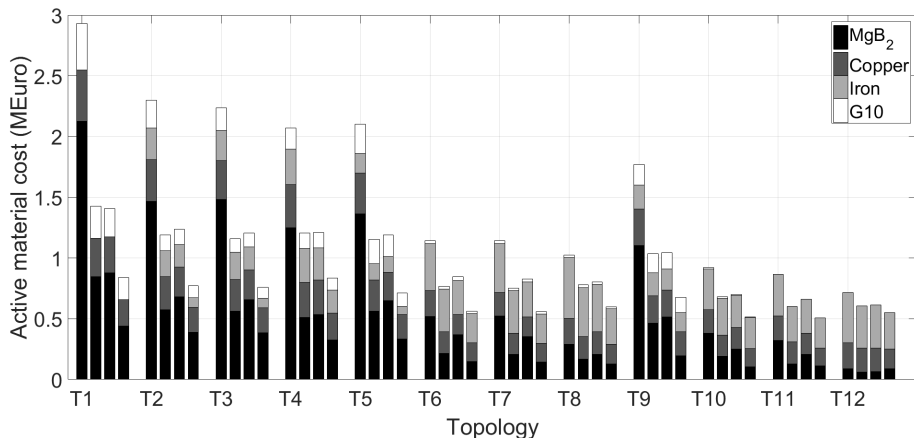makes most use of ferromagnetic cores.

Figure 3.20: Comparison of active material costs for twelve topologies. From the left to right within a topology are original case, Scenario 1, Scenario 2 and Scenario 3.

In the scenario study, the result of active material cost is quite similar to that of CoE. The main drive of the cost reduction is the lower cost of MgB_2 since the cost of the other active materials remains with a slight difference.

ACTIVE AXIAL LENGTH

Since the air gap diameter of the generator is fixed to 6 m, the active axial length of the generator can be obtained for sizing the generator as shown in Fig. 3.21. In the original case, the topologies T6-T8 and T10-T12 result in a relatively short generator compared to the other six topologies. The shortest topology is T6 but actually the differences of length among T6-T8 and T10-T12 are very small. We can say all of the six topologies provide small generator lengths.

In the scenario study, the scenarios take effect in reducing the active axial length. Similarly, the topologies with more non-magnetic cores (T1-T5 and T9) are much more affected. Differently, Scenario 3 is not effectively closing the difference of topology in this case. The topologies with more ferromagnetic cores (T6-T8 and T10-T12) provide shorter machines.
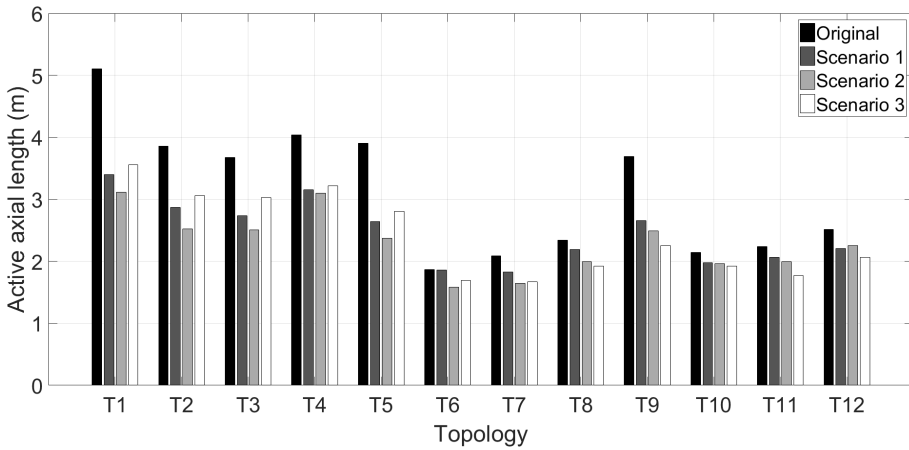

Figure 3.21: Comparison of active axial length for twelve topologies.

SUPERCONDUCTOR LENGTH

Not only does the length of used superconductor determine the active material cost, but it also indicate the difficulty in manufacturing the superconducting wire. A longer superconducting wire requires more complicated manufacturing technology and thus the manufacturing cost and wire quality may be significantly affected by the length of wire. The comparison of superconductor length in Fig. 3.22 shows clear trend.

In the original case, the topologies T6-T8 and T10-T12 require smaller supercon-ductor lengths compared to the other 6 topologies. T12 requires the smallest length and thus has remarkable performance in reducing the length of superconductor.
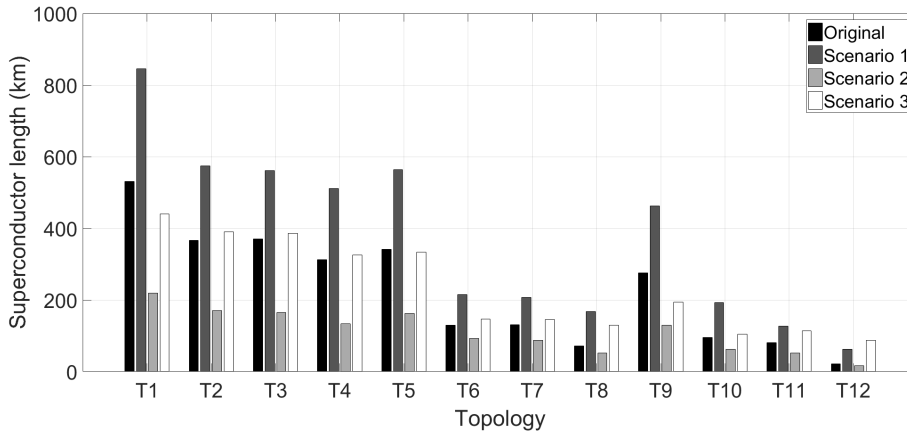
Figure 3.22: Comparison of superconductor length for twelve topologies.

In the scenario study, the result of superconductor length comparison is different from that of the above-mentioned quantities, because the unit cost or critical current density capability determines the amount of used superconductor. For example, Scenario 1 assumed a cheaper MgB_2 so the length of used MgB_2 goes much larger, but the difference is not as large as 4 times. Comparing Scenarios 1 and 2, a larger critical current density reduces the length of MgB_2 which makes sense, because less use of superconductor is needed to produce the same magnetic field intensity. From manufacturing difficulty point of view, Scenario 2 is more desirable since it results in a smaller length of superconductor.

ACTIVE MATERIAL MASS

Active material masses are also interesting for electromagnetic design. The comparison result is given in Fig. 3.23. In the original case, the topology T8 has the heaviest active material, because T8 uses a large amount of ferromagnetic iron. The trend from T2 to T12 is not so clear anymore, since the optimization has only dealt with cost and efficiency issue but the mass was not taken into account at all. From this sense, it is not correct to simply say that using ferromagnetic iron will increase the active material mass. Some topologies with more non-magnetic cores are also heavy, such as T2-T4, because they need a larger generator length to obtain the same power or torque, which brings more active materials and then a larger active material mass.

In the scenario study, the three scenarios effectively reduces the total active material mass. The comparison does not show a general trend from T1 to T12 for dif-
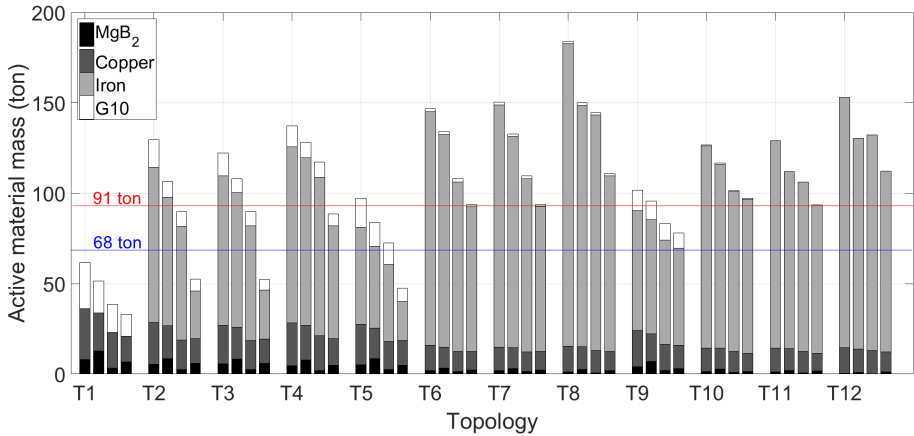
Figure 3.23: Comparison of active material mass for twelve topologies. From the left to right within a topology are original case, Scenario 1, Scenario 2 and Scenario 3. Reference low weights are shown by the red and blue lines.

ferent scenarios, but the topologies with more ferromagnetic cores tend to still be heavier than the other topologies. In addition, Scenario 3 is not effectively closing the difference of topologies.

A few reference generator masses can be introduced to define what a low weight is. One is the total mass of a 10 MW permanent magnet generator: $m_{PM} \approx 325$ ton [131]. One is the INNWIND.EU reference turbine drive train mass consisting of a medium speed gearbox and generator as well as the main shaft: $m_{innwind} \approx 227$ tons. [132]. The third is a reference total mass for a 10 MW SCSG design given in [133]. This reference mass indicates that a generator mass above 273 ton will significantly challenge the main bearing of the wind turbine rotor. The mass of 273 ton is about the average of m_{PM} and $m_{innwind}$. Therefore, this mass is used as a reference of low weight to evaluate the active material mass in Fig. 3.23. The active material mass could approximately be 1/3 to 1/4 of the generator mass (91 ton to 68 ton). This region of active material mass is also indicated in Fig. 3.23. In the original case, T1, T5 and T9 satisfy or almost satisfy 91 ton while only T1 satisfies 68 ton. None of the low-LCCoE topologies (T10-T12) meet these low weights. The scenarios result in more lightweight topologies. For example, T4, T6, T7, T10-T12 satisfy 91 tons and T1-T3 and T5 satisfy 68 in Scenario 3. However, the low-LCCoE topologies (T10-T12) are still far from 68 ton. The topologies that have a low LCCoE may not be good options for low weight. If low weight is essential, the topologies with more non-magnetic cores that have higher LCCoE should be considered.

3.8. DISCUSSIONS

3.8.1. LOSSES AND EFFICIENCY

P REVIOUSLY, we assumed a constant cryogenic cooling power of 50 kW, being 0.5% of the rated generator power. If sweeping this power from 0 to 1% of the rated generator power for the topology T12 in the original case, we obtain a series of generator system efficiency curves with respect to wind speeds in Fig. 3.24. The effect of the cryogenic cooling power on the efficiency mainly takes place at low wind speeds, i.e. partial load operations. If this power decreases, the partial load efficiency becomes higher. When the wind speed goes higher than the rated wind speed, the differences of efficiency become small. Due to the fact that wind turbines run at partial load most of the time, the energy production could be significantly increased by reducing the cryogenic cooling power.
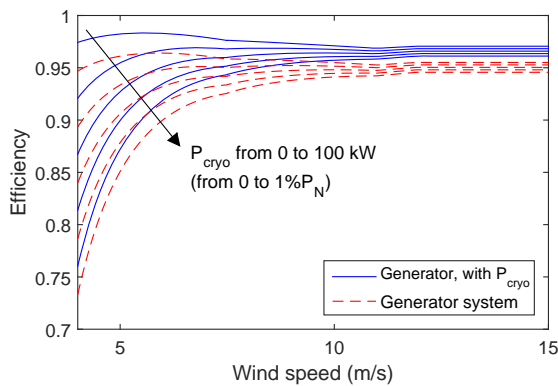

Figure 3.24: Effects of cryogenic cooling power on efficiency.

3.8.2. CONSIDERATION FOR REDUCING THE ACTIVE MATERIAL MASS

In the optimization for a minimum LCCoE, we did not consider any constraints on the active material mass. The optimization resulted in a large active material mass in some topologies with ferromagnetic cores (e.g. T6-T8). As explained before, the cost of energy is the first priority for the design of superconducting generators and the generator mass or the top head mass of the wind turbine may not be of major importance. In large wind turbines of 10-20 MW, the rotational speed of the rotor is quite low (below 10 rpm) which may cause mechanical stability issues on the turbine due to resonance. A large generator mass or top head mass may help decrease the natural frequency of the turbine and reduce the possibility of resonance.

In electrical machine design engineering, however, generator mass is always an
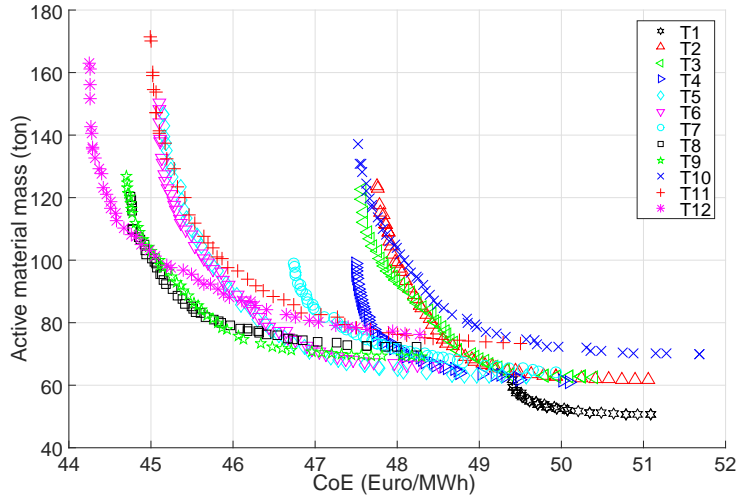
Figure 3.25: Trend of active material mass with variation of cost of energy for the twelve topologies.

important PI. The active material mass is indicative for the total generator mass, which needs consideration for evaluating an electromagnetic design. Here, we take into account the active material mass and find the conflicting relation between the total active material mass and the LCCoE for all the twelve topologies in the original case. These relations were obtained by a dual-objective optimization which uses both the total active material mass and the LCCoE as the objective functions.

The result is plotted in Fig. 3.25. This figure has the following indications:

• It shows the reachable boundaries of LCCoE and active material mass for each of the twelve topologies. For example, it is too hard for T12 to reach the total active material mass of 70 ton. The lower limit of LCCoE of T11 is about 45 €/MWh.

• With the same total active material mass, the difference or ranking of the LC-CoE of the twelve topologies can be clearly observed. With the same LCCoE, the heavier or lighter topologies can be identified.

• It shows how much the LCCoE needs increasing to achieve certain reduction of the total active material mass, or how much active material mass need increasing for a lower LCCoE. For example, the total active material mass of T12 can be reduced from 160 ton to 120 ton by increasing the LCCoE by less than 1%. Some topologies have a very steep change of active material mass near the minimum LCCoE region, and a small increase of LCCoE can result in a large reduction of the active material mass. This relation in Fig. 3.25 will be useful as a design reference if the generator

mass is also critical. In this chapter, we only focus on designing for a low LCCoE and the generator mass is considered less important.

3.9. CONCLUSION

THIS chapter compared twelve topologies for superconducting generator design, regarding the key performance indicator of LCCoE for a 10 MW wind turbine. Some other generator characteristics resulting from the capital-CoE-based optimal designs are also shown. The LCCoE was estimated and modeled. Each topology was optimized for its minimum LCCoE. The LCCoE and other generator characteristics of the optimum design were then compared. With the commercial MgB_2 wire in the field winding and based on the its current unit cost and characteristic, the topologies with more iron have lower LCCoEs than the other topologies with more non-magnetic cores. The fully iron-cored topology with salient poles is most advantageous regarding the LCCoE as well as the resulting AEP, active material cost and superconductor length.

As indicated in the scenario study, reducing the unit cost to a quarter or enhancing the current density capability to 4 times of the MgB_2 wire can effectively lower the LCCoE for all the topologies, especially those with more non-magnetic cores. If both these scenarios are combined as a long-term scenario, the difference of the LCCoE between the topologies will become very small. Then the topologies with more non-magnetic cores will become comparable to those with more iron. Aiming at a lower LCCoE, however, those topologies having the most iron are still the most promising candidates for both now and the long term, although they could result in large generator masses. If low weight is required, the topologies with more non-magnetic cores should be taken into account.

4

RIPPLE FIELD AC LOSSES IN MGB$_2$ SUPERCONDUCTING FIELD WINDINGS

4.1. Introduction

Partially superconducting (SC) generators have SC windings in the DC field winding and copper windings in the AC armature winding. This configuration aims at avoiding excessive AC losses appearing in presently available superconductors under AC conditions [25, 26, 67].

However, the DC field winding will also be exposed to a certain AC magnetic field ripple due to time and space harmonics. In the generator design phase the AC loss caused by this ripple field needs to be evaluated to assure both the avoidance of local overheating and the operation at a tolerable overall AC loss level. Consider that the power input to the cryogenic system, as a rule of thumb, should not exceed 1% of the power rating of the turbine to ensure an overall drive train efficiency around 95% [15]. The proportion of the power for cooling the ripple field loss cannot exceed one tenth of that, corresponding to 10 kW for a 10 MW generator. This is roughly estimated based on the fact that the majority of the cooling power consumption comes from other sources, e.g. conduction and radiation of heat. The ripple field loss, which is considered as a minor heat contributor, must be kept sufficiently small.

From the ripple field point of view there are several machine designs to consider. The use of ferromagnetic or non-magnetic armature teeth is of particular interest. Whereas non-magnetic teeth require more SC wires, ferromagnetic teeth introduce slotting effects which contribute significantly to the level of the magnetic field ripple [29], [119]. From the conclusions of Chapter 3, we see fully iron-cored topologies with iron teeth show better overall performance especially lower capital CoEs. However, their iron teeth could lead to unacceptable AC losses in the SC field winding, which needs to be evaluated in this chapter.

Another important design aspect to be studied in this chapter is the possibility to use an electromagnetic (EM) shield to reduce the influence of space harmonics on the field winding. Time harmonics in the armature currents are not considered in this study, because the power electronic converter with its filters can be independently designed for a very small harmonic content.

The objective of this chapter is to determine the applicability of different design solutions in terms of AC losses by estimating the AC loss level of 10 MW wind generator designs employing an MgB₂ SC field winding. The effects on AC losses are compared between non-magnetic and ferromagnetic teeth with different numbers of slots per pole per phase. The feasibility of the fully iron-cored topology with salient poles is evaluated from the AC loss perspective. The necessity of an EM shield is also evaluated based on the obtained loss levels.

Table 4.1: Basic generator design parameters based on the optimized topologies T8 and T12 from Chapter 3.

Parameter	NMT design	IT design
Nominal power P_N	10 MW	
Nominal torque T_N	10.6 MN·m	
Rated speed n_N	9.6 rpm	
No-load line voltage V_{Nl}	3300 V	
Specific electrical loading K	75 kA/m	
Mechanical air gap length g	6 mm	
Distance from field coil to air gap	50 mm	
Cryogenic temperature	20 K	
Armature bore diameter d_s	6 m	
Axial length l_s	2.34 m	2.56 m
Pole pair number p	12	20
Frequency at rated speed f_N	1.92 Hz	3.22 Hz
Field current density J_f	150 A/mm^2	175 A/mm^2
Field coil side dimension $h_f \times w_f$	10×111 mm^2	10×20 mm^2
Specific magnetic loading B	1.00 T	0.96 T
Number of turns per field coil	462	85
Armature slot height h_s	52 mm	102 mm
Ratio tooth width to slot pitch b_t/τ_s	0.31	0.65
MgB$_2$ wire length in slots l_{SC}	72.05 km	21.77 km

4.2. GENERATOR DESCRIPTION

4.2.1. GENERAL DESIGN

THE 10 MW three-phase generator to be studied is based on the optimized topologies T8 and T12 from Chapter 3. The generator has an MgB$_2$ SC field winding and employs a salient iron core for the field poles with an iron field back core. The armature yoke is also made from iron to confine the magnetic field inside the generator. Using iron cores can significantly reduce the cost and size of the generator [30], even if the iron is heavily saturated. Using salient iron poles maximally shortens the effective air gap length. The SC field coils are accommodated in modular cryostats around the salient poles. Each cryostat has only one field coil and this allows for easy maintenance and replacement of one module. Such a topology minimizes the cold mass and to some extent frees the position of the field coils in the radial direction [23].

The armature tooth material can be ferromagnetic or non-magnetic. The de-

signs with non-magnetic teeth (NMT) and iron teeth (IT) have been optimized for minimizing the capital cost of energy (CoE) of a 10 MW reference wind turbine in Chapter 3. In Chapter 3, the corresponding topologies are T8 and T12 for the NMT and the IT designs, respectively. The magnetic properties of the used armature core for the IT design are similar to those of M14 steel laminates [134]. The maximum flux density in the armature teeth for the IT design is 2.1 T. The basic design parameters of the two optimized designs are summarized in Table 4.1, and the optimal geometry of one pole of each design is plotted in Fig. 4.2 with no load flux densities.

Compared with non-magnetic teeth, ferromagnetic teeth introduce slotting effects which produce field harmonics in the field winding. However, the use of ferromagnetic teeth significantly reduces the reluctance of the machine, and therefore the generator length can become smaller [30]. To obtain a comparable generator length with non-magnetic teeth instead, much longer SC wires have to be used, as indicated in Table 4.1.

The number of slots per pole per phase q is an important factor for ferromagnetic teeth. A larger q means less slot effects but narrower teeth. The original machine design has $q = 4$ which is then modified to $q = 2$, 3 and 5 for analyzing its effects on AC losses. The number of q does not change the parameters shown in Table 4.1.

An EM shield can be used for screening the field harmonics from the armature. Usually this shield is part of a cryostat and made from a conductive metal, e.g. copper, aluminum. At the same time of screening harmonics, however, eddy current losses are induced by these harmonics. There should thus be a trade-off between the shielding effect and the eddy current loss production if an EM shield is required. The placement of the EM shield is illustrated in Fig. 4.1.

4.2.2. MAGNETIC FIELD

The magnetic field is computed without an EM shield in a 2D finite element model as shown in Fig. 4.2. This model applies a uniform current density in the field winding and the armature winding has a rated three-phase current to obtain the maximum torque. The field is a superposition of a DC field and AC field harmonics. The DC field determines the critical current density of an SC wire and the AC fields determine the AC losses. This machine model does not model the wires' superconductivity properties but only computes the external fields transverse to an SC wire.

For instance, the AC field components of the NMT design and the IT design with $q = 5$ at one point (Point M) in the field coil are illustrated in Fig. 4.3, in the form of time variation and frequency spectrum. In the NMT design only the 6th (11.52 Hz) and the 12th (23.04 Hz) harmonic appear, whereas in the IT design the 18th (57.60 Hz), 24th (76.80 Hz) and 30th (96.00 Hz) harmonics also contribute with the 6th
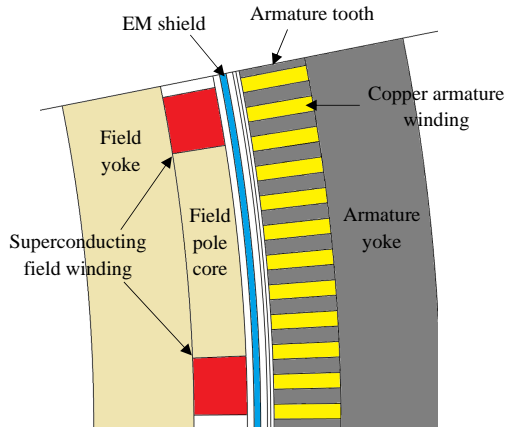
Figure 4.1: Sketch of the EM shield between the rotor and stator of a superconducting generator (taking the topology with non-magnetic rotor core as an example).
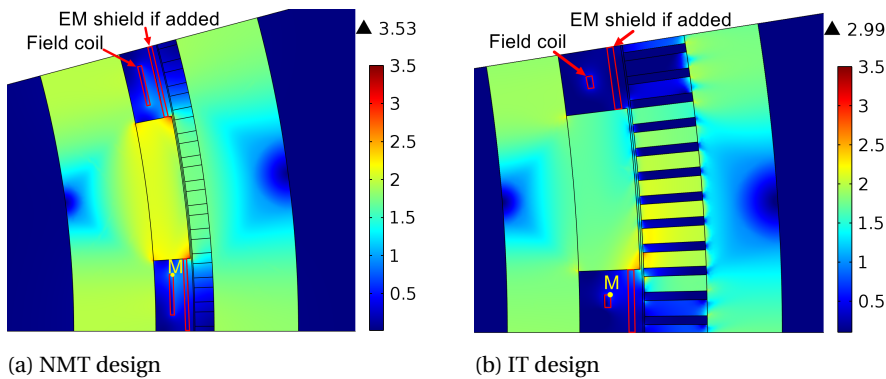

(a) NMT design

(b) IT design

Figure 4.2: Generator geometries with non-magnetic teeth (a) and ferromagnetic teeth (b). Magnetic flux density [T] in no load is shown by colorbar.

(19.20 Hz) and 12th (38.40 Hz) harmonics. In both of the designs the 6th harmonic dominates.

4.2.3. SUPERCONDUCTING WIRE

The cross-section of the employed MgB$_2$ wire (supplied by Columbus Superconductors [57]) is shown in Fig. 4.4a. The SC wire has 19 MgB$_2$ filaments embedded, and arranged approximately elliptically, in a nickel matrix. The fill factor is 21.5% and

(a) NMT, radial component

(b) NMT, tangential component

(c) IT, radial component
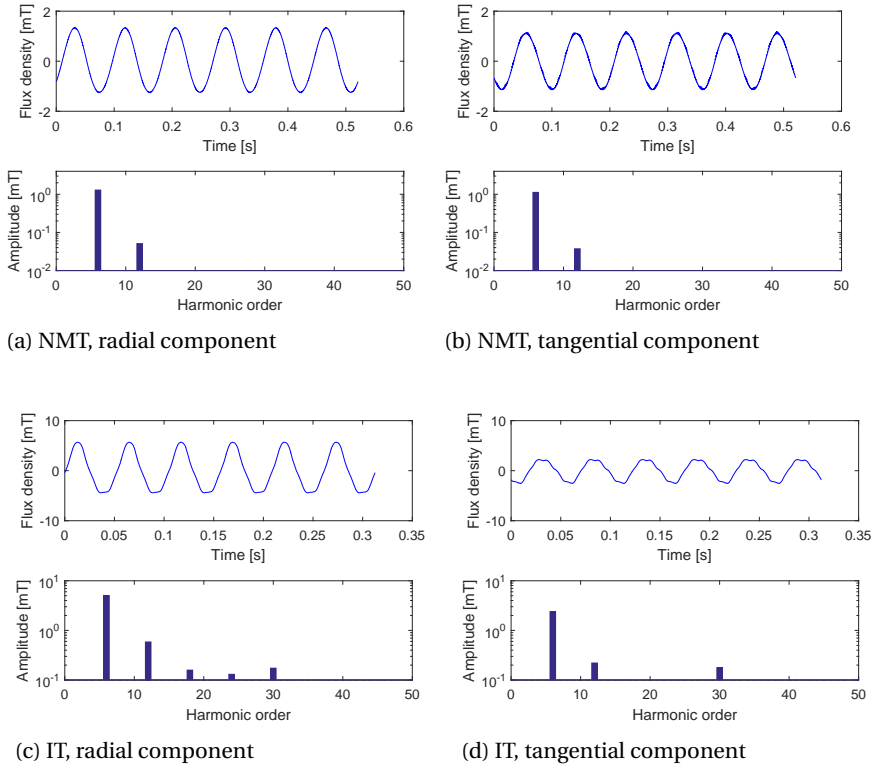

(d) IT, tangential component

Figure 4.3: AC component of flux density in one cycle and its frequency spectrum of the harmonics at Point M (marked in Fig. 4.2) in the field winding ($q = 5$).

the twist pitch is 0.3 m. The dimension is 0.5 mm x 3 mm with an additional 0.2 mm thick copper strip soldered to one longer side of the wire. The critical engineering current density for the NMT design is $J_e = 200$ A/mm^2 and for the IT design is $J_e = 239$ A/mm^2. The wires are operated with a safety margin of 25% to the critical engineering current density [122].

4.3. AC LOSS MODELING

4.3.1. APPROACH

THE models consider the AC losses produced in the SC field winding. Other losses within the cryogenic environment, i.e. losses in electrically conductive structures, are not considered.

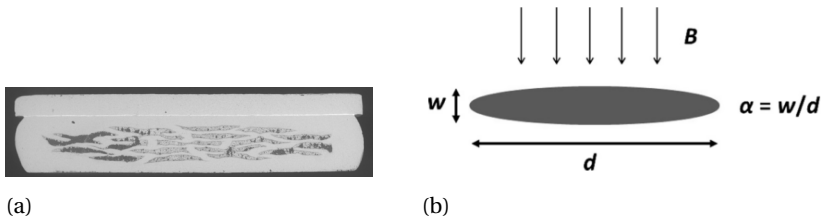(a)   (b)

Figure 4.4: Modeling of the SC wire. (a) Cross-section (3 mm wide). (b) Definition of the dimensions for the elliptical filament core region in an applied field B. B appear as perpendicular for $\alpha < 1$ and parallel for $\alpha > 1$ [32].

To estimate the AC losses due to ripple magnetic fields we apply 2D analytical hysteresis and coupling loss models as outlined below. The models are generally non-linear in magnetic field and valid for one frequency only. For the generator case, with one or a few contributing ripple frequencies, a good approximation is obtained by considering the harmonic(s) with the largest amplitude. This approximation can be supported by the following reasoning. When the ripple field is partially penetrating the superconductor, the hysteresis loss is proportional to the frequency but roughly proportional to the cube of the amplitude of the ripple field. With such partial field penetration, the coupling loss for long twist pitches is irrelevant to the frequency but proportional to the square of the amplitude of the ripple field. The AC losses are therefore much more sensitive to the amplitude than to the frequency.

To check the validity of this approximation, the AC losses will not be presented in the form of a value but a range. The loss due to the harmonic with the largest amplitude (one frequency only) is considered as the lower boundary of the loss range, and the loss due to all the most contributing frequencies are summed as the upper limit. If the range of losses turns out to be small, the harmonic with the largest amplitude can be used for estimating the AC losses.

In addition to wire dimensions and properties, the frequency and transverse magnetic field from Section 4.2 are used as input parameters to the AC loss models. As the magnetic field varies over one field coil, the cross-section of one coil is divided equally into 64 segments in which the AC loss is calculated individually. Then the results are summed to obtain the loss over the entire field coil and the entire field winding, assuming that the 2D analysis is identical along the generator length.

In our calculations we omit the end field winding, since in end winding regions longitudinal fields also exist but the slotting effect due to iron teeth becomes much weaker.

4.3.2. HYSTERESIS LOSS

Hysteresis losses are commonly modeled based on the critical state model [135], [136] and analytical expressions are available for simple geometries [137], [138]. Here we base our model on the work in [32], which in turn was based on the work by ten Haken et. al [139]. The model considers elliptical cross-sections of the filament region with arbitrary aspect ratios (see Fig. 4.4b). By setting the aspect ratio α above or below unity, magnetic fields parallel or perpendicular to the wire face are considered.

In the low field range (agreeing with this study), the loss becomes proportional to the cube of the ripple field and it becomes independent of the DC current, whereas the DC magnetic field influences the loss by its influence on the critical current (density). The hysteresis loss per unit length is:

$$P_{h0} = f A M_p B_p(\alpha) Q(B_{ac}), \tag{4.1}$$

where f is the frequency, A is the conductor area as given in Fig. 4.4b, M_p is the magnetization of the fully penetrated ellipsis, B_p is the field of full penetration depending on the aspect ratio α, and Q is the normalized energy loss per cycle of the AC magnetic flux density B_{ac} [32], [139].

The loss is calculated for parallel and perpendicular magnetic fields separately using the respective field components. These losses are then summed as an approximation which gives good accuracy in most of the winding [32].

4.3.3. COUPLING LOSS

Carr [137] developed a coupling loss model for a round wire in slowly changing magnetic fields. This model takes into account the case with a relatively long twist pitch, and therefore it can be applied to the MgB$_2$ wires in this study. To adapt to the shape of the wire for the model, the filament core region is approximated to be round by keeping the same cross-sectional area of the filament region. This approximation can be justified since the filaments operate in the fully coupled and low field region, where the coupling loss becomes determined by the full screening current passing the matrix twice every twist pitch (and the degree of coupling do not change with wire dimensions). The loss per unit length is given by

$$P_{c0} = \frac{8\pi^3 R_0^2 B_{ac}^2}{\mu_0^2 \sigma_\perp l_t^2}, \tag{4.2}$$

This is only valid for the frequency f of the ripple field fulfilling $\frac{1}{2\pi\sigma_\perp \mu_0 R_0^2} \geq f \geq \frac{4\pi}{l_t^2 \mu_0 \sigma_\perp}$, where l_t is the twist pitch, $R_0 = 0.463$ mm is the equivalent radius of the filament core region and $\sigma_\perp = 12.8 \times 10^7$ S/m is the transverse conductivity with no

contact resistance at 20 K. In this special case, the coupling loss is independent of frequency. The frequencies of the NMT and IT designs meet this range, so we can use Eq. (4.2) to estimate the coupling loss for the both designs.

4.4. RESULT AND DISCUSSION

Using the models Eqs. (4.1) and (4.2), the hysteresis loss and the coupling loss are calculated for the case with non-magnetic or ferromagnetic teeth and different q numbers. An EM shield is absent in all the cases. The distribution of the obtained hysteresis loss and coupling loss is plotted in Fig. 4.5 for the IT design with $q = 2$ for instance. It can be observed that one field coil side has more AC losses than the other and that more losses are produced in the regions closer to the armature.

The range of total AC losses with different numbers of q is shown in Fig. 4.6a, compared for the NMT and IT designs. The total AC loss is the sum of the hysteresis and coupling losses. Higher AC losses result from ferromagnetic teeth, but they are very small especially when q increases. The ranges of total AC losses are very small except for the IT design with $q = 2$. This proves the validity of the approximation for AC losses with a large q by using the field harmonic with the largest amplitude.

If the cryogenic cooling penalty factor at the temperature of 20 K is assumed as 1000, the required power at room temperature to cool the amount of AC losses for the IT design with $q = 2$ (the worst case in this comparison) will be no more than 9.1 kW. The currently available cryogenic refrigeration technology is capable of handling this power. Moreover, the reduction of generator efficiency due to this cooling power demand is negligibly small (less than 0.1% of 10 MW).

The employed analytical models for calculating the AC losses may not be sufficiently accurate since some assumptions and simplifications are used. If we assume a huge error of the models which increases the total AC loss by an order of magnitude, the required cryogenic cooling power for the IT design with $q = 2$ will be 91 kW which is almost 1% of the rated generator power. This cooling power may be too high. Then the number of slots per pole per phase can be increased to $q = 4$ and the cooling power will drop to only 31 kW which is about 0.3% of the rated generator power. This level of cooling power is considered acceptable in terms of both cooling system capability and sufficient efficiency.

The results also imply that it is not necessary to place an EM shield for reducing AC losses in normal operation. Firstly, with an EM shield the AC losses cannot be beneficially reduced, since the AC losses have already been very small. Secondly, placing an EM shield will introduce eddy current losses which could be much higher than the power demand for cooling the AC losses.

For testing purposes, a 10 mm thick copper shield is placed 10 mm far from the air gap, as shown in Fig. 4.2. The width of the shield occupies the width between two
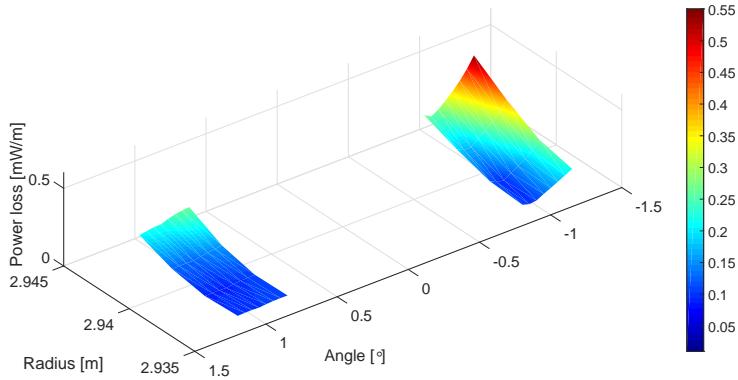
(a) Hysteresis loss
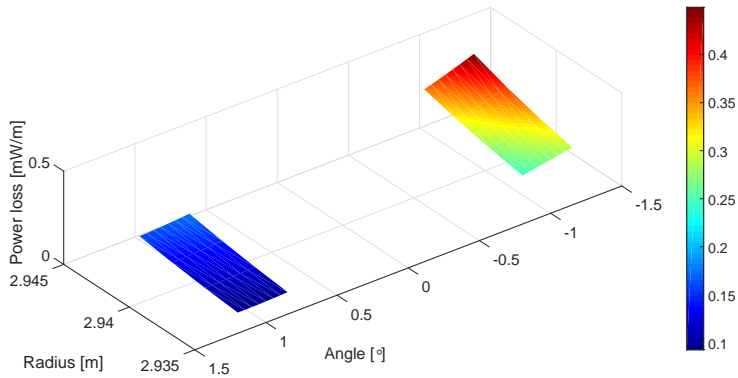
(b) Coupling loss

Figure 4.5: AC loss distribution in a field coil for the IT design, along the radial position and the circumferential angle of the generator, with $q = 2$.

adjacent poles. After adding this EM shield, the amplitudes of the five dominant field harmonics are all reduced. However, as indicated in Fig. 4.6b, the IT design with $q = 4$ and an EM shield produces an 8 kW loss in the shield, which is more than 2 times the power for cooling the corresponding AC loss (assuming a cryogenic cooling penalty factor of 1000).

Apparently, a larger q also reduces the loss in an EM shield because of less slotting harmonics. In terms of cryostat design, if conductive parts are inevitable between the field winding and the armature, the eddy current loss in such conductive parts can be reduced by using a larger q or non-magnetic teeth [119]. It is possible
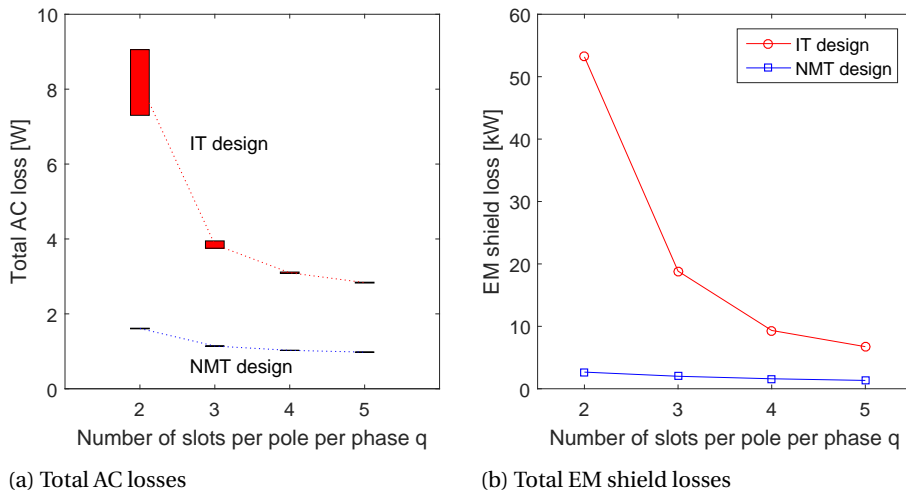
(a) Total AC losses (b) Total EM shield losses

Figure 4.6: Total AC losses and EM shield losses as a function of q.

to design an optimal EM shield for both low eddy current losses and good shielding effects, but this issue is beyond the scope of this chapter.

This low level of AC losses is obtained from the specific generator design described in Section 4.2. This design has a relatively large distance between the field winding and the armature because of the limitation of cryostat dimensions. If this distance is made smaller, the field harmonic contents will become higher and more AC losses will occur. Moreover, this design also has relatively wide teeth due to the fact that the machine optimization has found a balance between the saturation of teeth and the minimization of capital CoE.

4.5. CONCLUSION

THe models of hysteresis losses and coupling losses in a multi-filamentary strip MgB$_2$ wire were described and then applied to calculate the AC losses in two 10 MW SC wind generator designs. The results show

• that this generator design has a very small amount of AC losses with ferromagnetic teeth and without an EM shield, and

• that a larger number of slots per pole per phase q results in lower AC losses.

The results provide two important machine design suggestions. One is that the amount of AC losses produced by ferromagnetic teeth can be very small for an SC machine design, which implies that the fully iron-cored topology is feasible from

the perspective of AC loss production in the SC field winding. The other suggestion is that an EM shield can be unnecessary for AC loss reduction in normal operations. Conductive parts should thus be avoided as much between the field winding and the armature to minimize the induced eddy current losses. If conductive parts are inevitable, ferromagnetic teeth with a large q or non-magnetic teeth can be considered.

4

5

REDUCING THE SHORT CIRCUIT TORQUE

5.1. INTRODUCTION

Superconducting machines usually have larger magnetic air gaps than conventional generators because of space for a cryostat or use of non-magnetic cores. As a result, the inductance becomes lower and then the short circuit torque can become as high as more than 10 times the rated torque which is too high for wind turbine constructions.

A few approaches can be considered to reduce the short circuit torque. Since the sub-transient reactance of a synchronous generator determines the peak short circuit current, an electromagnetic (EM) shield between the rotor and stator could play a role to reduce the short circuit torque. An EM shield being part of the cryostat wall, as sketched in Fig. 4.1, is recommended to be used in a superconducting (SC) machine to attenuate harmonic magnetic fields from the armature to the field winding [118]. In an EM shield which is electrically conductive, eddy currents are induced during an armature winding short circuit. The eddy currents then excite magnetic fields to oppose the change of the air gap field. This reaction determines the sub-transient reactance X_d'' of an SC synchronous machine and then the short-circuit current and torque. In general, the larger the sub-transient reactance X_d'', the smaller the short-circuit current.

In addition, ferromagnetic core or multiple armature windings could be useful to reduce the short circuit torque [33]. Using ferromagnetic core increases the inductance. Using multiple armature windings assumes that not all the armature winding but only part of it is shorted since the chance of shorting all the armature segments at the same time is too low.

Multiple or, as we call it, segmented armature windings can be realized in a wind turbine by being connected to multiple back-to-back power electronic converters, as illustrated in Fig. 5.1. Each armature winding segment is connected to an individual converter. This generator system has been proposed in the INNWIND.EU project and performance indicators are evaluated in [140].

This chapter aims at assessing the effects of EM shields and armature segmentation on reducing the short circuit torque of SC synchronous generators (SCSGs). These SCSG designs have different topologies which change the combination of iron and non-magnetic cores. The calculation of short circuit torque uses FE methods (FE) methods which can model saturation changes during a short circuit.

5.2. FOUR GENERATOR DESIGNS

Four of the twelve topologies discussed in Chapter 3 have been proposed for 10 MW SCSGs in a few recent research projects. This chapter studies four 10 MW generator designs employing these four topologies, as illustrated in Fig. 5.2.

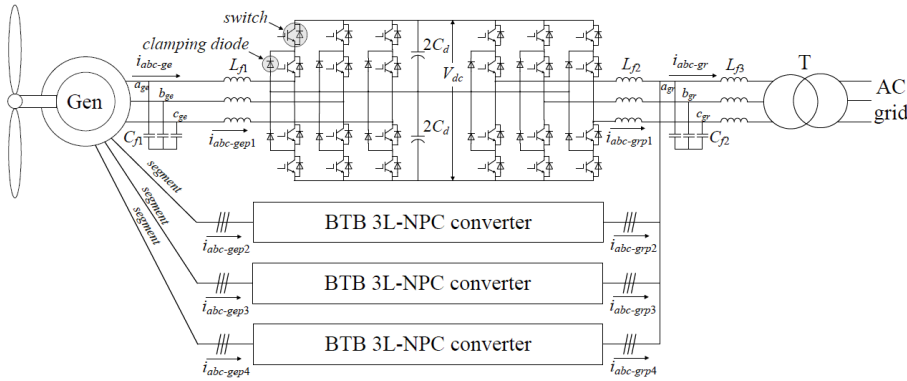Design A (based on the optimized topology T5 from Chapter 3) is considered

Figure 5.1: Block diagram of multiple power electronic converters for a 4-segments generator. [140]

as an air-core concept since all the cores but the armature yoke are non-magnetic. This concept is proposed in [122] for a 10 MW SCSG design. The advantage of this topology is low weight and no slotting effects. However, a large amount of SC wires is required to excite sufficient magnetic fields. Due to the non-magnetic core for the field winding, it is not possible to use salient poles.

Design B (based on the optimized topology T9 from Chapter 3) is considered as an air-rotor concept since the cores for the field winding are all non-magnetic while the cores for the armature winding are all made of steel laminates. This concept is proposed in [20] for a 10 MW SCSG design. The advantage of this topology is that laminate cores used in conventional generators can directly be used. However, a large amount of SC wires is also demanded and slotting effects exist due to iron teeth. This concept cannot use salient poles either.

Design C (based on the optimized topology T8 from Chapter 3) is considered as an air-winding concept since only the armature teeth are non-magnetic while all the other cores are made of iron. Salient poles can be used in this topology to minimize the distance between the field winding core to the armature winding. To apply this topology, modular cryostats have to be used as proposed by [23]. The main advantages of this topology are a small magnetic air gap and no slotting effects. The use of SC wires is effectively reduced compared to the designs A and B. However, non-magnetic teeth require special cooling methods since non-magnetic materials, e.g. glass fiber G10, are bad at thermal conduction.

Design D (based on the optimized topology T12 from Chapter 3) is considered as a fully iron-cored concept since all the cores are made of iron. This topology looks like conventional synchronous generators but the copper field winding is replaced

(a) Design A (T5)   (b) Design B (T9)

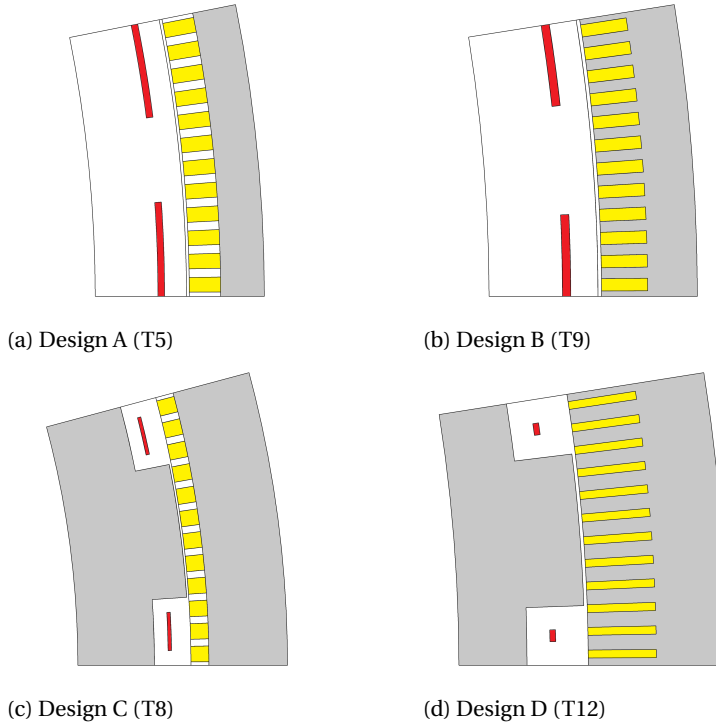(c) Design C (T8)   (d) Design D (T12)

Figure 5.2: Sketch of one pole of the topology of the SCSG designs. Red: SC field winding. Yellow: copper armature winding. Gray: iron core.

by an SC winding. The steel laminates can directly used for the armature cores. Modular cryostats also have to be used to enable the salient poles. The amount of SC wires is significantly reduced compared to the designs A, B and C. The cost of this topology is thus not very high. However, this topology may be very heavy and slotting effects may cause high torque ripples. This concept has been studied in [30, 120] and Chapter 4 of this thesis from different perspectives.

Each design using MgB_2 field windings has been optimized for the minimum capital cost of energy in a 10 MW reference wind turbine as presented in Chapter 3. The optimal geometry of one pole is shown in Fig. 5.2. The design parameters are summarized in Table 5.1. The cryogenic temperature for the MgB_2 field winding is still 20 K. The electrical loading of the designs is still limited to 75 kA/m to enable forced-air cooling on the armature winding [123]. The chosen number of slots per

pole per phase $q = 4$ is both to avoid significant slotting effects and to have the armature teeth sufficiently wide.

Table 5.1: Main Parameters of Four Superconducting Generator Designs

Design	A	B	C	D
Nominal power P_N		10 MW		
Rated speed n_N		9.6 rpm		
No-load voltage V_n		1905 V		
Number of phases m		3		
Armature bore diameter d_s		6 m		
Mechanical air gap length g		6 mm		
Rated armature current density J_s		3 A/mm^2		
Slot number per pole per phase q		4		
Axial length l_s (m)	4.08	3.75	2.34	2.57
Pole pair number p	16	20	12	20
Foil coil height h_f (mm)	14	14	10	10
Foil coil side width w_f (mm)	200	139	111	20
Armature slot height h_s (mm)	66	78	52	118
Tooth width/slot pitch b_t/τ_s	0.37	0.47	0.31	0.65
Operating field current I_f (A)	206.6	197.5	239.4	280.3
Number of turns per phase N_a	128	128	110	128
Number of turns per field pole N_p	1163	810	463	85

5.3. MODELING OF SHORT CIRCUIT

THree-phase short circuits are modeled by 2D FE methods to calculate the short circuit torque. No damper winding is used outer the field winding. The model couples the computation of magnetic fields and the generator's equivalent circuit and is called field-circuit-coupled model. The field model computes the induced voltage $\frac{d\lambda_a}{dt}$, $\frac{d\lambda_b}{dt}$ and $\frac{d\lambda_c}{dt}$ over the three phases and $\frac{d\lambda_f}{dt}$ over the field winding due to the resultant air gap magnetic field (including every flux leakage). The circuit model is used to calculate the current flowing in each phase i_a, i_b and i_c and in the field winding i_f. The circuit model can be written as

$$u_a = \frac{d\lambda_a}{dt} - R_s i_a - L_{ews} \frac{di_a}{dt} \tag{5.1}$$

$$u_b = \frac{d\lambda_b}{dt} - R_s i_b - L_{ews} \frac{di_b}{dt} \tag{5.2}$$

$$u_c = \frac{d\lambda_c}{dt} - R_s i_c - L_{ews}\frac{di_c}{dt} \tag{5.3}$$

$$u_f = \frac{d\lambda_f}{dt} + R_f i_f + L_{ewf}\frac{di_f}{dt} \tag{5.4}$$

where $L_{\sigma ews}$ is the end winding inductance per phase of the armature winding, $L_{\sigma ewf}$ is the end winding inductance of the field winding, u_f is the terminal voltage of the field winding which is very small, R_s is the resistance per phase and R_f is the resistance of the field winding.

The end winding inductance per phase of the armature winding is calculated with analytical models given by [123]:

$$L_{ews} = \frac{4m}{Q} q N_s^2 \mu_0 l_w \lambda_w \tag{5.5}$$

where is the total number of slots, N_s is the number of turns per phase, and $l_w \lambda_w$ is calculated by

$$l_w \lambda_w = 2 l_{ew} \lambda_{lew} + W_{ew} \lambda_W \tag{5.6}$$

where l_{ew} is the axial length of the end winding measure from the end of the stack, and W_{ew} is the coil span. λ_{lew} and λ_w are the corresponding permeance factors estimated in [123]. When the number of armature winding segments is N_{seg}, L_{ews} and R_s should be reduced to $1/N_{seg}$ time.

The end winding inductance of the field winding L_{ewf} is calculated by subtracting the inductances from 3D FE models by the inductance from 2D FE models. The resistance and the end winding inductances are summarized in Table 5.2. The field winding resistance R_f is caused by the small resistance in the current leads which are not superconducting [118].

Table 5.2: Resistances and End Winding Inductances

Design	A	B	C	D
End winding inductance L_{ews} (mH)	1.23	0.78	1.61	0.78
End winding inductance L_{ewf} (H)	15.2	10.2	8.6	2.4
Resistance R_s (mΩ)	54.1	48.1	34.7	36.4
Resistance R_f (mΩ)	20	20	20	20

The short circuit torque can be so high that the speed of an SCSG drops fast during a short circuit. The rotation of the generator is governed by

$$T_m - T_e = J\frac{d\omega_m}{dt} \tag{5.7}$$

where T_m is the mechanical torque driving the generator by the wind turbine. Since before the short circuit is there no load, this torque can be assumed to be $T_m = 0$ during the short circuit. T_e is the electromagnetic torque produced by the generator, and ω_m is the rotational speed of the generator. The moment of inertia J is estimated with a scaling function given in [141]:

$$J = \frac{14500}{9}P_N^{1.2}R_{tr}^2 \tag{5.8}$$

where P_N is the nominal power of the wind turbine in MW and R_{tr} m is the radius of the wind turbine rotor. In this chapter, we use a 10 MW reference wind turbine with a rotor diameter of 178 m [11].

The short circuit occurs in such a way that the generator's three phases are shorted at the terminal by applying zero voltages to u_a, u_b and u_c after a no-load operation of one electrical cycle. For assessing the effects armature winding segmentation on the short-circuit torque, no-load operation is sufficient which also simplifies FE modeling.

5.4. EFFECTS OF EM SHIELD

An EM shield is electrically conductive and usually the outer part of a cryostat wall. It cannot be placed too close to the SC field winding since it will introduce significant increase of thermal loads to the 20-K temperature dewar of the cryostat. Furthermore, the thickness of the EM shield cannot be too large. Otherwise the cryostat wall will push the field winding farther away from the armature winding to remain the same thermal insulation performance. This increase of distance of the field winding may not too much affect the topologies with salient iron pole but it will significantly affect the other topologies. As a result, four cases regarding the EM shield are compared:

- Case 1: the EM shield is placed just next to the 6-mm mechanical air gap and its thickness is 10 mm.

- Case 2: the EM shield is placed just next to the 6-mm mechanical air gap and its thickness is 20 mm.

- Case 3: the EM shield is placed 10 mm off the 6-mm mechanical air gap and its thickness is 10 mm. This case is chosen for comparison but it is less practical since the EM shield may go to the space of a lower temperature. The generated heat in the EM shield may significantly increase the thermal loads within the cryostat.

- Reference case: no EM shield is used.

The material of the EM shield is copper. Its conductivity is set to be 42.9 MS/m, assuming a working temperature of 120 °C. Using this conductivity assumes that the outer cryostat wall operates in a room-temperature environment since it is close to the mechanical air gap.

RESULTS

Designs A and B are investigated. The electromagnetic torques during the short circuit (five electrical cycles of rated frequency) in the four cases for Designs A and B are shown in Fig. 5.3. The effects of EM shield on reducing the peak torque are compared in Fig. 5.4. The effects of EM shield in Cases 1 and 3 on reducing the peak torque are both very small. Case 2 with a thicker EM shield shows better effects which are however still quite insufficient if a peak torque of about 3 p.u. is required.

From these results, using an EM shield does not effectively reduce the peak torque during a short circuit. A thinker EM shield may be more effective but a much thicker shield is not realistic due to space limitation.

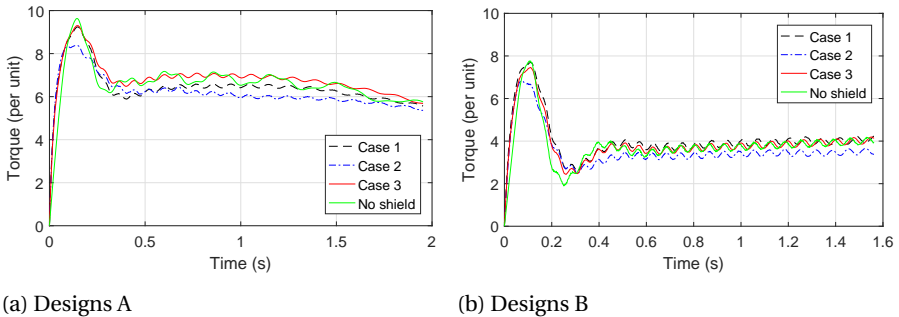(a) Designs A   (b) Designs B

Figure 5.3: Effects of EM shield on short circuit torque of Designs A and B during the short circuit for five electrical cycles of rated frequency in four cases.

5.5. ARMATURE SEGMENTATION

5.5.1. CHOSEN SCHEME OF ARMATURE SEGMENTATION

IN this chapter, the armature winding is segmented in such way that certain pole pairs belong to each segment and these pole pairs of one segment are evenly distributed along the generator circumference. The numbers of pole pairs of the four SCSG designs allow the number of segments to be 2 or 4. The segmentation way for the design D is sketched in Fig. 5.5 for 2 and 4 segments, for example. The pole pairs with S1 is connected to an individual converter and the pole pairs with S2 is connected to another individual converter, and so on.
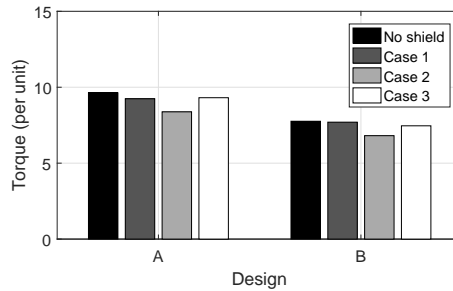
Figure 5.4: Effects of EM shield on peak torque of Designs A and B in four cases.

Evenly distributing the segments and their own pole pairs makes sure symmetry along the generator circumference. The purpose is to avoid significant unbalanced forces during a short circuit.

Short circuits at the armature winding terminals are usually caused by the failure of power electronic switches used in the converters. By dividing the armature winding into a few identical segments, the chance of a three-phase short circuit on the whole generator is greatly reduced. Since the probability of a three-phase short circuit in a non-segmented generator is small, the probability of three-phase short circuits occurring in all segments of a segmented generator at the same time is much smaller [33]. Thus, this chapter only examines the case when a three-phase short circuit only occurs to one of the armature winding segments, since the chance for it to happen is higher than the other cases.

5.5.2. FINITE ELEMENT MODELING OF ARMATURE SEGMENTATION

This chapter aims at assessing the feasibility of applying armature segmentation to reduce the short circuit torque. A 2D FE model is used to simulate the armature segmentation with two assumptions that simplify the problem.

ASSUMPTIONS

In this chapter, two assumptions are made for modeling the armature segmentation by FE methods:

• The armature winding has a single layer. This means that the overlapping of armature coils between adjacent segments is neglected in the slots.

• The end winding is neglected. This means that the overlapping of armature coils between different segments is neglected at the winding end.

These two assumptions result in independent armature segments and enable 2D transient FE modeling of short circuits. However, large practical power generators
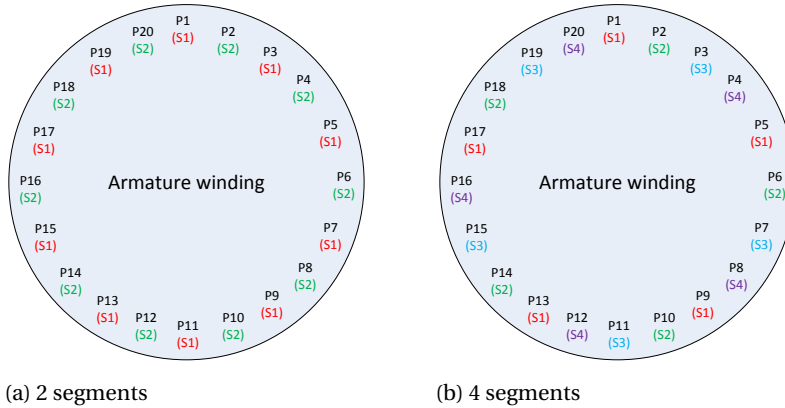
(a) 2 segments   (b) 4 segments

Figure 5.5: Sketch of segmentation and pole pair distributions for Design D. P- pole pair numbering. S-armature winding segment numbering.

usually apply double-layer windings. In addition, armature coils at the end winding have overlapping. In future work, these practical issues should be taken into consideration in the model. This chapter is just a starting point for studying the feasibility of armature segmentation for reducing the short circuit torque. If this study with these assumptions did not give effective reduction of the short circuit torque, it would not be needed to take further steps to assess this method. This is because dependent armature segments will introduce coupling of adjacent segments and weaken the reduction of short circuit torque.

MODELING
The FE model is illustrated in Fig. 5.6, using Design D with two armature segments as an example. The healthy segment and the faulted segment are adjacent. Since only one segment is faulted, the faulted segment is followed by a healthy segment as seen from the SC field winding. If the number of segment becomes four, the faulted segment will be followed by three healthy segments.

5.5.3. RESULTS
The FE short circuit model simulates five electrical cycles of the rated frequency. Figure 5.7 shows the current waveform of phase A of Design A, for instance, with and without armature segmentation. The peak currents remain in the same level in all the three cases. This result matches the rough estimation by $I_{peak} \propto (E_f/X_l)$, where E_f is the no-load voltage and X_l is the leakage reactance. When the number of armature segments is N_{seg}, the no-load voltage and leakage reactance of each
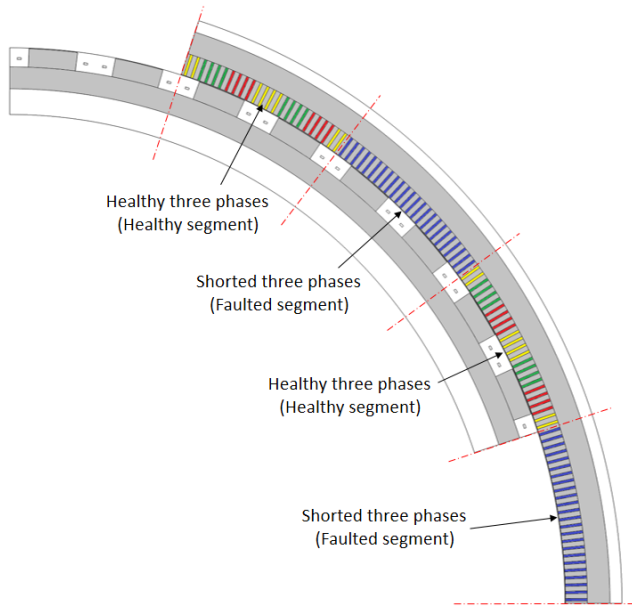
Figure 5.6: Modeling of armature segmentation in the FE model for short circuit simulation. Design D with two segments is shown as an example.

segment become E_f/N_{seg} and X_l/N_{seg}, respectively. Therefore, the peak current I_{peak} remains almost the same. The change of frequency is due to the decrease of rotational speed caused by the short-circuit torque.

Figure 5.7: Current of phase A of Design A with $N_{seg} = 1, 2$ and 4.

The electromagnetic torque T_e of the four SCSG designs are calculated in the

cases of non-segmented, 2-segments and 4-segments armature windings. The torque during the short circuit in each case is shown in Fig. 5.8. The torque during the whole short circuit process can effectively be sup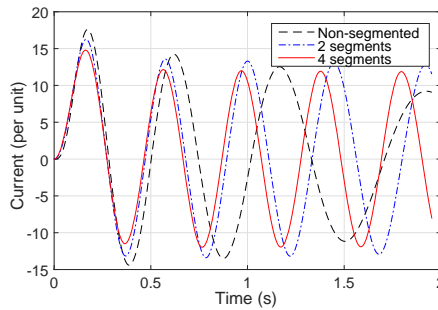pressed by armature winding segmentation. In the cases with armature winding segmentation, the short circuit torque has large ripples. This is a result of the field winding which is not segmented. p/N_{seg} of the field winding has to pass once the shorted segment every electrical cycle and all field poles pass healthy and shorted segments alternately, where N_{seg} is the number of segments. As a result, large ripples are induced in the field current, which then produce torque ripples.

(a) Designs A

(b) Designs B

(c) Designs C
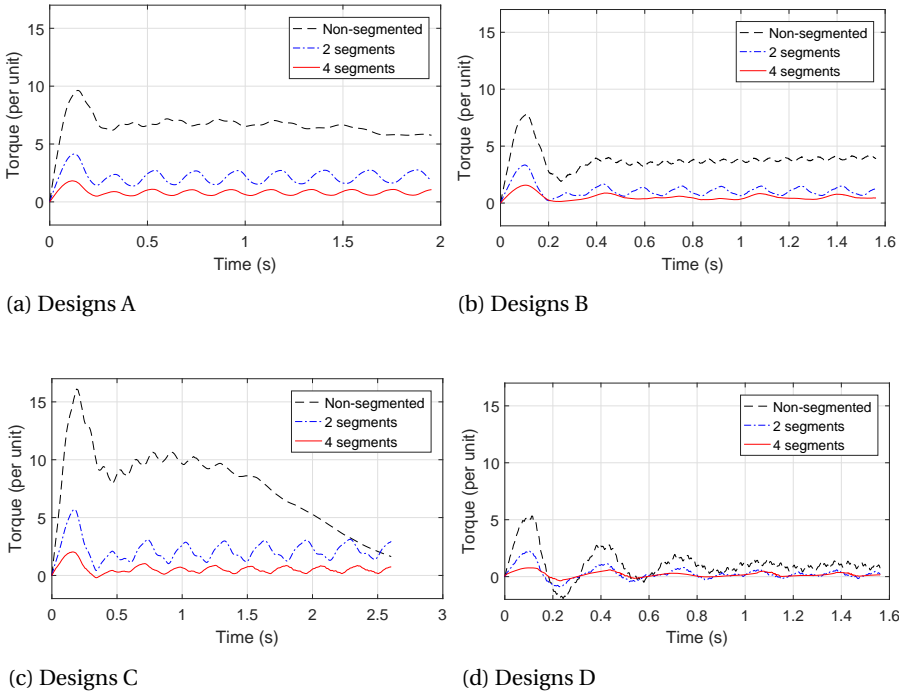
(d) Designs D

Figure 5.8: Effects of armature segmentation on short circuit torque of Designs A, B, C and D during the short circuit for five electrical cycles of rated frequency.

The peak torque is compared in Fig. 5.9. These results show that segmentation of the armature winding effectively reduces the short-circuit torque. If the number of segments is N_{seg}, the peak torque of the segmented SCSG is even a bit lower than $1/N_{seg}$ the peak torque of the non-segmented SCSG. Like the peak current, these results of peak torque match the rough estimation by $T_{e,peak} \propto (E_f^2/X_l)$. Normally, the

mechanical constructions for a wind turbine drive train are designed to withstand 3 times the rated torque. As the results show, dividing the armature winding into 4 segments can meet this requirement. With 2 segments, the peak torque is still too high.

Figure 5.9: Effects of armature segmentation on peak torque of Designs A, B, C and D with $N_{seg} = 1, 2$ and 4.

Designs B and D with iron armature teeth show lower peak torques than Designs A and C with non-magnetic teeth. Because of no damper winding, the peak torque is only determined by the armature leakage inductance. Design C has a small leakage inductance in the armature winding because the salient pole and the short armature teeth together reduce the slot leakage flux. In Designs B and D, the saturated iron teeth result in more slot leakage flux and their peak torques are therefore lower.

The speed change of the generator during the short circuit is shown in Fig. 5.10. The speed is governed by Eq. (5.7) and determined by the electromagnetic torque T_e. With no segmentation, the speed decreases fast in Designs A and C. With segmentation, the speed decreases become much smaller. Using 4 segments results in a very gentle deceleration.

5.6. CONCLUSION

Excessively high short circuit torques could be suppressed in a few ways for SC-SGs. This chapter assessed two approaches. One was making use of the EM shield which is part of the cryostat. The other divided the armature winding into a few identical segments. Four 10 MW SCSG designs differing in topologies were examined: two for the approach of using EM shield while four for the approach of armature segmentation. 2D finite element models were built to simulate the short circuit. The results show that the peak torque was not effectively reduced by using an EM shield if considering reasonable positions and thicknesses of the EM shield. However, the peak torque can effectively be suppressed by armature segmentation if one segment encounters a three-phase short at the terminal. Four segments are
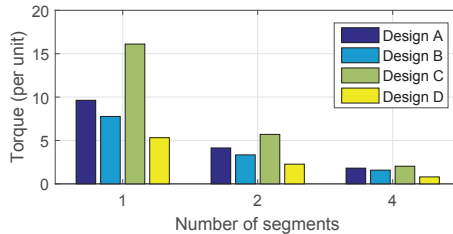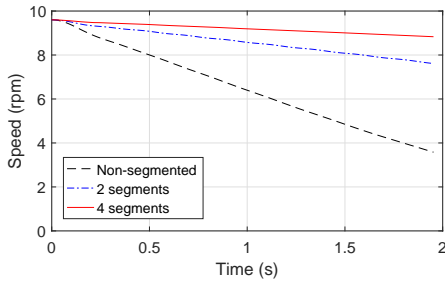
(a) Designs A
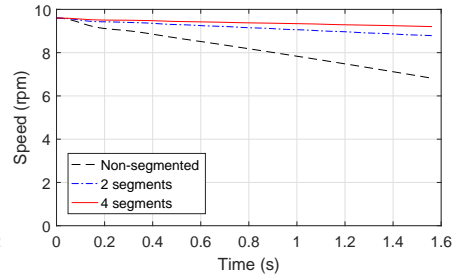
(b) Designs B
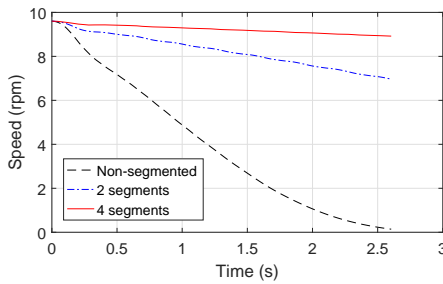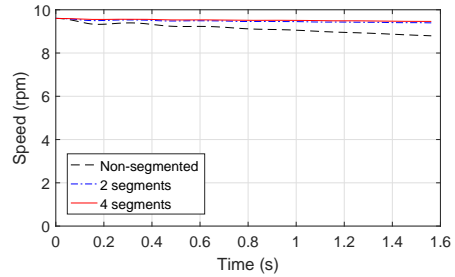
(c) Designs C

(d) Designs D

Figure 5.10: Speed change of Designs A, B, C and D during the short circuit for five electrical cycles of rated frequency.

more effective than two segments. More segments may be needed to meet the requirement of mechanical constructions of a wind turbine drive train, although additional costs due to multiple converters would be introduced.

In this chapter, we assumed that each armature segment is independent of the others by assuming a single-layer armature winding without the end winding. However, dependent segments with a double-layer armature winding with overlapping end windings are more often in practice. Dependent segments could weaken the effects of segmentation on reducing the short circuit torque. Dependent segments will be modeled and studied in the future work.

6

COMPARING SUPERCONDUCTING GENERATORS AND PERMANENT MAGNET GENERATORS

6.1. INTRODUCTION

Fᴿᴼᴹ Chapters 3, we found that the topology T12 with full iron cores and salient iron poles have lower capital CoEs and better overall performance. From Chapter 4, we found that iron teeth used in T12 do not produce unacceptable AC losses in the MgB$_2$ field winding. From Chapter 5, we found that the short circuit torque can effectively be suppressed by armature segmentation. Therefore, we can design a superconducting synchronous generator (SCSG) based on the topology T12 since T12 can now be considered most feasible for 10 MW direct-drive wind turbines. This design should be compared with a permanent magnet generator (PMSG) for evaluating its competitiveness.

At this moment, however, the technology readiness level of SCSGs for large wind turbines is so low that commercialization of such novel generators has not been realized yet. Comparing superconducting generators with technically mature PMSGs may not be fully fair, but it will be very interesting to compare their performance based on the same design and optimization method. Such comparisons are expected to provide feasibility insights for commercialization of SCSGs and to draw attention from the wind energy industry.

The objective of this chapter is to compare SCSGs and a PMSGs for 10 MW direct-drive wind turbines. Firstly we design an SCSG and a PMSG through the same design and optimization method for the minimum capital cost of energy (CoE) as developed in Chapter 3. Both the designed generators operate with the same wind turbine, wind condition and phasor diagram, and the optimization combines finite element (FE) and analytical models. Then this chapter compares the performance and important characteristics of the two generator designs with each other and another PMSG design available in the literature [131]. This PMSG design is compared as a reference since it employed a different design method established before. The quantities for comparison are: generator sizes, capital CoE of the wind turbine, annual energy production (AEP), and generator active material costs and masses.

6.2. GENERATOR DESIGN

6.2.1. GENERAL PARAMETERS

Aɴ SCSG and a PMSG are designed under the same conditions for the 10 MW reference direct-drive wind turbine used in previous chapters. The rated rotational speed is 9.6 rpm. The generator is directly connected to a back-to-back power electronic converter through a no-load line voltage of 3300 V. The generator parameters are listed in Table 6.1.

The diameter of the generator is not easy to decide. It is always a question whether to enlarge the diameter to around 10-m or to limit the diameter to a com-

Table 6.1: General characteristics of the 10 MW generator.

Parameter	Value
Nonimal torque	$T_n = 10.6\,\text{MNm}$
No-load line voltage	3300 V
Air gap diameter	$D_s = 6\,\text{m or } 10\,\text{m}$
Armature winding type	Distributed
Rated RMS amature current density	$J_s = 3\,\text{A/mm}^2$
Armature winding fill factor	$k_{fil}=0.6$

pact level (e.g. 6 m) for both the generator types. The diameter of 10 m or even larger has been extensively proposed for 10 MW direct-drive PMSGs [131, 142, 143] while a smaller diameter is considered to take more advantage of superconductivity for an SCSG.

This chapter considers both 6 m and 10 m as the air gap diameter of the SCSG and the PMSG. The diameter of 6 m may be too small for PMSGs, but it could indicate whether superconductivity is beneficial for reducing generator sizes and weights. Accordingly, the air gap length is set to 0.1% of the diameter, which is 6 mm for 6 m diameter and 10 mm for 10 m diameter.

The electrical loading of the armature winding is constrained below 75 kA/m to enable the use of forced air cooling for the stator. Direct cooling is costly and water cooling is complex for the wind turbine nacelle.

Two PMSG designs were proposed in [131] (for pitch control and active speed stall control, respectively) for a slightly different 10 MW wind turbine. The air gap diameter was 10 m. We select the pitch control design for the comparison in this chapter since most new wind turbines adopt pitch control nowadays. The generator design can be found in [131] in great detail.

6.2.2. OPERATION OF WIND TURBINE AND GENERATOR
The operation of the wind turbine and the phasor diagram for the generator operation have been introduced in Chapter 3. This chapter applies the same operations as described in Section 3.5.5.

6.2.3. SCSG
The SCSG design comes from the optimization results in Chapter 3 based on the unit cost and performance of currently available MgB_2 wires (the original case). The optimized topology T12 is chosen since it provide the best overall performance especially a lowest capital CoE. In Chapter 4, this SCSG design refers to as the IT de-

sign. In Chapter 5, this SCSG design refers to as the Design D. This SCSG design has an air gap diameter of 6 m. By using the same design and optimization method, we obtained the SCSG design with an air gap diameter of 10 m. One pole of the SCSG with the notation of optimization variables is sketched in Fig. 6.1.
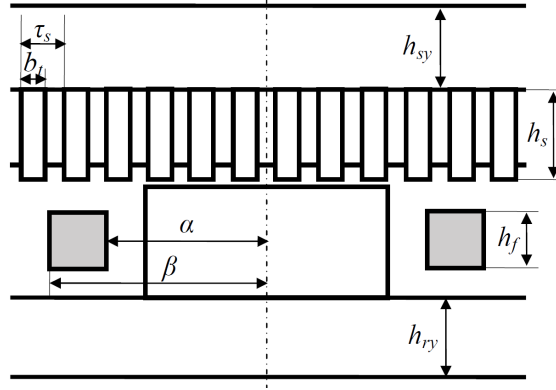
Figure 6.1: Sketch of one pole of an SCSG with the notations of the optimization variables. The gray blocks are the superconducting field coil accommodated in a modular cryostat. The space left around the field coil is fixed and occupied by the modular cryostat.

6.2.4. PMSG

The PMSG has surface-mounted permanent magnets on the rotor. The remanent magnetic flux density of the magnets is $B_r = 1.2$ T. The number of slots per pole per phase in the stator is set to $q = 2$ to allow for smaller pole pitches and achieve low losses in the magnets. One pole of the PMSG with the notation of optimization variables is sketched in Fig. 6.2.

The PMSG optimized in this chapter is referred to as PMSG-O and the referenced PMSG designed in [131] is referred to as PMSG-R. The PMSG-R design from [131] has an armature slot filling factor of 0.65 instead of 0.60. To constrain the electrical loading no higher than 75 kA/m and the armature tooth no narrower than 2 cm ($b_t \geq 20$ mm), we adjust the original design a bit: the slot height increases from 80 mm to 106 mm, and the ratio of armature tooth width to slot pitch increases from 0.50 to 0.61. The armature filling factor is changed to 0.60. Other design parameters remain the same. This adjustment makes sure that all the generator designs to be compared comply with the same conditions and constraints.
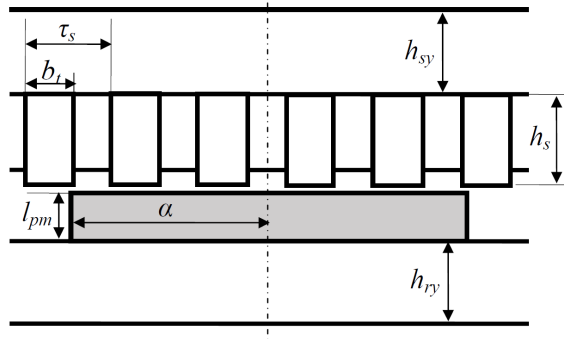
Figure 6.2: Sketch of one pole of a PMSG with the notations of the optimization variables. The gray block is the permanent magnet.

OPTIMIZATION

The optimization for the PMSGs is almost the same as that for the SCSGs except the following points:

• The objective function of the capital CoE now becomes

$$CoE = \frac{C_{CAPEX}}{a \cdot E_{AEP} \cdot T_{LT}} = \frac{C_{act}(X) + C_{str}(X) + C_{PE} + C_{other}}{a \cdot E_{AEP} \cdot T_{LT}} \tag{6.1}$$

where the cryogenic cooling power C_{cryo} has disappeared, and X is the set of optimization variables. For optimizing the SCSGs, the structural mass C_{str} is assumed to be a constant (as explained in Chapter 3). For optimizing the PMSGs, C_{str} is no more a constant but can be roughly estimated by scaling functions. The scaling function used in this chapter is based on the PhD thesis by Shrestha [27]. This PhD thesis developed scaling functions for structural mass as a function of the rated power and the aspect ratio of PMSGs. Since the 10 MW PMSG design in [131] is used as the reference for the scaling function, only the aspect ratio is taken into account in the scaling. In this chapter, the single bearing concept is chosen for the PMSG. The mechanical structure of this concept consists of beams and cylinders in the rotor and stator. Since the cost of the structure is proportional to the mass of the structure, the mass in the original scaling function is now replaced by the cost.

The scaling function for the cost of beams is given by

$$\frac{C_{beam}}{C_{beam,ref}} = (\frac{k_{asp,ref}}{k_{asp}})^{\frac{1}{3}} \tag{6.2}$$

where C_{beam} and $C_{beam,ref}$ are the structural beam costs of the PMSG to be optimized and the reference PMSG, respectively, and k_{asp} and $k_{asp,ref}$ are the aspect

ratios of the PMSG to be optimized and the reference PMSG, respectively.

The scaling function for the cost of beams is given by

$$\frac{C_{cy}}{C_{cy,ref}} = (\frac{k_{asp,ref}}{k_{asp}})^0 = 1 \tag{6.3}$$

where C_{cy} and $C_{cy,ref}$ are the structural cylinder costs of the PMSG to be optimized and the reference PMSG, respectively.

In this PhD thesis, Shrestha also estimated the ratio of the beam mass to the cylinder mass for the single bearing concept for different generator power ratings. For 10 MW, this ratio is about 4.5. Therefore, the ratio of the beam cost to the cylinder cost is also about $C_{beam}/C_{cy} = 4.5$. As a result, the scaling function for the structural cost for a 10 MW PMSG can be given by

$$\frac{C_{str}}{C_{str,ref}} = 0.818(\frac{k_{asp,ref}}{k_{asp}})^{\frac{1}{3}} + 0.182 \tag{6.4}$$

where $C_{str,ref}$ is the structural cost of the reference PMSG. The reference PMSG-R has a structural cost of $c_{str,ref} = 780$ k€ and an aspect ratio of $k_{asp,ref} = 0.16$ [131].

In this chapter, we assume that the unit cost of permanent magnet (NdFeB) is 50 €/kg. The cost of components of the 10 MW reference wind turbine for calculating C_{other} is estimated in Table 6.2. The energy production is obtained through calculating the power losses in the PMSGs. Compared to SCSGs, PMSGs do not have the cryogenic cooling power P_{cryo} and the eddy current loss in the armature copper conductors $P_{Cus,eddy}$ (as given in Eq. (3.13)).

Table 6.2: Cost estimation for the 10 MW reference wind turbine with SCSGs and PMSGs.

Component	Estimated cost		
Generator type	SCSG	PMSG-O	PMSG-R
Wind turbine (exl. generator)	7,500 k€		
Balance of plant	17,000 k€		
Power electronics C_{PE}	800 k€		
Cryogenic system C_{cryo}	710 k€(6 m), 600 k€(10 m)	n/a	n/a
Generator structural material C_{str}	500 k€(6 m), 700 k€(10 m)	To be optimized	780 k€
Generator active material C_{act}	To be optimized	To be optimized	620 k€[†]

[†]The unit cost of permanent magnets is adapted from 25 €/kg to 50 €/kg.

Table 6.3: Optimization variables and their optimal values.

		SCSG		PMSG-O		PMSG-R[†]
	Air gap diameter D_s (m)	6	10	6	10	10
	Generator active length l_s (m)	2.56	1.15	4.67	1.53	1.74
x_1	Pole pair number p	20	38	74	94	160
x_2	Inner pole span angle α (electrical degree)	66	66	62	72	73
x_3	Outer pole span angle β (electrical degree)	74	72	n/a	n/a	n/a
x_4	Field coil height h_f or magnet length l_m (mm)	10	10	18	28	20
x_5	Armature slot height h_s (mm)	102	114	98	118	80
x_6	Armature yoke height h_{sy} (mm)	122	114	50	60	40
x_7	Field yoke height h_{ry} (mm)	118	108	26	38	40
x_8	Ratio of armature tooth width to slot pitch b_t/τ_s	0.65	0.65	0.58	0.65	0.61

[†] These variables are not from optimization but from the design parameters provided in [131]. The generator
active length and the ratio of tooth width to slot pitch are adapted to the electrical loading of 75 kA/m.

6.3. COMPARISON

T HE optimal values of the optimization variables are listed in Table 6.3. The benefit of using superconductors to reduce the generator size can be observed but is small for the same diameter. The SCSGs need thicker stator and rotor yokes to reduce the capital CoE while the PMSGs show a feature of smaller outer diameters. With the optimized geometry, the SCSGs use resulting field current densities in the MgB$_2$ wire of 175 A/mm^2 for both $D_s = 6$ m and 180 A/mm^2 for $D_s = 10$ m.

The optimal SCSG and PMSG-O have had their respective minimum capital CoEs and are compared in Fig. 6.3 with each other and with the PMSG-R design. The capital CoE of the PMSG-R design is calculated with the identical assumptions and conditions for the SCSG and PMSG-O designs. For the same generator diameter, the SCSGs have higher capital CoEs than the PMSGs. For the SCSGs and the PMSGs, respectively, the larger diameter reduces a bit the capital CoE.

The AEP, used to indicate the capacity factor (CF) of a wind turbine, is extracted from the capital CoE and compared in Fig. 6.4. All the generators have CFs over 0.5. For the diameter of 6 m, the SCSG and the PMSG-O have almost the same AEP. When the diameter increases to 10 m, both the PMSG-O and PMSG-R produce more energy than the SCSG.

The total generator material cost is compared in Fig. 6.5 which breaks down the total cost into the active material, structural material and cryostat costs. The PMSGs have almost the same generator cost for both the diameters. For the SCSG, the larger diameter slightly reduces the generator cost. Compared with the PMSGs, the SC-
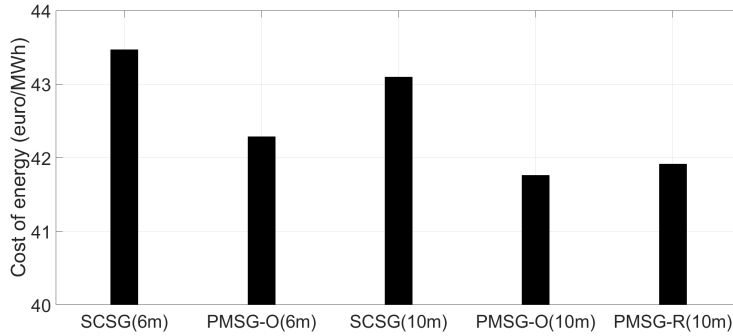
Figure 6.3: Capital CoE for SCSGs, PMSG-Os and PMSG-R.
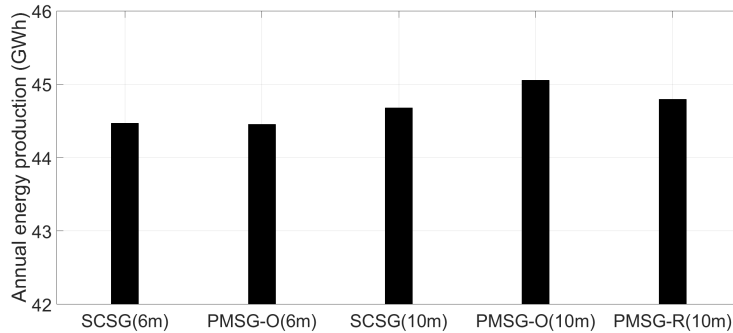
Figure 6.4: AEP for SCSGs, PMSG-Os and PMSG-R. The resulting capacity factors are 0.507, 0.507, 0.510, 0.514 and 0.511, respectively.

SGs have higher generator costs. The 10-m SCSG even has a higher generator cost than the 6-m PMSG. Further cost breakdown for the generator's active material cost shows the reason in Fig. 6.6. The SCSGs show their great advantage of reducing the active material cost as the required amount of permanent magnets for the PMSGs is rather costly. However, the cryostat used for the SCSGs significantly increases the total generator cost.

The generator's active material mass, resulting from the optimization merely for the capital CoE, is compared in Fig. 6.7. Due to the great amount of iron used to reduce the capital CoE, the SCSGs are rather heavy in this comparison, especially with the air gap diameter of 6 m. The SCSGs do not show effective mass reduction which should have benefited from using superconductors. Using lightweight core materials may help as discussed in Chapter 3. The PMSGs have small weights with
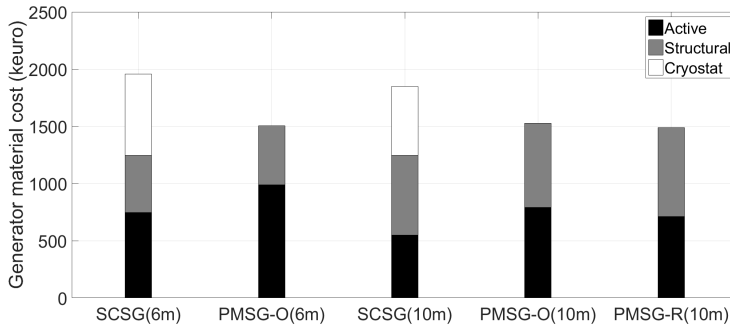
Figure 6.5: Generator material costs for SCSGs, PMSG-Os and PMSG-R.
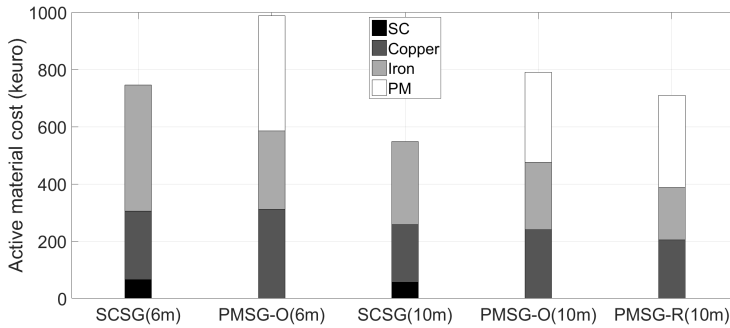
Figure 6.6: Active material costs for SCSGs, PMSG-Os and PMSG-R.

small pole pitches as expected.
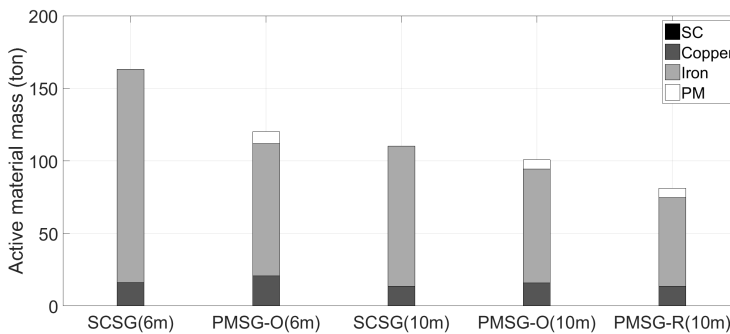
Figure 6.7: Active material masses for SCSGs, PMSG-Os and PMSG-R.

6.4. CONCLUSION

This chapter aimed to compare novel SCSGs and conventionally employed PMSGs for 10 MW direct-drive wind turbines. The method of modeling the costs and losses have been presented with certain assumptions and constraints. Regarding the capital CoE and the total generator cost, the SCSGs are still more expensive than their PMSG counterparts. If installation, operation and maintenance costs and reliability issues related to (cooling) superconductors are taken into consideration, the SCSGs will become even more expensive. Furthermore, the SCSGs do not have the advantages of low weight over the PMSGs when the capital CoE is considered as the primary design objective. In summary, the SCSGs seem not competitive yet at the moment. It is needed to look for significant advantages which will make SCSGs sufficiently attractive in the wind energy industry.

6

7

POTENTIAL OF PARTIALLY SUPERCONDUCTING GENERATORS

7.1. Introduction

This chapter aims at assessing the potential of partially superconducting (SC) generators for 10 MW direct-drive wind turbines. Partially SC generators can be designed based on the properties of currently available SC materials, like what have been done in Chapter 3 and Chapter 6. However, the designs proposed in the literature have been facing various challenges, such as large amounts of costly SC materials [20, 122], low efficiencies [20, 23, 120–122], large diameters [23, 120] or large active material weights (Chapter 6 of this thesis and [23]). These designs partly or entirely use iron cores, which tend to increase the generator weight [20, 23, 120, 121]. Large air gap diameters with more poles can be adopted to reduce the weight [23, 120]. However, this approach increases the generator and nacelle sizes and challenges the mechanical construction [27]. To reduce the diameter, higher electrical loadings may be used but the results are higher copper losses and lower efficiencies [23, 120]. As concluded in Chapter 6, the partially SC generators are not competitive yet if the cost or cost of energy is chosen as the primary design objective. Other design objectives are therefore needed to show the advantages of SC generators.

A partially SC generator has a much wider range of field excitation than permanent magnet and copper-field-winding generators. Moreover, the superconductor technology is developing rapidly. Thus, it does not make sense to base SC generator designs only on the properties of currently available superconductors. It is therefore interesting to evaluate the potential performance of an SC generator by disregarding the superconductor type, eliminating the limitation of critical characteristics and increasing the current density capability of the superconductors. We can then find out the required superconductor types that meet the magnetic field level and required current density for achieving certain high generator performance.

The objective of this chapter is to find the potential of partially SC generators. Such generators can only be attractive if they have significant advantages over permanent magnet synchronous generators (PMSGs). Typically, a PMSG has shear stresses in the order of 53 kPa and efficiencies of 96%. Therefore, it is investigated what excitation is required to obtain a doubled shear stress of 106 kPa and an efficiency of 98%. Other generator characteristics, such as normal stress, stack length and active material mass, are also investigated to show the effects of increasing the excitation. Commercial superconductors, i.e. low- and high-temperature superconductors and MgB_2 superconductors are evaluated to meet the magnetic field and field current density resulted from the required excitation.
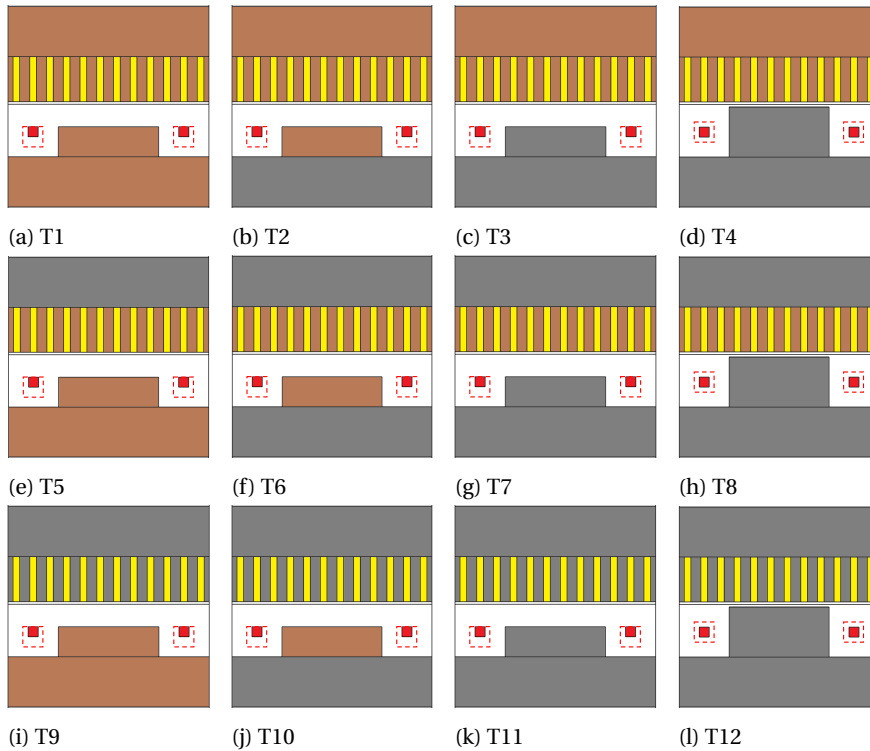
Figure 7.1: Twelve topologies to be compared. Red: SC field winding. Yellow: copper armature winding. Brown: non-magnetic core. Gray: iron core. The dashed boxes are the contours for a larger coil.

7.2. GENERATOR TO BE STUDIED

T HE partially SC generator for the study in this chapter is the same one as used in Chapter 3: a 10 MW direct-drive wind turbine with a rated speed of 9.6 rpm. The rated torque is therefore about 10 MN·m [11].

7.2.1. TWELVE TOPOLOGIES

The topologies to be studied in this chapter are the same as the twelve topologies studied in Chapter 3. The sketch of these topologies is repeated here in Fig. 7.1 with dashed red boxes indicating a larger coil area to be studied in this chapter.

7.2.2. DIMENSIONING

One pole of the SC generator is dimensioned as illustrated in Fig. 7.2. Then this single pole can be applied to different generator diameters. The size of the generator is then determined by the number of poles according to specific requirements.
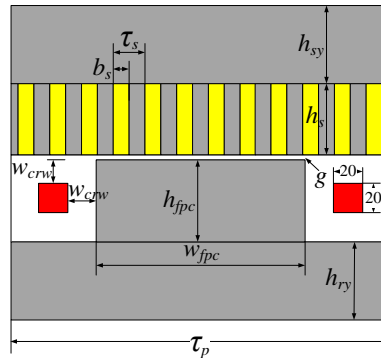
Figure 7.2: Sketch of dimensioning parameters of one pole.

The basic generator design and pole dimensioning are rough but generalized for all the topologies. The design parameters are set to achieve realistic designs although they may affect each topology a bit differently. Since the purpose of topology comparison is to show trends with the excitation currents and then no optimization is involved, the basic design which provides the same conditions is considered acceptable for performance comparison.

The pole pitch is set to $\tau_p = 0.4$ m and three reasons support this choice:

• According to the design proposals available in the literature, pole pitches between 0.379 m [20] and 0.660 m [23] are all possible.

• The comparison study in Chapter 3 for a low cost of energy has shown that the pole pitch lies between 0.4 m and 0.7 m for different topologies. The generator design resulting in the lowest cost has a small pole pitch about 0.4 m.

• The pole pitch should be larger than the minimum bending diameter of the superconductor which differs from type to type. It is thus not allowed to wind an SC field coil with a very small pole pitch.

The mechanical air gap length of the machine is $g = 10$ mm which is roughly around 0.1% of possible air gap diameters. In the rotor, the pole core width is assumed to be $w_{fpc} = 0.5\tau_p = 0.2$ m. The heights of the rotor back core and the stator yoke are thus equally set to $h_{ry} = h_{sy} = 0.5w_{fpc} = 0.1$ m. The pole core height is $h_{fpc} = 60$ mm for topologies T1-T3, T5-T7 and T9-T11, and $h_{fpc} = 100$ mm for topologies T4, T8 and T12 (the difference of 40 mm is due to the extension of the

pole core). The cryostat wall thickness with thermal insulations occupies $w_{crw} = 40$ mm, which makes the effective air gap length of T1-T3, T5-T7 and T9-T11 become $g_{eff}=g + w_{crw} = 50$ mm.

In the stator, the number of phases is $m = 3$. The number of slots per pole per phase is $q = 4$. The ratio of slot width to slot pitch is $b_s/\tau_s = 0.5$ (an equal fraction for a slot and a tooth). The slot height of $h_s = 84$ mm is determined for achieving an electrical loading of 75 kA/m for forced-air cooling [123], with the rated current density in the stator winding being $J_s = 3$ A/mm^2 (RMS value). The armature current density of $J_s = 3$ A/mm^2 is usually a starting point for designing a large electrical machine [144]. Many designs of SC generators for wind turbines in the literature have used this current density or slightly lower [20, 23, 120, 122]. However, the efficiency of these designs may not be high. A lower current density could be used to improve the efficiency. Therefore, this study will also investigate $J_s = 2$ A/mm^2 and compare it with $J_s = 3$ A/mm^2. Accordingly, the slot height is adjusted to $h_s = 126$ mm for $J_s = 2$ A/mm^2 to maintain the electrical loading of 75 kA/m.

The excitation or excitation current NI is calculated by the current density J_f multiplied by the cross-sectional area of the field coil A_f. In this paper, the cross-sectional dimension of one side of an SC field coil is fixed to 20 mm by 20 mm. As a result, the excitation is only determined by the current density applied in the SC field winding. However, only the excitation, which is equal to the area of $A_f = 400$ mm^2 multiplied by the current density J_f, takes effect for calculating the performance indicators and generator characteristics. Therefore, we do not need to know specifically either the current density or area until the feasibility of superconductors is evaluated, which will be presented in Section 7.6.

7.2.3. MODELING METHODS AND GENERATOR OPERATION

The performance indicators and generator characteristics are modeled and calculated regarding their relation with the excitation current for the twelve topologies. 2D finite element (FE) models have to be used to calculate the magnetic field because this study involves the linear low field region, the non-linear medium field region and the linear high field region of the B-H curve of iron (Fig. 3.7). Then these quantities are calculated with analytical equations.

For calculating all these quantities, the generator is operated in such a way that the armature magnetic field is perpendicular to the excitation field. In the d-q reference frame, this operation corresponds to the zero d-axis current control.

7.3. PERFORMANCE INDICATORS

The shear stress and efficiency (or total loss) are performance indicators for assessing a generator.

7.3.1. SHEAR STRESS

The shear stress σ_t is used for sizing an electrical machine by

$$T_e = \frac{\pi}{2}\sigma_t D_s^2 L_s,\tag{7.1}$$

where T_e is the electromagnetic torque, D_s is the air gap diameter, and L_s is the stack length. The shear stress needs to be calculated first of all. In 2D FE models, the shear force per unit length on one pole F_t is calculated with the Maxwell stress tensor by

$$F_t = \frac{1}{\mu_0}\int_{l_1=0}^{l_2=\tau_p} B_r B_t\, dl \tag{7.2}$$

where τ_p is the pole pitch, and B_r and B_t are the radial and tangential components of the air gap flux density.

The shear force F_t is an average value calculated from two stationary FE simulations. These two simulations differ in the relative position between the rotor and stator, and the phase angle of the armature current. From the first position to the second, the rotor rotates with an angle of $1/(4mq)$ of a mechanical cycle while the phase current shifts by a time of $1/(4m)$ of an electrical cycle. Choosing these two positions is under the assumption that the 6_{th} time harmonic of the magnetic field contributes to the force ripples most. Then, an electrical cycle has 6 cycles of force ripples. Compared with a complete transient simulation of the shear force, the error resulted from this averaging method is less than 3%. Since the aim of this study is just to find trends, this accuracy is acceptable. This method is the same as used in Section 3.5.4 in Chapter 3.

Then the shear stress σ_t is obtained by averaging F_t over the pole pitch τ_p:

$$\sigma_t = \frac{F_t}{\tau_p} \tag{7.3}$$

The effects of excitation currents on the shear stress of the twelve topologies are shown in Fig. 7.3. At low excitation, the shear stress increases fast when the excitation increases. Saturation starts to play a role with a higher excitation and the increase of shear stress becomes slow. Finally, the relative permeability of iron becomes $\mu_r \approx 1$ with a significantly high excitation, and the shear stress varies linearly.

The twelve topologies, in general, follow the trend: the shear stress becomes higher from T1 to T12. With a very high excitation, the shear stress of all the topologies finally becomes parallel with each other. This result implies that using iron cores can effectively increase the shear stress even though it is saturated.

7

(a) Full range   (b) Zoom in (low excitation)
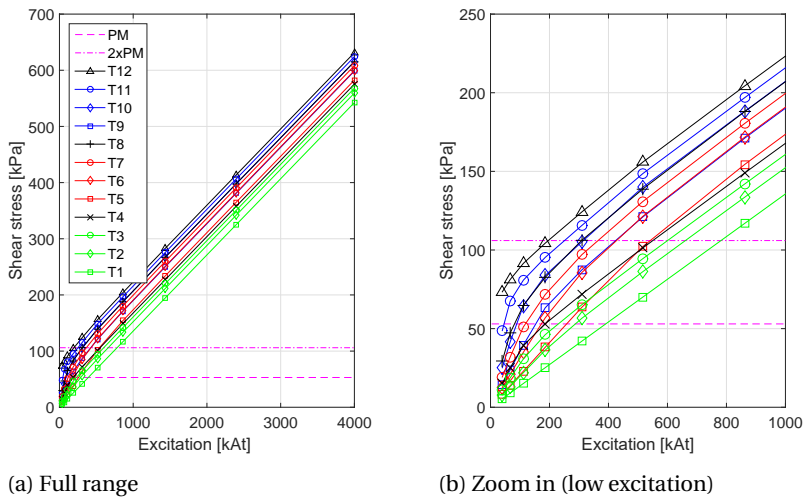
Figure 7.3: Shear stress with respect to excitation currents of the topologies T1-12. Dashed horizontal lines indicate the typical shear stress of a PMSG (lower) and twice the PMSG generator level (upper).

The typical shear stress of a PMSG generator is about 53 kPa which is also plotted in Fig. 7.3. This number is estimated by considering an air gap magnetic field of 1 T (amplitude) and an electrical loading of 75 kA/m (RMS). If we want to achieve a doubled shear stress, i.e. 106 kPa, as indicated in Fig. 7.3, the excitation must be sufficiently high. However, the difficulty in reaching 106 kPa is quite different for the twelve topologies. The topologies with more iron show higher shear stresses than the others. The topology T12 achieves 106 kPa much more easily than T1. For 106 kPa, T12 requires the excitation of 200 kAt while T1 requires 800 kAt. The other topologies lie in between.

7.3.2. EFFICIENCY AT RATED LOAD (SIMPLIFIED LOSS MODEL)

An efficiency is actually dependent on the torque, speed and machine size. However, calculation of efficiency can be simplified if armature copper Joule losses are dominant and other losses, such as iron losses and copper eddy current losses, are neglected. Such simplification can facilitate basic observation of how efficiency is related to the key variables.

The total loss primarily comes from the copper loss in the armature winding and the core loss in the iron, if the cooling power consumption is not taken into account. The copper loss consists of Joule losses and eddy current losses. For the purpose of making an efficiency independent of the power rating, the iron loss can

be assumed to be negligible due to the low frequency of the direct-drive generator. The copper eddy current loss can also be assumed to be negligible by assuming very fine stranding of copper filaments. Therefore, only the Joule loss is left in efficiency calculation. Then the efficiency η can be calculated by:

$$\eta = 1 - \frac{C \cdot J_s^2 (1 + \frac{L_{ew}}{L_s})}{\sigma_t v} \qquad (7.4)$$

where L_{ew} is the length of one end of an armature winding turn, L_s is the stack length, J_s is the RMS current density in the armature winding, σ_t is the shear stress calculated from Eq. (7.3), and v is the relative linear speed between the generator rotor and stator. The constant C is defined as

$$C = \rho_{Cu} h_s k_{fil} (\frac{b_s}{\tau_s}) \qquad (7.5)$$

where ρ_{Cu} is the resistivity of copper, k_{fil} is the fill factor of the armature slots, and h_s, b_s and τ_s have been defined in Section 7.2.2. From Eq. (7.4), it is clear that the efficiency can be increased by reducing the armature current density J_s or the ratio of end winding length to stack length L_{ew}/L_s, or by increasing the linear speed v.

The efficiencies at rated load with an armature current density of $J_s = 3$ A/mm^2 are plotted in Fig. 7.4, assuming the end winding length is much smaller than the stack length whereby the term L_{ew}/L_s is neglected in Eq. (7.4). The topologies T1 and T12 are shown as two extreme cases (fully non-magnetic compared with fully iron-cored with salient poles). In Fig. 7.4, T12 is much more efficient than T1 in the excitation region lower than e.g. 1000 kAt. With a higher excitation, the differences become small. This result matches the comparison of shear stress σ_t in Fig. 7.3 since T12 has much higher shear stresses than T1. This result also implies that using more iron cores can effectively increase the generator efficiency, especially when the excitation is limited.

7.3.3. LOSSES AT RATED LOAD (DETAILED LOSS MODEL)

For calculating all the losses, we use the rated torque of $T_e = 10$ MN·m and the rated angular speed of $n_N = 9.6$ rpm. Three air gap diameters $D_s = 6.11$ m, 10.19 m and 14.26 m are compared which cover the range of commonly applied diameters proposed in the literature. These diameters contain 48, 80 and 112 poles, respectively, as a result of the fixed pole pitch of $\tau_p = 0.4$ m defined in Section 7.2.2.

Three types of losses are usually considered and calculated in an electrical machine:

- Copper Joule loss (I^{2}R loss)
- Copper eddy current loss
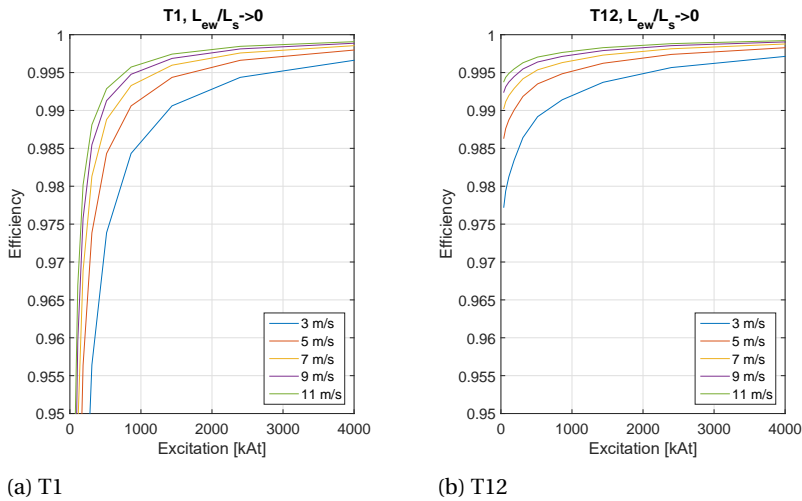
Figure 7.4: Efficiency of topologies T1 and T12 with $J_s = 3$ A/mm^2, when only armature copper Joule losses are considered and $L_{ew}/L_s \to 0$ is assumed in Eq. (7.4).

• Iron loss

In Section 7.3.2, the first loss has been calculated and the latter two losses were neglected, because the power rating and the generator size were both assumed unknown. In this section, we have set a rated power and three air gap diameters so we can then calculate all these three losses.

A few assumptions are made for calculating these losses:

• Iron will saturate when the excitation becomes high. Under heavy saturation, the hysteresis loop can be illustrated in Fig. 7.5. We may increase the excitation to such a high level that iron is fully saturated. Thus, the most important assumption for iron losses is that the relative permeability of iron becomes $\mu_r = 1$ after the magnetic flux density is over a particular value. Here we assume this value to be $B_{hys} = 2.5$ T. This assumption also implies that the area of the hysteresis loop reaches its maximum at $B_{hys} = 2.5$ T at point U (also point X). With a higher magnetic field, the area of the hysteresis loop will not expand anymore.

• The copper eddy current loss is calculated only in the stack length without the end winding. This allows for 2D analyses with an acceptable accuracy. For calculating the copper Joule loss, the end winding is included.

• The rotor iron is assumed to be loss free, so iron losses only occur in the stator iron cores.

• In the calculation of losses due to an alternating magnetic field, only the fun-
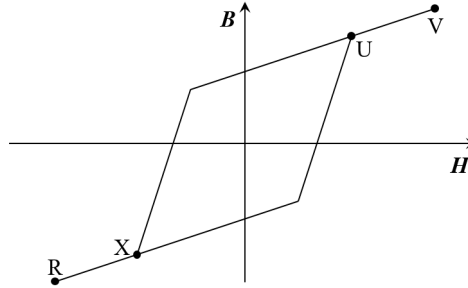
Figure 7.5: Hysteresis loop of iron with heavy saturation. The area of hysteresis loop become maximum and constant when the magnetic field is above B_{hys} at the point of U (also X). The relative permeability becomes $\mu_r = 1$ from U to V and from X to R.

damental components of the field are used.

COPPER LOSSES

The copper Joule loss $P_{Cu,joul}$ can easily be calculated. However, the calculation for the copper eddy current loss is a bit complicated since it is a function of the magnetic flux density and the fineness of stranding or transposing. Here only stranding is employed and modeled while the transposing is not. The copper eddy current loss can be expressed by [126]

$$P_{Cu,eddy} = \frac{1}{24\rho_{Cu}}\omega^2(a^2\hat{B}_r^{\,2} + b^2\hat{B}_t^{\,2})V_{Cu,s} \tag{7.6}$$

where ω is the angular electrical frequency, $\hat{B}_r$ and $\hat{B}_t$ are the radial and tangential components of the flux density (amplitude) in the copper conductor respectively, $V_{Cu,s}$ is the copper volume only in the stack length, and a and b are the height and width of a copper strand. We assume very fine strands for the copper conductors with $a = b = 1$ mm.

IRON LOSSES

The eddy current loss per unit iron mass is basically calculated by [127]

$$P_{Fe,eddy} = 2k_e(\frac{f}{50\text{ Hz}})^2[(\frac{\hat{B}_r}{1.5\text{ T}})^2 + (\frac{\hat{B}_t}{1.5\text{ T}})^2] \tag{7.7}$$

where $k_e = 0.5$ W/kg is the eddy current loss per unit iron mass with the field of 1.5 T and the frequency of 50 Hz, B_r and B_t are the radial and tangential components of the flux density (amplitude) in the iron core respectively. Equation (7.7) applies to both the stator iron teeth and the stator iron yoke.

The hysteresis loss per unit iron mass is calculated by

$$P_{Fe,hys} = 2k_h(\frac{f}{50 \text{ Hz}})(\frac{B_{norm}}{1.5 \text{ T}})^2 \tag{7.8}$$

where $k_h = 2.0$ W/kg is the hysteresis loss per unit iron mass with the field of 1.5 T and the frequency of 50 Hz, B_{norm} is the norm of the flux density (peak value) in the iron core. Equation (7.8) applies to both the stator iron teeth and the stator iron yoke.

The factor of 2 is included in Eqs. (7.7) and (7.8) because the flux density distribution contains harmonics, which increases the iron losses. In addition, manufacturing of steel laminates into a core increases the iron losses [127]. This factor is approximated to range from 1.6 to 2.0 according to [123].

The hysteresis loss per unit volume is the area of the hysteresis loop multiplied by the frequency. When the applied magnetic field exceeds the upper field of the maximum hysteresis loop (e.g. B_{hys}), the hysteresis loss per unit volume per electrical cycle will become constant as the area of the maximum hysteresis loop. This maximum loop implies that the hysteresis loss has an upper limit even if a higher magnetic field can be imposed on the iron.

This upper limit also leads to the fact that it is not convenient anymore to separate the field into two orthogonal components because it is hard to define the upper limit in either of the orthogonal components. By using the norm of the flux density, the upper limit can be assumed to be $B_{hys} = 2.5$ T, above which the hysteresis loss remains maximum and constant.

The total iron loss in the stator P_{Fes} is therefore given by

$$P_{Fes} = P_{Fe,eddy} + P_{Fe,hys} \tag{7.9}$$

TOTAL LOSS

The total loss P_{loss} is obtained by adding up the three losses:

$$P_{loss} = P_{Cu,joul} + P_{Cu,eddy} + P_{Fes} \tag{7.10}$$

The effects of excitation on the total loss are shown in Fig. 7.6 for two armature current densities and three air gap diameters. The dashed lines of 3% and 2% of the rated power of 10 MW are also plotted to indicate two reference loss levels for an SC generator. A loss of 2% plus a cryogenic cooling power of roughly 0.5% results in a higher efficiency (97.5%) compared to a PMSG (96%) [145].

Compared to the study on the efficiency in Section 7.3.2, the total loss here consists of not only copper Joule losses but also iron losses and copper eddy current losses. The latter two losses are functions of the frequency or the number of poles

and the amplitude of magnetic fields according to Eqs. (7.6)-(7.8). As a result, a larger air gap diameter, i.e. a larger linear speed v, does not definitely mean a lower total loss anymore. For the case of $D_s = 14.26$ m as shown in Fig. 7.6, the total loss turns reversely to go higher when the excitation reaches a very high level, e.g. 1000 kAt with $J_s = 2$ A/mm^2. This is mainly a result of a higher copper eddy current loss together with a higher iron loss due to such a high excitation and frequency. For the same diameter of $D_s = 14.26$ m, the total loss cannot even reach the 2%-loss level with $J_s = 3$ A/mm^2 no matter how far the excitation increases. Reducing the armature current density to $J_s = 2$ A/mm^2 makes it possible to achieve 2% but only in a small range of excitation. This result implies that reducing the armature current density apparently reduces the total loss while increasing the air gap diameter may not.

(a) 3 A/mm^2, 6.11 m   (b) 3 A/mm^2, 10.19 m   (c) 3 A/mm^2, 14.26 m

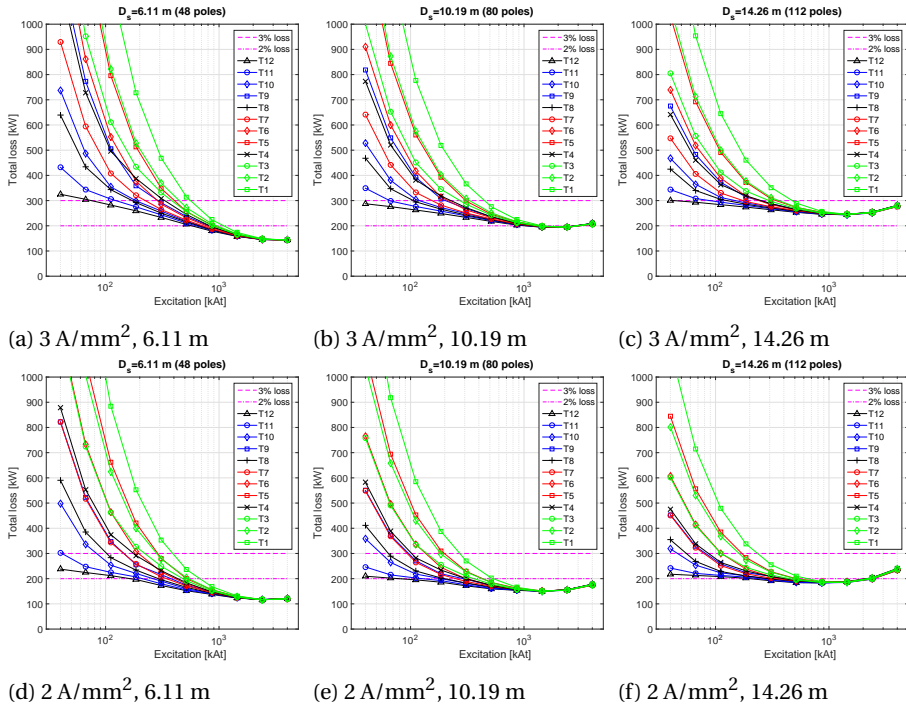(d) 2 A/mm^2, 6.11 m   (e) 2 A/mm^2, 10.19 m   (f) 2 A/mm^2, 14.26 m

Figure 7.6: Total loss of topologies T1-T12 with respect to excitation currents for diameters of 6.11 m, 10.19 m and 14.26 m as well as current density of $J_s = 3$ A/mm^2 and $J_s = 2$ A/mm^2. The horizontal dashed lines indicate loss levels of 2% and 3%, respectively.

The topologies with more iron cores, e.g. T9-T12, reach the 2%-loss level more

easily than the topologies with more non-magnetic cores, e.g. T1-T4. The other topologies lie in between. At low excitation, e.g. below 200 kAt, the total loss of the topologies is considerably different. The topologies of T11 and T12, are much more efficient than the other topologies. However, the difference becomes much smaller when the excitation increases significantly, since heavy saturation makes the magnetic circuit similar for all the topologies and produces more iron losses in the topologies with iron stator cores.

7.4. Generator Characteristics

The generator characteristics, such as normal stress, stack length and active material mass, are calculated to show the trend of increasing the excitation current. For calculating the normal stress, it is not needed to know the rated torque, rated speed and air gap diameter. For calculating the other generator characteristics, we use the rated torque of $T_e = 10$ MN·m and the rated angular speed of $n_N = 9.6$ rpm. Three air gap diameters $D_s = 6.11$ m, 10.19 m and 14.26 m are compared.

7.4.1. Normal stress

The normal stress σ_r indicates the attractive force between the rotor and stator and influences the structural mass which contributes to the total generator mass. Here we only estimate the normal stress at no load, because the armature load current contributes much less to the normal stress than the field current in a partially SC generator. For example, the fraction is only about 1% for the topology T12. This no load means that no force is produced by armature currents and the normal force is only produced between field currents and stator iron cores.

Firstly we calculate the resultant normal force on one pole F_r with the Maxwell stress tensor by

$$F_r = \frac{1}{2\mu_0} \int_{l_1=0}^{l_2=\tau_p} (B_r^2 - B_t^2)dl \tag{7.11}$$

Although not uniformly distributed over one pole, the normal stress σ_r can be calculated by averaging F_r over one pole:

$$\sigma_r = \frac{F_r}{\tau_p} \tag{7.12}$$

The average normal stress between the rotor and stator is plotted in Fig. 7.7 with respect to the excitation current, assuming an unchanged air gap length. As an example, the normal stress of a PMSG (200 kPa) is also indicated in both of the subfigures for comparison [27]. The topologies with iron stator teeth (T9-T12) have

higher normal stresses than the topologies with non-magnetic stator teeth (T5-T8). In the topologies with an ironless stator (T1-T4), the normal stress is $\sigma_r = 0$.

(a) Full range   (b) Low AT range
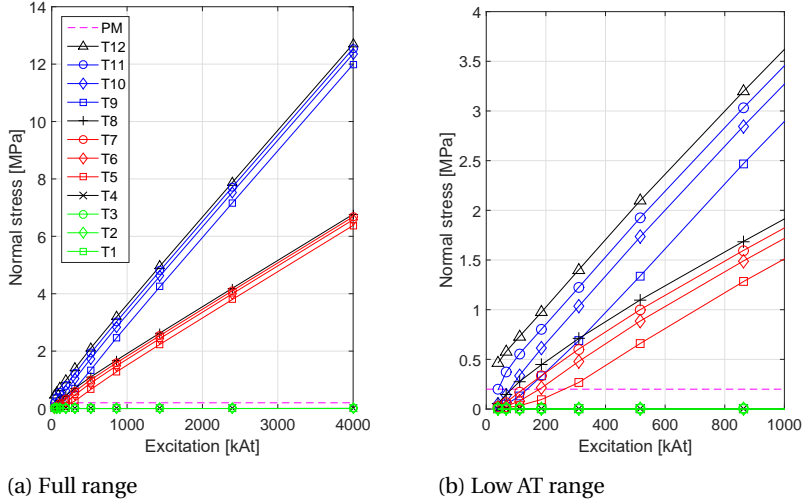
Figure 7.7: Average normal stress (attractive force density) per pole between the rotor and stator with respect to excitation currents. The horizontal dashes line indicates the typical level of a PMSG.

With a higher excitation, the normal stress becomes much greater in the topologies with iron stator teeth (T9-T12) or iron stator yoke (T5-T8). These normal stresses are much higher than those of a PMSG machine. As a result, the mechanical structure must be designed to support the rotor and stator under such high normal stresses. High normal stresses will thus be a significant challenge if a higher excitation has to be used for a high shear stress and a low total loss.

7.4.2. STACK LENGTH

The stack length L_s is calculated from the sizing equation Eq. (7.1):

$$L_s = \frac{2}{\pi} \frac{T_e}{\sigma_t D_s^2} \tag{7.13}$$

if we set the torque to $T_e = 10$ MN·m for a 10 MW direct-drive wind turbine. The results of stack length obtained with $J_s = 3$ A/mm^2 are shown in Fig. 7.8. In general, the stack length decreases when the excitation increases. The stack length of the topologies with more non-magnetic cores decreases very fast, whereas that of the topologies with more iron cores decreases slowly. However, the fact is that the

topologies with more iron cores already have much smaller stack lengths at low excitation.

(a) 6.11 m   (b) 10.19 m   (c) 14.26 m
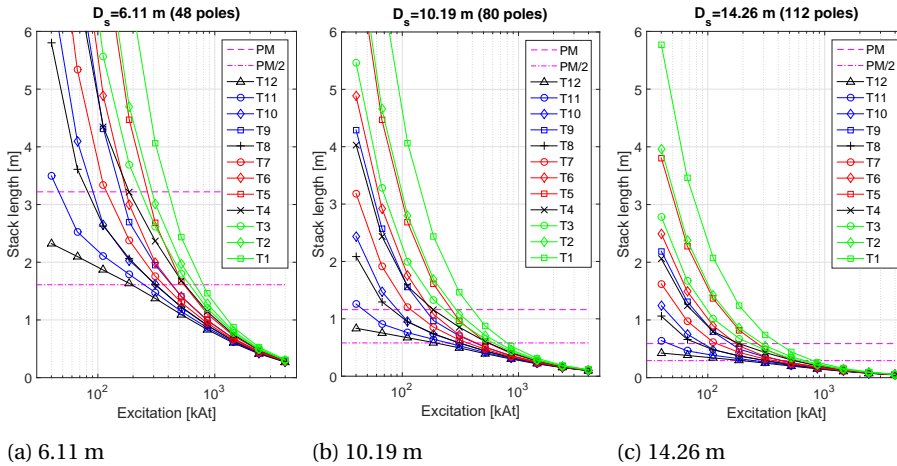
Figure 7.8: Stack length with respect to excitation currents for diameters of 6.11 m, 10.19 m and 14.26 m. Dashed horizontal lines indicate the typical stack length of a PMSG (upper) and half the PMSG level (lower).

The reference stack length of a 10 MN·m PMSG is also indicated by the dashed lines in this figure. This stack length is obtained by assuming a shear stress of 53 kPa. A half of this stack length is also shown for the shear stress of 106 kPa. This stack length will be achieved when the excitation is as high as 200 kAt for T12 and 800 kAt for T1 for both the diameters. The other topologies lie in between. The topologies with more iron require lower excitation currents.

If the excitation increases to about 4000 kAt, the difference of stack length for the topologies becomes minuscule. This vanishing difference is because the completely saturated iron behaves like a non-magnetic material, and then all the topologies have the same magnetic reluctance.

7.4.3. ACTIVE MATERIAL MASS

The active material mass consists of the core mass and the copper mass, neglecting the insignificant mass of the SC field winding. The iron mass density is 7650 kg/m^3 and the non-magnetic core material (i.e. glass fiber G10) has a mass density of 1850 kg/m^3. The copper mass density is 8900 kg/m^3.

The active material mass is not fully but nearly proportional to the stack length. It thus follows a trend similar to the stack length, as shown in Fig. 7.9. A larger

diameter reduces the active material mass, but it does not change the ranking of the compared twelve topologies. Also, with a high excitation, e.g. above 300 kAt, the difference between the active material mass of all the topologies becomes small.

With the same excitation in the region of low excitation (e.g. lower than 100 kAt), using iron cores can provide a lower active material mass. Using lightweight non-magnetic core materials, e.g. composites, is thus not the only choice to reduce the active material mass. For a higher excitation over 100 kAt, however, using either iron cores or non-magnetic cores with the same excitation does not make big differences.

(a) 6.11 m   (b) 10.19 m   (c) 14.26 m
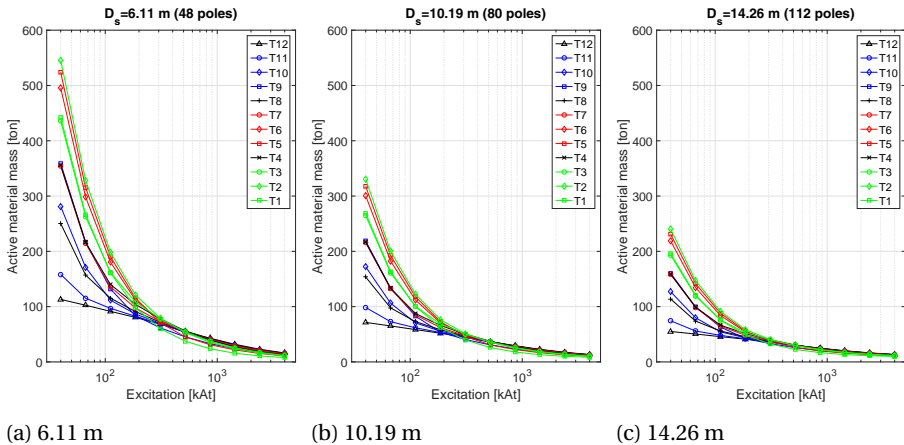
Figure 7.9: Active material mass with respect to excitation currents for diameters of 6.11 m, 10.19 m and 14.26 m, with $J_s = 3 \text{ A/mm}^2$.

7.5. DISCUSSION ON DESIGN EXAMPLES IN LITERATURE

IN the literature, a few designs have been proposed for partially SC generators for 10 MW direct-drive wind turbines. Four available design examples which provide sufficient design details are summarized in Table 7.1. They use different excitation currents (Exci.), superconductor types (SC type), cryogenic temperatures (Temp.), armature current densities (J_s), shear stresses (σ_t) and air gap diameters (D_s), resulting in the different stack length (L_s), active material mass (M_{act}) and rated-load efficiency (only considering copper and iron losses in the generator). Each of these designs originates from one of the twelve topologies listed in Fig. 7.1 and their corresponding topologies are also indicated in Table 7.1. The fifth design is from this thesis. This design is the optimized topology T12 from Chapter 3, the IT design in Chapter 4, the Design D in Chapter 5 and the 6-m SCSG design in Chapter 6 (they

are the same design). This design is referred to Liu's design in this section.

• GE design employing NbTi at 4 K has already obtained a competitively small size (4.34 m diameter) and active material mass with a very high excitation of 928 kAt. The resulting shear stress is as high as 179 kPa. Its efficiency is only 96% and can not comply with the efficiency demand of 98%. It is also observed that no further efficiency increase can be obtained by increasing the excitation. However, the efficiency could be improved by, for example, enlarging the air gap diameter or reducing the armature current density.

• Abrahamsen's and Liu's designs both have small diameters of 6 m but the generators are both long due to relatively low shear stresses of 75 kPa. Abrahamsen's design is lightweight because of its non-magnetic cores, but it employs the topology T5 which results in a bulky and costly SC field winding [122]. On the contrary, Liu's design using the topology T12 has heavy active materials due to a large amount of iron, but it uses much less superconductors and then could have a lower active material cost. This large active material mass needs to be reduced by increasing the excitation.

• Tecnalia's and Xu's designs have higher shear stresses compared to Abrahamsen's and Liu's designs. Tecnalia's design based on the topology T8 also uses a large air gap diameter (10.10 m) as well as a high electrical loading (120 kA/m) to achieve its axial length (0.74 m) and active material mass (118 tons). Xu's design also based on the topology T12 uses an even larger air gap diameter (13.40 m) as well as a high electrical loading (120 kA/m) to achieve a lightweight generator design (49 tons). However, these two designs both have efficiencies below 97% and their high electrical loadings increase the complexity of cooling the armature winding.

None of the five designs in Table 7.1 provide an efficiency of over 98% (or the 2%-loss level) without considering the cryogenic cooling power. Reducing the armature current density or increasing the air gap diameter together with a much higher excitation current can be considered to address this challenge.

7.6. FEASIBILITY OF COMMERCIAL SUPERCONDUCTORS

Not all SC wires can achieve the high excitation for a shear stress of 106 kPa and a 2%-loss level, because the current density is limited by the critical engineering current density J_e as shown in Fig. 7.10 for different SC wires. When evaluating the superconductors, we need to know the magnetic flux density B which the superconductors are exposed to. The magnetic flux density is produced by the excitation of SC field windings.

The four topologies (T5, T8, T9 and T12) of the five design examples shown in Table 7.1 will be used to evaluate the feasibility of superconductors.

Table 7.1: Design examples of partially SC generators for 10 MW direct-drive wind turbines.

Design	Topology	SC type	Temp. (K)	Exci. (kAt)	J_s (A/mm^2)	σ_t (kPa)	τ_p (m)	D_s (m)	L_s (m)	M_{act} (ton)	Efficiency	Reference
Abrahamsen	T5	MgB$_2$	20	470	3.0	75	0.536	5.46	3.10	52	[†]96.7%	[122]
Tecnalia	T8	MgB$_2$	20	230	3.0	112	0.660	10.10	0.74	118	[††]96.2%	[23]
GE	T9	NbTi	4	928	[†††]2.5	179	0.379	4.34	1.88	[††]70	95.7%	[20]
Xu	T12	HTS	50	31	3.0	[††††]109	0.438	13.40	0.31	49	96.8%	[120]
Liu	T12	MgB$_2$	20	25	3.0	74	0.471	6.00	2.56	149	96.9%	This thesis

[†]   Estimated with the copper Joule loss of 2.3% given in [122], considering an additional copper eddy current loss of roughly 1%.
[††] Estimated with the parameters provided in [20].
[†††] Estimated with the overall efficiency of 95.2% provided in [23], plus assumed 1% for cryogenic cooling and auxiliary components.
[††††] Estimated with the generator size and torque provided in [120].

7
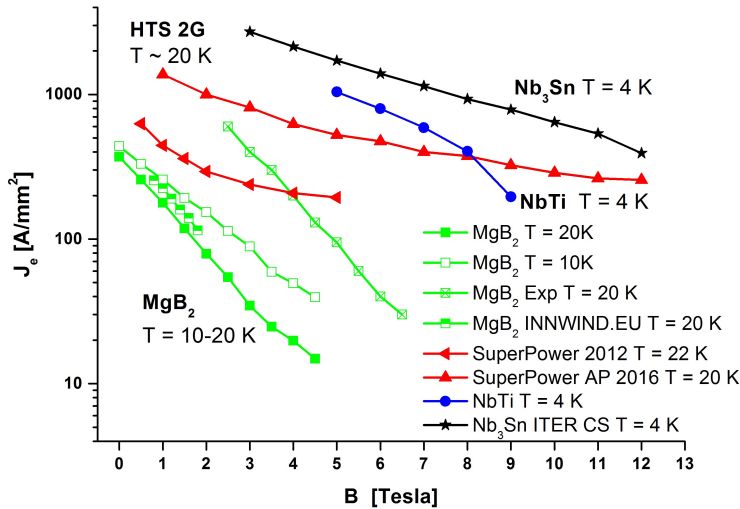
Figure 7.10: Critical engineering current density J_e of commercial superconducting wires. References: NbTi from [20], Nb$_3$Sn from [146], MgB$_2$ from [147], HTS 2G SuperPower 2012 from [148] and HTS 2G SuperPower 2016 from [149]. The base MgB$_2$ is the production wire in 2013. MgB$_2$ Exp is an experimental wire reported in 2013. MgB$_2$ INNWIND.EU is from the deliverable report for the INNWIND.EU project.

7.6.1. REQUIRED EXCITATION

By comparing Fig. 7.3 and Fig. 7.6, it is seen, that it is harder to reach the 2%-loss level than reaching the shear stress of 106 kPa for $J_s = 3$ A/mm^2. If the armature current density is reduced to $J_s = 2$ A/mm^2, the 2%-loss level will be fulfilled before the shear stress demand of 106 kPa is reached. Therefore, the criteria for selecting the required excitations are to achieve the 2%-loss level for $J_s = 3$ A/mm^2 and to achieve the shear stress of 106 kPa for $J_s = 2$ A/mm^2.

Table 7.2 shows the excitations required by the four topologies. Three air gap diameters (6.11 m, 10.19 m and 14.26 m) and two armature current densities (3 A/mm^2 and 2 A/mm^2) are investigated. The other parameters of the generator design are identical to those used in the studies of Sections 7.3 and 7.4 and have been described in Section 7.2.2. For $J_s = 3$ A/mm^2, the required excitations are obtained when the total loss equals 2%. As a result, the shear stresses with these excitations are much higher than 106 kPa. For $J_s = 2$ A/mm^2, the required excitations are obtained when the shear stress equals 106 kPa. As a result, the total losses with these excitations are a bit lower than 2%.

As shown in Fig. 7.6c, none of the four topologies can achieve the 2%-loss level for the air gap diameter of $D_s = 14.26$ m with $J_s = 3$ A/mm^2. For $J_s = 3$ A/mm^2 and

D_s = 6.11 m, T12 requires as high as 580 kAt and the other topologies require even higher. Reducing J_s = 3 A/mm^2 to J_s = 2 A/mm^2 makes the required excitations much lower as shown in Table 7.2. Then, the topology T12 requires only 200 kAt for the three diameters. With J_s = 2 A/mm^2, the three diameters of 6.11 m, 10.19 m and 14.26 m have the same required excitation for the same topology. The diameters make no difference of the require excitation so it is not needed to select a specific diameter for this evaluation of superconductors.

Also note that the required excitations listed in Table 7.2 are obtained from the design dimensioned in Section 7.2.2 for a pole pitch of τ_p = 0.4 m. This design was not optimized. Thus, the numbers of required excitations listed in Table 7.2 may not apply to other designs but are used as reference numbers.

Table 7.2: Required excitation (kAt) for different topologies to achieve the shear stress of 106 kPa and the 2%-loss level

J_s	†3 A/mm^2			††2 A/mm^2		
D_s (m)	6.11	10.19	14.26	6.11	10.19	14.26
T5	910	1370	n/a	550	550	550
T8	680	1250	n/a	310	310	310
T9	820	1280	n/a	450	450	450
T12	580	1050	n/a	200	200	210

†The loss level is just equal to 2% while σ_t is higher than 106 kPa.

$^{\dagger\dagger}\sigma_t$ is just equal to 106 kPa while the loss level is lower than 2%.

7

7.6.2. RESULTING MAGNETIC FIELDS

The maximum magnetic flux density in the SC coil winding produced by the required excitation is calculated in 2D FE models. These fields depend on the cross-sectional area of the field coil. Thus, we set two realistic areas for this evaluation: 20×20 mm^2 and 40×40 mm^2. The contour of the larger field coil is sketched by the dashed boxes in Fig. 7.1. Figure 7.11 shows the maximum flux density perpendicular to the SC wires B_{mp} and the maximum norm flux density in the SC wires $|B_m|$ as a function of excitation currents (with no armature current). The perpendicular field B_{mp} is used for evaluating the SC wires which are tapes, such as HTS and MgB$_2$. The norm field $|B_m|$ is used for evaluating the round SC wires such as NbTi and Nb$_3$Sn. By looking up the required excitations in Table 7.2 and the field-excitation relations in Fig. 7.11, the values of B_{mp} and $|B_m|$ for the four topologies are identified and given in Table 7.3 and Table 7.4. These two tables show sixteen cases (C1a, C1b ...C8a, C8b) of combining the maximum field and current density in the SC field coil.

(a) Perpendicular component

(b) parallel component
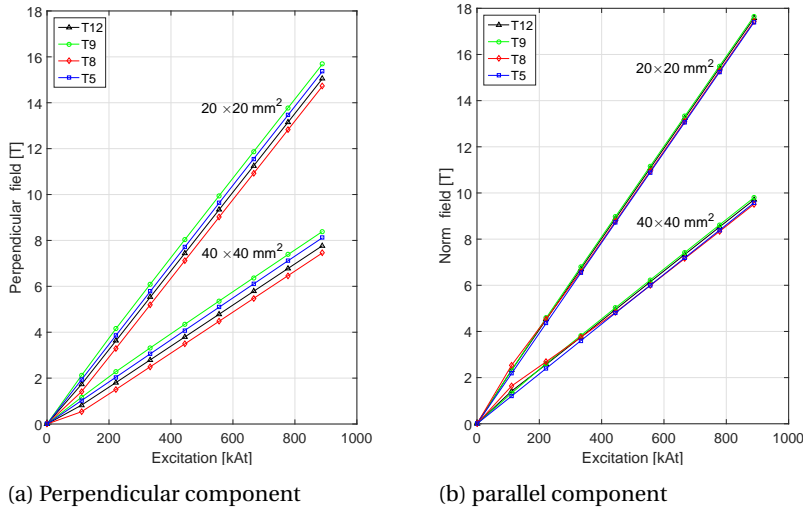
Figure 7.11: Maximum magnetic field at the surface of the SC field winding with respect to excitation currents for selected topologies.

The combination of $J_s = 3$ A/mm^2 and $D_s = 6.11$ m is a starting point. However, the maximum fields seem too high compared to Fig. 7.10 in most of the cases as indicated in Table 7.3. Thus, we could use $J_s = 2$ A/mm^2 instead to effectively lower the maximum fields as shown in Table 7.4. From this point of view, $J_s = 3$ A/mm^2 may not be a good option. The armature current densities of the design examples in Table 7.1 could be reduced for higher generator performance. In addition, a larger cross-sectional area of the field coil produces a lower maximum field in the field coil, as indicated in Fig. 7.11, Table 7.3 and Table 7.4.

7.6.3. REQUIRED FIELD CURRENT DENSITIES

The required current density in the SC field winding J_f is calculated by dividing the required excitation in Table 7.2 by the cross-sectional area of the field coil. The values of J_f are shown in Table 7.3 and Table 7.4 for the two cross-sectional areas of the field coil and for $J_s = 3$ A/mm^2 and $J_s = 2$ A/mm^2, respectively. The cross-sectional area of the SC field coil plays an important role in determining the current density. A larger area results in a lower current density and thus a looser requirement to the superconductor. However, a larger area means a higher cost of the SC field winding.

Table 7.3: Required surface magnetic flux density and current density for different topologies to achieve the 2%-loss level and a shear stress of over 106 kPa ($J_s = 3$ A/mm^2, $D_s = 6.11$ m)

		20×20 mm^2		
Topology	Case	B_{mp} (T)	$|B_m|$ (T)	J_f (A/mm^2)
T5	C1a	15.7	17.8	2275
T8	C2a	11.1	13.3	1700
T9	C3a	14.5	16.3	2050
T12	C4a	9.8	11.6	1450
		40×40 mm^2		
Topology	Case	B_{mp} (T)	$|B_m|$ (T)	J_f (A/mm^2)
T5	C5a	8.3	9.8	569
T8	C6a	5.6	7.3	425
T9	C7a	7.8	9.1	513
T12	C8a	5.0	6.4	363

Table 7.4: Required surface magnetic flux density and current density for different topologies to achieve the shear stress of 106 kPa and a loss level lower than 2% ($J_s = 2$ A/mm^2)

		20×20 mm^2		
Topology	Case	B_{mp} (T)	$|B_m|$ (T)	J_f (A/mm^2)
T5	C1b	9.5	10.8	1375
T8	C2b	4.8	6.2	775
T9	C3b	8.1	9.1	1125
T12	C4b	3.2	4.1	500
		40×40 mm^2		
Topology	Case	B_{mp} (T)	$|B_m|$ (T)	J_f (A/mm^2)
T5	C5b	5.0	5.9	344
T8	C6b	2.3	3.5	194
T9	C7b	4.4	5.1	281
T12	C8b	1.6	2.3	125

7

7.6.4. FEASIBLE SUPERCONDUCTORS

To evaluate the feasibility of superconductors, we compare the sixteen cases with the critical engineering current density J_e of the superconductors in Fig. 7.10. Note that B_{mp} is used for HTS and MgB$_2$ while $|B_m|$ is used for LTS. The feasibility of these superconductors for the sixteen cases and the four topologies is summarized in Table 7.5.

Table 7.5: Feasibility of Different Superconducting Wires

Superconductor	Feasible case	Feasible topology
MgB$_2$ 20 K	None	None
MgB$_2$ INNW. 20 K	None	None
MgB$_2$ 10 K	C8b	T12
MgB$_2$ Exp 20 K	C6b, C8b	T8, T12
2G HTS-2012 22 K	C6b, C8b	T8, T12
2G HTS-2016 20 K	C8a, C4b, C5b	T5, T8,
	C6b, C7b, C8b	T9, T12
NbTi 4 K	C8a, C4b, C5b	T5, T8,
	C6b, C7b, C8b	T9, T12
Nb$_3$Sn 4 K	C6a, C7a, C8a,	T5, T8
	C2b, C4b, C5b,	T9, T12
	C6b, C7b, C8b	

Compared with the other SC materials, the LTS, i.e. NbTi and Nb$_3$Sn, are more feasible to achieve the shear stress of 106 kPa and the 2%-loss level for a partially SC generator. All the four topologies can employ the LTS. However, LTS operates at 4.2 K and thus requires rigorous cooling. The HTS-2012 (SuperPower) is feasible for fewer cases than the LTS but the newly developed HTS-2016 (SuperPower) is comparable to the NbTi. However, they have to be cooled down to 20 K, although they have critical temperatures of T_C = 93 K. The MgB$_2$ reported in [147] is not yet feasible for any of the four topologies at 20 K but feasible for T12 at 10 K with the larger field coil of 40 × 40 mm^2. A much lower temperature, such as 4 K, could be an option but this will drastically reduce the advantage of MgB$_2$ intended for 10-20 K. The MgB$_2$ used in the INNWIND.EU project seems infeasible at 20 K either if a realistic safety margin of current density, e.g. 20%, is considered. The new lab-tested MgB$_2$ shows its potential at 20 K to be feasible for T8 and T12 with the field coil of 40 × 40 mm^2. However, this lab-tested MgB$_2$ is not commercially available yet.

7.7. CONCLUSION

THe attractive performance of a shear stress of 106 kPa and a 2%-loss level can be achieved in all the twelve topologies by significantly increasing the excitation. The topologies with more iron, especially the fully iron-cored topology with salient poles, reach this performance more easily than the other topologies. Four of the twelve topologies are particularly investigated and they require excitations ranging from 200 kAt to 550 kAt with the armature current density of 2 A/mm^2. A higher ar-

mature current density, e.g. $3\,A/mm^2$, may not be a good option since it significantly increases the required excitations and challenges the superconductors.

The four topologies with such high excitations have different maximum magnetic fields in the superconducting field coil and the superconducting wires carry different current densities. By examining the critical engineering current density of commercial superconducting wires, the LTS, i.e. NbTi and Nb_3Sn, are capable of many of these magnetic fields and current densities at 4 K and thus feasible for all the four topologies. Some of the topologies may need a larger cross-sectional area of the field coil. The HTS may need to be cooled down to a relatively low temperature, e.g. 20 K, to increase its current density capability. At 20 K, the HTS is feasible for fewer topologies than the LTS but the newly developed HTS is comparable to the NbTi. The currently available MgB_2 is not feasible yet for any of the four topologies at 20 K but only feasible for the fully iron-cored topologies with salient poles at 10 K. MgB_2 superconductors, which are proposed for temperatures of 10-20 K, need further development to carry sufficient current densities in high magnetic fields.

7

8

CONCLUSION

IN 2012, the INNWIND.EU project initiated this research to investigate superconducting generators for 10-20 MW direct-drive offshore wind turbines. Superconducting generators are expected to be compact and lightweight because of the high magnetic field produced by superconducting windings. This technology is facing a few key feasibility challenges, such as high costs of superconducting wires, AC losses in superconductors and high short circuit torque. If these challenges are not solved, the feasibility of superconducting generators will remain low. Moreover, superconducting generators must have significant advantages over the mature conventional generators to enable commercialization. Another interesting issue is that many different electromagnetic designs have been proposed for superconducting generators. Each of them has its own advantages and disadvantages. There has not been an agreement on how to make the most feasible electromagnetic design for superconducting generators.

8.1. SOLVED RESEARCH PROBLEM

This thesis aims at increasing the feasibility of superconducting generators for 10 MW wind turbines and identifying the most feasible generator designs. This research problem is solved by answering the five research questions.

QUESTION 1
The first research question is: *Which topologies result in the lowest cost of energy, based on currently available superconductors?*

149

To answer this question, this thesis starts with looking into a wide range of electromagnetic designs by comparing as many generator topologies in Chapter 3. The purpose is to find the most feasible topologies from this large design space. The levelized cost of energy (LCoE) is considered as the key performance indicator for evaluating the feasibility of a new wind turbine technology. Due to the fact that 10 MW wind turbines do not exist yet, however, the simplified form of LCoE: the levelized capital cost of energy (LCCoE) is chosen as the criterion for a first comparison of generator topologies. In this LCCoE model, only the capital costs are considered. Moreover, the capital cost of the other wind turbine components except the active material cost of the superconducting generator are assumed to be constants. These assumed costs are based on a 10 MW reference wind turbine provided in the INNWIND.EU project and the superconducting generator designs proposed in the literature. Partially superconducting generators are chosen since their feasibility regarding AC losses is much higher than fully superconducting generators. Magnisium diboride (MgB_2) superconducting wires are employed in the field winding. They are less expensive than high temperature superconductors (HTS) while they require less rigorous cooling than low temperature superconductors (LTS). Twelve most applicable radial-flux generator topologies are optimized for the minimum LCCoE and then compared. A program using the genetic algorithm is developed in Chapter 3 for this optimization task.

In this comparison, not only are the current unit cost and current density capability of the MgB_2 wire used, but three scenarios are also studied by assuming a lower unit cost (1/4) and a higher current density capability (4 times). Such scenarios are to take into account the influence of the development of the superconductor technology on the comparison results. The comparison shows that the generator topologies with more iron in the core result in a lower LCCoE than the topologies with more non-magnetic cores, based on the current MgB_2 wire. When the MgB_2 wire becomes cheaper or capable of higher current densities, however, the topologies with more non-magnetic cores will become close to the topologies with more iron in the core regarding the LCCoE. This result implies that using iron cores will always be an effective option to reduce LCCoE for both now and far future. Required magnetic loadings can be produced in these topologies by using a small amount of costly superconducting wires.

The needed length of superconducting wires in these iron-core based topologies is more feasible than that in the other topologies in terms of fabrication and winding technologies. At present, manufacturing and winding very long superconducting wires (e.g. hundreds of kilometers) without performance degradation are very difficult. Therefore, although it is intended to use more superconducting wires to increase the torque density of the generator, the costs and manufacturing technology still make shorter wires more attractive. However, generators using these

iron-core based topologies tend to be heavy and thus, lightweight generator designs may not be obtained. When superconducting wires become sufficiently cheap compared to the other active materials of the generator, more non-magnetic cores can be employed if both a low generator weight and a low LCCoE are desired.

QUESTION 2

The second research question is: *What are the levels of AC losses in the superconducting winding of different electromagnetic designs due to ripple magnetic fields? Are the AC losses acceptably small or not?*

From the comparison in Chapter 3, the fully iron-cored topology with salient iron poles is found to be most feasible regarding LCCoE at present. Its AC loss level is examined in Chapter 4 since its iron stator teeth may cause high AC losses in the MgB_2 superconducting field winding. This topology is also compared with the topology with non-magnetic teeth. The result shows that using iron stator teeth in this topology does not lead to excessive AC losses. Using large numbers of slots per pole per phase (e.g. 4 or 5) can further reduce the AC losses. Therefore, this topology is considered most feasible and chosen for further comparison with the mature technology of permanent magnet generators.

QUESTION 3

The third research question is: *How can the short circuit torque be effectively suppressed by electromagnetic design?*

In partially superconducting generators, the large magnetic air gap leads to excessive short circuit torque. Such high torque challenges the mechanical construction of the wind turbine drive train. It is considered that the short circuit torque of the generator should be sufficiently low to adapt to the mechanical construction. In Chapter 5, three approaches are investigated to reduce the short circuit torque to no higher than 3 times the rated torque. Using an electromagnetic shield or more iron in the core is not effective. Using segmented armature winding with multiple power electronic converters can be an effective option when four segments are used for a 10 MW generator and only one segment is shorted. This approach needs further investigation since the model used for the armature winding segmentation assumed independent segments which simplified the winding construction in the model. However, the result implies that armature winding segmentation is a possible way to effectively reduce the short circuit torque of a superconducting generator.

QUESTION 4

The fourth research question is: *How competitive is a superconducting generator compared with a permanent magnet generator?*

8

In Chapter 6, the LCCoE-optimal generator design based on the fully iron-cored topology with salient poles is compared with 10 MW permanent magnet generators. However, this superconducting generator design does not have significant advantages over permanent magnet generators regarding the LCCoE and the generator cost, size and weight.

QUESTION 5

The fifth research question is then: *What is the potential of a superconducting generator for large wind turbines? What are the design parameters and suitable superconductors required to achieve high generator performance?*

Since the LCCoE at present is not yet the performance indicator that makes superconducting generators competitive, high generator performance from other perspectives must be achieved instead. Such high generator performance should be so attractive to the wind energy industry that the resulting high generator costs and added complexities of cryogenic systems can be considered worthwhile. For this purpose, shear stress and efficiency are chosen as the evaluating performance indicators since they are expected to be the breakthroughs by applying superconducting generators.

In Chapter 7, it is shown that increasing the excitation of the field winding to a high level can achieve high shear stresses and rated-load efficiencies. As an example, it is investigated what excitation is needed to reach both a shear stress as twice as that of a typical permanent magnet generator and a rated-load efficiency of 98%. The twelve generator topologies are again compared. All the topologies can achieve this high performance with a low armature current density of $2 \, \text{A/mm}^2$. The topologies with more iron in the core reach this performance more easily than the topologies with more non-magnetic cores. The fully iron-cored topology with salient iron poles is again most feasible. Besides, to achieve such high generator performance, the required high excitation leads to a high current density and a high magnetic field in the superconducting wire. By examining current commercial superconducting wires, LTS and HTS are more feasible than MgB_2 wires to withstand the required high current density and high magnetic field. Although MgB_2 wires can be considered for the fully iron-cored topology with salient iron poles, they still need further development to be capable of the higher magnetic fields in the other topologies. In contrast, LTS and HTS are suitable for more generator topologies. However, LTS require 4-Kelvin operation and HTS are quite expensive, which also limits their feasibility.

ANSWER TO THE RESEARCH PROBLEM

In summary, from the perspective of electromagnetic design, this thesis points out a direction to increase the feasibility of superconducting generators for large direct-

drive wind turbines:

- Aiming at a lower LCCoE, iron-core based generator topologies are more feasible than the other topologies and the used lengths of superconducting wires are shorter. The fully iron-cored topologies are most feasible and their AC loss level is acceptably low. If a low generator weight and a low LLCoE are both desired, however, the topologies with more non-magnetic cores will become competitive once the superconducting wire is much cheaper and capable of much higher current densities.

- Currently, the superconducting generators do not show significant advantages of LCCoE over permanent magnet generators. To make superconducting generators attractive to wind energy industry, the shear stress and efficiency of the generator should be much higher than those of permanent magnet generators. Such advantages may offset the disadvantages of high generator costs and complicated cryogenic cooling.

- To achieve competitive shear stresses and efficiencies, the excitation of the superconducting field winding should be increased to a high level. To realize such high excitation, LTS and HTS are more feasible than MgB_2 wires at present. In addition, iron-core based generator topologies are again more feasible than the other topologies to reach high shear stresses and efficiencies, especially the fully iron-cored topology with salient poles.

- Aiming at an acceptable short circuit torque, armature winding segmentation with multiple power electronic converters can be considered.

This direction may not be the only one. However, it takes into account the key feasibility issues at the moment from the electromagnetic design perspective. Prototypes can be built following this direction to demonstrate and prove this technology.

8.2. Scientific Contributions

This thesis has two scientific contributions. The first contribution is finding the superconducting generator topology having the lowest LLCoE. This finding provides a design guideline to reduce the LLCoE of superconducting generators for wind turbine applications. Unlike the conclusions in the other literature, however, this finding from this thesis is not only using the current cost and properties of the superconducting wire (i.e. MgB_2 in this thesis) but also based on a scenario study which looks for future trends. This finding will thus be valid for both now and long terms.

The other contribution is finding the generator design requirements to achieve an attractive shear stress and generator efficiency. These requirements include field excitation, generator topology, armature current density and superconductor type. These required design parameters form another design guideline for superconducting generators to compete with permanent magnet generators in direct-drive wind turbine applications.

8

8.3. RECOMMENDATION FOR FUTURE WORK

To evaluate a wind turbine technology, the most complete way is to use LCoE as the criterion. An LCoE contains all the effects of size, weight, efficiency, cost, reliability and availability of the generator and the correlations among them. In this thesis, only the superconducting generator's active material cost and the resulting capital cost are variable in the the LCoE model. The other costs of the wind turbine components are assumed to be constants. In fact, some costs are hardly influenced by the electromagnetic design while the other costs more or less depend on the electromagnetic design. As 10 MW wind turbines are emerging in the near future, these dependences will be found and the LCoE and LCCoE models need to become more accurate.

As concluded in this thesis, the generator topologies with more iron in the core shows the advantages of reducing the LCCoE and achieving high shear stresses and efficiencies. However, they may have large magnetic forces between the rotor and stator because of the iron core in the stator. Such large magnetic forces will challenge the generator's structural support to maintain the air gap. It is interesting to evaluate the effects of iron-based generator topologies on the magnetic force and the design of the generator structure. This effect combined with the effect of active material mass can then be used to improve the LCCoE model and the assumed constant structural cost will become dependent on the topology. The advantage of the iron-based topologies to have a lower LCCoE may then be reduced. Moreover, the large magnetic force may also reduce the advantage of iron-based topologies that have high shear stresses and efficiencies to compete permanent magnet generators. Therefore, structural models of a superconducting generator are needed as future work to improve the LCCoE model and the evaluation of the potential generator performance.

By increasing the performance of the superconducting wire, the difference between the LLCoE of the generator topologies with iron core and non-magnetic core becomes small, while weight differences become significant. We neglected the influence of weight in the LLCoE model. However, in situations where weight is important, e.g. floating wind turbines, more radical superconducting generator concepts may be interesting, including fully superconducting generators.

Effectively reducing the short circuit torque of a superconducting generator is always an interesting topic. Using armature winding segmentation shows its potential in this thesis as a starting point. In future work, this approach needs further development. For example, a model with fewer assumptions needs to be developed with the consideration of the winding segmentation construction. This model then needs experimental validation.

This thesis makes a step of contribution to increase the technology readiness

level of superconducting generators for large direct-drive wind turbines. Efforts are still going on to achieve a mature superconducting generator design that is compact, lightweight, efficient, reliable and affordable. As 8 MW wind turbines using conventional direct-drive permanent magnet generators or geared induction generators are available in the market, superconducting generators will face more challenges from these conventional generators at the 10 MW power level. It is therefore urgent now to prove the superconducting generator technology. Besides theoretical studies and magnet pole demonstrations in various ongoing projects, construction and testing of full-scale superconducting generators seem highly demanded at the moment. It is hoped that the design direction or guidelines concluded from this thesis can help such work.

However, it cannot be ignored that the limited security of supply of permanent magnet materials may change the prospect of permanent magnet generators. Therefore, superconducting generators will stay as an interesting alternative for future large wind turbines and keep developing.

8

ACKNOWLEDGEMENTS

When I decided to do Ph.D., I did not expect so many challenges and difficulties, both in the research work and in my private life. Great thanks to my parents first of all, who have supported me every microsecond from China. I would not have achieved so far without their love and encouragement. They always trusted me with no hesitation and gave me full confidence and courage to overtake the various difficulties in my Ph.D. research and private life. Confucius remarked, "While his parents are living, a son should not go far abroad; if he does, he should let them know where he goes." Unfortunately, I broke it. I came to the Netherlands and have stayed for more than six years. Sometimes I myself did not know where to go during the four years of my Ph.D.. Sometimes I was drowned in my research and sometimes I was lost in my private life. They did not complain but unreservedly gave me their love and pushed me forward to today to finish my Ph.D.. I hope that the success of obtaining my doctoral degree will give the greatest reward to my parents who have sacrificed so much to support my dreams and desires.

Next, I would like to thank my co-promotor and daily supervisor dr. Henk Polinder. He also supervised my master thesis. Then he offered me this precious Ph.D. position. During the four years of Ph.D., I learned a lot from Henk about research methodology, critical thinking and how to design an electrical machine. Although the amount might be only 1% of his expertise, these knowledge and experience are already sufficient for me to start my career as an electrical machine and power conversion engineer. Henk was also concerned about my life and helped me ease my negative emotions from time to time. It was my luck to have Henk as my daily supervisor.

I would also like to thank dr. Asger B. Abrahamsen who is my second co-promotor. During my whole Ph.D. period, Asger was my project partner and we closely cooperated in the INNWIND.EU project. I learned a lot from Asger about superconducting materials and generators. In the last year of my Ph.D. when I was trying hard to publish journal papers, Asger provided many advices and suggestions and helped me a lot. One time he helped me revise a paper till midnight. It was my pleasure to have such a kind project partner and supervisor.

Thanks to my promotor prof. dr. Jan A. Ferreira. Although he was rather busy with his presidency in the IEEE Power Electronics Society in recent years, he still spent a few hours per month to evaluate the progress of my Ph.D. work and provide

his feedback. He could not supervise all the students at the same time but I could tell that he was trying to do his best. He was very patient on me when my progress was disappointing. I could not ask for more.

In these four years, I met many people around me. Some became my good friends. Some helped me a lot. I am afraid of forgetting to thank any of them. Xuezhou Wang was my Ph.D. colleague. Thanks to him for having lunch together, discussing machines, sharing life experiences, etc., almost everyday. Xiaowei Song was a Ph.D. student from Technical Univeristy of Denmark. We both worked on superconducting generators so we shared opinions while we also competed. Therefore, we grew up with each other. It is quite interesting that we have many other similarities, too. Are they due to coincidence or whatever reason? I do not know yet.

I am grateful for having had the Ph.D. colleagues and staff members of former EPP group and current DCE&S group, from Anoop Jassal to Tim Strous, from Tsegay Hailu to Jiayang Wu, from Sharmila Rattansingh to Harrie Olsthoorn.

I cherish very much my Chinese friends whom I have known since my master study in Delft. Those friends staying in the Netherlands made my life joyful. Thanks to Yating Ren, Fei Sun, Xinwei Sun, Zhuowei Liu, Long Kong, Fengli Wang, Fanhe Kong, Lu Zheng, Bo Fan, Qian Feng, Qing Shen, Ye Qiu. Those friends who have left the Netherlands left precious memories to me. Thanks to Shan Du, Ruoshi Wang, Haoyan Xue, Hejiang Chen, Xin Li.

In particular, thanks to Mrs. Ken Chao-Hsi and her Love Home. From her and the events at Love Home, I started to know more about Christianity and Christian culture. Every event at Love Home was full of love and fun and made me feel cured from anxiety and pressure.

Certainly, many thanks to XEMC Darwind B.V. for offering me my current job. I could not find another job that fit my interest and background so well in the Netherlands. Everyone of the company is so kind that I always feel happy nowadays. Special thanks to my colleagues Robert Rutteman and Michiel Damen for translating the summary of this thesis into Dutch.

Last but not least, I must thank the INNWIND.EU project. This project financially sponsored my Ph.D. study and research and provided an excellent platform to me to learn wind turbine technologies. It also provided many chances of presenting my work so my presentation skill was well trained. I will never forget those half-year meetings of the project held allover Europe, the insightful presentations in those meetings and the banquet at the foot of Acropolis of Athens. Here I would like to thank all the project partners involved in the INNWIND.EU project.

Curriculum Vitæ

Dong Liu was born in Lanzhou, Gansu, China on 22nd December 1984. He finished his high school education at High School Attached to Northwest Normal University, Lanzhou, China in 2003 and in the same year he went to Harbin Institute of Technology, Harbin, China for his bachelor education. In 2007, he graduated with Bachelor of Engineering and started his first job as a technical service engineer at Shenzhen NARI Technology Ltd., Shenzhen, China. In 2010, he started his master program at Delft University of Technology, Netherlands. In 2012, he received his Master of Science in Electrical Engineering.

Since December 2012 he has been working towards his Ph.D. degree at the Department of Electrical Sustainable Energy at Delft University of Technology, Netherlands. His Ph.D research results are compiled in this thesis. He is currently working as Electrical Machine & Power Conversion Engineer at XEMC Darwind B.V., Hilversum, Netherlands.

LIST OF PUBLICATIONS

JOURNAL ARTICLES

17. **D. Liu, H. Polinder, A. B. Abrahamsen and J. A. Ferreira**, *Potential of partially superconducting generators for large direct-drive wind turbines*, IEEE Transactions on Applied Superconductivity. (Accepted)

16. **D. Liu, H. Polinder, A. B. Abrahamsen and J. A. Ferreira**, *Topology comparison of superconducting generators for 10-MW direct-drive wind turbines: cost of energy based*, IEEE Transactions on Applied Superconductivity. **27**, 4 (2017)

15. **D. Liu, H. Polinder, A. B. Abrahamsen and J. A. Ferreira**, *Effects of armature winding segmentation with multiple converters on the short circuit torque of 10-MW superconducting wind turbine generators*, IEEE Transactions on Applied Superconductivity, **27**, 4 (2017).

14. **D. Liu, H .Polinder, A. B. Abrahamsen, E. Stehouwer, B. Hendriks and N. Magnusson**, *Optimization and comparison of superconducting generator topologies for a 10 MW wind turbine applications*, International Journal of Applied Electromagnetics and Mechanics. **53**, S2 (2017)

13. **D. Liu, H. Polinder, N. Magnusson, J. Schellevis and A. B. Abrahamsen**, *Ripple field AC losses in 10-MW wind turbine generators with a MgB_2 superconducting field winding*, IEEE Transactions on Applied Superconductivity, **26**, 3 (2016).

12. **X. Song, D. Liu, H. Polinder, N. Mijatovic, J. Holbøll and B. B. Jensen**, *Short circuits of a 10 MW high temperature superconducting wind turbine generator*, IEEE Transactions on Applied Superconductivity, **27**, 4 (2017).

11. **N. Magnusson, A. B. Abrahamsen, D. Liu, M. Runde and H. Polinder**, *Hysteresis losses in MgB_2 superconductors exposed to combinations of low AC and high DC magnetic fields and transport currents*, Physica C: Superconductivity and its Applications, **506** (2014).

CONFERENCE PUBLICATIONS

10. **D. Liu, H. Polinder, X. Wang and J. A. Ferreira**, *Evaluating the cost of energy of a 10 MW direct-drive wind turbine with superconducting generators*, 2016 XXII International Conference on Electrical Machines (ICEM), Lausanne, Switzerland, 2016, pp. 318-324.

161

9. **D. Liu, H. Polinder, A. B. Abrahamsen, X. Wang and J. A. Ferreira**, *Comparison of superconducting generators and permanent magnet generators for 10-MW direct-drive wind turbines*, 2016 19th International Conference on Electrical Machines and Systems (ICEMS), Chiba, Japan, 2016.

8. **D. Liu, H. Polinder, A. B. Abrahamsen and J. A. Ferreira**, *Comparison of 10 MW superconducting generator topologies for direct-drive wind turbines*, 2015 IEEE International Electric Machines & Drives Conference (IEMDC), Coeur d'Alene, USA, 2015, pp. 174-180.

7. **D. Liu, H. Polinder, A. B. Abrahamsen and J. A. Ferreira**, *Effects of an electromagnetic shield and armature teeth on the short-circuit performance of a direct drive superconducting generator for 10 MW wind turbines*, 2015 IEEE International Electric Machines & Drives Conference (IEMDC), Coeur d'Alene, USA, 2015, pp. 709-714.

6. **D. Liu, A. Jassal, H. Polinder and J. A. Ferreira**, *Validation of eddy current loss models for permanent magnet machines with fractional-slot concentrated windings*, 2013 IEEE International Electric Machines & Drives Conference (IEMDC), Chicago, USA, 2013, pp. 678-685.

5. **X. Wang, D. Liu, H. Polinder, D. Lahaye and J. A. Ferreira**, *Comparison of nested-loop rotors in brushless doubly-fed induction machines*, 2016 19th International Conference on Electrical Machines and Systems (ICEMS), Chiba, Japan, 2016.

4. **X. Wang, D. Liu, H. Polinder, D. Lahaye and J. A. Ferreira**, *Finite element analysis and experimental validation of eddy current losses in permanent magnet machines with fractional-slot concentrated windings*, 2016 19th International Conference on Electrical Machines and Systems (ICEMS), Chiba, Japan, 2016.

3. **A. B. Abrahamsen, N. Magnusson, D. Liu, E. Stehouwer, B. Hendriks and H. Polinder**, *Design study of a 10 MW MgB_2 superconductor direct drive wind turbine generator*, Proceedings of 2014 European Wind Energy Conference, Brussels, Belgium, 2014.

2. **A. B. Abrahamsen, N. Magnusson, B. B. Jensen, D. Liu and H. Polinder**, *Design of an MgB_2 race track coil for a wind generator pole demonstration*, Journal of Physics: Conference Series, **507**, 3 (2014).

1. **D. Kostopoulos, D. Liu, G. Genani and H. Polinder**, *Feasibility study of a 10 MW MgB_2 fully superconducting generator for offshore wind turbines*, Proceedings of EWEA Offshore 2013 conference, Frankfurt, Germany, 2013.

REFERENCES

[1] Z. Zhao, P. Wu, B. Xia, and M. Skitmore, *Development route of the wind power industry in China,* Renewable and Sustainable Energy Reviews **34**, 1 (2014).

[2] European Environment Agency, *Europe's onshore and offshore wind energy potential- an assessment of environmental and economic constraints,* EEA Technical report series: ISSN 1725-2237 (2009), 10.2800/11373.

[3] J. Kaldellis and M. Kapsali, *Shifting towards offshore wind energy—Recent activity and future development,* Energy Policy **53**, 136 (2012).

[4] M. Bilgili, A. Yasar, and E. Simsek, *Offshore wind power development in Europe and its comparison with onshore counterpart,* Renewable and Sustainable Energy Reviews **15**, 905 (2011).

[5] R. Texeira, *Multi-Terminal DC Networks System Integration, Dynamics and Control*, Ph.D. thesis, Delft University of Technology, CPI Koninklijke Wöhrmann (2014).

[6] AWS Truepower, `https://www.awstruepower.com/knowledge-center/maps/`, [Online], [Last accessed May 2017].

[7] EWEA, *The European offshore wind industry -key trends and statistics 2015,* `https://windeurope.org/wp-content/uploads/files/about-wind/statistics/EWEA-European-Offshore-Statistics-2015.pdf`, [Online], [Last accessed May 2017].

[8] Siemens, *Siemens 8.0 MW offshore wind turbine,* `http://www.siemens.com/content/dam/internet/siemens-com/global/market-specific-solutions/wind/brochures/siemens-wind-power-offshore-swt-8.0-154-productflyer-web-doublepages.pdf`, [Online], [Last accessed May 2017].

[9] MHI Vestas, `http://www.mhivestasoffshore.com/v164-8-0-mw-breaks-world-record-for-wind-energy-production/`, [Online], [Last accessed May 2017].

[10] F. Spinato, P. J. Tavner, G. J. W. V. Bussel, and E. Koutoulakos, *Reliability of wind turbine subassemblies,* IET Renewable Power Generation **3**, 387 (2009).

[11] INNWIND.EU, `http://www.innwind.eu/`, [Online], [Last accessed May 2017].

[12] K. Atallah and D. Howe, *A novel high-performance magnetic gear,* IEEE Transactions on Magnetics **37**, 2844 (2001).

[13] K. Atallah, J. Rens, S. Mezani, and D. Howe, *A novel "Pseudo" direct-drive brusheless permanent magnet machine,* IEEE Transactions on Magnetics **44**, 4349 (2008).

[14] H. Polinder, J. Ferreira, B. Jensen, A. Abrahamsen, K. Atallah, and R. McMahon, *Trends in wind turbine generator systems,* IEEE Journal of Emerging and Selected Topics in Power Electronics **1**, 174 (2013).

[15] A. B. Abrahamsen, N. Mijatovic, E. Seiler, T. Zirngibl, C. Træholt, P. B. Nørgård, N. F. Pedersen, N. H. Andersen, and J. Østergård, *Superconducting wind turbine generators,* Superconductor Science and Technology **23**, 034019 (2010).

[16] B. B. Jensen, N. Mijatovic, and A. B. Abrahamsen, *Development of superconducting wind turbine generators,* Journal of Renewable and Sustainable Energy **5**, 023137 (2013).

[17] S. S. Kalsi, B. B. Gamble, G. Snitchler, and S. O. Ige, *The status of HTS ship propulsion motor developments,* in *2006 IEEE Power Engineering Society General Meeting* (2006) pp. 5 pp.–.

[18] H. W. Neumüller and et al., *Advances in and prospects for development of high-temperature superconductor rotating machines at siemens,* Superconductor Science and Technology **19**, S114–S117 (2006).

[19] A. M. Campbell, *Superconducting and conventional machines,* Superconductor Science and Technology **27**, 124012 (2014).

[20] R. Fair, *Superconductivity for Large Scale Wind Turbines*, Tech. Rep. (DOE report DE-EE0005143, 2012).

[21] G. Snitchler, *Progress on high temperature superconductor propulsion motors and direct drive wind generators,* in *Power Electronics Conference (IPEC), 2010 International* (2010) pp. 5–10.

[22] AML, `http://amlsuperconductivity.com/applications/energy/doe-approved-wind-turbine-solution/`, [Online], [Last accessed May 2017].

[23] I. Marino, A. Pujana, G. Sarmiento, S. Sanz, J. M. Merino, M. Tropeano, J. Sun, and T. Canosa, *Lightweight MgB$_2$ superconducting 10 mw wind generator,* Superconductor Science and Technology **29**, 024005 (2016).

[24] O. Keysan and M. Mueller, *A modular and cost-effective superconducting generator design for offshore wind turbines,* Superconductor Science and Technology **28**, 034004 (2015).

[25] S. S. Kalsi, *Superconducting Wind Turbine Generator Employing MgB$_2$ Windings Both on Rotor and Stator,* IEEE Transactions on Applied Superconductivity **24**, 47 (2014).

[26] X. Song, N. Mijatovic, B. B. Jensen, and J. Holbøll, *Design study of fully superconducting wind turbine generators,* IEEE Transactions on Applied Superconductivity **25**, 1 (2015).

[27] G. Shrestha, *Structural Flexibility of Large Direct Drive Generators for Wind Turbines,* Ph.D. thesis, Delft University of Technology (2013).

[28] P. J. Masson, *Superconducting generators for large wind turbine: design trade-off and challenges,* (presented at the 1st European Workshop SOWiT, 2011).

[29] R. Qu, Y. Liu, and J. Wang, *Review of superconducting generator topologies for direct-drive wind turbines,* IEEE Transactions on Applied Superconductivity **23**, 5201108 (2013).

[30] H. Karmaker, M. Ho, and D. Kulkarni, *Comparison between different design topologies for multi-megawatt direct drive wind generators using improved second generation high temperature superconductors,* IEEE Transactions on Applied Superconductivity **25**, 5201605 (2015).

[31] K. Sivasubramaniam, X. H. X. Huang, D. Ryan, K. Weeber, J. Bray, E. Laskaris, L. Tomaino, J. Fogarty, and S. Ashworth, *AC losses in a high temperature superconducting generator,* IEEE Transactions on Applied Superconductivity **15**, 2162 (2005).

[32] N. Magnusson, A. B. Abrahamsen, D. Liu, M. Runde, and H. Polinder, *Hysteresis losses in MgB$_2$ superconductors exposed to combinations of low AC and high DC magnetic fields and transport currents,* Physica C: Superconductivity and its Applications **506**, 133 (2014).

[33] Y. Liu, R. Qu, J. Wang, H. Fang, X. Zhang, and H. Chen, *Influences of generator parameters on fault current and torque in a large-scale superconducting wind generator,* IEEE Transactions on Applied Superconductivity **25**, 1 (2015).

[34] H. K. Onnes, *Disappearance of the electrical resistance of mercury at helium temperatures,* Electrician **67**, 657 (1911).

[35] R. de Bruyn Ouboter, *Superconductivity: Discoveries during the early years of low temperature research at leiden 1908-1914,* IEEE Transactions on Magnetics **23**, 355 (1987).

[36] CCAS, *Superconductivity: Present and Future Applications*, Tech. Rep. (Coalition for the Commercial Application of Superconductors (CCAS), 2014).

[37] A. P. Drozdov, M. I. Eremets, I. A. Troyan, V. Ksenofontov, and S. I. Shylin, *Conventional superconductivity at 203 kelvin at high pressures in the sulfur hydride system,* Nature **525**, 73 (2015).

[38] W. Meissner and R. Ochsenfeld, *Ein neuer effekt bei eintritt der supraleitfähigkeit,* Naturwissenschaften **21**, 787 (1933).

[39] S. Blundell, *Superconductivity, a very short introduction* (Oxford Univeristy Press, 2009).

[40] P. J. Lee, *Superconductivity and magnetism,* in *Engineering Superconductivity* (Wiley-IEEE Press, 2001) pp. 1–185.

[41] Y. Iwasa, *Case Studies in Superconducting Magnets, Second Edition* (Springer US, 2009).

[42] T. Berlincourt, *Type II superconductivity: Quest for understanding,* IEEE Transactions on Magnetics **23**, 403 (1987).

[43] R. G. Sharma, *Type II Superconductors,* in *Superconductivity: Basics and Applications to Magnets* (Springer International Publishing, Cham, 2015) pp. 49–69.

[44] M. R. Osorio, A. P. Morales, J. G. Rodrigo, H. Suderow, and S. Vieira, *Demonstration experiments for solid-state physics using a table-top mechanical Stirling refrigerator,* European Journal of Physics **33**, 757 (2012).

[45] M. Garber, M. Suenage, W. B. Sampson, and R. L. Sabatini, *Critical current studies on fine filamentary NbTi accelerator wires,* Advances in Cryogenic Engineering Materials SE-84 **32**, 707 (1986).

[46] N. high-magnetic-field lab, https://nationalmaglab.org/images/magnet_development/asc/plots/JeChart041614-1022x741-pal.png/, [Online], [Last accessed May 2017].

[47] M. P. Oomen, *AC loss in superconducting tapes and cables*, Ph.D. thesis, Delft University of Technology, Universiteit Twente (2000).

[48] P. Kováč, T. Melišek, and I. Hušek, *Ic anisotropy of in situ made MgB$_2$ tapes,* Superconductor Science and Technology **18**, L45 (2005).

[49] J. Durrell, *Critical Current Anisotropy in High Temperature Superconductors,* Ph.D. thesis, University of Cambridge (2001).

[50] B. ten Haken, J.-J. Rabbers, and H. H. ten Kate, *Magnetization and AC loss in a superconductor with an elliptical cross-section and arbitrary aspect ratio ,* Physica C: Superconductivity **377**, 156 (2002).

[51] STI, http://www.suptech.com/about_superconducting_wire_n.php/, [Online], [Last accessed May 2017].

[52] Aarnink, René and Overweg, Johan, *Magnetic resonance imaging, a success story for superconductivity,* Europhysics News **43**, 26 (2012).

[53] CERN, https://home.cern/, [Online], [Last accessed May 2017].

[54] ITER, https://www.iter.org/, [Online], [Last accessed May 2017].

[55] R. Zuijderduin, *Integration of High-T$_c$ Superconducting Cables in the Dutch Power Grid of the Future,* Ph.D. thesis, Delft University of Technology, Delft University of Technology (2016).

[56] M. Noe and M. Steurer, *High-temperature superconductor fault current limiters: concepts, applications, and development status,* Superconductor Science and Technology **20**, R15 (2007).

[57] Columbus Superconductors, http://www.columbussuperconductors.com/, [Online], [Last accessed May 2017].

[58] J. C. H. Bone, *Influence of rotor diameter and length on the rating of induction motors,* Electric Power Applications, IEE Journal on **1**, 2 (1978).

[59] K. J. Binns and D. W. Shimmin, *The relationship between performance characteristics and size of permanent magnet motors,* in *1995 Seventh International Conference on Electrical Machines and Drives (Conf. Publ. No. 412)* (1995) pp. 423–427.

[60] P. C. Sen, *Principles of Electric Machines and Power Electronics* (John Wiley & Sons, 1997).

[61] J. L. Kirtley, J. L. Smith, and S. D. Umans, *Cryogenic isolating torque tubes for a superconducting generator-detailed model and performance analysis,* IEEE Transactions on Energy Conversion **6**, 267 (1991).

[62] N. Mijatovic, B. Jensen, C. Træholt, and A. Abrahamsen, *Superconducting wind turbine generators*, Ph.D. thesis (2014).

[63] S. Kalsi, D. Madura, T. MacDonald, M. Ingram, and I. Granta, *Operating experience of superconductor dynamic synchronous condenser*, in *2005/2006 IEEE/PES Transmission and Distribution Conference and Exhibition* (2006) pp. 899–902.

[64] T.-J. Yang, L. Horng, H.-S. Koo, and K. Chen, *Investigation of the bending effect and the critical current density on a Bi-Based superconducting tape*, in *Advances in Superconductivity V: Proceedings of the 5th International Symposium on Superconductivity (ISS '92), November 16–19, 1992, Kobe*, edited by Y. Bando and H. Yamauchi (Springer Japan, Tokyo, 1993) pp. 803–806.

[65] Y. Yang, G. Li, M. Susner, M. Sumption, M. Rindfleisch, M. Tomsic, and E. Collings, *Influence of twisting and bending on the Jc and n-value of multi-filamentary MgB$_2$ strands*, Physica C: Superconductivity and its Applications **519**, 118 (2015).

[66] J. C. Eliassen, *Winding and Testing of Superconducting Coils*, Master's thesis, Norwegian University of Science and Technology, Department of Electric Power Engineering, Norway (2015).

[67] D. Kostopoulos, D. Liu, G. Genani, and H. Polinder, *Feasibility study of a 10 mw mgb$_2$ fully superconducting generator for offshore wind turbines*, in *2013 EWEA Offshore Proceedings* (2013) pp. 1–11.

[68] J. R. Bumby, *Superconducting Rotating Electrical Machines* (Oxford Univeristy Press, 1984).

[69] K. Kajikawa, Y. Uchida, T. Nakamura, H. Kobayashi, T. Wakuda, and K. Tanaka, *Development of stator windings for fully superconducting motor with MgB$_2$ wires*, IEEE Transactions on Applied Superconductivity **23**, 5201604 (2013).

[70] Y. Terao, M. Sekino, and H. Ohsaki, *Electromagnetic design of 10 MW class fully superconducting wind turbine generators*, IEEE Transactions on Applied Superconductivity **22**, 5201904 (2012).

[71] P. Tixador, Y. Brunet, P. Vedrine, Y. Laumond, and J. L. Sabrie, *Electrical tests on a fully superconducting synchronous machine*, IEEE Transactions on Magnetics **27**, 2256 (1991).

[72] P. N. Barnes, M. D. Sumption, and G. L. Rhoads, *Review of high power density superconducting generators: Present state and prospects for incorporating YBCO windings,* Cryogenics **45**, 670 (2005).

[73] Q. Jiang, M. Majoros, Z. Hong, A. M. Campbell, and T. A. Coombs, *Design and ac loss analysis of a superconducting synchronous motor,* Superconductor Science and Technology **19**, 1164 (2006).

[74] O. Tsukamoto, N. Amemiya, T. Takao, S. Akita, K. Ohishi, H. Shimizu, Y. Tanaka, and Y. Uchikawa, *Development of 30 kVA class fully superconducting generator,* IEEE Transactions on Magnetics **28**, 283 (1992).

[75] O. Tsukamoto, N. Amemiya, K. Yamagishi, T. Takao, S. Akita, S. Torii, K. Ohishi, and H. Shimizu, *Development and electrical test of a 30 kVA class fully superconducting generator,* IEEE Transactions on Magnetics **30**, 2308 (1994).

[76] J. R. Bumby and R. Martin, *Axial-flux permanent-magnet air-cored generator for small-scale wind turbines,* IEE Proceedings - Electric Power Applications **152**, 1065 (2005).

[77] A. S. Mcdonald, M. A. Mueller, and H. Polinder, *Structural mass in direct-drive permanent magnet electrical generators,* IET Renewable Power Generation **2**, 3 (2008).

[78] D. Bang, *Design of Transverse Flux Permanent Magnet Machines for Large Direct-Drive Wind Turbines*, Ph.D. thesis, Delft University of Technology (2010).

[79] A. Zavvos, D. Bang, A. McDonald, H. Polinder, and M. Mueller, *Structural analysis and optimisation of transverse flux permanent magnet machines for 5 and 10 MW direct drive wind turbines,* Wind Energy **15**, 19 (2012).

[80] M. Mueller and A. Zavvos, *Electrical generators for direct drive systems: a technology overview,* in *Electrical drives for direct drive renewable energy systems*, edited by M. Mueller and Henk Polinder (Woodhead Publishing, 2013) pp. 3–29.

[81] O. Keysan and M. A. Mueller, *A transverse flux high-temperature superconducting generator topology for large direct drive wind turbines,* Physics Procedia **36**, 759 (2012).

[82] D. Bang, H. Polinder, G. Shrestha, and J. A. Ferreira, *Review of generator systems for direct-drive wind turbines,* European Wind Energy Conference & Exhibition, Belgium , 1 (2008).

[83] A. Cavagnino, M. Lazzari, F. Profumo, and A. Tenconi, *A comparison between the axial flux and the radial flux structures for PM synchronous motors,* IEEE Transactions on Industry Applications **38**, 1517 (2002).

[84] U. Lucia, *Carnot efficiency: Why?* Physica A: Statistical Mechanics and its Applications **392**, 3513 (2013).

[85] A. B. Abrahamsen and et al., *First assessment of PI's for 10-20 MW SC and PDD generators,* Tech. Rep. (INNWIND.EU, 2013).

[86] T. Wada and A. Sato, *Basic experiment on the indirect cooling for superconducting magnets,* in *Advances in Cryogenic Engineering: Part A & B,* edited by R. W. Fast (Springer US, Boston, MA, 1990) pp. 849–856.

[87] F. N. Werfel and et al., *Technology, preparation, and characterization,* in *Applied Superconductivity* (Wiley-VCH Verlag GmbH & Co. KGaA, 2015) pp. 193–402.

[88] S. S. Kalsi, *Cooling and thermal insulation systems,* in *Applications of High Temperature Superconductors to Electric Power Equipment* (Wiley-IEEE Press, 2011) pp. 35–58.

[89] R. Radenbaugh, *Refrigeration for superconductors,* Proceedings of the IEEE **92**, 1719 (2004).

[90] W. E. Gifford, *The Gifford-McMahon Cycle,* in *Advances in Cryogenic Engineering: Proceedings of the 1965 Cryogenic Engineering Conference Rice University Houston, Texas August 23–25, 1965,* edited by K. D. Timmerhaus (Springer US, Boston, MA, 1966) pp. 152–159.

[91] M. Thirumaleshwar and S. Subramanyam, *Gifford-McMahon cycle — a theoretical analysis,* Cryogenics **26**, 177 (1986).

[92] R. Sier, *Hot Air Caloric and Stirling Engines: A history,* v. 1 (L.A. Mair, 1999).

[93] G. Popescu, V. Radcenco, E. Gargalian, and P. R. Bala, *A critical review of pulse tube cryogenerator research,* International Journal of Refrigeration **24**, 230 (2001).

[94] J. Ekin, *Experimental Techniques for Low-Temperature Measurements* (Oxford University Press, 2006).

[95] Babcock Noell GmbH, `http://www.bng.bilfinger.com/en/`, [Online], [Last accessed May 2017].

[96] J. He, Y. Tang, J. Li, L. Ren, J. Shi, J. Wang, R. Qu, L. Su, X. Li, Y. Xu, and Z. Zhu, *Conceptual design of the cryogenic system for a 12 MW superconducting wind turbine generator,* IEEE Transactions on Applied Superconductivity **24**, 1 (2014).

[97] S. Santiago and et al., *First modular cryostat,* Tech. Rep. (Suprapower, 2015).

[98] Suprapower, `http://www.suprapower-fp7.eu/summary.php/`, [Online], [Last accessed May 2017].

[99] Stirling cryogenics, `http://www.stirlingcryogenics.com/Rotating-machines/`, [Online], [Last accessed May 2017].

[100] B. B. Gamble, S. Kalsi, G. Snitchler, D. Madura, and R. Howard, *The status of HTS motors,* in *IEEE Power Engineering Society Summer Meeting,*, Vol. 1 (2002) pp. 270–274 vol.1.

[101] B. Gamble, G. Snitchler, and T. MacDonald, *Full power test of a 36.5 MW HTS propulsion motor,* IEEE Transactions on Applied Superconductivity **21**, 1083 (2011).

[102] R. Fair, C. Lewis, J. Eugene, and M. Ingles, *Development of an HTS hydroelectric power generator for the hirschaid power station,* Journal of Physics: Conference Series **234**, 032008 (2010).

[103] T. A. Keim, T. E. Laskaris, J. A. Fealey, and P. A. Rios, *Design and manufacture of a 20 MVA superconducting generator,* IEEE Power Engineering Review **PER-5**, 56 (1985).

[104] K. Sivasubramaniam, T. Zhang, M. Lokhandwalla, E. T. Laskaris, J. W. Bray, B. Gerstler, M. R. Shah, and J. P. Alexander, *Development of a high speed HTS generator for airborne applications,* IEEE Transactions on Applied Superconductivity **19**, 1656 (2009).

[105] H. W. Neumüller, W. Nick, B. Wacker, M. Frank, G. Nerowski, J. Frauenhofer, W. Rzadki, and R. Hartig, *Advances in and prospects for development of high-temperature superconductor rotating machines at siemens,* Superconductor Science and Technology **19**, S114 (2006).

[106] AMSC, `http://www.amsc.com/documents/seatitan-10-mw-wind-turbine-data-sheet/`, [Online], [Last accessed May 2017].

[107] Ecoswing, `https://ecoswing.eu/`, [Online], [Last accessed May 2017].

[108] ICMAB CSIC, `http://departments.icmab.es/suman/2016/12/12/csic-institutes-materials-science-barcelona-aragon-together-gamesa-innovation-technology-develop-first-prototype-electric-superconducting-generator-medium-power-wi/`, [Online], [Last accessed May 2017].

[109] Z. Chen, *Power electronic converter systems for direct drive renewable energy applications,* in *Electrical drives for direct drive renewable energy systems*, edited by M. Mueller and Henk Polinder (Woodhead Publishing, 2013) pp. 106–135.

[110] E. de Vries, *6 - wind turbine drive systems: a commercial overview,* in *Electrical Drives for Direct Drive Renewable Energy Systems*, Woodhead Publishing Series in Energy, edited by M. Mueller and H. Polinder (Woodhead Publishing, 2013) pp. 139 – 157.

[111] E. Hau, *Mechanical drive train and nacelle,* in *Wind Turbines: Fundamentals, Technologies, Application, Economics* (Springer Berlin Heidelberg, Berlin, Heidelberg, 2013) pp. 305–383.

[112] J. N. Stander, G. Venter, and M. J. Kamper, *Review of direct-drive radial flux wind turbine generator mechanical design,* Wind Energy **15**, 459 (2012).

[113] Siemens Wind Power, `http://www.siemens.com/global/en/home/markets/wind.html/`, [Online], [Last accessed May 2017].

[114] D. Dabrowski, A. Natarajan, and E. Stehouwer, *Structural optimization of an innovative 10 MW wind turbine nacelle,* in *Proceedings of the EWEA Annual Event and Exhibition 2015* (European Wind Energy Association (EWEA), 2015) paper for poster presentation.

[115] G. Snitchler, *A direct drive wind turbine HTS generator,* in *IEEE Power Engineering Society General Meeting* (2007) pp. 1–8.

[116] G. Snitchler, B. Gamble, C. King, and P. Winn, *10 MW class superconductor wind turbine generators,* IEEE Transactions on Applied Superconductivity **21**, 1089 (2011).

[117] B. Maples, M. M. Hand, and W. D. Musial, *Comparative assessment of direct drive high temperature superconducting generators in multi-megawatt class wind turbines,* Tech. Rep. (Golden, CO: National Renewable Energy Laboratory, 2010).

[118] S. S. Kalsi, *Rotating ac machines,* in *Applications of High Temperature Superconductors to Electric Power Equipment* (Wiley-IEEE Press, 2011) pp. 59–128.

[119] Y. Liu, R. Qu, and J. Wang, *Comparative analysis on superconducting direct-drive wind generators with iron teeth and air-gap winding,* IEEE Transactions on Applied Superconductivity **24**, 1 (2014).

[120] Y. Xu, N. Maki, and M. Izumi, *Electrical design study of 10-MW salient-pole wind turbine HTS synchronous generators,* IEEE Transactions on Applied Superconductivity **24**, 1 (2014).

[121] D. Liu, H. Polinder, N. Magnusson, J. Schellevis, and A. B. Abrahamsen, *Ripple field ac losses in 10-mw wind turbine generators with a MgB_2 superconducting field winding,* IEEE Transactions on Applied Superconductivity **26**, 1 (2016).

[122] A. B. Abrahamsen, N. Magnusson, B. B. Jensen, D. Liu, and H. Polinder, *Design of an MgB_2 race track coil for a wind generator pole demonstration,* Journal of Physics: Conference Series **507**, 032001 (2013).

[123] J. Pyrhonen, T. Jokinen, and V. Hrabovcova, *Design of Rotating Electrical Machines* (New York: Wiley, 2009).

[124] J. Manwell, J. McGowan, and A. Rogers, *Wind Energy Explained: Theory, Design and Application: 2nd edition* (Wiley, 2009).

[125] T. Burton, N. Jenkins, D. Sharpe, and E. Bossanyi, *Wind Energy Hand Book: 2nd edition* (Wiley, 2011).

[126] A. A. Arkadan, R. Vyas, J. G. Vaidya, and M. J. Shah, *Effect of toothless stator design and core and stator conductors eddy current losses in permanent magnet generators,* IEEE Transactions on Energy Conversion **7**, 231 (1992).

[127] H. Polinder, F. F. A. van der Pijl, G. J. de Vilder, and P. J. Tavner, *Comparison of direct-drive and geared generator concepts for wind turbines,* IEEE Transactions on Energy Conversion **21**, 725 (2006).

[128] K. Deb, A. Pratap, S. Agarwal, and T. Meyarivan, *A fast and elitist multiobjective genetic algorithm: NSGA-II,* IEEE Transactions on Evolutionary Computation **6**, 182 (2002).

[129] S. Lin, http://nl.mathworks.com/matlabcentral/fileexchange/31166-ngpm-a-nsga-ii-program-in-matlab-v1-4/, [Online], [Last accessed May 2017].

[130] N. Bianchi and S. Bolognani, *Design optimisation of electric motors by genetic algorithms,* IEE Proceedings - Electric Power Applications **145**, 475 (1998).

[131] H. Polinder, D. Bang, R. P. J. O. M. van Rooij, A. S. McDonald, and M. A. Mueller, *10 MW wind turbine direct-drive generator design with pitch or active speed stall control,* in *2007 IEEE International Electric Machines Drives Conference,* Vol. 2 (2007) pp. 1390–1395.

[132] P. Chaviaropoulos and A. Natarajan, *Definition of Performance Indicators (PIs) and Target Values,* Tech. Rep. (INNWIND.EU, 2014).

[133] A. B. Abrahamsen and A. Natarajan, *Variation of extreme and fatigue design loads on the main bearing of a front mounted direct drive system,* Journal of Physics: Conference Series **765**, 112006 (2016).

[134] J. F. Gieras, *Advancements in Electric Machines* (Springer-Verlag, 2008).

[135] H. London, *Alternating current losses in superconductors of the second kind,* Physics Letter **6**, 162 (1963).

[136] C. P. Bean, *Magnetization of high-field superconductors,* Reviews of Modern Physics **36**, 31 (1964).

[137] W. J. Carr, *AC Loss and Macroscopic Theory of Superconductors* (CRC Press, 2001).

[138] M. N. Wilson, *Superconducting Magnets* (Clarendon, 1983).

[139] B. ten Haken, J. J. Rabbers, and H. H. J. ten Kate, *Magnetization and AC loss in a superconductor with an elliptical cross-section and arbitrary aspect ratio,* Physica C: Superconductivity **377**, 156 (2002).

[140] Z. Chen and et al., *Deliverable 3.31: Converter designs tailored to SC and PDD concepts,* Tech. Rep. (INNWIND.EU) [Online], [Last accessed May 2017].

[141] J. Morren, J. Pierik, and S. W. de Haan, *Inertial response of variable speed wind turbines,* Electric Power Systems Research **76**, 980 (2006).

[142] H. Li, Z. Chen, and H. Polinder, *Optimization of multibrid permanent-magnet wind generator systems,* IEEE Transactions on Energy Conversion **24**, 82 (2009).

[143] C. Stuebig, A. Seibel, K. Schleicher, L. Haberjan, M. Kloepzig, and B. Ponick, *Electromagnetic design of a 10 MW permanent magnet synchronous generator for wind turbine application,* in *2015 IEEE International Electric Machines Drives Conference (IEMDC)* (2015) pp. 1202–1208.

[144] A. K. Sawhney, *A Course in Electrical Machine Design* (Delhi: Dhanpat Rai & Co., 2006).

[145] Z. Zhang, A. Matveev, S. Øvrebø, R. Nilssen, and A. Nysveen, *State of the art in generator technology for offshore wind energy conversion systems,* in *2011 IEEE International Electric Machines Drives Conference (IEMDC)* (2011) pp. 1131–1136.

[146] E. Seiler, D. Richter, B. Bordini, L. Bottura, D. Bessette, A. Vostner, and A. Devred, *Hysteresis losses and effective $j_c(b)$ scaling law for ITER Nb3Sn strands,* IEEE Transactions on Applied Superconductivity **26**, 1 (2016).

[147] D. Doll and et al., *The markets that are opening for mgb$_2$ superconductors and related applications,* (Presented at 11th European Conference on Applied Superconductivity, Contribution 1M-WT-I1, Genova, 2013).

[148] D. W. Hazelton, *2G HTS Conductors at SuperPower,* (presented at Low Temperature High Field Superconductor Workshop 2012 (LTHFSWS2012), Napa, CA, USA, 2012).

[149] R. Nakasakiet and et al., *Progress of 2G HTS wire development at SuperPower,* (Presented at Applied Superconductivity Conference, ASC 2016, 1MOr2A-03, September 4-9, 2016, Denver, CO, USA, 2016).